

**MASS SPECTROMETRY IONIZATION STUDIES AND METHOD
DEVELOPMENT FOR THE ANALYSIS OF COMPLEX MIXTURES OF
SATURATED HYDROCARBONS AND CRUDE OIL**

by

Jeremy M. Manheim

A Dissertation

Submitted to the Faculty of Purdue University

In Partial Fulfillment of the Requirements for the degree of

Doctor of Philosophy



Department of Chemistry

West Lafayette, Indiana

May 2020

**THE PURDUE UNIVERSITY GRADUATE SCHOOL
STATEMENT OF COMMITTEE APPROVAL**

Dr. Hilkka I. Kenttämäa, Chair

Department of Chemistry

Dr. Scott A. McLuckey

Department of Chemistry

Dr. Mingji Dai

Department of Chemistry

Dr. Peter T. Kissinger

Department of Chemistry

Approved by:

Dr. Christine Hrycyna

For my amazing parents, Kevin and Amy Manheim, and my best friend, Juliet Prieto.

ACKNOWLEDGMENTS

First, I must thank my research advisor, Professor Hilkka I. Kenttämäa, for her dedication to my development as a scientist. I am thankful for her openness, honesty, and guidance throughout my graduate research. I especially appreciate the long hours she committed to help strengthen my technical writing. I would also like to acknowledge my committee members, Professor Scott McLuckey, for helping me call professors by their first name, Professor Mingji Dai, for answering all of my organic chemistry questions even when they were not during office hours, and Professor Peter Kissinger, for always making Analytical Seminar welcoming and entertaining.

I would also like to express my gratitude to my undergraduate research advisor, Professor Igor K. Lednev, who was the driving force behind my decision to apply to graduate school. I am incredibly thankful for your belief in me that I could succeed at the graduate level as well as our continued contact after I graduated from the University at Albany.

Earning my PhD would not have been possible without the help from my peers and friends that I have made while at Purdue University. From the Jonathan Amy Facility for Chemical Instrumentation (JAFCI), I would like to thank Mark Carlsen, Randy Repogle, and Dr. Hartmut Hedderich for their kindness and willingness to help me with my research projects. To my former Kenttämite group members, Mark Romanczyk, Chunfen Jin, Joann Max, Ravikiran Yerabolu, Xueming Dong, and John Kong, thank you so much for teaching me the ropes and for being great mentors during my first years in graduate school. I want to give a special thank you to my labmates Zaikuan (Josh) Yu, Edouard Niyonsaba, Katherine Wehde, and Jacob Milton for not only making my time in lab enjoyable, but also for the friendships we have formed. To all my current Kenttämites, Rashmi Kumar, Xin Ma, Dr. Duanchen Ding, Yuyang Zhang, Lan Xu,

Leah Easterling, Brent Modereger, Jifa Zhang, Hao-Ran (Ben) Lei, Judy Kuan-Yu Liu, Erlu Feng, Victoria Boulos, Wanru Li, Yue (Nancy) Fu, Kawthar Alzarieni, and Jeff Zhang, thank you for making graduate school a great experience.

Finally, this would not be possible without the never-ending love and support from my family. I would like to thank my mom, Amy Manheim, my dad, Kevin Manheim, and my sister, Rachel Manheim, for always being there for me and for calling to check-up on me at least once a week. I am so thankful for their continuous encouragement in all that I do, and they have helped me become the person I am today. A heartfelt and sincere thank you to my wonderful fiancé, Juliet Prieto, who joined me in this adventure to the Midwest to pursue our graduate degrees. I truly appreciate her love, understanding, and her constant reminders to take a break. I am so thankful that I had my best friend and partner in crime with me throughout every stressful moment and accomplishment in graduate school.

TABLE OF CONTENTS

LIST OF TABLES	9
LIST OF FIGURES	10
LIST OF SCHEMES.....	16
ABSTRACT.....	17
CHAPTER 1. INTRODUCTION	18
1.1 Thesis Overview	18
1.2 References.....	19
CHAPTER 2. INSTRUMENTATION THEORY AND OPERATION	20
2.1 Introduction to Mass Spectrometry.....	20
2.2 Ion Generation	23
2.2.1 Atmospheric Pressure Chemical Ionization (APCI).....	24
2.3 Introduction to Linear Quadrupole Ion Trap (LQIT) Mass Spectrometers	31
2.3.1 API House Box and API Stack Regions.....	32
2.3.2 Ion Optics.....	33
2.3.3 Linear Quadrupole Ion Trap	36
2.3.3.1 Ion Storage.....	37
2.3.3.1.1 Ion Trajectory	40
2.3.3.2 Automatic Gain Control	42
2.3.3.3 Ion Manipulation	44
2.3.3.3.1 Ion Ejection	44
2.3.3.3.2 Ion Ejection for Ion Isolation	45
2.3.3.3.3 Collision-activated Dissociation (CAD) in the Ion Trap	47
2.3.3.3.4 CAD in the Ion Optics.....	48
2.3.3.3.5 Ion-Molecule Reactions in an LQIT	48
2.3.3.3.6 Ion Detection.....	51
2.4 Orbitrap Mass Spectrometer	53
2.5 Introduction to Gas Chromatography×Gas Chromatography/Time-of-flight Mass Spectrometry	56
2.5.1 Sample Preparation and Injection.....	59

2.5.2	Development of a GC×GC Method.....	60
2.6.2.1	Development of a Modulator Method.....	62
2.5.3	Development of an EI MS Method.....	67
2.6	References.....	70
CHAPTER 3. AN AUTOMATED METHOD FOR CHEMICAL COMPOSITION ANALYSIS OF LUBRICANT BASE OILS BY USING ATMOSPHERIC PRESSURE CHEMICAL IONIZATION MASS SPECTROMETRY.....		
		78
3.1	Introduction.....	78
3.2	Experimental Section.....	80
3.3	Results and Discussion.....	83
3.3.1	Selection of the Solvent/APCI Reagent for Automated Experiments.....	84
3.3.2	Sample Carryover and Linear Dynamic Range Tests.....	88
3.3.3	Analysis of Base Oil Mass Spectra Measured by Using the Automated (+)APCI/O ₂ /Isooctane Method.....	91
3.4	Conclusions.....	99
3.5	References.....	99
CHAPTER 4. PROTON TRANSFER REACTIONS CAUSE FRAGMENTATION OF SATURATED HYDROCARBONS UPON ATMOSPHERIC PRESSURE CHEMICAL IONIZATION 103		
		103
4.1	Introduction.....	103
4.2	Experimental Section.....	104
4.3	Results and Discussion.....	109
4.3.1	Fragmentation of <i>n</i> -Butylcyclohexane Dissolved in Isooctane upon APCI.....	109
4.3.2	Ion-Molecule Reaction Experiments Between Neutral Saturated Hydrocarbons and Ions Proposed to Cause Their Fragmentation.....	111
4.3.3	New Ion Source Experiments.....	115
4.3.4	Ion-Molecule Reaction Experiments Between Neutral Saturated Hydrocarbons and Ions Generated from Air.....	117
4.3.5	Determination of the Ion-Molecule Reaction Mechanism Between Protonated Molecules and Saturated Hydrocarbons.....	123
4.3.6	Proposal for the Reduction of Saturated Hydrocarbon Fragmentation Upon APCI	128

4.4	Conclusions.....	132
4.5	References.....	133
CHAPTER 5. IDENTIFICATION AND QUANTITATION OF LINEAR SATURATED HYDROCARBONS IN LUBRICANT BASE OILS BY USING GC×GC/EI TOF MASS SPECTROMETRY.....		
		136
5.1	Introduction.....	136
5.2	Experimental Section.....	138
5.3	Results and Discussion.....	144
5.3.1	Identification of the Linear Saturated Hydrocarbons in Base Oils.....	144
5.3.2	Determination of the Accuracy and Precision of the GC×GC/EI TOF MS Method to Quantitate Linear Saturated Hydrocarbons.....	149
5.3.3	Determination of the Percentage of Total Linear Saturated Hydrocarbon Content in Base Oils.....	151
5.4	Conclusions.....	153
5.5	References.....	154
CHAPTER 6. ANALYSIS OF CRUDE OIL COMPONENTS THAT STRONGLY BIND TO KAOLINITE 157		
6.1	Introduction.....	157
6.2	Experimental Section.....	159
6.3	Results and Discussion.....	165
6.3.1	Removal of KBO from Kaolinite and Fractionation of KBO and NBO.....	166
6.3.2	Comparison of the Chemical Compositions of KBO and NBO.....	170
6.3.3	Model Compound Study.....	176
6.4	Conclusions.....	179
6.5	References.....	180
VITA.....		183
PUBLICATIONS.....		184

LIST OF TABLES

Table 3.1 Experimental sequence for evaluating base oil carryover and determining the shortest cleaning time required between sample measurements.	89
Table 3.2 Saturated hydrocarbon class distribution percentages for each base oil determined based on the average of 18 positive-ion mode APCI/O ₂ /isooctane mass spectra.	93
Table 3.3 Within day, between day, and total precision for the automated (+)APCI/O ₂ /isooctane method to determine the saturated hydrocarbon class distribution percentages in each base oil. 94	
Table 4.1 Proton affinities for the potential conjugate bases of the ions of <i>m/z</i> 29 and the neutral molecules selected for bracketing experiments.	121
Table 5.1 Overview of the GC×GC MS method used in the following experiments.	140
Table 5.2 Experimental conditions of GC×GC FID analysis.	141
Table 5.3 Retention times in the polar and nonpolar columns for standard linear saturated hydrocarbons that have similar retention times as compounds in Base Oil A and Base Oil B. N/A denotes “not applicable” as a compound with this retention time was not found in the base oils.	149
Table 5.4 Average accuracy, average within day precision, average between day precision, and total precision for GC×GC/EI TOF MS quantitation of mixtures of model linear saturated hydrocarbons C ₁₄ -C ₁₈ at four different mass fractions.	151
Table 5.5 Example set of concentrations (ppm) of the linear saturated hydrocarbons identified in each base oil as determined by GC×GC/EI TOF MS. Peak areas in both columns were used. The concentration of pentadecane (C ₁₅) in Base Oil B falls outside of the linear dynamic range of the calibration curve.	152
Table 5.6 Total linear saturated hydrocarbon (by weight percent) content identified in each base oil as determined by GC×GC/EI TOF MS and GC×GC/FID.	153
Table 6.1 Average molecular weight of compounds in individual fractions of nonbound oil components (NBO) and kaolinite bound oil components (KBO) determined from low-resolution mass spectra.	170
Table 6.2 Average RDBE and number of carbons for compounds in the individual fractions collected for the NBO and KBO samples as determined from high-resolution mass spectra. ...	173
Table 6.3 Gravimetric weight percentage of the fractions of nonbound oil components (NBO) and kaolinite bound oil components (KBO).	174

LIST OF FIGURES

Figure 2.1. Positive-ion mode 70 eV EI low-resolution mass spectrum of chlorobenzene obtained from the NIST library. Reprinted courtesy of the National Institute of Standards and Technology, U.S. Department of Commerce. Not copyrightable in the United States.	22
Figure 2.2 Diagram of an APCI source in the API house box of the LQIT mass spectrometers used here.....	26
Figure 2.3 Illustration of the APCI mechanism for analyte ion formation via a series of ion-molecule reactions occurring upon and/or after a corona discharge.....	29
Figure 2.4 Positive ion mode APCI mass spectrum of hexane measured on the LQIT used in this dissertation.	31
Figure 2.5 Profile view of the API house box and API stack region with the pressures in each section (red).	33
Figure 2.6 Schematic of the ion optics portion of the LQIT MS with the different pressure regions indicated (red).	34
Figure 2.7 Diagram indicating the DC voltages that were applied to the different multipoles and lenses of the ion optics to create the downhill potential gradient.	35
Figure 2.8 Representative graph of the RF voltages applied to opposite pairs of rods of the multipoles. “A” shows the polarity of the voltages applied to the x- and y-pair of rods at some point in time, while “B” shows the point in time when these pairs of rods have a voltage with the opposite polarity applied to them than that applied at time “A.”.....	36
Figure 2.9 Schematic of the ion trap showing the three different sections and the slit in x-rods where ions exited to the detector.	37
Figure 2.10 The potential energy well that formed by lowering the DC voltage applied to the center section below that of the front and back sections. Ions were confined to the middle of the trap after collisions with the helium buffer gas because they do not have enough kinetic energy to exit via the front and back sections.....	38
Figure 2.11 Two images of the ion trap comparing the spatial distribution of the ions in the trap when helium buffer gas is not present (top) to when it is present (bottom).	39
Figure 2.12 Mathieu stability diagram. The y- and x-axes are the Mathieu stability parameters, a and q, respectively. A q value of 0.908 indicates the trajectory where ions become unstable on the x-axis. Three ions of different m/z ratios, purple, orange, and green, are depicted where their a and q values would lie in the stability region. Since the green ion is the smallest ion, it has the highest q value, while the largest ion, purple, has the lowest q value.....	41
Figure 2.13 Diagram showing the voltages to the gate lens when it was “open”, i.e., has a lower voltage than lens 1 applied to it, vs when it was “closed”, i.e. had a higher voltage than lens 1 applied to it.	43

Figure 2.14 A distribution of frequencies between 5 and 500 kHz, comprising the secular frequencies of all ions except that of the ion to be trapped, was applied to the <i>x</i> -rods. All ions except the ion of interest (red) were removed from the trap.....	46
Figure 2.15 Diagram of the Brauman double-well potential energy surface model. The lines above the reactants and the transition state represent the rovibrational energy levels; their spacing is indicative of the relative “tightness” of each transition state.....	49
Figure 2.16 The setup utilized to introduce neutral compounds in a controlled manner into the ion trap of the LQIT to study ion-molecule reactions.....	51
Figure 2.17 A conversion dynode and an electron multiplier makeup the two detectors for the LQIT. Ions (green) strike the conversion dynode, releasing secondary particles that accelerate into the electron multiplier, hit its surface and eject electrons from its surface. A measurable current reaches the anode and an electric signal is sent to the data system.	52
Figure 2.18 Schematic of the two electrodes of the orbitrap mass analyzer and the ion motion between them.	55
Figure 2.19 Schematic of the LQIT coupled to an orbitrap mass spectrometer.	56
Figure 2.20 Schematic of a GC×GC/EI TOF MS. The GC×GC consists of two columns and the modulator, while the TOF MS consists of the EI source, the TOF mass analyzer, and the detector.	58
Figure 2.21 Reversed phase 2D-GC×GC/EI TOF MS total ion current chromatogram of a base oil. Each black dot represents a single compound that has eluted from both columns and was detected by the TOF MS.	59
Figure 2.22 Three GC×GC/EI TOF MS total ion current chromatograms that show how the secondary column retention times for three highlighted peaks decrease as the secondary oven offset temperature increases from 5 °C (left), to 15 °C (middle), and to 30 °C (right).	62
Figure 2.23 Schematic of the quad-jet dual stage thermal modulator. Each stage consists of a hot jet and a cold jet.	63
Figure 2.24 The four phases of hot and cold jet pulses over the course of one modulation period. Purple circles represent compounds that are in the gas phase, while blue circles represent cryo-focused compounds. The arrows represent the direction in which the compounds travel starting from the primary column, through stage 1 of the modulator, to stage 2 of the modulator, and finally into the secondary column.	64
Figure 2.25 Three 2D-GC×GC/EI TOF MS total ion current chromatograms that show how the secondary column retention times for three highlighted peaks change as the time of the modulation period increases from 1 s (left), to 2 s (middle), and to 8 s (right).	66
Figure 2.26 Flow chart of the different times the hot and cold jets are turned on in each stage given a 4 s modulation period and 0.5 s hot pulse time.....	67
Figure 2.27 Positive-ion mode EI mass spectrum measured for an unknown compound (top) that was predicted to be pentadecane based on the closest match with an EI mass spectrum in the NIST	

library (bottom). The NIST library mass spectrum has a 93% similarity match with the measured EI mass spectrum.	68
Figure 2.28 Picture of the folded flight path of ions in the TOF MS employed here. Ions travel in a zig-zag motion between the gridless mirrors and through the periodic ion lenses from the first section into the last section and then back to the first section where they strike the detector.	70
Figure 3.1 Direct-infusion positive-ion mode APCI/O ₂ mass spectra of a 2 mM equimolar saturated hydrocarbon mixture dissolved in hexane (A), methylcyclohexane (B), and isooctane (C).	86
Figure 3.2 Direct-infusion positive-ion mode APCI/O ₂ mass spectra of each neat saturated hydrocarbon model compound dissolved in isooctane. The most abundant fragment ions are present in the squalane and 5- α -cholestane mass spectra.	87
Figure 3.3 Relative abundance of the [M-H] ⁺ ions of pristane and fragment ions of saturated hydrocarbons in base oils (ions of <i>m/z</i> 267) dissolved in isooctane after spiking the middle viscosity base oil with six different amounts of pristane.	90
Figure 3.4 Triplicate measurements of the relative abundances of the [M-H] ⁺ ions (<i>m/z</i> 267) of pristane and fragment ions of saturated hydrocarbons in base oils (ions of <i>m/z</i> 267) dissolved in isooctane as a function of the concentration of pristane in the middle viscosity base oil. A linear relationship was observed between 0.3 mg/mL and 3.0 mg/mL.	91
Figure 3.5 Individual (not averaged) positive ion mode APCI/O ₂ /isooctane mass spectra of the low, middle, and heavy viscosity base oils after injection using the automated method.	92
Figure 3.6 Three positive ion mode APCI/O ₂ /isooctane mass spectra measured on the same day (right; top and middle mass spectra) and in different days (right; top and middle mass spectra vs. bottom mass spectrum) for the middle viscosity base oil by using the automated method. Total ion chromatograms (left of the mass spectra) end at two minutes due to the two minute sample analysis time.	95
Figure 3.7 Ion abundance plotted as a function of the number of carbons for the six saturated hydrocarbon classes in the low viscosity base oil in isooctane. Ion abundances are an average of those measured in 18 mass spectra. Error bars represent the range of ion abundances for each carbon number.	97
Figure 3.8 Ion abundance plotted as a function of the number of carbons for the six saturated hydrocarbon classes in the middle viscosity base oil in isooctane. Ion abundances are an average of those measured in 18 mass spectra. Error bars represent the range of ion abundances for each carbon number.	97
Figure 3.9 Ion abundance plotted as a function of the number of carbons for the six saturated hydrocarbon classes in the heavy viscosity base oil in isooctane. Ion abundances are an average of those measured in 18 mass spectra. Error bars represent the range of ion abundances for each carbon number.	98
Figure 3.10 Ion abundances plotted as a function of <i>m/z</i> values ions generated from the mono-, di-, tri- and tetracyclic and acyclic saturated hydrocarbons with 36-46 carbon atoms in the heavy viscosity base oil in isooctane.	98

Figure 4.1 (A) Picture of the positioning of the stainless steel (SS) tube ion source in the API max house box. (B) Picture of the SS tube ion source. (C) Sketch of the SS tube ion source and commercial APCI source in the API house box. Voltages applied to the SS tube ion source and direction of sheath/auxiliary gas (N₂), reagent gas and sample flow are indicated on the diagram. Red, orange, and green dots represent reagent ions generated in the SS tube ion source. Purple dots represent neutral analyte compounds that come from the APCI source without a corona discharge needle. 107

Figure 4.2 Photograph of the arrangement and connections of the equipment used to introduce gaseous solvent through the SS tube ion source. 108

Figure 4.3 (A) Full and zoomed-in direct-infusion (+)APCI mass spectra of *n*-butylcyclohexane (MW 140 Da) dissolved in isooctane. The [M-H]⁺ and fragment ions of *n*-butylcyclohexane and isooctane are blue and red, respectively. (B) (+)APCI mass spectrum of neat *n*-butylcyclohexane. (C) (+)APCI mass spectrum of neat isooctane. 111

Figure 4.4 (A) Direct-infusion (+)APCI mass spectrum of neat *n*-butylcyclohexane. (B) Ion-molecule mass spectrum measured after 0.03 ms reaction between molecular ions of *m/z* 32 with neutral *n*-butylcyclohexane in the ion trap. The [M-H]⁺ ions of *n*-butylcyclohexane are colored blue, the M⁺ ions of *n*-butylcyclohexane are colored red, odd-mass fragment ions of *n*-butylcyclohexane are colored orange, and even-mass fragment ions are colored purple. 113

Figure 4.5 Direct-infusion (+)APCI mass spectrum of neat *n*-butylcyclohexane (A). Ion-molecule mass spectra measured after 500 ms reaction between the most abundant fragment ion of isooctane of *m/z* 57 and *n*-butylcyclohexane at normalized CAD energies of (B) 0, (C) 0.1, and (D) 4.0 (arbitrary units). CAD greater than 4 resulted in a poor signal. The [M-H]⁺ ion of *n*-butylcyclohexane is colored blue and the fragment ions of *n*-butylcyclohexane are colored orange. Overlap between the isolated ion of *m/z* 57 and product fragment ions of *m/z* 57 from *n*-butylcyclohexane is unlikely because the more abundant fragment ions of *m/z* 83 and 97 are not observed. 114

Figure 4.6 Direct-infusion (+)APCI mass spectrum of neat *n*-butylcyclohexane (A). The [M-H]⁺ ion of *n*-butylcyclohexane is colored blue and the fragment ions of *n*-butylcyclohexane are colored orange. Ion-molecule mass spectra measured after 1000 ms reaction between the minor fragment ions of isooctane of *m/z* 71 (B) and *m/z* 99 (C) and *n*-butylcyclohexane. 115

Figure 4.7 (A) Direct-infusion (+)APCI mass spectrum of the middle viscosity base oil dissolved in isooctane. (B) Direct-infusion (+)SS tube ion source mass spectrum of the middle viscosity base oil dissolved in isooctane. 116

Figure 4.8 (A) Direct-infusion (+)APCI mass spectrum measured for N₂ gas without accelerating voltages. (B) Direct-infusion (+)APCI mass spectrum measured for N₂ gas with 100 V accelerating voltages. 117

Figure 4.9 (A) Direct-infusion (+)APCI mass spectrum of neat *n*-butylcyclohexane. (B) Ion-molecule mass spectrum measured after 0.03 ms reaction between ions of *m/z* 29 and neutral *n*-butylcyclohexane. The [M-H]⁺ ion of *n*-butylcyclohexane is colored blue and fragment ions of *n*-butylcyclohexane are colored orange. Both mass spectra are zoomed-in on the *m/z* range 55–150. 119

Figure 4.10 Flow chart demonstrating the possible identities of ions of m/z 29 from proton transfer reactions.	122
Figure 4.11 Ion-molecule mass spectra measured after 0.03 ms reaction between ions of m/z 29 with (A) benzene, (B) hexafluorobenzene, (C) carbon dioxide. Protonated product ions were observed in all three mass spectra.....	123
Figure 4.12 (A) Direct infusion (+)APCI mass spectrum of neat <i>n</i> -butylcyclohexane. (B) Full and zoomed-in ion-molecule mass spectra measured after 0.03 ms reaction between protonated formaldehyde (m/z 31) and neutral <i>n</i> -butylcyclohexane. The $[M-H]^+$ ion of <i>n</i> -butylcyclohexane is colored blue and fragment ions of <i>n</i> -butylcyclohexane are colored orange.	125
Figure 4.13 Ion-molecule mass spectra measured after 0.03 ms reaction between protonated formaldehyde (m/z 31) and cyclohexane (A) and cyclohexane- d_{12} (B). The $[M-H]^+$ ion of cyclohexane is colored blue, and the $[M-D]^+$ and $[M-D_2+H]^+$ ions of cyclohexane- d_{12} are colored orange.....	127
Figure 4.14 MS/MS/MS CAD mass spectra of the ion of m/z 94 (top) and the ion of m/z 93 (bottom). Mass spectra were measured at normalized collision energy of 20. The $[M-D]^+$ ion of cyclohexane- d_{12} is colored orange, the fragment ion of m/z 94 is colored black, the $[M-D_2+H]^+$ ion of cyclohexane- d_{12} is colored blue, and the fragment ions of m/z 93 are colored purple.	127
Figure 4.15 Direct infusion (+)APCI mass spectrum of neat isooctane (A). Ion-molecule mass spectra measured after 0.03 ms reaction between the protonated molecule of nitrogen (m/z 29) with neutral isooctane (B). Ion-molecule mass spectra measured after 0.03 ms reaction between the protonated molecule of formaldehyde (m/z 31) with neutral isooctane (C). The $[M-H]^+$ ion of isooctane is colored blue and fragment ions are colored orange. All mass spectra are zoomed-in on the m/z range 50-140.	129
Figure 4.16 Direct infusion (+)APCI mass spectrum of neat hexane (A). Ion-molecule mass spectra measured after 0.03 ms reaction between the protonated molecule of nitrogen (m/z 29) with neutral hexane (B). Ion-molecule mass spectra measured after 0.03 ms reaction between the protonated molecule of formaldehyde (m/z 31) with neutral isooctane (C). The $[M-H]^+$ ion of hexane is colored blue and fragment ions are colored orange. All mass spectra are zoomed-in on the m/z range 50-140.	130
Figure 5.1 Direct-infusion (+)APCI/O ₂ /isooctane LQIT mass spectra measured for Base Oil A (top) and Base Oil B (bottom). The ions of m/z 391 originated from the PEEK tubing.....	145
Figure 5.2 EI (70 eV) TOF mass spectrum measured for tetradecane by GC×GC/EI TOF MS (top) and the best matched EI mass spectrum from the NIST library- pentadecane.	146
Figure 5.3 EI (70 eV) TOF mass spectrum measured for pentadecane by GC×GC/EI TOF MS (top) and the best matched EI mass spectrum from the NIST library- heptadecane.	147
Figure 5.4 GC×GC total ion current chromatograms measured for Base Oil A (left) and Base Oil B (right), respectively, by using GC×GC/EI TOF MS. Black squares represent the linear saturated hydrocarbons, green dots represent the branched saturated hydrocarbons, red dots represent the mono-, di-, and tricyclic saturated hydrocarbons, and blue dots represent the tetra- and pentacyclic saturated hydrocarbons. The greyscale legend at the right of each total ion current chromatogram is indicative of the chromatographic peak areas.	148

Figure 5.5 Calibration plots for mixtures of standard linear saturated hydrocarbons C₁₄-C₁₈. Each point is the average of three measurements and the error bars represent the standard deviation. 150

Figure 6.1 Flow chart demonstrating how the KBO and NBO samples were prepared and fractionated into three fractions of different polarities. 161

Figure 6.2 TGA plot (top) and FTIR spectrum (bottom) measured for pure kaolinite. A 13.3% mass loss is observed between 450 – 650 °C in the TGA plot. 167

Figure 6.3 TGA plot of kaolinite with KBO (sample #1; red), kaolinite with KBO after elution by *n*-hexane (sample #2, green), kaolinite with KBO after elution by *n*-hexane and dichloromethane (sample #3, pink), and kaolinite with KBO after elution by *n*-hexane, dichloromethane, and isopropanol (sample #4, black). Dashed traces are the first derivatives of the solid traces. For instance, the red dash is the first derivative of the solid red dash. 168

Figure 6.4 FTIR spectra of kaolinite with KBO (sample #1; light blue), kaolinite with KBO after elution by *n*-hexane (sample #2; light green), kaolinite with KBO after elution by *n*-hexane and dichloromethane (sample #3; dark green), and kaolinite with KBO after elution by *n*-hexane, dichloromethane, and isopropanol (sample #4; pink). 169

Figure 6.5 Direct-infusion (+)APCI mass spectra of the *n*-hexane (A), dichloromethane (B), and isopropanol (C) fractions of the KBO sample. Ions marked with * are due to impurities. 171

Figure 6.6 Direct-infusion (+)APCI mass spectra of the *n*-hexane (A), dichloromethane (B), and isopropanol (C) fractions of the NBO sample. Ions marked with * are impurities. 172

Figure 6.7 RDBE presented as a function of the number of carbon atoms for compounds in the *n*-hexane, dichloromethane, and isopropanol fractions of KBO (A, C, and E, respectively) and NBO (B, D, and F, respectively). Black dots represent compounds that contain only carbon and hydrogen atoms. Red dots represent compounds that contain carbon and hydrogen atoms as well as heteroatoms, including oxygen, nitrogen, and/or sulfur. 174

Figure 6.8 Approximate consolidated weight percentages for compounds with different elemental compositions derived from equation 6.3 for compounds in KBO and NBO. The subscripts x, y, and z are any positive integer numbers (not zero). 176

Figure 6.9 Structures of the four model compounds that were used to make the model mixture. 177

Figure 6.10 Relative GC peak area for each model compound in the nonbound and kaolinite bound samples measured by using GC/EI MS. 179

LIST OF SCHEMES

Scheme 2.1. Gas-phase ionization reactions that can occur between a reagent (R) ion and analyte (M) upon CI.	24
Scheme 2.2 Gas-phase ionization reactions that can occur between nitrogen nebulizing gas and atmospheric molecules in the presence of a corona discharge.	27
Scheme 2.3 Electron transfer reaction gas-phase ionization reactions that can occur when nebulizing gas, solvent (R), and analyte (M) are in the presence of a corona discharge. This is the major reaction when R ⁺ ions are not Bronsted acids.	28
Scheme 2.4 Ion-molecule reactions proposed to occur upon corona discharge of hexane (R) to generate [R-H] ⁺ ions of hexane.....	29
Scheme 4.1 The newly proposed APCI mechanism of saturated hydrocarbons. Methylcyclohexane is used as the example saturated hydrocarbon analyte. Step 4 shows the formation of [M-H] ⁺ product ions; this step also leads to the formation of fragment ions.	131

ABSTRACT

Crude oil is a mixture of hydrocarbons so complex that it is predicted to comprise as many compounds as there are genes in the human genome. Developing methods to not only recover crude oil from the ground but also to convert crude oil into desirable products is challenging due to its complex nature. Thus, the petroleum industry relies heavily on analytical techniques to characterize the oil in reservoirs prior to enhanced oil recovery efforts and to evaluate the chemical compositions of their crude oil based products. Mass spectrometry (MS) is the only analytical technique that has the potential to provide elemental composition as well as structural information for the individual compounds that comprise petroleum samples. The continuous development of ionization techniques and mass analyzers, and other instrumentation advances, have primed mass spectrometry as the go-to analytical technique for providing solutions to problems faced by the petroleum industry. The research discussed in this dissertation can be divided into three parts: developing novel mass spectrometry-based methods to characterize mixtures of saturated hydrocarbons in petroleum products (Chapters 3 and 5), exploring the cause of fragmentation of saturated hydrocarbons upon atmospheric pressure chemical ionization to improve the analysis of samples containing these compounds (Chapter 4), and developing a better understanding of the chemical composition of crude oil that tightly binds to reservoir surfaces to improve chemically enhanced oil recovery (Chapter 6).

CHAPTER 1. INTRODUCTION

1.1 Thesis Overview

Mass spectrometry (MS) is one of the most powerful analytical techniques for determining the elemental composition and structure of unknown compounds in mixtures. MS was introduced at the turn of the 20th century by the physicist J.J. Thomson, who was most famous for his Nobel Prize winning discovery of electrons.¹ Thomson, along with Francis Aston (1922 Nobel Prize winner in Chemistry), built the first mass spectrometer and succeeded in separating and measuring the masses of charged atoms.¹ Mass spectrometry has evolved into an essential analytical technique for addressing numerous scientific challenges including resolving ionic isotopes,¹ elucidating the structures of unknown compounds,² and sequencing proteins.³

The principles of mass spectrometry have not changed since its inception. Neutral compounds cannot be separated with this technique, so analysis by mass spectrometry requires the evaporation and ionization of compounds. Gas-phase ions can be manipulated and separated based on their mass-to-charge ratio (m/z) under high vacuum by taking advantage of electromagnetic fields.⁴ The relative abundances of all the gas-phase ions are plotted as a function of their m/z in a mass spectrum. In addition to the mass of an ion, an ion's elemental composition can be determined with high-resolution mass spectrometers.⁵ Furthermore, several mass spectrometers can be used for tandem mass spectrometry (MS^n) experiments to facilitate the determination of an ion's structure.⁶

The research presented in this dissertation focuses on improving the mass spectrometry analysis of mixtures of saturated hydrocarbons and crude oil. Chapter 2 of this thesis provides an overview of mass spectrometry as well as the ionization techniques and mass spectrometers utilized in this research. Chapter 3 describes the development of an automated method to obtain

precise chemical information for base oils. This new method uses atmospheric pressure chemical ionization mass spectrometry (APCI MS) with O₂ gas as the sheath/auxiliary gas and isooctane as the APCI solvent/reagent. Chapter 4 focuses on determining the cause of fragmentation of saturated hydrocarbons upon APCI via ion-molecule reactions in a linear quadrupole ion trap mass spectrometer. Chapter 5 discusses the validation of a two-dimensional gas chromatography/ (electron ionization) time-of-flight mass spectrometry method to identify and quantify the linear saturated hydrocarbons in base oils. Chapter 6 details the characterization of those compounds in crude oil that are most strongly bound to kaolinite, a clay mineral commonly found in oil reservoirs, via high-resolution mass spectrometry measurements.

1.2 References

- (1) Griffiths, J. A Brief History of Mass Spectrometry. *Anal. Chem.* **2008**, *80* (15), 5678–5683.
- (2) Hunt, D. F.; Yates, J. R.; Shabanowitz, J.; Winston, S.; Hauer, C. R. Protein Sequencing by Tandem Mass Spectrometry. *Proc. Natl. Acad. Sci. U S A* **1986**, *83* (17), 6233–6237.
- (3) Kind, T.; Fiehn, O. Advances in Structure Elucidation of Small Molecules Using Mass Spectrometry. *Bioanal. Rev.* **2010**, *2* (1–4), 23–60.
- (4) Hoffmann, E. de; Stroobant, V. *Mass Spectrometry: Principles and Applications*, 3rd edition.; Wiley-Interscience: Chichester, 2007.
- (5) Marshall, A. G.; Rodgers, R. P. Petroleomics: Chemistry of the Underworld. *PNAS* **2008**, *105* (47), 18090–18095.
- (6) McLuckey, S. A.; Goeringer, D. E. Special Feature: Tutorial Slow Heating Methods in Tandem Mass Spectrometry. *J. Mass Spectrom.* **1997**, *32* (5), 461–474.

CHAPTER 2. INSTRUMENTATION THEORY AND OPERATION

2.1 Introduction to Mass Spectrometry

Mass spectrometry (MS) has become an essential analytical tool in many fields of science, including petroleum research,¹ biochemistry,² environmental science,³ materials science,⁴ forensic science,⁵ and medicine.⁶ MS has been utilized to determine the chemical structures of unknown compounds,⁷⁻¹⁰ identify thousands of compounds in complex samples such as crude oil,¹¹ and determine the rates of chemical reactions.^{12,13} The success of MS and its wide range of applications are owed to the continuous development of ionization techniques, mass analyzers, and ways to couple other instrumentation to the MS, such as gas and liquid chromatography.

There are three essential components of every mass spectrometer: 1) an ion source that converts the sample into gas-phase ions, 2) a mass analyzer that separates gas-phase ions based on their mass-to-charge (m/z) ratios, and 3) a detector. To generate positive or negative gas-phase ions from liquid samples, the liquid can either be 1) ionized in the liquid phase first before evaporation into the gas phase, or 2) evaporated followed by ionization. The former is accomplished with ionization techniques such as electrospray ionization (ESI) and matrix-assisted laser desorption ionization (MALDI), while the latter is accomplished with ionization techniques such as electron impact (EI) ionization and atmospheric pressure chemical ionization (APCI).¹⁴⁻¹⁶ Polar polymers and proteins, for example, are ionized efficiently using ESI or MALDI as these ionization techniques work well for compounds with ionizable functional groups that decompose when heated.^{17,18} Hydrocarbons, on the other hand, are most effectively ionized by APCI as APCI is best suited for compounds that are not thermally labile.¹⁹

After ionization, the ions are separated in the mass analyzer based on their m/z . After this, they are either detected or subjected to tandem mass spectrometry (MS^n) experiments to determine

their chemical structures or to study their gas-phase reactions;²⁰⁻²² not all mass spectrometers can conduct MSⁿ experiments. Typical tandem mass spectrometry experiments involve isolating ions of a specific m/z in the mass analyzer, accelerating them, and subjecting them to energetic collisions with a neutral gas in a reaction chamber to produce fragment ions that are characteristic of the ion's structure.²³ Alternatively, the isolated ions can be subjected to ion-molecule reactions with a neutral reagent gas. The reaction products and rates of product formation can often be studied.^{24,25} Product ions generated by either fragmentation or ion-molecule reactions can be further isolated and subjected to fragmentation and/or ion-molecule reactions in MSⁿ experiments ($n \geq 2$). After the last MSⁿ event, product ions are separated based on their m/z in the mass analyzer and transmitted to the detector.

The data are presented in a mass spectrum that shows relative ion abundances (y -axis) as a function of the ions' m/z values (x -axis). As most of this dissertation focuses on interpreting mass spectra, a brief overview on how to interpret a mass spectrum is presented. Figure 2.1 shows an example of a low-resolution 70 eV electron ionization (EI) mass spectrum of chlorobenzene; EI will be discussed in greater detail in sections 2.2 and 2.5. A high-resolution mass spectrometer (capable of highly accurate mass measurements) could be used to assign the elemental compositions for the ions, however, this type of mass spectrometer was not used to measure this EI mass spectrum. First, the peak at m/z 112 is assigned to correspond to the molecular ion (M^{++}) as it is the peak with the greatest m/z -value and still reasonable isotope peaks associated with it: ¹³C peak at m/z 113 and ³⁷Cl peak at m/z 114 with roughly a third of the height of the peak at m/z 112. This ratio is the same as the naturally occurring abundance of the ³⁷Cl isotope compared to the ³⁵Cl isotope. Furthermore, a peak of m/z 77 corresponds to an ion that has lost a chlorine atom from the molecular ion ($[M-Cl]^+$) as no ³⁷Cl isotope peak is observed. A peak at m/z 77 is usually

indicative of a benzene ring in the compound. The wealth of information that can be obtained from a mass spectrum demonstrates the strength of mass spectrometry as a powerful technique for determining the identity and structure of unknown chemical compounds.

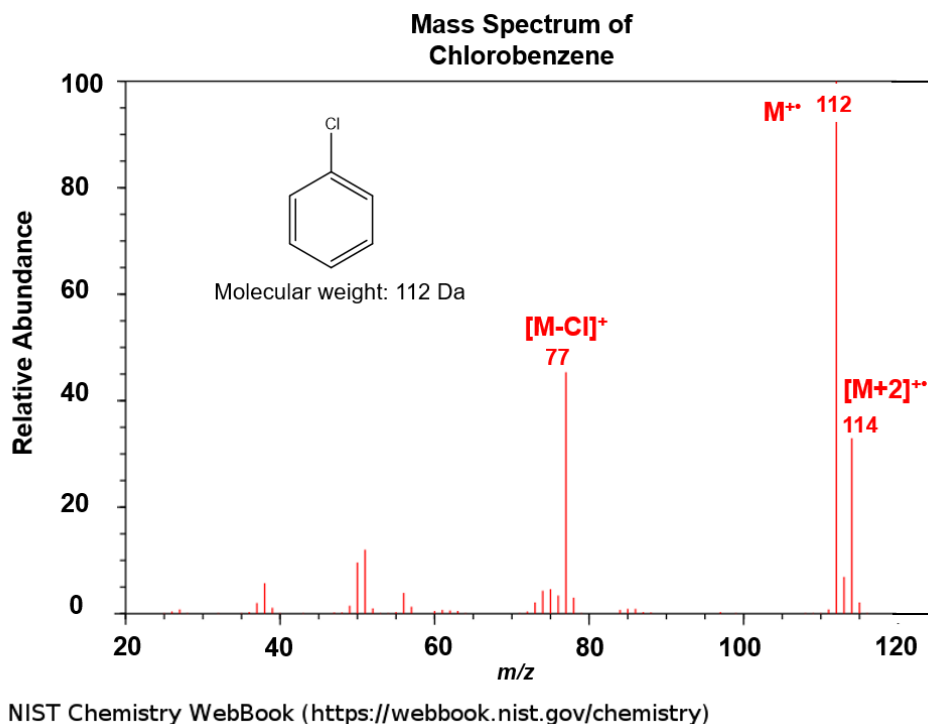
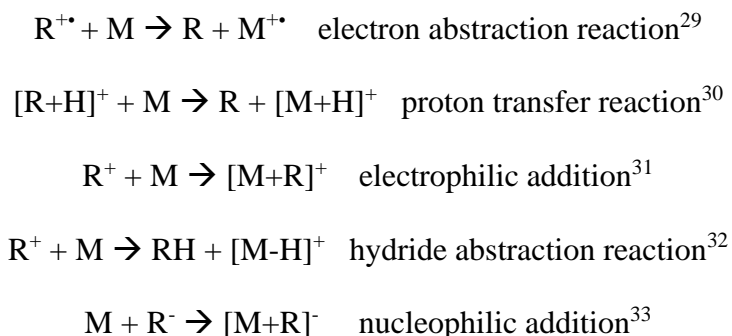


Figure 2.1. Positive-ion mode 70 eV EI low-resolution mass spectrum of chlorobenzene obtained from the NIST library. Reprinted courtesy of the National Institute of Standards and Technology, U.S. Department of Commerce. Not copyrightable in the United States.

In this dissertation, APCI and EI were used to generate gas-phase ions. The background and ionization mechanism of APCI will be described in section 2.2, while EI will be reviewed in sections 2.2 and 2.5. In the sections following, the theory and operation of the three mass spectrometers utilized for this work, a linear quadrupole ion trap mass spectrometer (LQIT MS), an orbitrap mass spectrometer, and a two-dimensional gas chromatograph/electron ionization time-of-flight mass spectrometer (GC×GC/(EI) TOF MS), will be discussed.

2.2 Ion Generation

One of the early ionization techniques to generate gas-phase ions under vacuum conditions was electron ionization (EI).²⁶ In EI, the sample is first evaporated (usually thermally) and then transferred into an ion source in vacuum. Vaporized compounds are then bombarded by a beam of high-energy electrons (70 eV kinetic energy), which results in the ejection of an electron from them, generating molecular ions (M^+ ions). For many compounds, EI causes complete fragmentation such that no molecular ion is observed in the EI mass spectrum. This makes determination of the MW and the elemental composition of an unknown analyte challenging. Therefore, “softer” ionization methods have been developed to ionize compounds without breaking the original structure. Chemical ionization (CI) was one of the first soft ionization techniques.¹⁴ It was developed by Talrosen in the 1950’s and made universally applicable in the 1960’s by Munson and Field.^{27,28} Unlike in EI, where a gaseous sample is ionized by an electron beam, CI utilizes a reagent gas that is in excess to the analyte by 10^3 - 10^4 times. The reagent gas is ionized first by electron bombardment, generating reagent ions (molecular ions and/or fragment ions) that then ionize the gaseous analyte. The selection of the reagent gas influences the type of product ions formed from the analyte (Scheme 2.1).



Scheme 2.1. Gas-phase ionization reactions that can occur between a reagent (R) ion and analyte (M) upon CI.

Both EI and CI are conducted in low-pressure ion sources. In the 1970's, the development of new ionization techniques that could operate in atmosphere began for two reasons: 1) the desire to use a mass spectrometer as the analyzer and detector for online liquid chromatographic (LC) separations,¹⁴ and 2) nonvolatile and thermally labile compounds, such as polymers and biomolecules, decompose upon thermal evaporation prior to EI and CI. One of the most popular atmospheric pressure ionization (API) methods developed was APCI.³⁴ The next section delves into the history and the yet controversial mechanism(s) of APCI.

2.2.1 Atmospheric Pressure Chemical Ionization (APCI)

Three common approaches were initially employed for the generation of gas-phase analyte ions upon API: 1) irradiation by α particles,³⁵ 2) irradiation by β particles - traditionally from a nickel-63 source,³⁶ and 3) electron ionization by a corona discharge.³⁷ The major drawback of using α particles was that it required radioactive materials. Therefore, this method of ionization is no longer used. When comparing the ionization efficiency of a nickel-63 source to a corona discharge, it was determined that a corona discharge generated three times as many analyte ions as a nickel-63 source.³⁸ Additionally, a corona discharge was easier to design and maintain than a

nickle-63 source.³⁹ Therefore, ionization of gaseous analytes via a corona discharge was the most popular of these API techniques- this technique is termed APCI.

APCI is essentially the atmospheric-pressure variation of vacuum chemical ionization (described previously in section 2.2).³⁴ In APCI, a corona discharge is initiated between a stainless steel needle and a counter electrode to generate a reagent plasma. Gaseous ions formed in the reagent plasma undergo numerous collisions with neutral particles to initiate a series of ion-molecule reactions to form reagent ions that ionize gaseous analytes via similar reactions as shown in scheme 2.1. A diagram of an APCI source, like the one used in this work, is presented in Figure 2.2. Liquid samples are injected into a heated source either with a syringe or via a LC at flow rates of 3-100 $\mu\text{L}/\text{min}$ and 200-2,000 $\mu\text{L}/\text{min}$, respectively. Sample flows through a 0.15 mm inner diameter (ID) silica tube towards the spray nozzle where it is mixed with a nebulizer gas (nitrogen) and dispersed into droplets. The nebulizer gas helps direct the flow of sample to the MS inlet as well as aid in sample evaporation.⁴⁰⁻⁴² The aerosolized liquid then enters the ceramic heater where it is vaporized at temperatures 150-450 $^{\circ}\text{C}$. The higher the boiling point of the compound, the higher the vaporizer temperature needs to be to ensure that all of the compounds are in the gas phase prior to ionization.

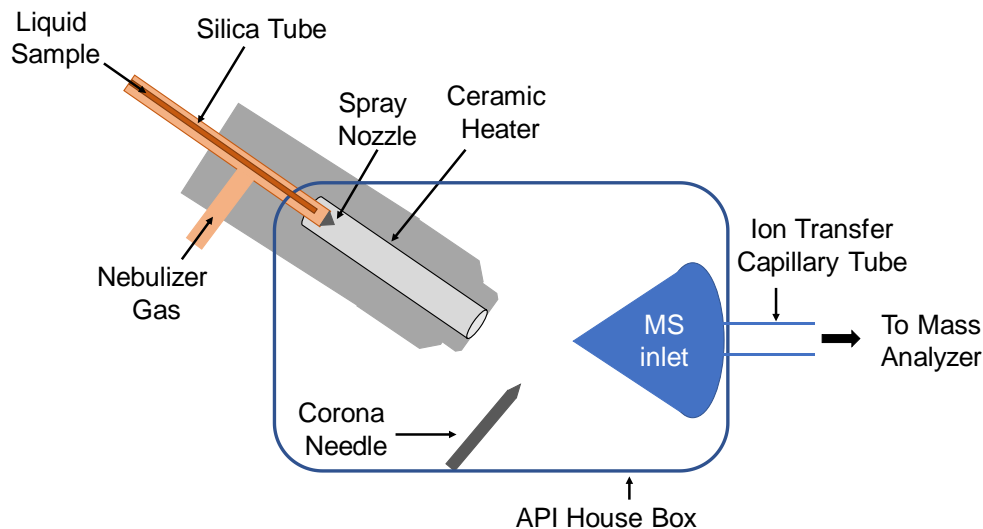
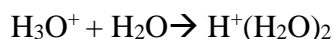
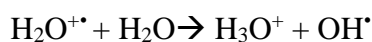
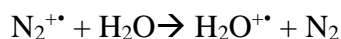
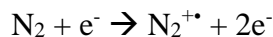


Figure 2.2 Diagram of an APCI source in the API house box of the LQIT mass spectrometers used here.

The gaseous sample then enters the “API house” box where the corona needle and the MS inlet are located. Between the point of the corona needle, kept at $\pm 3\text{-}5$ kV, and the MS inlet, kept at $\pm 0\text{-}60$ V, is an electric field. At the tip of the needle, where the electric field is the strongest, high energy electrons collide with neutral molecules in the air and generate atmospheric ions around the tip of the corona needle; this is referred to as a corona induced plasma, or corona discharge.⁴³ The ions formed in the corona discharge are the species proposed to be responsible for initiating the APCI process.

Extensive fundamental studies on APCI have been carried out to understand how ions are formed by this technique. M. M. Shahin, one of the first scientists to study the APCI mechanism, analyzed the ions generated in atmosphere by a corona discharge when only nebulizing gases (no liquid sample) were used.⁴⁴ Interestingly, protonated clusters of water, such as $(\text{H}_2\text{O})_n\text{H}^+$, and other ionic clusters, such as $(\text{H}_2\text{O})_n(\text{NO}^+)$, where n is 1-8, were detected when air, nitrogen, and oxygen, each with and without water vapor present, were used. These results were similar to those obtained in API experiments that utilized α - and β -particles.^{38,45} Based on these results, several ion-molecule

reactions must be taking place between the tip of the corona needle and the mass analyzer.³⁷ Scheme 2.2 summarizes the ion-molecule reactions proposed to occur when only a nebulizing gas was introduced into the APCI source. Although Scheme 2.2 shows only nitrogen nebulizing gas, this scheme was also applied to oxygen nebulizing gas.⁴⁴

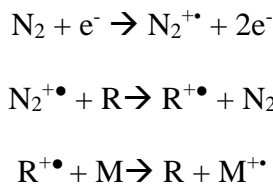


Scheme 2.2 Gas-phase ionization reactions that can occur between nitrogen nebulizing gas and atmospheric molecules in the presence of a corona discharge.

In the above APCI reaction sequence, nitrogen nebulizing gas is ionized first because it is the most abundant species present in the corona discharge. When generating positive ions, high energy electrons bombard nitrogen molecules, ejecting an electron from some of the nitrogen molecules to form nitrogen molecular ions, $\text{N}_2^{+\bullet}$. $\text{N}_2^{+\bullet}$ ions will then undergo electron abstraction reactions with neutral atmospheric molecules, such as water, to generate the molecular ions of water, $\text{H}_2\text{O}^{+\bullet}$. Electron transfer between $\text{N}_2^{+\bullet}$ and neutral water is favorable because the ionization energy (IE) of nitrogen is greater (15.58 eV) than that of water (12.62 eV).⁴⁶ Next, $\text{H}_2\text{O}^{+\bullet}$ protonates surrounding neutral water molecules to form H_3O^+ cations and hydroxy radicals, OH^\bullet , as shown in step 3 of Scheme 2.2. This reaction is favorable because hydrogen atom-containing molecular ions are strong Brønsted acids.⁴⁷ Similar to ionization energy for electron transfer reactions, when the proton affinity of a neutral molecule is greater than that of the conjugate base of a protonated

molecule, a favorable proton-transfer reaction occurs. Lastly, in step 4, neutral water molecules solvate protonated water.⁴⁸

Introduction of gaseous solvent and analyte molecules into the corona discharge, in addition to the nebulizing gas, changes the ions observed in the APCI mass spectrum. Protonated water clusters, for example, are no longer observed in the APCI mass spectrum because atmospheric water is present in much lower abundances compared to the solvent and analyte.⁴² Instead, ions derived from the analyte, and sometimes from the solvent, are observed in the APCI mass spectrum. Scheme 2.3 shows the general APCI mechanism when solvent and analyte are introduced through the APCI source; Scheme 2.3 only shows an electron transfer reaction. After $N_2^{+\bullet}$ ions are formed from the nebulizing gas, $N_2^{+\bullet}$ ions are proposed to abstract an electron from the solvent (R); the solvent is the second most abundant species present in the corona discharge. Reagent ions ($R^{+\bullet}$) that are not Bronsted acids will undergo electron transfer reactions with analytes (M) to generate molecular ions ($M^{+\bullet}$); the analyte is the next most abundant species in the corona discharge. $R^{+\bullet}$ ions that are Bronsted acids will prefer to transfer a proton to the analyte to generate protonated analytes ($[M + H]^+$). Figure 2.3 depicts the ion-molecule reactions occurring in the APCI mechanism proposed for all analytes.



Scheme 2.3 Electron transfer reaction gas-phase ionization reactions that can occur when nebulizing gas, solvent (R), and analyte (M) are in the presence of a corona discharge. This is the major reaction when $R^{+\bullet}$ ions are not Bronsted acids.

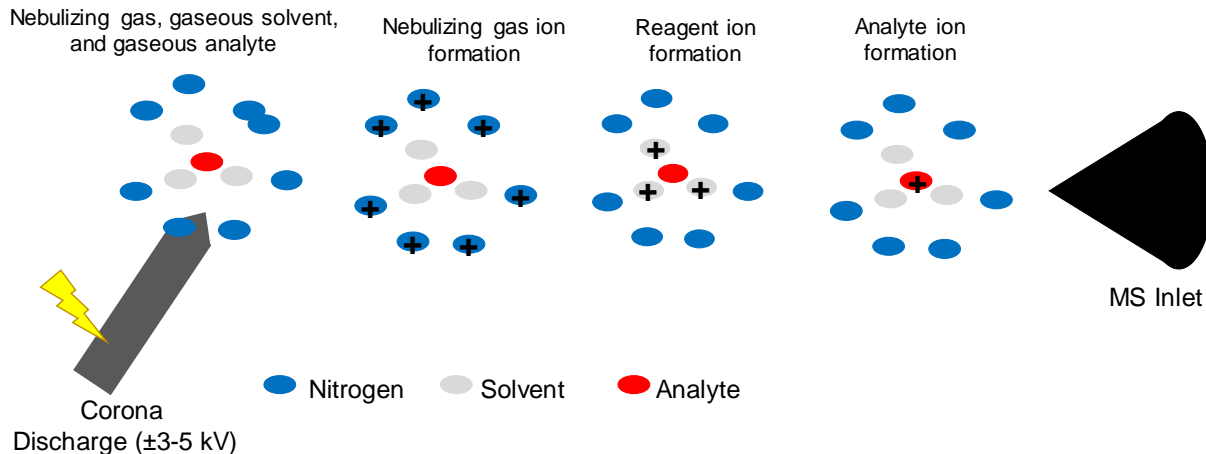
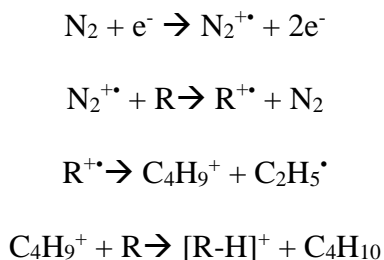


Figure 2.3 Illustration of the APCI mechanism for analyte ion formation via a series of ion-molecule reactions occurring upon and/or after a corona discharge.

The APCI mechanism presented in Scheme 2.3 can differ depending on the solvent/APCI reagent. For example, APCI of the solvent carbon disulfide (CS_2) generates only molecular ions (R^+) as shown in Scheme 2.3, while APCI of the solvent hexane (C_6H_{14}) primarily generates $[\text{R}-\text{H}]^+$ ions.^{40,49} Carroll et al. were the first to propose the APCI mechanism for saturated hydrocarbons.⁵⁰ The positive ion mode APCI mass spectrum of hexane (MW = 86 Da) displays an abundant ion of m/z 85, $[\text{R}-\text{H}]^+$, and several smaller fragment ions separated by 14 m/z units. The formation of the $[\text{R}-\text{H}]^+$ ion of hexane upon APCI was rationalized by Carroll et al.⁵⁰ as follows:



Scheme 2.4 Ion-molecule reactions proposed to occur upon corona discharge of hexane (R) to generate $[\text{R}-\text{H}]^+$ ions of hexane.

In Scheme 2.4, ion-molecule reactions occur between $N_2^{+•}$ and neutral hexane to produce $R^{+•}$ ions of hexane; this is similar to step 2 in Scheme 2.2 and Scheme 2.3. In step 3 of Scheme 2.4, $R^{+•}$ ions are proposed to dissociate, generating fragment ions of m/z 57, $C_4H_9^+$, and the neutral radical, $C_2H_5^•$. Step 3 of Scheme 2.3 (not in the general APCI mechanism) likely occurs because removing an electron from a saturated hydrocarbon, containing only single bonds, weakens the bonds in the entire molecule leading to facile fragmentation. In the final step of the proposed APCI mechanism for saturated hydrocarbons, ions of m/z 57 abstract a hydride from neutral hexane molecules to generate $[R-H]^+$ ions.⁵⁰ Previous CI studies on NO^+ reagent ions led to the proposal that carbenium ions can abstract a hydride from saturated hydrocarbons to generate $[R-H]^+$ ions and fragment ions.^{51,52} Therefore, *hydride abstraction* by carbenium ions was proposed to be the APCI mechanism for saturated hydrocarbons.⁵⁰

Fragmentation of saturated hydrocarbons upon APCI is a major obstacle for the MS analysis of this class of compounds. For example, the fragment ions of hexane in the APCI mass spectrum (Figure 2.4) could be misinterpreted as $[R-H]^+$ ions of pentane ($[R-14]^+$), butane ($[R-29]^+$), and propane ($[R-43]^+$). Therefore, one could mistakenly conclude from this APCI mass spectrum that four saturated hydrocarbons, rather than only hexane, are present. Eliminating, or reducing, saturated hydrocarbon fragmentation upon APCI is a major focus of this dissertation and is detailed in Chapter 4.

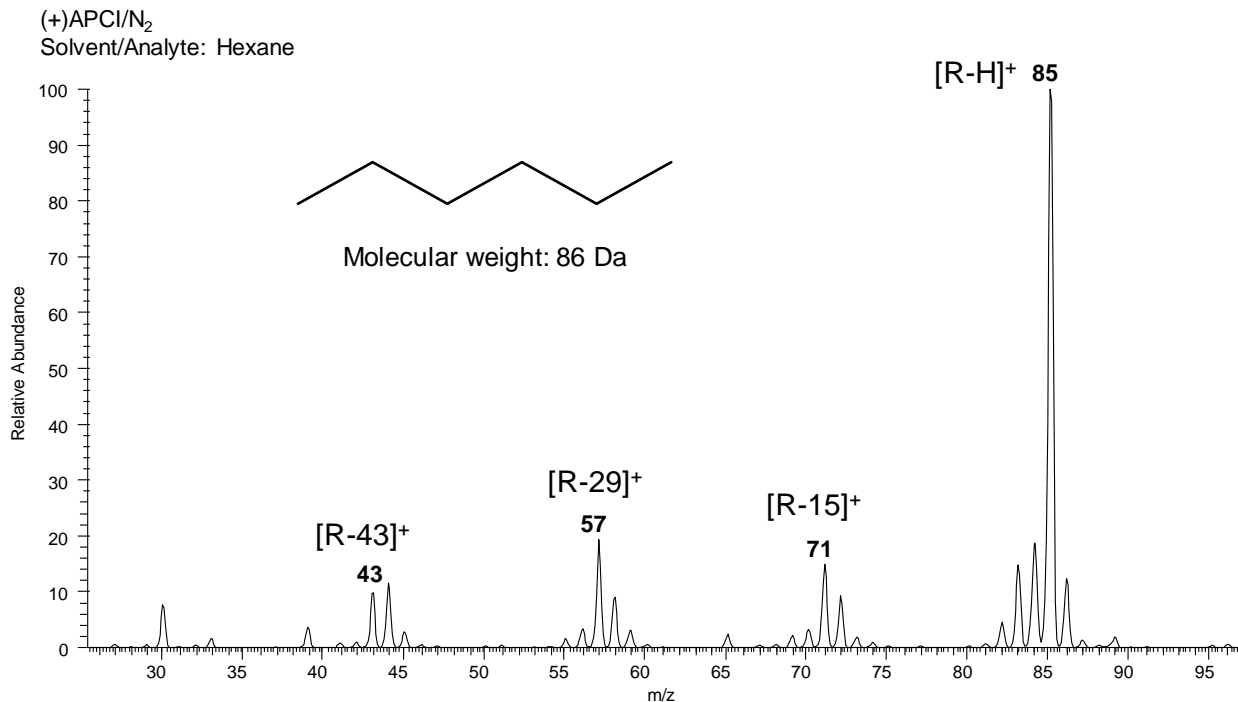


Figure 2.4 Positive ion mode APCI mass spectrum of hexane measured on the LQIT used in this dissertation.

2.3 Introduction to Linear Quadrupole Ion Trap (LQIT) Mass Spectrometers

In this dissertation, gas-phase ions generated by APCI were studied using a Thermo Scientific LTQ two-dimensional, or linear, quadrupole ion trap (LQIT) mass spectrometer (MS). Invented in 2002 by Schwartz et al., the LQIT MS is the upgraded version of the three-dimensional quadrupole ion trap (QIT) as it can trap a greater number and wider mass range of ions.^{53,54} An additional advantage is that ions trapped in the LQIT are ejected through two sides of the ion trap for detection in two electron multipliers, unlike in QIT wherein the ions are only detected using one electron multiplier.⁵⁵ Furthermore, the LQIT design enables easier coupling to other instrumentation, such as a high-resolution orbitrap MS.⁵³ The four parts of the LQIT MS that will be discussed in detail in the following sections are: 1) the API house box, 2) the ion optics, 3) the linear quadrupole ion trap (LQIT) - the mass analyzer, and 4) the detectors.

2.3.1 API House Box and API Stack Regions

Figure 2.5 displays the parts of the API house box and API stack, and the pressures in each region. Two external connections on the outside of the box (**green**) provided sheath and auxiliary gas (nebulizing gas) to the APCI source, while two additional connections provided voltages to the APCI source and the corona needle. The downhill pressure gradient between the API house box and API stack (760 torr to 1 torr) helped draw ions into the mass spectrometer. Two Edwards E2M30 rotary-vane mechanical pumps (650 L/min) maintained the 1 torr pressure in the API stack; the pressure was constantly monitored by a convectron gauge. The API stack contained the ion transfer capillary tube, tube lens, and skimmer. DC voltages applied to the ion transfer capillary tube, ± 0 -60 V, and the tube lens, ± 10 -100 V, positive voltage for positive ions and negative voltage for negative ions, decelerated and focused ions into the center of the ion transfer capillary tube, while opposite polarity ions collided into its sides and got neutralized. The greater the magnitude of the DC voltages, the better the focusing of larger ions; however, this may cause undesired fragmentation.

A downhill potential gradient existed between the tube lens and the narrow opening of the skimmer that was held at 0 V. This assisted in drawing ions further into the mass spectrometer in a controlled manner. Furthermore, the skimmer was positioned offset from the axis of the ion transfer capillary tube and tube lens, causing neutral molecules to crash into the walls of the skimmer. In this manner, only ions made it through to the ion optics.

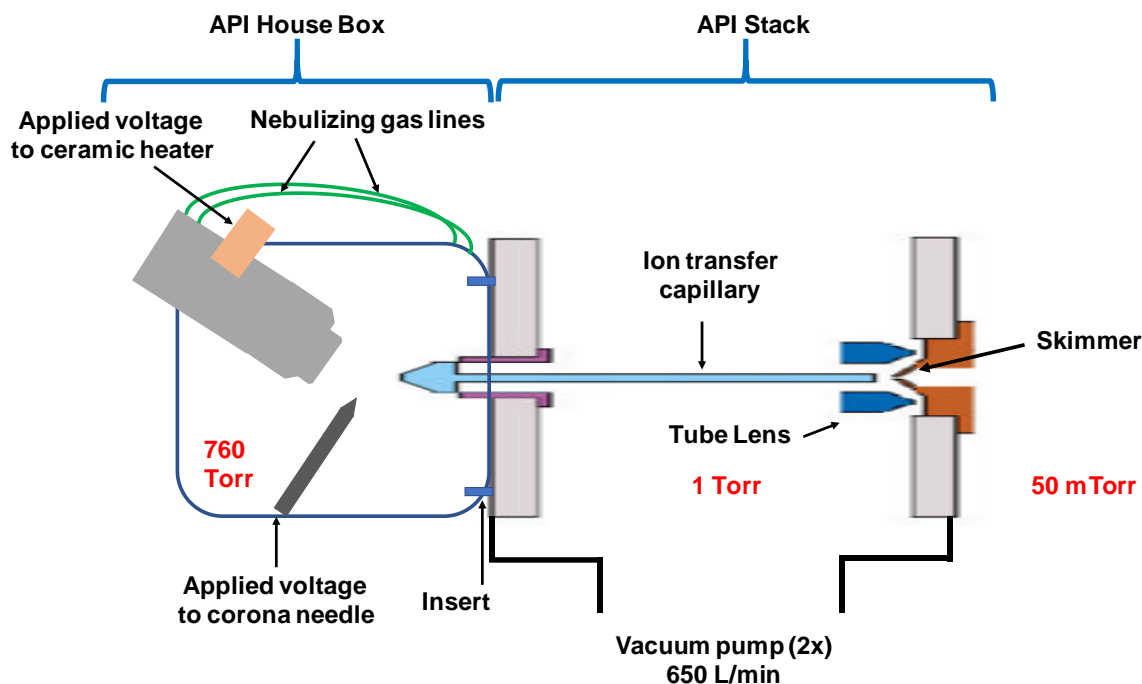


Figure 2.5 Profile view of the API house box and API stack region with the pressures in each section (red).

2.3.2 Ion Optics

The purpose of the ion optics section of the LQIT MS was to control the injection of ions into the mass analyzer. When ions entered the higher vacuum regions of the mass spectrometer from atmosphere, they underwent *thermal expansion*. This means that the ions' position and trajectory changed dramatically from the original path in the ion transfer capillary after they passed into the API stack and ion optic regions. Without any means of focusing ions back into the center and controlling their movement, they could not be successfully analyzed.

Figure 2.6 shows the different multipoles, lenses, and pressures in the ion optics region. Three multipole ion guides: two square-rod quadrupoles, Q00 and Q0, and one round octupole, Q1 were part of this region. The combination of square quadrupoles and a round octupole allowed for a wide mass range of ions to have stable trajectories.⁵⁴ Additionally, this combination of

multipoles enabled high ion transfer efficiency between each successive region of the ion optics. The optical lenses focused the ions toward the center as well as acted as vacuum baffles between each multipole. Applied to each of the three multipoles and four lenses (lens 0, lens 1, gate lens, and front lens), was a DC voltage of opposite polarity to that of the ions. For positive ions, negative voltages were applied. The negative DC voltage applied to each multipole and lens became greater in magnitude as the ions travelled through. In this way, an increasing negative potential gradient was established along the center of the mass spectrometer (z -direction) that pulled the ions toward the ion trap. Figure 2.7 depicts the potential gradient that existed between the APCI source and the front lens.

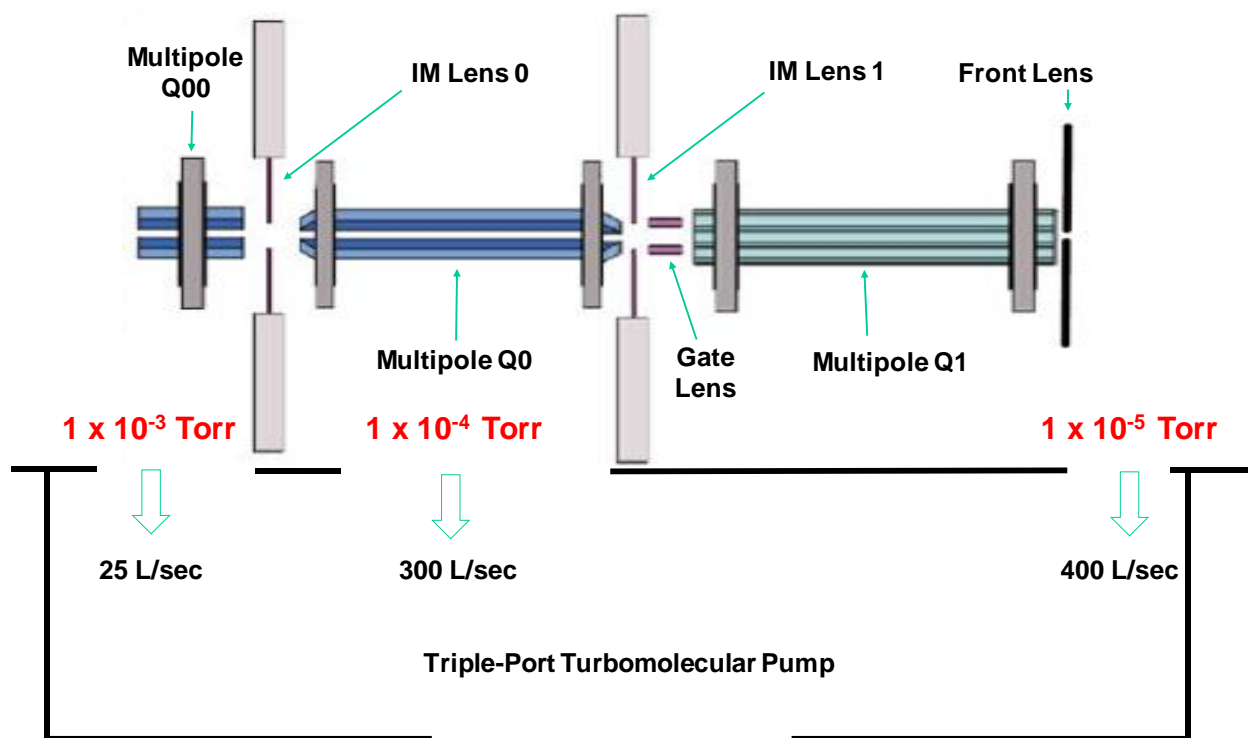


Figure 2.6 Schematic of the ion optics portion of the LQIT MS with the different pressure regions indicated (red).

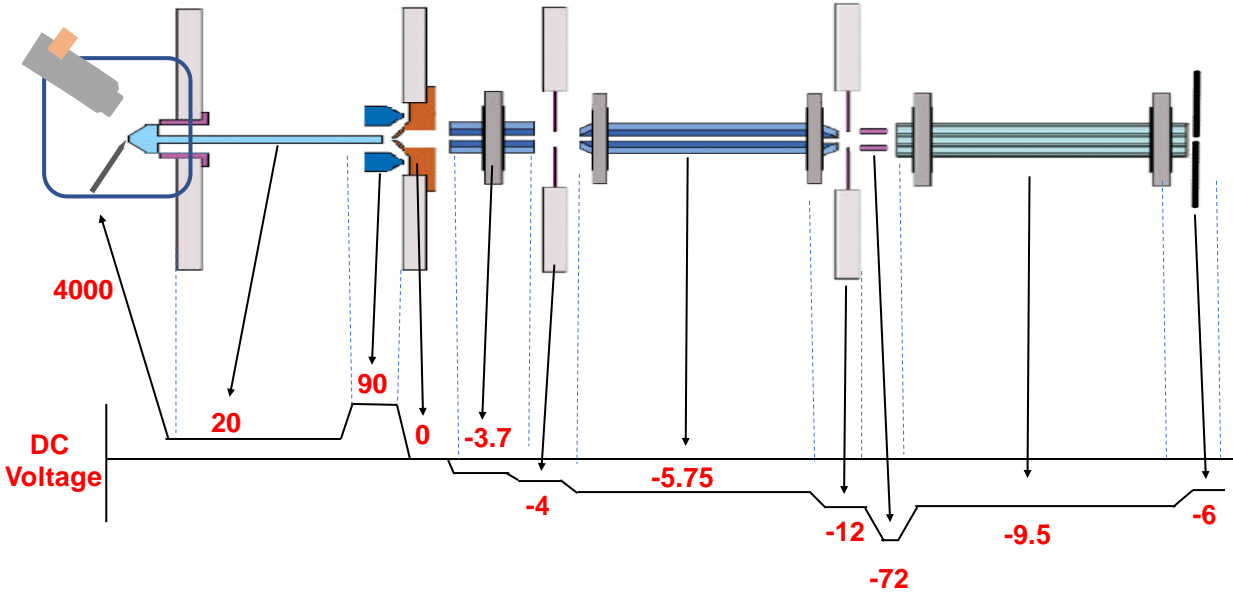


Figure 2.7 Diagram indicating the DC voltages that were applied to the different multipoles and lenses of the ion optics to create the downhill potential gradient.

Ions had to be focused in the x - and y -directions to avoid collisions with the sides of the rods or lenses. Therefore, a radio frequency (RF) voltage with the same amplitude and phase was applied to opposite rods but one that was 180° out-of-phase was applied to adjacent rods to accomplish this task. Figure 2.8 shows a plot of the oscillating RF voltages where the y -axis is the amplitude of the RF voltage and the x -axis is time. The RF voltage oscillates in a characteristic sine wave where when one set is positive, the other is negative, and vice versa over time. Positive ions will be attracted towards the rods with negative voltages applied to them while they will be repelled by the rods with positive voltages applied to them. Since the polarity of the voltages applied to adjacent rods is alternating rapidly, the ions approach each rod without colliding into them. The ions' motion through the RF field is best described as resembling a corkscrew.

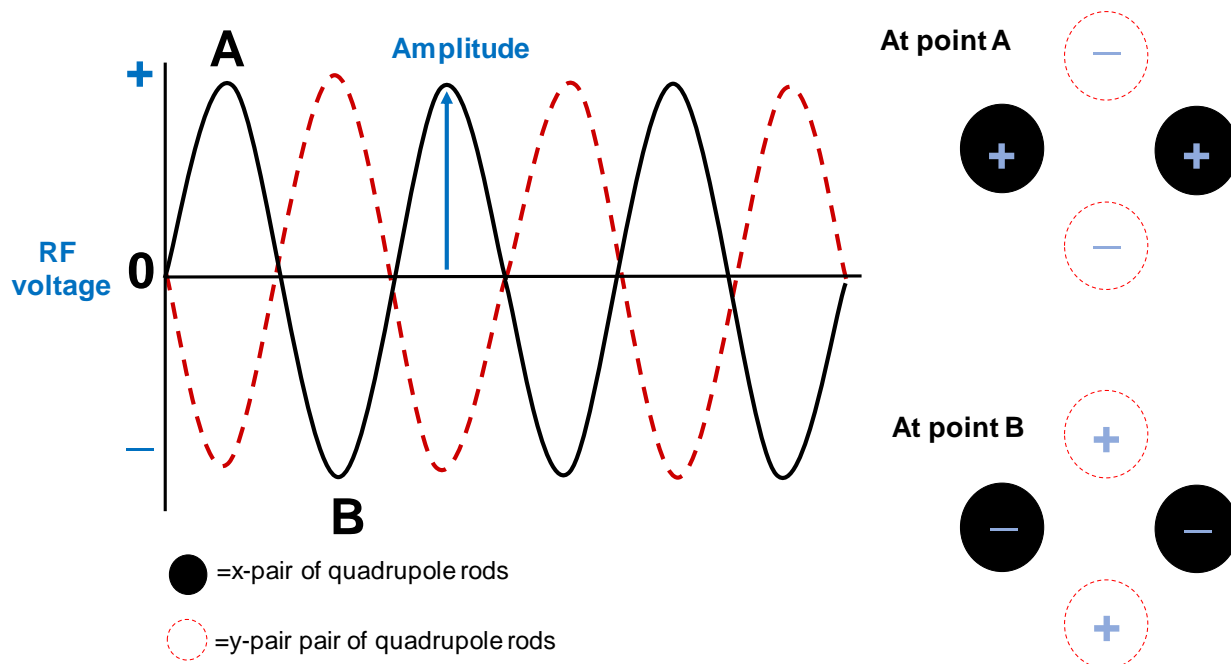


Figure 2.8 Representative graph of the RF voltages applied to opposite pairs of rods of the multipoles. “A” shows the polarity of the voltages applied to the x- and y-pair of rods at some point in time, while “B” shows the point in time when these pairs of rods have a voltage with the opposite polarity applied to them than that applied at time “A.”

2.3.3 Linear Quadrupole Ion Trap

The ion trap mass analyzer was held at a pressure of 10^{-5} torr to facilitate the manipulation of ions. It was made up of four precision-machined and precision aligned hyperbolic rods, two x-rods and two y-rods. Each rod had a front, middle, and back section (Figure 2.9). The pair of x-rods had slits in the middle section that ions were ejected through to the detector. Through a combination of DC and RF voltages as well as an inert buffer gas, this mass analyzer can be used to store, isolate, fragment and detect ions. The principles that govern these functions of the ion trap will be elaborated on in the following four parts.

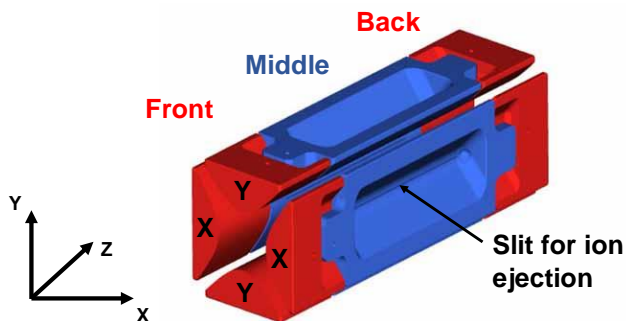


Figure 2.9 Schematic of the ion trap showing the three different sections and the slit in x-rods where ions exited to the detector.

2.3.3.1 Ion Storage

Ions were stored in the middle section of the ion trap before being ejected out for ion isolation or detection. This was achieved by using a combination of DC and RF voltages and a buffer gas. For positively charged ions, negative DC voltages of equal magnitude were applied to the front and back sections of the ion trap. These two voltages were lower in magnitude (less negative) than the DC voltage applied to the middle section. In this manner, the DC voltages created a potential energy well in the z -direction.⁵⁶ Figure 2.10 depicts the potential energy well that was generated by the DC voltages applied to the three parts of the ion trap. As ions traveled through the front and middle section of the ion trap due to the downhill potential gradient, they encountered an uphill potential gradient between the middle and back sections. This prevented the incoming ions from exiting the trap. The ions then cycled back and forth in the z -direction between the front and back sections, colliding with helium buffer gas and cooling down (explained in the last paragraph of this section), thus remaining confined to the middle of the trap.

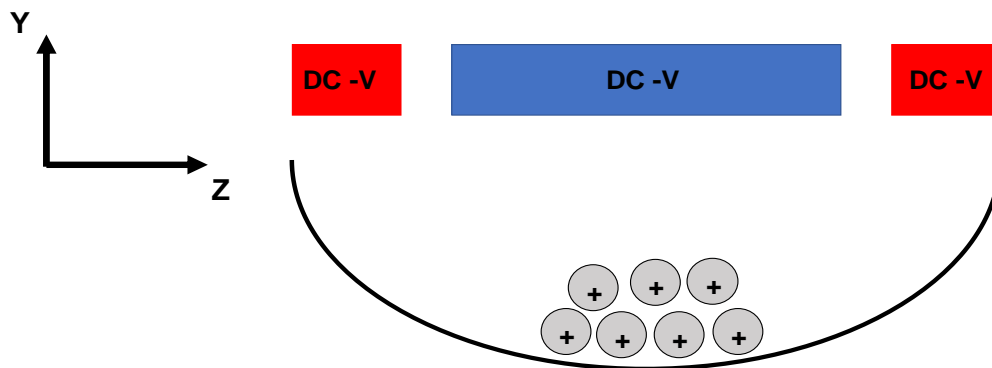


Figure 2.10 The potential energy well that formed by lowering the DC voltage applied to the center section below that of the front and back sections. Ions were confined to the middle of the trap after collisions with the helium buffer gas because they do not have enough kinetic energy to exit via the front and back sections.

The RF voltages prevented ions from colliding with the sides of the hyperbolic rods. Similar to the RF voltages in the ion optics, these RF voltages oscillated the ions in the x - and y -dimensions. This was accomplished by applying RF voltages of the same magnitude, phase and frequency to opposite pairs of rods but voltages that were 180° out-of-phase to adjacent rods in all three sections; this RF voltage will be referred to as the *main RF voltage* throughout the rest of section 2.3. The main RF voltage applied to all four hyperbolic rods generated a *quadrupolar field* that influenced the radial (side-to-side) motion of ions in the trap.⁵⁷ In a quadrupolar field, the force exerted by the electric potential on an ion increases as it travels further away from the center of the trap. This *restoring force* focused the ions into the center, thus enabling easier manipulation of the ions for isolation, excitation, and detection.⁵⁶

Lastly, the buffer gas assists in storing and detecting ions by cooling them down, which locates them into the center of the middle section. When ions collided with the buffer gas, they transferred some of their kinetic energy into the gas. The more collisions the ions underwent, the lower were their kinetic energies, i.e., the ions were located in the center of the trap in a smaller volume. Helium gas is typically used as the buffer gas for three reasons: 1) it has low chemical

reactivity, 2) it is a small atom, and 3) it is relatively inexpensive.⁵⁸ The benefit of using this inert gas is that collisions between ions and helium do not lead to unwanted reaction product ions or fragment ions. Figure 2.11 depicts the position of the ions in the ion trap with and without buffer gas.

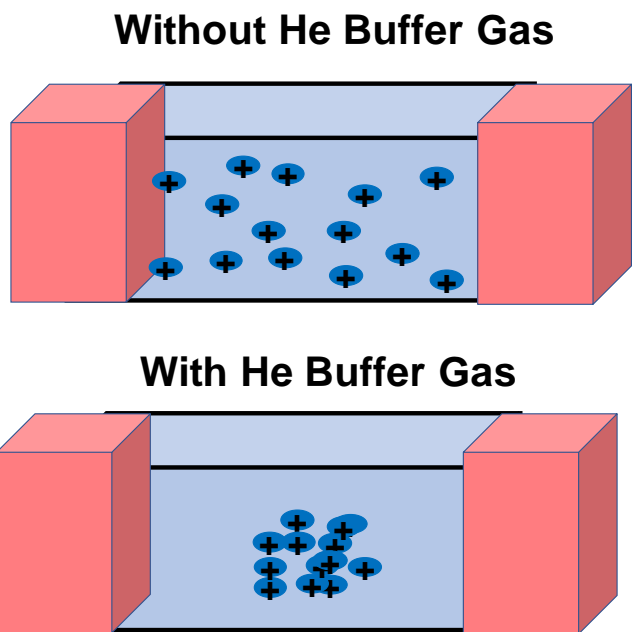


Figure 2.11 Two images of the ion trap comparing the spatial distribution of the ions in the trap when helium buffer gas is not present (top) to when it is present (bottom).

Without above three conditions, DC and RF voltages and helium buffer gas, ions could not be stored in the ion trap. However, the size of the ion trap as well as the magnitudes of the DC voltage and amplitude of the RF voltage limit the number and the mass range of the ions that can be successfully stored. In other words, there is a maximum number of ions within a defined mass range that can be stored in the ion trap.

2.3.3.1.1 Ion Trajectory

As briefly eluded to in the above section, the position of the ions in the middle of the ion trap was influenced by the electric potential that was created by the RF voltages applied to all four hyperbolic rods. To successfully store ions, it was important to understand the relationship between the strength of the electric field and the trajectory of the ions in the trap. The Mathieu differential equation is used in quadrupole mass spectrometry to accurately describe the trajectory of an ion's motion.⁵⁹ The Mathieu differential equation is shown below:

$$\frac{d^2u}{d\xi^2} + (a_u + 2q_u \cos 2\xi)u = 0 \quad (\text{Equation 2.1})$$

where u is a single coordinate (x , y , or z), ξ is a term proportional to time by $\xi = \Omega t/2$, where Ω is the angular frequency of the main RF voltage, and a_u and q_u are dimensionless *Mathieu parameters* that are related to the DC voltage and the amplitude of the main RF voltage, respectively. The Mathieu parameters, a_u and q_u , describe an ion's motion in the ion trap based on the different regions of the *Mathieu stability diagram* as shown in Figure 2.12. Any ion whose trajectory lies within the stability region of the diagram is predicted to be confined in the ion trap, while other ions outside the stability region will collide with the rods or exit the trap. The relationship between the Mathieu parameters and DC voltage and amplitude of the main RF voltage are more clearly depicted in the following equations:

$$a_u = a_x = (-)a_y = \frac{8zeU}{mr_0^2\Omega^2} \quad (\text{Equation 2.2})$$

$$q_u = q_x = (-)q_y = \frac{4zeV}{mr_0^2\Omega^2} \quad (\text{Equation 2.3})$$

where m is the mass of the ion, z is the charge of the ion, r_0 is the radius of the ion trap, U is the applied DC voltage, and V is the amplitude of the applied RF voltage. It is evident from these

equations that as the magnitude of the DC voltage and the amplitude of the main RF voltage increase, values of the Mathieu parameters increase as well. Additionally, a and q are related to the reciprocal of m/z ; therefore, for the same change in the DC voltage or the main RF amplitude, large ions will have a small change in their Mathieu parameters, while small ions will have a large change in their Mathieu parameters.

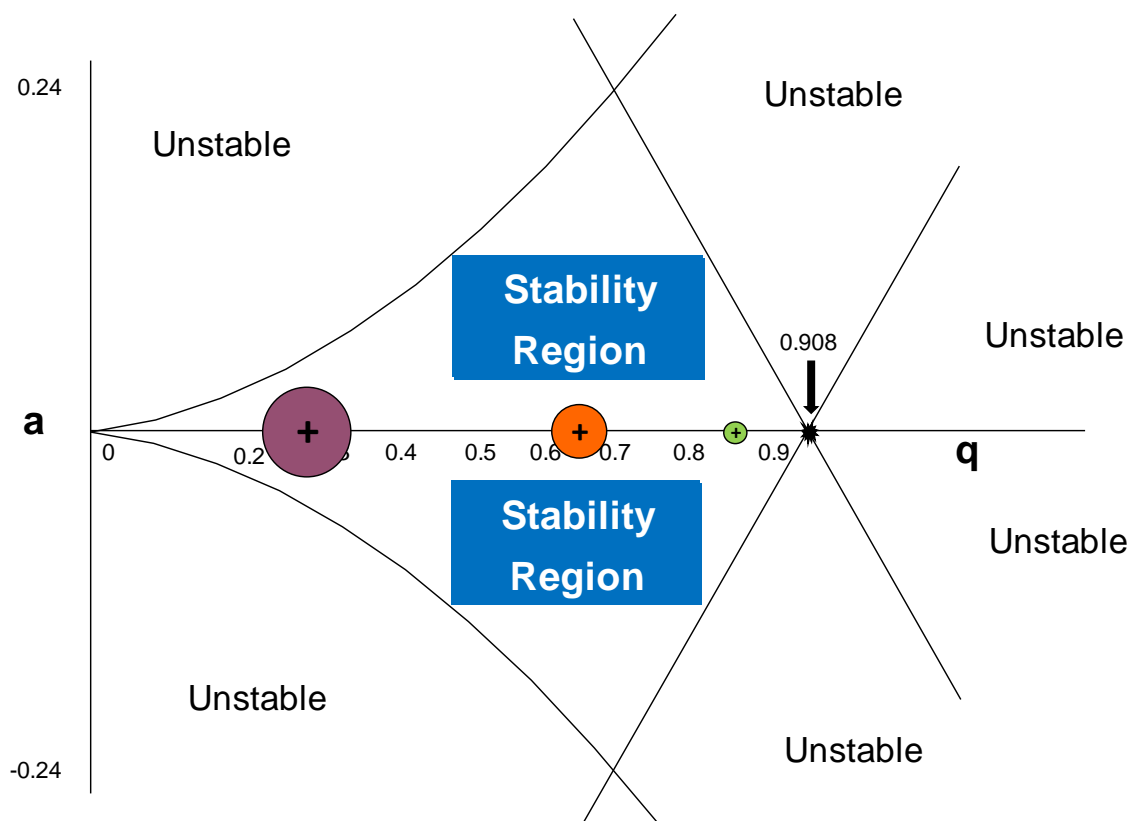


Figure 2.12 Mathieu stability diagram. The y - and x -axes are the Mathieu stability parameters, a and q , respectively. A q value of 0.908 indicates the trajectory where ions become unstable on the x -axis. Three ions of different m/z ratios, purple, orange, and green, are depicted where their a and q values would lie in the stability region. Since the green ion is the smallest ion, it has the highest q value, while the largest ion, purple, has the lowest q value.

Furthermore, changing the magnitude of the applied DC voltages and amplitude of the applied main RF voltage would greatly impact the mass range of the ions that have stable motions in the ion trap. To store the widest mass range of ions, the Mathieu parameter a_{H} was usually set to

zero. Therefore, the amplitude of the main RF voltage influenced the mass range of ions that could be successfully confined in the ion trap. The widest three mass ranges that can be achieved with the LQIT MS were m/z 15-200 (low-mass range), m/z 50-2000 (normal-mass range), and m/z 100-4000 (high-mass range).

2.3.3.2 Automatic Gain Control

An automatic gain control, or AGC, a feature of the LQIT mass spectrometer, helped to determine the optimal amount of time to allow ions to enter the ion trap from the ion optics. The AGC controlled the length of time the gate lens in the ion optics was “open” or allowed ions to travel through the gate lens; this is referred to as the ion injection time (IT). The gate lens was “open” when the DC voltage applied to it was more negative than the voltage applied to lens 1 and was “closed” when the DC voltage applied to the gate lens was more positive than the voltage applied to lens 1 (see Figure 2.13). The optimal IT was determined by first measuring the number of ions that entered the ion trap in one ms “open” time; this is referred to as the pre-scan. Next, the maximum number of ions that could be successfully stored in the ion trap, typically 30,000 ions, was divided by the number of ions that were measured during the pre-scan - this value is the IT (Equation 2.4):

$$IT \text{ (how long the gate lens is open)} = \frac{\text{Target Value (30,000)}}{\text{Number of ions measured during pre-scan}} \quad \text{(Equation 2.4)}$$

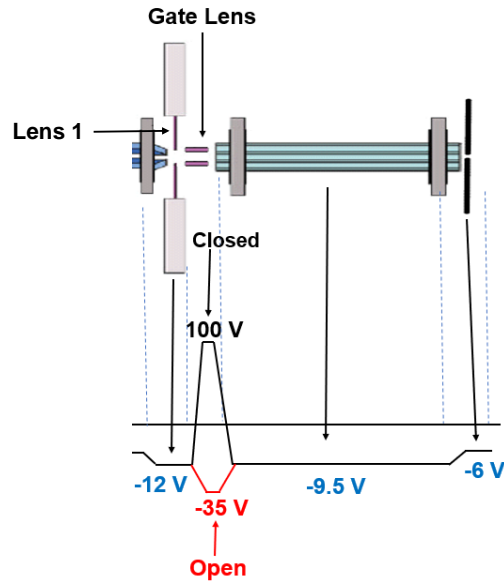


Figure 2.13 Diagram showing the voltages to the gate lens when it was “open”, i.e., has a lower voltage than lens 1 applied to it, vs when it was “closed”, i.e. had a higher voltage than lens 1 applied to it.

The AGC improved the quality of the mass spectrum that was measured by ensuring that the ideal number of ions entered the trap. If an excess number of ions entered the ion trap, the density of ions per unit area in the middle section would be too large, resulting in *space charging*.⁶⁰ This phenomenon is due to closely packed ions of the same charge repelling one another and causing their positions in the ion trap to be displaced from the center. This leads to a decrease in the mass resolution and mass accuracy.⁶⁰ On the other hand, if too few ions were in the ion trap, the total ion current measured could vary tremendously due to small deviations in the number of ions in the trap. This inconsistency would result in irreproducible mass spectra as well as difficulties detecting ions present in low abundances.

2.3.3.3 Ion Manipulation

2.3.3.3.1 Ion Ejection

After ions were stored and any manipulation had been completed, they were scanned out through the slits of the x -rods of the middle section of the ion trap for detection. Ions were separated by m/z as they were ejected; this was conducted via *mass selective instability scanning with resonance ejection*.⁵⁹ In this type of scan, the amplitude of the main RF voltage was linearly increased, thus increasing the q -value for all ions. Although ion ejection is possible when an ion's q -value exceeds 0.908, the stability limit, ejecting ions like this at the stability limit can lead to poor mass resolution and mass accuracy.⁵⁹ Therefore, a second RF voltage was applied to only the x -rods of the ion trap to improve ion ejection.

The second RF voltage was called the *resonance ejection frequency voltage*.⁵⁹ The frequency of this supplemental RF voltage is the same as an ion's secular frequency when the ion has a q -value of 0.880, near the Mathieu stability boundary. It is important to note that the secular frequency of the motion of every ion is the same when their q -value is the same. The secular frequency, $\omega_{u,0}$, of the motion of an ion is defined as the frequency at which an ion oscillates in an electric field.⁵⁹ The following three equations show how an ion's secular frequency is influenced by the amplitude of the main RF voltage:

$$\omega_{u,0} = \frac{\beta_u \Omega}{2} \quad (\text{Equation 2.5})$$

where Ω is the angular frequency of the main RF voltage and β_u , known as the Dehmelt approximation, is related to the Mathieu parameters by:

$$\beta_u = \left(a_u + \frac{q_u^2}{2} \right)^{\frac{1}{2}} \quad (\text{Equation 2.6})$$

When a_u is zero and q_u is represented by Equation 2.3, the secular frequency of an ion can be rewritten as:

$$\omega_{u,0} = \frac{zV\sqrt{2}}{\Omega u_0^2 m} \quad (\text{Equation 2.7})$$

Based on Equation 2.7, as the amplitude of the main RF voltage increases, an ion's secular frequency increases; therefore, an ion's secular frequency is proportional to q .

During mass selective instability scanning with resonance ejection, when an ion's q -value was equal to 0.880, the ion's secular frequency came into resonance with the frequency of the resonance ejection frequency voltage. This caused the ions to gain kinetic energy and increased the ions' motion in the x -direction. Ions were able to overcome the restoring force and were ejected through the slits on the x -rods. Since secular frequency is inversely proportional to m/z , lighter ions were ejected first followed by heavier ions. The lower the *scan rate*, i.e., the rate at which the amplitude of the main RF voltage was increased, the better the mass resolution.⁶¹ However, ion abundance may decrease when using low scan rates.⁶¹ Therefore, scan rates were adjusted to maximize resolution while minimally sacrificing ion abundance.

2.3.3.3.2 Ion Ejection for Ion Isolation

One of the main advantages of the LQIT was that it can be used for multiple-stage tandem mass spectrometry experiments (MS^n ; $n > 2$). These experiments can be used to obtain further information for the structure of an unknown ion and differentiate isomers.⁶² In the ion trap, ions of a specific m/z can be selectively excited and ejected by using two RF voltages to isolate an ion of interest via ejection of all other ions. To accomplish this, an *ion isolation waveform voltage* was applied to the x -rods of the ion trap. The frequency of the ion isolation waveform voltage was swept through frequencies corresponding to the secular frequencies of the ions in the trap, *except*

for the ion to be isolated. In this manner, the trajectories of all ions, except for the isolated ion, became unstable and the ions were ejected. The isolation waveform is visualized in Figure 2.14.

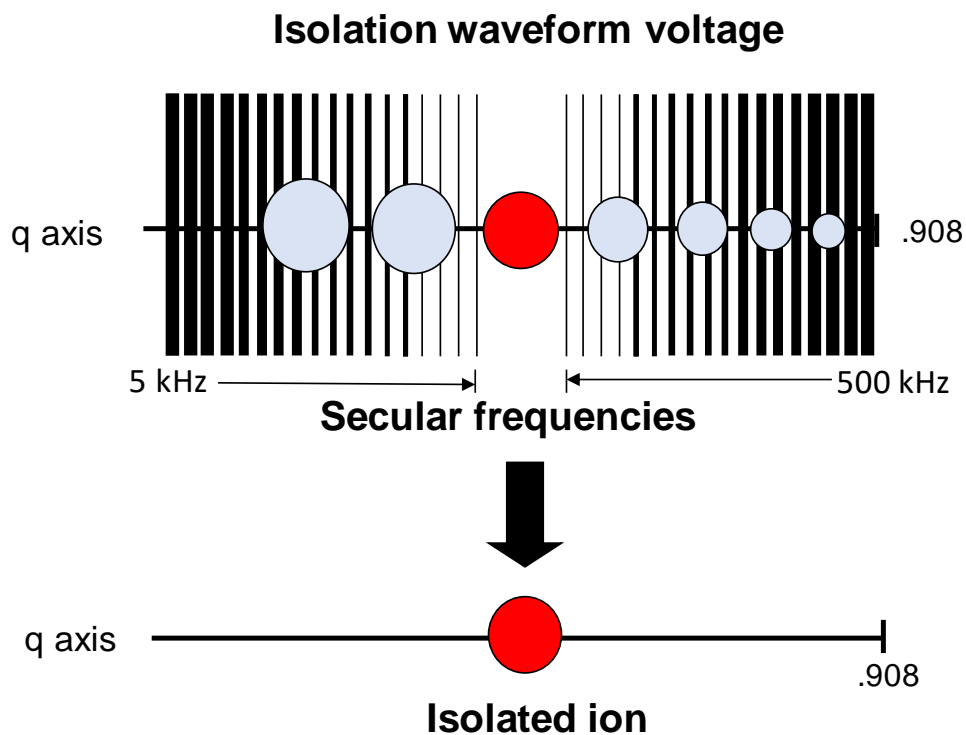


Figure 2.14 A distribution of frequencies between 5 and 500 kHz, comprising the secular frequencies of all ions except that of the ion to be trapped, was applied to the x -rods. All ions except the ion of interest (red) were removed from the trap.

The software for the LQIT allowed the user to define the ion isolation “window”. The value of the isolation window informed the software which frequencies to remove from the ion isolation waveform voltage. The more frequencies were excluded from the isolation waveform voltage, i.e., the larger the isolation window, the larger the total ion signal for the isolated ion of interest. However, large isolation windows may result in isolating unwanted ions, in addition to the ion of interest. For example, if ions of m/z 499, 500, and 501 were present in the ion trap, isolating only ions of m/z 500 would *likely* require a small isolation window, $\pm 0.5 m/z$ units, rather than a typical

isolation window of ± 1 m/z units. If an isolation window of 500 ± 1 m/z units was used, then all three ions would *most likely* be isolated.

2.3.3.3.3 Collision-activated Dissociation (CAD) in the Ion Trap

Excitation (acceleration) of isolated ions for CAD in the ion trap was achieved by applying a resonance excitation voltage to the x -rods of the ion trap. The frequency of this voltage was typically set equal to the ion's secular frequency of motion when the ion had a q -value of 0.250. The q -value at which the ions are resonantly excited can be changed by using the LQIT software; the higher the isolated ion's q -value, the higher the low m/z -cutoff for the product ions, i.e., some of the lower mass fragment ions may not be detected. The amplitude of this voltage was not great enough to cause isolated ions to overcome the restoring force and exit the trap. However, the resonance excitation voltage supplied the stored ions with enough kinetic energy that when they underwent multiple collisions with the helium buffer gas, the isolated ions usually fragmented. The reason why ions fragment upon collisions with the buffer gas is similar to why an egg breaks when thrown against a hard surface. When the egg is thrown, it has kinetic energy. After colliding with a hard surface, its kinetic energy is converted into internal energy and it fragments. Similarly, the kinetic energy of the accelerated ions is converted into internal energy as they collide with the buffer gas; this internal energy may be large enough to cause the bonds in the ions to break, resulting in the production of fragment ions. The longer the ions underwent CAD (0.03 ms to 10,000 ms) - or the greater the ion acceleration, the greater the abundance of the fragment ions. Additionally, the formation of different fragmentation products may occur.⁶³ The isolated ions and fragment ions are ejected for detection in the same way as described in section 2.3.3.3.1.

2.3.3.3.4 CAD in the Ion Optics

CAD in the ion trap was a tandem mass spectrometry experiment because an ion with a specific m/z was isolated and then fragmented. Another important technique for fragmenting ions called in-source CAD is not a tandem mass spectrometry experiment because in this technique, no ion isolation occurs and hence, all of the ions formed in the ion source are fragmented. In the LQIT MS, in-source CAD was accomplished by increasing the DC voltages on the multipoles and lenses in the ion optics (see Figure 2.6 and Figure 2.7) to create a steeper than normal potential gradient. This resulted in the ions to gain more kinetic energy than under normal conditions, which caused them to fragment upon collisions with atmospheric particles. The ions that entered the ion trap were a mixture of pre-cursor ions and their fragment ions. In-source CAD experiments were useful, for example, for distinguishing isobaric analytes,⁶⁴ analyzing inorganic explosives,⁶⁵ and determining the location of heteroatoms in polyaromatic compounds in complex mixtures.⁶⁶

2.3.3.3.5 Ion-Molecule Reactions in an LQIT

Gas-phase ion-molecule reactions conducted in the ion trap were useful for differentiating isomeric ions that cannot be differentiated using CAD.⁶⁷⁻⁶⁹ Furthermore, these reactions were useful for exploring the fundamental chemical properties of ionic reactive intermediates, including charged radicals and carbenes, and improving the understanding of the fundamental aspects of ionization methods.^{12,24,68,69} In most ion-molecule reaction experiments, a neutral molecule was introduced into the ion trap through an external reagent mixing manifold⁷⁰ and allowed to interact with isolated ions stored in the trap for 0.03 - 10,000 ms before scanning out all ions for detection.

Developed in 1977 by John Brauman and co-workers, the *Brauman double-well potential energy surface model* was widely used to understand as well as predict what product ions would be generated upon ion-molecule reactions (Figure 2.15).⁷¹ Based on this model, the ion-molecule

reaction began when the two reactants formed a reactant complex due to ion-dipole or ion-induced dipole attractive forces. These forces provide additional kinetic energy to the reactants in the complex that is transformed into rovibrational energy - this extra energy is referred to as the *solvation energy*. Once the two reactants formed this complex, they either reacted to form new product ions and neutral molecules or they separated and reformed the reactants. A reaction can proceed to generate a product complex if the solvation energy was large enough to overcome any barriers along the reaction pathway and overcoming the barrier was entropically favorable. Once over the transition state, a product complex formed, and the reaction may continue to form the separated products if the total reaction is exothermic.

5

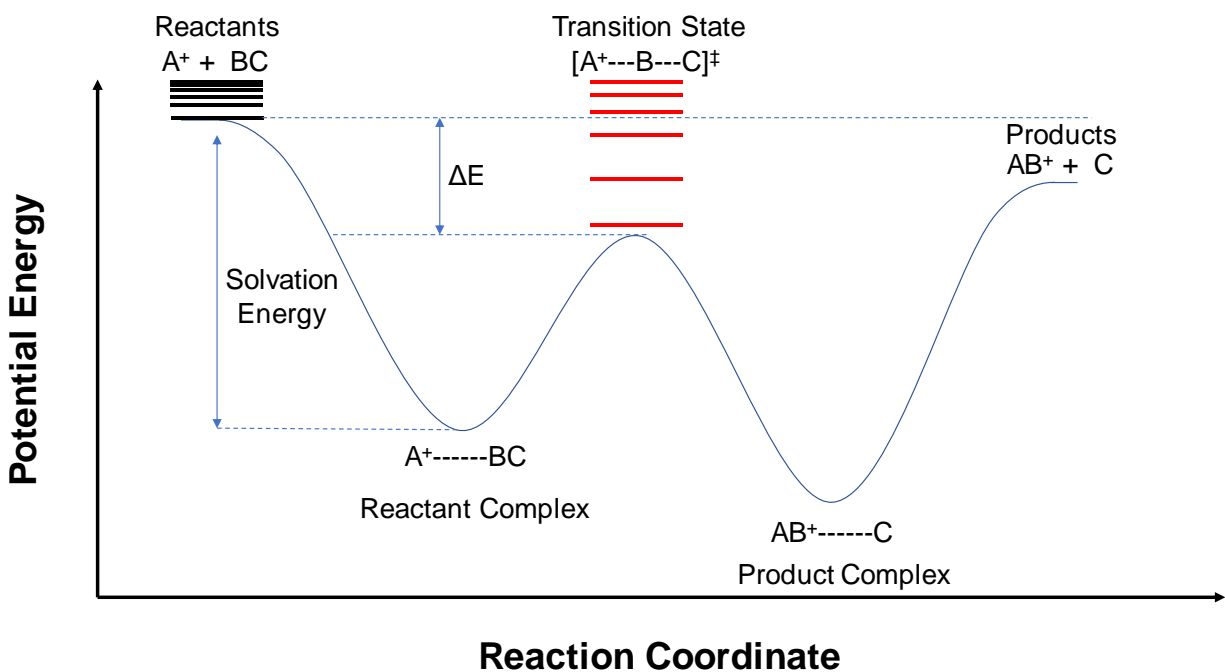


Figure 2.15 Diagram of the Brauman double-well potential energy surface model. The lines above the reactants and the transition state represent the rovibrational energy levels; their spacing is indicative of the relative “tightness” of each transition state.

Generally, the rate at which above reactions occur depends on difference between the total energy of the system (potential energy and extra rovibrational energy gained upon solvation) and the barrier height (potential energy) of the transition state. The greater the energy difference, ΔE , the faster the reaction. However, for *endothermic reactions*, the potential energy of the products is larger than that of the reactants, and no matter how large the ΔE is, the reaction will not occur. In certain cases, even *exothermic reactions* may not lead to products. When transition states are “tight,” the ions and neutral molecules must be in a specific orientation and position to form products. Therefore, despite having enough energy to overcome the transition state, it is *entropically* (number of accessible energy states) more favorable for the reaction to go back to the separated reactants than to the products. This restriction is called an *entropy constraint*, the smaller the number of accessible energy states, the lower the entropy. Under these circumstances, the reaction will progress slowly if at all. On the other hand, the “looser” the transition state, the greater the number of accessible energy states and the greater the entropy. Consequently, the reaction proceeds faster.

Figure 2.16 displays the different parts of the manifold that were required to help introduce gaseous neutral compounds into the ion trap. First, neutral compounds were introduced into the manifold by using a syringe pump at a flow rate of 2-5 $\mu\text{L/hr}$. The neutral compounds were diluted with helium gas, flow rate of 100-500 mL/min, in a region of the manifold that was held at 70 °C to ensure evaporation of the compounds before entering the ion trap. A Granville-Phillips leak valve acted as the injector for the neutral compounds from the manifold into the ion trap. As the neutral compounds entered the ion trap, the pressure of the vacuum chamber fluctuated up from its typical pressures of $0.6\text{-}1.0 \times 10^{-5}$ torr. To maintain a constant pressure between these values, a gas-flow regulator was utilized to vary the concentration of the neutral compounds in the helium

gas; this was accomplished by directing some of the mixture to waste. After ion-molecule reaction experiments were completed, the manifold was baked out at 200 °C and under vacuum. This was done to prevent contamination of any residual neutral compounds in the manifold. To avoid contamination, the boiling points of the neutral compounds must be below 200 °C; this was a major limitation of the method.

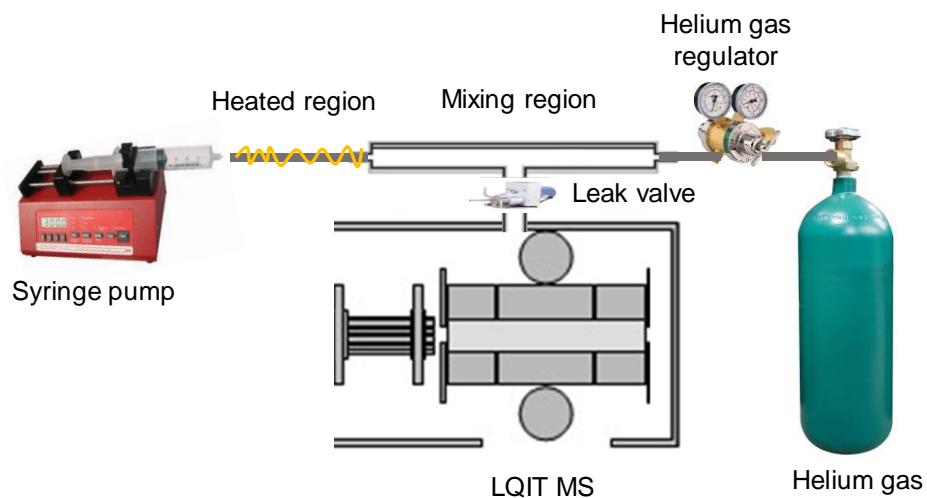


Figure 2.16 The setup utilized to introduce neutral compounds in a controlled manner into the ion trap of the LQIT to study ion-molecule reactions.

2.3.3.3.6 Ion Detection

After ions were ejected through the two slits in the x -rods, they were attracted towards the detectors - each included a conversion dynode and a channel electron multiplier (Figure 2.17). The conversion dynode consisted of a metal surface in the shape of a crescent moon that had a potential of -15 kV applied to it when detecting positive ions and +15 kV applied to it when detecting negative ions. The charge on the conversion dynode attracted the incoming beam of ions of opposite charge to its surface. After an individual ion struck the conversion dynode, one or more secondary particles were knocked off. These secondary particles were electrons when a positive ion struck, and positive ions when a negative ion struck. The number of particles ejected from the

metal surface was proportional to the number ions that collided with it. The trajectories of the secondary particles were then focused in the direction of the electron multiplier by the curved surface of the conversion dynode. They were accelerated toward the electron multiplier by a voltage gradient.

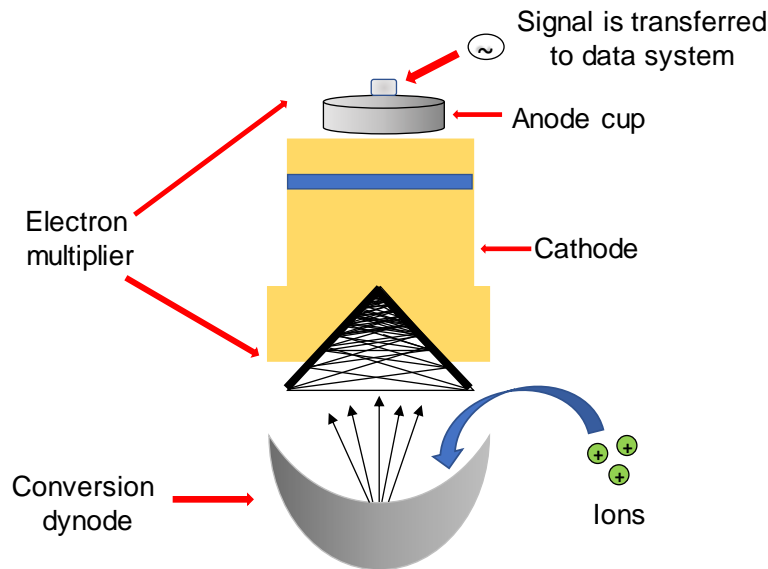


Figure 2.17 A conversion dynode and an electron multiplier makeup the two detectors for the LQIT. Ions (green) strike the conversion dynode, releasing secondary particles that accelerate into the electron multiplier, hit its surface and eject electrons from its surface. A measurable current reaches the anode and an electric signal is sent to the data system.

The electron multiplier consisted of two parts, a cathode and an anode. The cathode was shaped like a funnel, while the anode was designed like a small cup, and was placed at the exit of the cathode funnel. First, secondary particles from the conversion dynode hit the inner walls of the cathode with enough energy to eject electrons. The ejected electrons were attracted further into the cathode funnel by the increasingly positive potential gradient. The electrons collided with the inner wall of the cathode, releasing more electrons. These electrons then hit the opposite side of the funnel, generating a cascade of electrons. After multiple collision events with the walls of the

cathode, a significant number of electrons were produced that resulted in a measurable current when they reached the anode cup. The number of electrons detected by the anode cup was proportional to the number of secondary particles that collided with the cathode. Therefore, the measured current was related to the number of ions ejected from the ion trap. Lastly, this signal was transferred from the anode cup to the data system where the mass spectrum was generated.

2.4 Orbitrap Mass Spectrometer

As previously mentioned, one of the advantages of the LQIT was that it can be coupled to a high-resolution orbitrap mass analyzer. The LQIT provided unit resolution for all ions, which made it incapable of differentiating *isobaric ions* - ions of the same nominal m/z but different elemental compositions. The orbitrap mass spectrometer had a maximum resolution of 100,000 for ions of m/z 400 and mass accuracies as low as ~ 0.01 ppm. At such high resolution and mass accuracy, the orbitrap mass spectrometer can be used to provide reliable elemental compositions as well as the number of double-bonds and/or rings for many ions. High-resolution mass spectra were highly valuable for the analysis of complex mixtures such as crude oil and base oils, which will be highlighted later in this dissertation.^{40,72}

The fundamental principles that govern an orbitrap mass spectrometer were first experimentally tested by K.H. Kingdon in 1923.⁷³ The Kingdon trap, as it was later called, consisted of a thin metal wire positioned in the center of a large metal cylinder that was closed off at the ends. A DC voltage, opposite charge from that of the ions entering the trap, was applied to the thin wire, while the metal cylinder was held at ground (0 V), creating a DC potential gradient between them. Interestingly, ions that were accelerated into the Kingdon trap did not collide with the wire, but rather spiraled around it. The initial kinetic energy of the ions was large enough to keep them in an orbit around the wire- hence the name orbitrap. This phenomenon is similar to

why the Earth remains in an orbit around the sun despite the sun's large gravitational field; the Earth is orbiting with sufficient velocity to prevent it from being pulled into the sun. Although the Kingdon trap did not generate mass spectra, this concept led to the invention of the commercial orbitrap mass spectrometer in 2005 by Thermo Fisher Scientific.⁷⁴

The orbitrap mass spectrometer was maintained at ultrahigh vacuum at 10^{-9} torr by three turbopumps; the higher resolution of the orbitrap compared to that of the LQIT was partially due to its lower pressure. Figure 2.19 shows the schematic of the LQIT-orbitrap mass spectrometer that was utilized in this dissertation for high-resolution measurements. Similar to the Kingdon trap, the orbitrap consisted of an outer barrel shaped electrode (30 mm inner diameter) and an inner spindle shaped electrode in the center of it (12 mm inner diameter) (Figure 2.18). As ions of different m/z oscillated axially around the spindle electrode, they separated from one another. The ions with the same m/z -values formed coherent packets as they moved from one end of the spindle to the other. Ions were separated within the orbitrap because ions of each m/z have their own unique axial frequencies that were defined by:

$$\omega_a = \sqrt{\left(\frac{z}{m}\right) k} \quad (\text{Equation 2.8})$$

where ω_a is the axial frequency of oscillation of the ions, z is the charge of the ions, m is their mass in Da, and k is a constant related to the potential difference between the outer and inner electrodes.

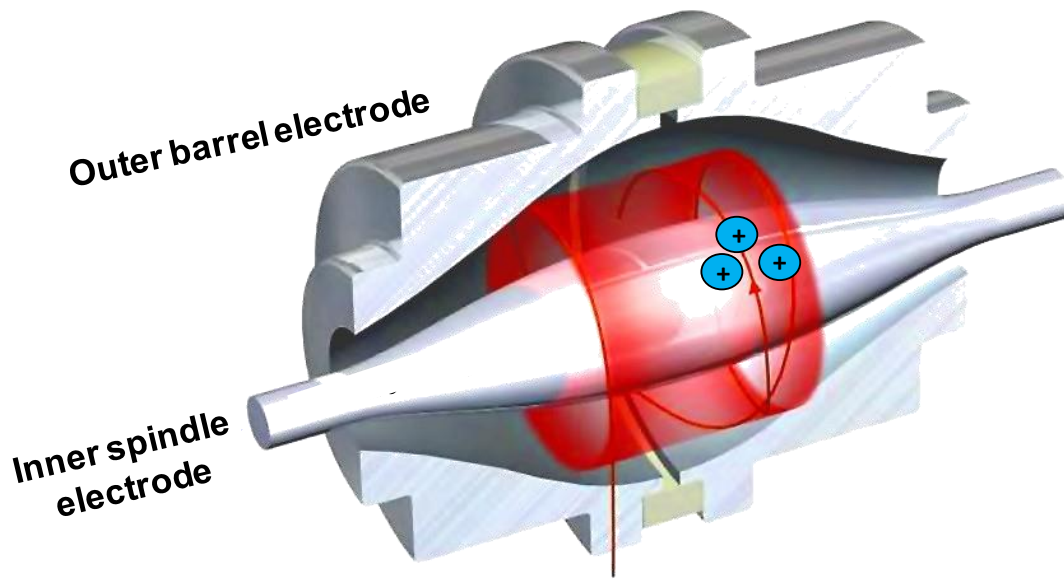


Figure 2.18 Schematic of the two electrodes of the orbitrap mass analyzer and the ion motion between them.

Ions entered the orbitrap from the ion trap via a transfer octupole and a *C-trap*. First, ions stored in the ion trap were accelerated via a DC voltage potential gradient through the back of the trap into the transfer octupole. Next, the ions entered a curved shape quadrupole with ion trapping lenses on either side called the C-trap. The C-trap was filled with N₂ gas at ~1 mTorr of pressure to cool the incoming ions. Nitrogen gas was used instead of helium gas because it was better at removing kinetic energy from the ions.⁷⁴ Ions were then focused into the center of the C-trap via a combination of DC and RF voltages. Finally, the ions were orthogonally ejected as a tight group from the C-trap through a small opening into the orbitrap mass analyzer.

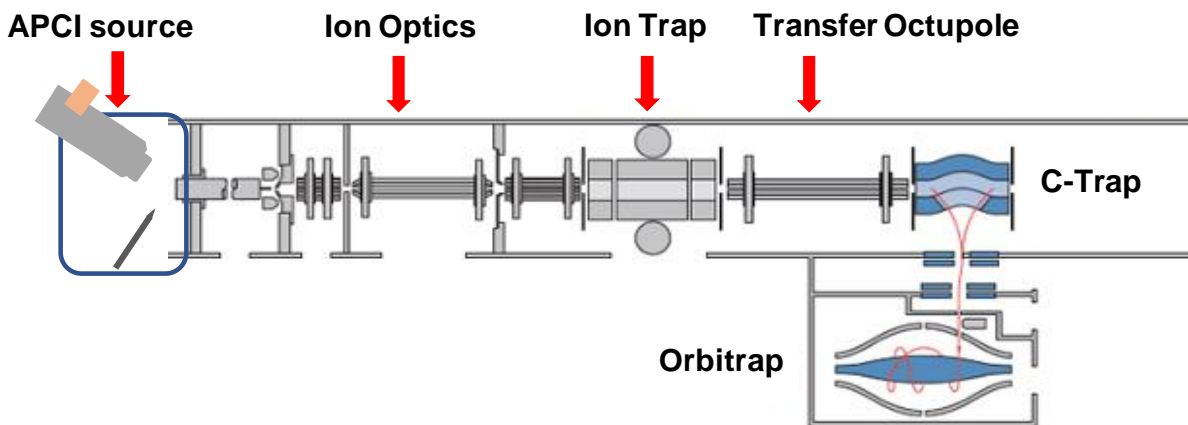


Figure 2.19 Schematic of the LQIT coupled to an orbitrap mass spectrometer.

Unlike the LQIT where ions were separated in the ion trap and then ejected for detection, the orbitrap was designed to both separate and detect ions. Ion detection was accomplished via amplification of the *image current* produced by the ions on the outer electrode.⁷⁵ In an orbitrap, the image current was changing as different packets of ions moved along the inner electrode; therefore, different currents were detected. The signals were Fourier transformed into a frequency/magnitude spectrum followed by conversion into a mass spectrum. In this manner, the orbitrap was both a mass analyzer and a detector.

2.5 Introduction to Gas Chromatography×Gas Chromatography/Time-of-flight Mass Spectrometry

Coupling chromatography instrumentation with a mass spectrometer enabled on-line separation of compounds prior to ionization and mass analysis. Gas chromatography (GC) is a common chromatography technique that is utilized for the analysis of volatile compounds that do not decompose upon vaporization caused by heating.^{76–79} To separate very complex mixtures, a GC×GC technique was used in this thesis research. The stationary phase used here was a polymer that coated the inside of a borosilicate capillary column, while the mobile phase was helium gas.

The primary oven temperature ranged from room temperature to 300 °C, while the secondary oven temperature ranged from room temperature to 330 °C.

The introduction of two GC columns connected to one another (GC×GC), each with a different polarity, by Zaiyou Liu and John Phillips in 1991, demonstrated significant improvements in the separation of complex mixtures.⁸¹ Compared to 1D GC, the GC×GC technique has superior resolution and greater sensitivity and a greater number of compounds can be detected.⁸² In normal phase GC×GC, the primary column was functionalized with nonpolar compounds, while the secondary column was functionalized with polar compounds. Normal phase GC×GC was primarily used for the separation of compounds that have a wide range of polarities, as for example, crude oil,⁸³ soil extracts,⁸⁴ and wastewater.⁸⁵ On the other hand, reversed phase GC×GC has the opposite configuration where the first column was functionalized with mostly polar compounds, while the second column was functionalized with nonpolar compounds. This column configuration was useful for separating mixtures that primarily contain nonpolar hydrocarbons including base oils and jet fuels; this geometry was used in this dissertation.^{86,87}

When coupled with a mass spectrometer (GC×GC/MS), a powerful analytical instrument is created.⁸⁸ Time-of-flight (TOF) mass spectrometers with electron ionization (EI) sources were perfect for coupling with GC×GC due to their high scan speeds (100-500 Hz) and medium-high resolution (25,000-75,000). Figure 2.20 and Figure 2.21 display a schematic of the two-dimensional gas chromatograph/(electron ionization) time-of-flight mass spectrometer (GC×GC/EI TOF MS) utilized in this research and a typical GC×GC/EI TOF MS total ion current chromatogram measured for a base oil, respectively. In Figure 2.21, the *x*-axis is the primary column elution time (s) and the *y*-axis is the secondary column elution time (s). Each black dot in the 2D-chromatogram indicates the apex of a chromatographic peak from both columns and

represents a single compound in the base oil. An EI mass spectrum was measured for each compound after it eluted from the secondary column to identify unknown compounds (see section 2.5.3 for more details).

The level of difficulty for developing a suitable GC×GC MS method for the analysis of an unknown sample can vary drastically; the more complicated the mixture, the longer it takes to optimize the method. Selection of the columns and carrier gas, programming the GC×GC oven temperatures, adjusting the modulator conditions, and controlling the TOF MS settings were all critical for method development. In the following sections, the theory and operation of GC×GC/EI TOF MS, similar to the one used for the experiments in this dissertation, will be discussed.

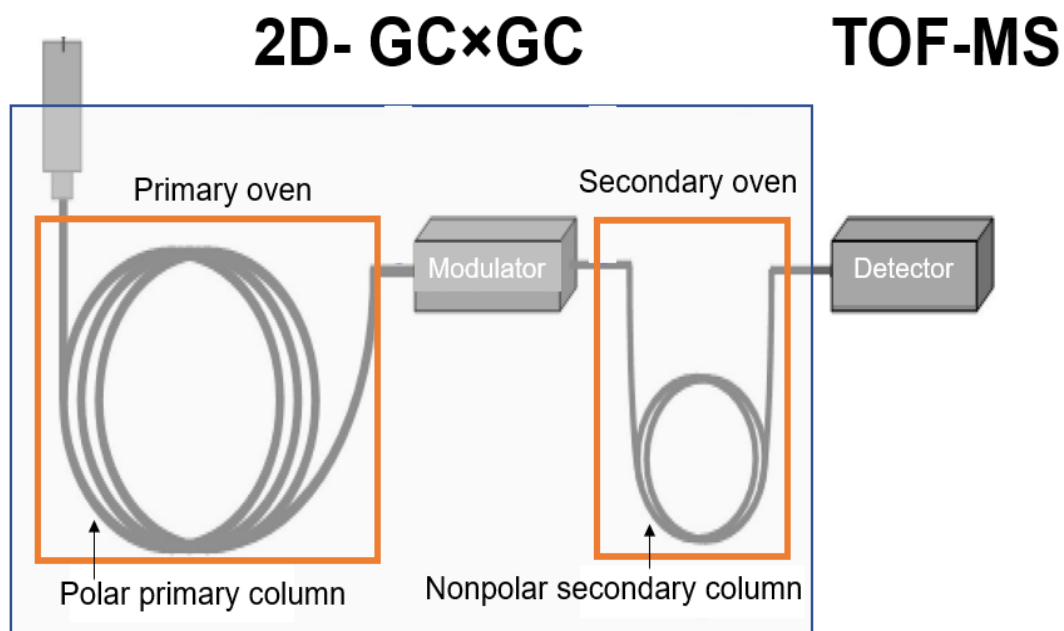


Figure 2.20 Schematic of a GC×GC/EI TOF MS. The GC×GC consists of two columns and the modulator, while the TOF MS consists of the EI source, the TOF mass analyzer, and the detector.

2D-GC×GC chromatogram of a base oil

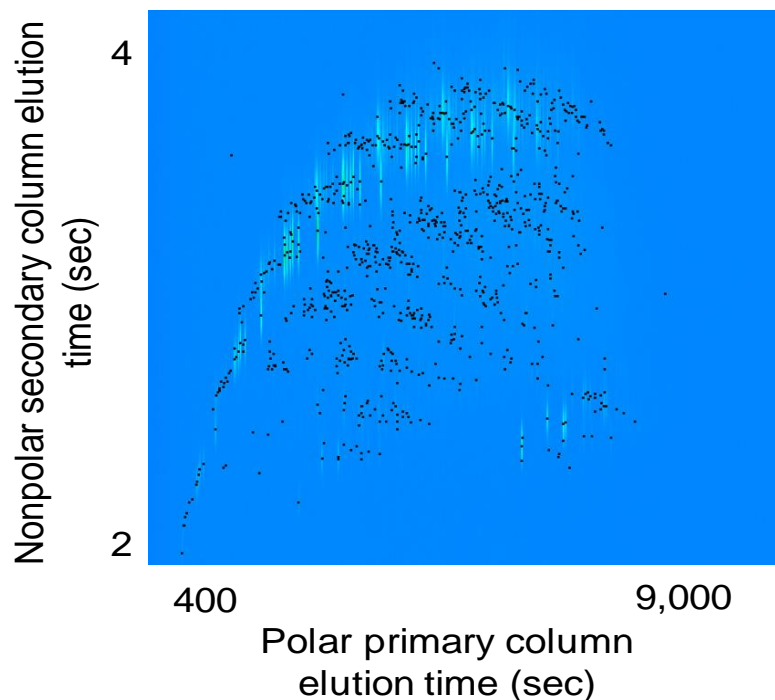


Figure 2.21 Reversed phase 2D-GC×GC/EI TOF MS total ion current chromatogram of a base oil. Each black dot represents a single compound that has eluted from both columns and was detected by the TOF MS.

2.5.1 Sample Preparation and Injection

Samples must be diluted in a suitable solvent prior to injection into GC×GC. An appropriate solvent should dissolve all the compounds in the sample and have the lowest boiling point of all compounds in the mixture. The sample concentration must be large enough so that all of the compounds in the sample can be detected and identified but low enough to prevent *column overloading* – sample remains on the column from the previous experiment. Additionally, if the sample concentration is too high, compounds can co-elute, resulting in lower resolution and less confident identification of unknown compounds. For a mixture with an unknown concentration of

compounds, a heavily diluted sample is injected first to determine the ideal concentration for sample analysis.

When many similar samples need to be analyzed, an autosampler is commonly used to automatically inject the samples onto the GC×GC. The autosampler utilized for the experiments in this dissertation was an Agilent 7693. It had 16 slots available for sample vials, two slots for solvent vials, and three slots for waste vials. Before sample injection, the 10 µL syringe attached to the autosampler was programmed to draw up a full volume of solvent and deposit it into the waste vial three to five times to clean out any residual sample from previous measurements. Next, the syringe would draw sample from the sample vial. The draw speed of the syringe depended on the viscosity of the sample, i.e., the more viscous the sample, the slower the draw speed to avoid air bubbles in the syringe. Finally, the syringe was lowered through a septum into the GC×GC inlet to inject 1 – 10 µL of the diluted sample.

2.5.2 Development of a GC×GC Method

After sample injection, the helium gas (the mobile phase) carried a portion, or all, of the sample onto the primary column – this was referred to as a splitless injection. In splitless injection mode, the entire volume of the sample was injected into the GC×GC. This mode was preferred when the concentrations of the compounds in the sample were very low. When using split injection mode, the user defines the amount of sample that will be injected into the column and the amount that will be directed to waste. For example, a 99 split ratio for 10 µL of sample means that 9.9 µL were directed into the waste, while 0.1 µL were injected into the GC×GC. The rate of the flow of the helium gas that was perpendicular to the entrance to the primary column changed based on the selected split ratio; the greater the split ratio, the higher the gas flow. Typically, the complexity of the sample and the concentrations of the different compounds in it dictated the optimal split ratio.

Regardless of the sample's concentration, the helium gas flow into and through the columns was held constant at 1-1.25 $\mu\text{L}/\text{min}$.

The oven temperature program for both the primary (polar) and secondary (nonpolar) columns was one of the most important parameters for determining the success of separation of the compounds in a sample. The starting temperature in the primary oven is commonly set several degrees below the boiling point of the compound in the sample with the lowest boiling point. Conversely, the highest temperature of the primary oven is set to be greater than the boiling point of the compound with the highest boiling point in the sample. The difference of the temperatures between the primary and secondary ovens (offset temperature) also matters. For example, if the temperature range in the primary oven was 40- 240 $^{\circ}\text{C}$, and the secondary oven offset temperature was +30 $^{\circ}\text{C}$, then the temperature range in the secondary oven was 70-270 $^{\circ}\text{C}$. The greater the offset temperature, the faster the compounds eluted through the secondary column; this led to sharper peaks. However, the hotter the temperature in the second column, the closer the peaks appear to one another. Figure 2.22 compares the second-dimension retention times for three compounds when using three different secondary oven offset temperatures. This figure demonstrates that as the offset temperature increases, the faster the compounds elute off the secondary column but the closer to each other they elute.

Additionally, optimization of the temperature ramp rate between the lowest and highest temperatures is critical to achieve ideal separation. While a lower temperature ramp rate will yield better separation, peak sharpness will suffer, i.e., wider peaks are produced in the GC \times GC chromatogram.

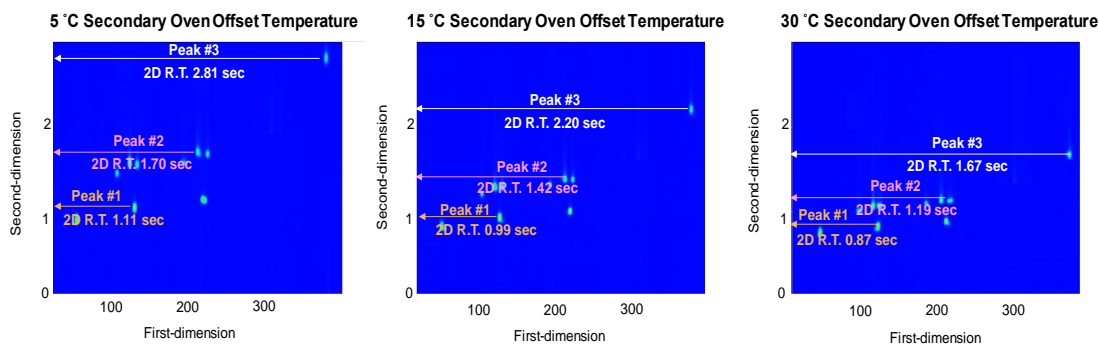


Figure 2.22 Three GC×GC/EI TOF MS total ion current chromatograms that show how the secondary column retention times for three highlighted peaks decrease as the secondary oven offset temperature increases from 5 °C (left), to 15 °C (middle), and to 30 °C (right).

2.6.2.1 Development of a Modulator Method

A major contribution to the superior separation of compounds in 2D-GC compared to 1D-GC is the inclusion of a modulator.⁸⁹ The modulator has two main functions: 1) cryo-focus eluate exiting the primary column and 2) heating and injecting the cryo-focused eluate into the secondary column. The first function of the modulator preserves the separation achieved with the primary column before injecting compounds into the secondary column. For the Agilent 7890A GC×GC used in this research, a quad-jet dual stage thermal modulator (Figure 2.23) was used to accomplish this task. The use of this modulator was broken up into two stages where each stage consisted of a hot and a cold jet. Each jet shot out nitrogen gas to either stop the eluate from moving (cold jet) or to inject the eluate into the next stage (hot jet). For a description of how the cold and hot jets work in the modulator, refer to Figure 2.24.

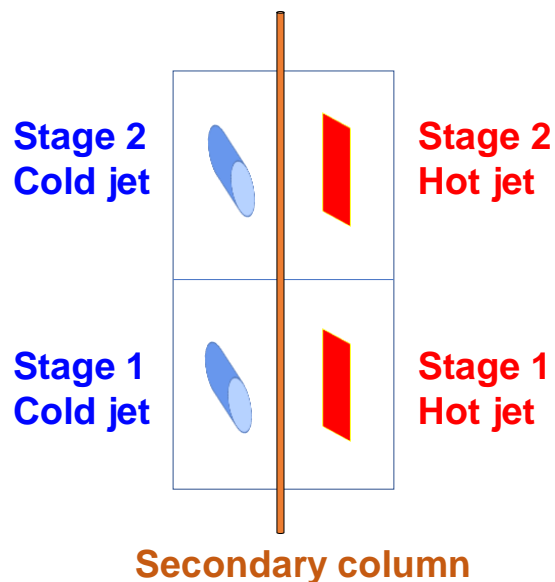


Figure 2.23 Schematic of the quad-jet dual stage thermal modulator. Each stage consists of a hot jet and a cold jet.

Three programmed cold and hot jet combinations were used during the *modulation period* - the length of time the eluate is in the modulator before injection onto the secondary column. Figure 2.24 shows the four phases of the hot and cold jet pulses. In the first phase, the cold jet pulse was turned on in the first stage, allowing chilled nitrogen gas to cryo-focus eluate exiting the primary column. In the second stage of the first phase, the hot jet pulse was turned on, allowing hot nitrogen gas to inject compounds into the secondary column that had escaped the first stage and entered the second stage. Next, in the second phase, the hot jet was turned on in the first stage to move the cryo-focused eluate from the first stage into the second stage, where the cold jet was turned on to cryo-focus the compounds. For the third phase, the cold jet was turned on in the first stage to prevent additional eluate from travelling to the second stage, while the second stage maintained the cold jet to generate a tighter packet of eluate for injection into the secondary column. In the fourth phase, the modulation period has come to a full circle where the cold jet was turned

on in the first stage and the hot jet was turned on in the second stage. In this manner, the eluate of the primary column that was cryo-focused was injected into the secondary column.

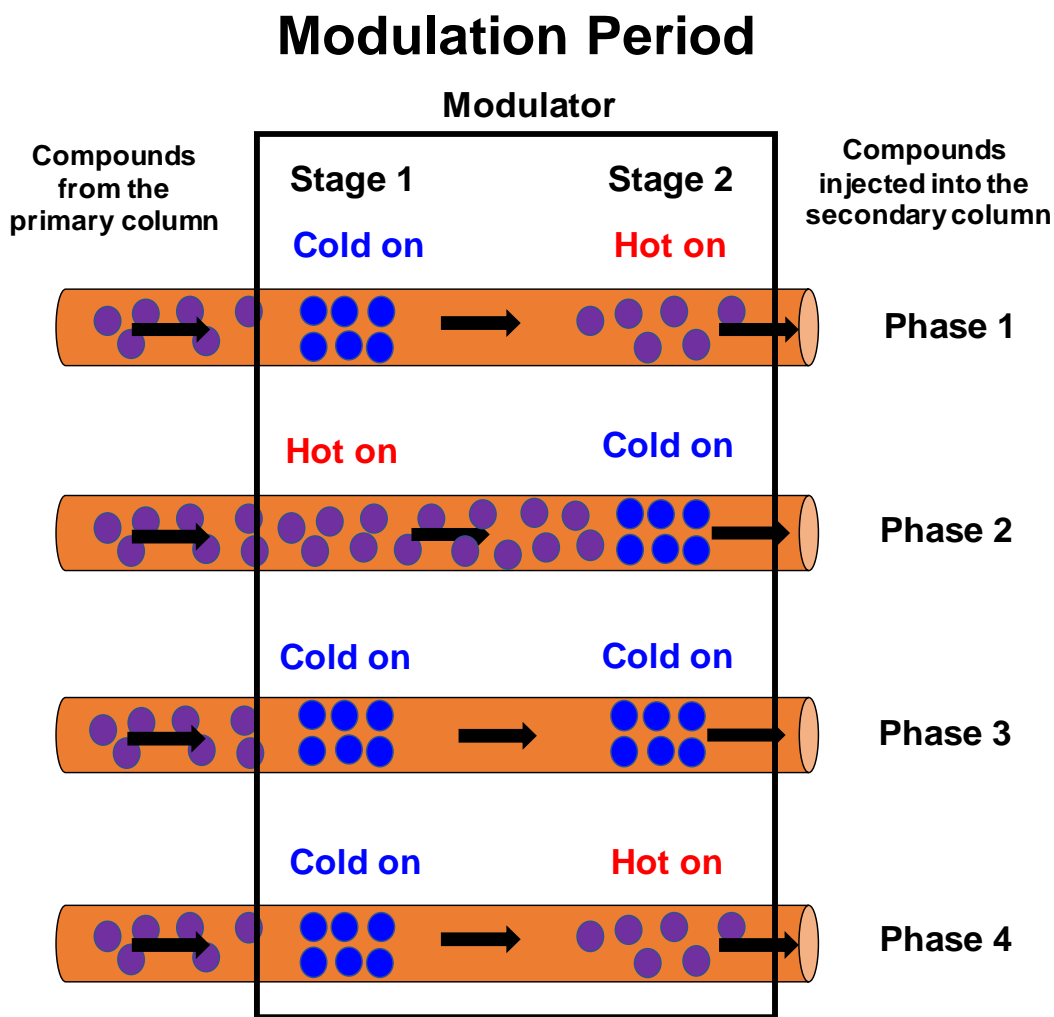


Figure 2.24 The four phases of hot and cold jet pulses over the course of one modulation period. **Purple** circles represent compounds that are in the gas phase, while **blue** circles represent cryo-focused compounds. The arrows represent the direction in which the compounds travel starting from the primary column, through stage 1 of the modulator, to stage 2 of the modulator, and finally into the secondary column.

The length of time of the modulation period and the duration of the hot and cold jet pulses greatly affect peak sharpness and compound separation. As previously mentioned, the length of the modulation period was the same as the maximum elution time of compounds from the second

column. Therefore, compounds that took longer than the modulation period to elute from the secondary column remained on the secondary column when the next eluate was injected into the modulator; this leads to the phenomenon known as *wrap around*. If wrap around has occurred, the second-dimension elution time of compounds will be shorter than it should be and can lead to coelution with eluates from the following modulation period. Wrap around can be corrected by either increasing the modulation period or increasing the secondary oven offset temperature. Figure 2.25 demonstrates how the secondary column elution time changes for two compounds when the modulation period is increased. Intuitively, the longer the modulation period, the greater the amount of time the eluate has to exit the secondary column before the next eluate is injected. However, if the modulation period is too long, one risks losing separation in the first dimension and secondary column overload. For instance, compounds that were separated on the first column may recombine with one another in the modulator if the modulation time is too long. On the other hand, the hotter the secondary offset temperature, the less the eluate interacts with the secondary column, and thus the faster it moves through the column. However, as previously discussed, increasing the secondary oven offset temperature can cause loss of separation in the second dimension.

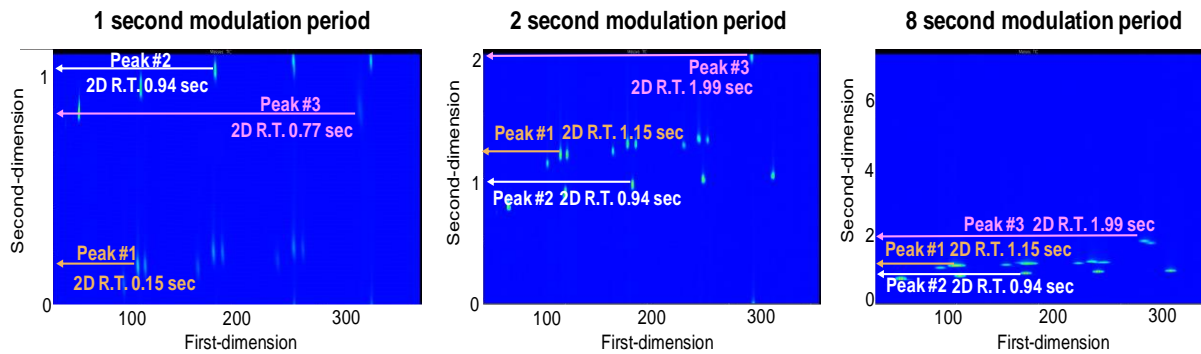


Figure 2.25 Three 2D-GC×GC/EI TOF MS total ion current chromatograms that show how the secondary column retention times for three highlighted peaks change as the time of the modulation period increases from 1 s (left), to 2 s (middle), and to 8 s (right).

The modulation period is broken up into two parts between each stage. Figure 2.26 depicts the breakdown of the hot and cold jet times in each stage based on the overall modulation period. A long hot jet time was ideal for rapidly evaporating cryo-focused compounds in the modulator. If the duration of the hot jet was too short, some of the heavier compounds may not get injected into the secondary column. Contrary to this, if the hot jet duration was too long, the cold jet pulse time may be too short to cryo-focus the more volatile compounds in the sample, thus resulting in the loss of their first-dimension separation.

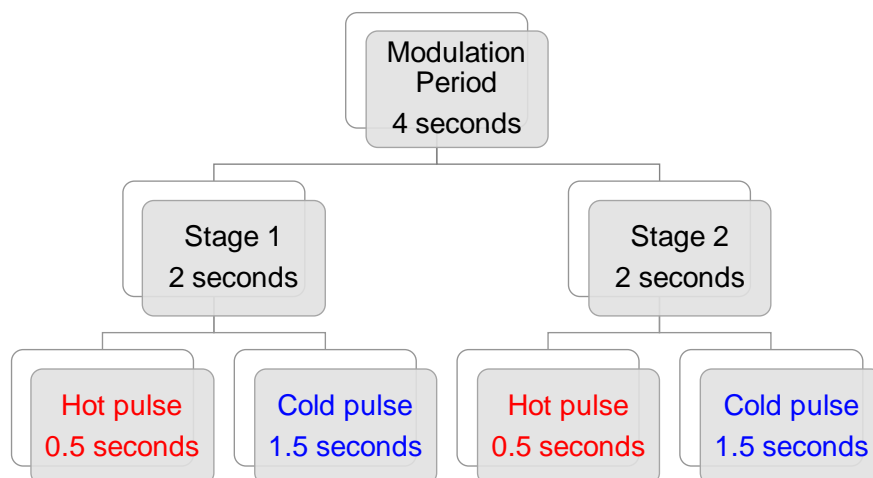


Figure 2.26 Flow chart of the different times the hot and cold jets are turned on in each stage given a 4 s modulation period and 0.5 s hot pulse time.

2.5.3 Development of an EI MS Method

As individual compounds eluted from the secondary column, they were directed through a transfer line into the EI source where the compounds were ionized. In EI, a metal filament heated with electric current released a beam of electrons. The electrons were accelerated to high kinetic energies (14-70 eV) by a potential gradient. The separated compounds exiting the transfer line from the GC×GC travelled perpendicular to the beam of electrons. Upon bombardment of the neutral compounds by the high energy electrons, an electron was sometimes ejected from a neutral compound, generating molecular ions and fragment ions. 70 eV was the kinetic energy chosen for the electron beam because this energy was large enough to ionize any organic compound in a reproducible manner. To facilitate identification of ionized compounds, the measured mass spectra can be compared to 70 eV EI mass spectra collected for over 200,000 compounds in a data base established by the National Institute of Technology and Standards (NIST). Figure 2.27 displays two EI mass spectra: the measured EI mass spectrum for an unknown compound in a

lubricant base oil and the closest matching EI mass spectrum obtained from the NIST library. A user can program the software (ChromaTof) to list up to 10 possible predictions for an unknown compound made based on a comparison of the measured mass spectrum to the EI mass spectra in the NIST library. A similarity score was assigned for each prediction - the higher the similarity score the more accurate the prediction of the identity of the unknown compound. However, if the EI mass spectrum of the unknown compound was not present in the NIST library, or the molecular ion of the analyte was not present in the measured EI mass spectrum, then incorrect predictions by the software were possible (see Chapter 5).

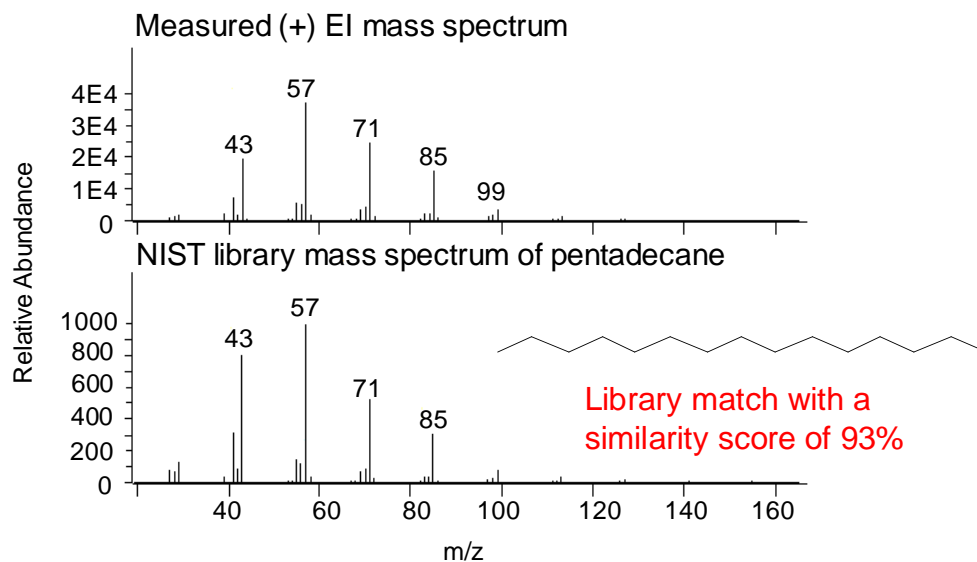


Figure 2.27 Positive-ion mode EI mass spectrum measured for an unknown compound (top) that was predicted to be pentadecane based on the closest match with an EI mass spectrum in the NIST library (bottom). The NIST library mass spectrum has a 93% similarity match with the measured EI mass spectrum.

To preserve the life-span of the filament, the acceleration grid of the EI source was commonly programmed to turn on after the solvent had eluted through the transfer tube. Since the solvent was in excess, ionization of the solvent can overload the EI source and can cause the EI filament to break. Therefore, a filament delay time was implemented. To determine the filament

delay time, gas in the headspace of a vial of solvent that the sample was dissolved in was injected onto the instrument. The time it took the vapors of the solvent to elute from both columns was recorded. The filament delay time implemented in the method was several seconds longer than the time it took for the vapors of the solvent to be detected.

In this research, a folded flight path TOF MS was utilized to measure the ions generated by the EI source. In this design, ions were orthogonally injected into the “flight chamber,” consisting of four sections called periodic ion lenses (Figure 2.28). As the ions flew through the first lens, they were redirected by a gridless mirror through the second lens and so on. The kinetic energy (KE) of each ion can be described by Equation 2.8:

$$KE = zV = \frac{1}{2}mv^2 \quad (\text{Equation 2.9})$$

where KE is ion kinetic energy, z is ion charge, V is the acceleration potential, m is the ion mass, and v is the ion velocity. If we take the path length of the folded flight path, L , and the time it takes for any given ion to travel through it, T , Equation 2.9 can be rewritten as:

$$T = L \sqrt{\frac{m}{z} * \frac{1}{2V}} \quad (\text{Equation 2.10})$$

Therefore, ions were separated from one another based on the time they took to travel the length of the flight tube. The smaller ions struck the detector (electron multiplier) first followed by the heavier ions. Medium-resolution (~25,000) and high-resolution (~50,000) EI mass spectra can be collected with the folded flight path design by varying the total distance the ions must travel before striking the detector. Specifically, ions are made to travel through the folded flight path once (20 m) for medium resolution but twice (40 m) for high resolution.

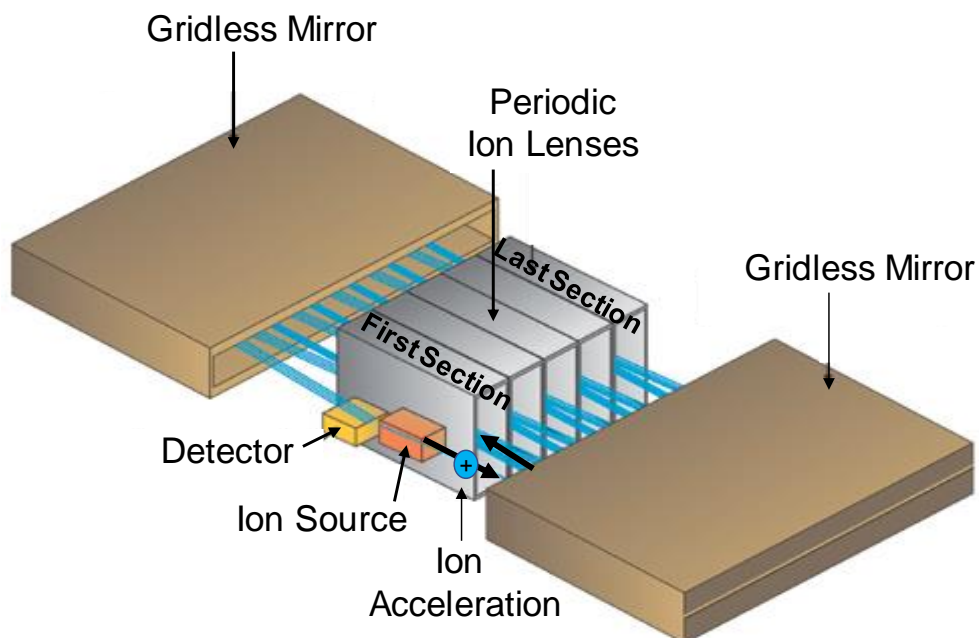


Figure 2.28 Picture of the folded flight path of ions in the TOF MS employed here. Ions travel in a zig-zag motion between the gridless mirrors and through the periodic ion lenses from the first section into the last section and then back to the first section where they strike the detector.

2.6 References

- (1) Marshall, A. G.; Rodgers, R. P. *Petroleomics: Chemistry of the Underworld*. *PNAS* **2008**, *105* (47), 18090–18095.
- (2) Griffiths, W. J.; Jonsson, A. P.; Liu, S.; Rai, D. K.; Wang, Y. *Electrospray and Tandem Mass Spectrometry in Biochemistry*. *Biochem. J.* **2001**, *355*, 545–561.
- (3) Richardson, S. D. *Mass Spectrometry in Environmental Sciences*. *Chem. Rev.* **2001**, *101* (2), 211–254.
- (4) Becker, J. S. *Applications of Inductively Coupled Plasma Mass Spectrometry and Laser Ablation Inductively Coupled Plasma Mass Spectrometry in Materials Science*. *Spectrochim. Acta B* **2002**, *57* (12), 1805–1820.
- (5) Maurer, H. H. *Mass Spectrometry for Research and Application in Therapeutic Drug Monitoring or Clinical and Forensic Toxicology*. *Ther. Drug Monit.* **2018**, *40* (4), 389–393.
- (6) Carr, S. A.; Abbatiello, S. E.; Ackermann, B. L.; Borchers, C.; Domon, B.; Deutsch, E. W.; Grant, R. P.; Hoofnagle, A. N.; Hüttenhain, R.; Koomen, J. M.; et al. *Targeted Peptide Measurements in Biology and Medicine: Best Practices for Mass Spectrometry-*

- Based Assay Development Using a Fit-for-Purpose Approach. *Mol. Cell. Proteomics* **2014**, *13* (3), 907–917.
- (7) Thomas, M. C.; Mitchell, T. W.; Blanksby, S. J. Ozonolysis of Phospholipid Double Bonds during Electrospray Ionization: A New Tool for Structure Determination. *J. Am. Chem. Soc.* **2006**, *128* (1), 58–59.
 - (8) Perchalski, R. J.; Yost, R. A.; Wilder, B. J. Structural Elucidation of Drug Metabolites by Triple-Quadrupole Mass Spectrometry. *Anal. Chem.* **1982**, *54* (9), 1466–1471.
 - (9) P. Demarque, D.; M. Crotti, A. E.; Vessecchi, R.; C. Lopes, J. L.; P. Lopes, N. Fragmentation Reactions Using Electrospray Ionization Mass Spectrometry: An Important Tool for the Structural Elucidation and Characterization of Synthetic and Natural Products. *Nat. Prod. Rep.* **2016**, *33* (3), 432–455.
 - (10) Cheng, C.; Gross, M. L.; Pittenauer, E. Complete Structural Elucidation of Triacylglycerols by Tandem Sector Mass Spectrometry. *Anal. Chem.* **1998**, *70* (20), 4417–4426.
 - (11) Niyonsaba, E.; Manheim, J. M.; Yerabolu, R.; Kenttämää, H. I. Recent Advances in Petroleum Analysis by Mass Spectrometry. *Anal. Chem.* **2019**, *91* (1), 156–177.
 - (12) Price, J. M.; Petzold, C. J.; Byrd, H. C. M.; Kenttämää, H. I. Examination of Barriered and Barrierless Hydrogen Atom Abstraction Reactions by Organic Radical Cations: The Cytosine Radical Cation. *Int. J. of Mass Spectrom.* **2001**, *212* (1), 455–466.
 - (13) Li, Z.; Singh, S.; Woodward, W.; Dang, L. Kinetics Study of OH Radical Reactions with n-Octane, n-Nonane, and n-Decane at 240–340 K Using the Relative Rate/Discharge Flow/Mass Spectrometry Technique. *J. Phys. Chem. A* **2006**, *110* (44), 12150–12157.
 - (14) Gross, J. H. Chemical Ionization. In *Mass Spectrometry: A Textbook*; Gross, J. H., Ed.; Springer: Berlin, Heidelberg, 2004; pp 331–354.
 - (15) Eberlin, M. N. Electrospray Ionization Mass Spectrometry: A Major Tool to Investigate Reaction Mechanisms in Both Solution and the Gas Phase. *Eur. J. Mass Spectrom.* **2007**, *13* (1),
 - (16) Zenobi, R.; Knochenmuss, R. Ion Formation in MALDI Mass Spectrometry. *Mass Spectrom. Rev.* **1998**, *17* (5), 337–366.
 - (17) Strupat, K. Molecular Weight Determination of Peptides and Proteins by ESI and MALDI. In *Methods in Enzymology; Mass Spectrometry: Modified Proteins and Glycoconjugates*; Academic Press, 2005; Vol. 405, pp 1–36.
 - (18) Murgasova, R.; Hercules, D. M. Polymer Characterization by Combining Liquid Chromatography with MALDI and ESI Mass Spectrometry. *Anal. Bioanal. Chem.* **2002**, *373* (6), 481–489.

- (19) Gao, J.; Owen, B. C.; Borton, D. J.; Jin, Z.; Kenttämä, H. I. HPLC/APCI Mass Spectrometry of Saturated and Unsaturated Hydrocarbons by Using Hydrocarbon Solvents as the APCI Reagent and HPLC Mobile Phase. *J. Am. Soc. Mass Spectrom.* **2012**, *23* (5), 816–822.
- (20) Eberlin, M. N. Structurally Diagnostic Ion/Molecule Reactions: Class and Functional-Group Identification by Mass Spectrometry. *J. Mass Spectrom.* **2006**, *41* (2), 141–156.
- (21) Nägele, E.; Moritz, R. Structure Elucidation of Degradation Products of the Antibiotic Amoxicillin with Ion Trap MSⁿ and Accurate Mass Determination by ESI TOF. *J. Am. Soc. Mass Spectrom.* **2005**, *16* (10), 1670–1676.
- (22) Pittenauer, E.; Allmaier, G. The Renaissance of High-Energy CID for Structural Elucidation of Complex Lipids: MALDI-TOF/RTOF-MS of Alkali Cationized Triacylglycerols. *J. Am. Soc. Mass Spectrom.* **2009**, *20* (6), 1037–1047.
- (23) Fetterolf, D. D.; Yost, R. A. Energy-Resolved Collision-Induced Dissociation in Tandem Mass Spectrometry. *Int. J. Mass Spectrom. Ion Phys.* **1982**, *44* (1), 37–50.
- (24) Stirk, K. M.; Kiminkinen, L. K. M.; Kenttämä, H. I. Ion-Molecule Reactions of Distonic Radical Cations. *Chem. Rev.* **1992**, *92* (7), 1649–1665.
- (25) Watkins, M. A.; Price, J. M.; Winger, B. E.; Kenttämä, H. I. Ion–Molecule Reactions for Mass Spectrometric Identification of Functional Groups in Protonated Oxygen-Containing Monofunctional Compounds. *Anal. Chem.* **2004**, *76* (4), 964–976.
- (26) Dempster, A. J. A New Method of Positive Ray Analysis. *Phys. Rev.* **1918**, *11* (4), 316–325.
- (27) Munson, M. S. B.; Field, F. H. Reactions of Gaseous Ions. XVI. Effects of Additives on Ionic Reactions in Methane. *J. Am. Chem. Soc.* **1965**, *87* (19), 4242–4247.
- (28) Tal’roze, V. L.; Ljubimova, A. K. Secondary Processes in the Ion Source of a Mass Spectrometer (Presented by Academician N.N. Semenov 27 Viii 1952)—Reprinted from Report of the Soviet Academy of Sciences, Volume LXXXVI, -N5 (1952). *J. Mass Spectrom.* **1998**, *33* (6), 502–504.
- (29) Einolf, N.; Munson, B. High Pressure Charge Exchange Mass Spectrometry. *Int. J. Mass Spectrom. Ion Phys.* **1972**, *9* (2), 141–160.
- (30) Martinsen, D. P.; Buttrill, S. E. Determination of the Site of Protonation of Substituted Benzenes in Water Chemical Ionization Mass Spectrometry. *Org. Mass Spectrom.* **1976**, *11* (7), 762–772.
- (31) Hunt, D. F.; Harvey, T. Michael. Nitric Oxide Chemical Ionization Mass Spectra of Olefins. *Anal. Chem.* **1975**, *47* (13), 2136–2141.
- (32) Vairamani, M.; Mirza, U. A.; Srinivas, R. Unusual Positive Ion Reagents in Chemical Ionization Mass Spectrometry. *Mass Spectrom. Rev.* **1990**, *9* (2), 235–258.

- (33) Bouma, W. J.; Jennings, K. R. Negative Chemical Ionization Mass Spectrometry of Explosives. *Org. Mass Spectrom.* **1981**, *16* (8), 331–335.
- (34) Gross, J. H. Chemical Ionization. In *Mass Spectrometry: A Textbook*; Gross, J. H., Ed.; Springer International Publishing: Cham, 2017; pp 439–496.
- (35) Kebarle, P.; Hogg, A. M. Mass-Spectrometric Study of Ions at Near Atmospheric Pressures. I. The Ionic Polymerization of Ethylene. *J. Chem. Phys.* **1965**, *42* (2), 668–674.
- (36) Carroll, D. I.; Dzidic, I.; Stillwell, R. N.; Horning, M. G.; Horning, E. C. Subpicogram Detection System for Gas Phase Analysis Based upon Atmospheric Pressure Ionization (API) Mass Spectrometry. *Anal. Chem.* **1974**, *46* (6), 706–710.
- (37) Shahin, M. M. Mass-Spectrometric Studies of Corona Discharges in Air at Atmospheric Pressures. *J. Chem. Phys.* **1966**, *45* (7), 2600–2605.
- (38) Dzidic, I.; Carroll, D. I.; Stillwell, R. N.; Horning, E. C. Comparison of Positive Ions Formed in Nickel-63 and Corona Discharge Ion Sources Using Nitrogen, Argon, Isobutane, Ammonia and Nitric Oxide as Reagents in Atmospheric Pressure Ionization Mass Spectrometry. *Anal. Chem.* **1976**, *48* (12), 1763–1768.
- (39) Lloyd, J. R.; Hess, S. A Corona Discharge Initiated Electrochemical Electrospray Ionization Technique. *J. Am. Soc. Mass Spectrom.* **2009**, *20* (11), 1988–1996.
- (40) Jin, C.; Viidanoja, J.; Li, M.; Zhang, Y.; Ikonen, E.; Root, A.; Romanczyk, M.; Manheim, J.; Dziekonski, E.; Kenttämä, H. I. Comparison of Atmospheric Pressure Chemical Ionization and Field Ionization Mass Spectrometry for the Analysis of Large Saturated Hydrocarbons. *Anal. Chem.* **2016**, *88* (21), 10592–10598.
- (41) Acter, T.; Cho, Y.; Kim, S.; Ahmed, A.; Kim, B.; Kim, S. Optimization and Application of APCI Hydrogen–Deuterium Exchange Mass Spectrometry (HDX MS) for the Speciation of Nitrogen Compounds. *J. Am. Soc. Mass Spectrom.* **2015**, *26* (9), 1522–1531.
- (42) Kolakowski, B. M.; Grossert, J. S.; Ramaley, L. Studies on the Positive-Ion Mass Spectra from Atmospheric Pressure Chemical Ionization of Gases and Solvents Used in Liquid Chromatography and Direct Liquid Injection. *J. Am. Soc. Mass Spectrom.* **2004**, *15* (3), 311–324.
- (43) Chang, J.-S.; Lawless, P. A.; Yamamoto, T. Corona Discharge Processes. *IEEE T. Plasma Sci.* **1991**, *19* (6), 1152–1166.
- (44) Shahin, M. M. Use of Corona Discharges for the Study of Ion—Molecule Reactions. *J. Chem. Phys.* **1967**, *47* (11), 4392–4398.
- (45) Kebarle, P.; Hogg, A. M. Heats of Hydration and Solvation by Mass Spectrometry. *J. Chem. Phys.* **1965**, *42* (2), 798–799.

- (46) Zavilopulo, A. N.; Chipev, F. F.; Shpenik, O. B. Ionization of Nitrogen, Oxygen, Water, and Carbon Dioxide Molecules by near-Threshold Electron Impact. *Tech. Phys.* **2005**, *50* (4), 402–407.
- (47) Nelsen, S. F.; Ippoliti, J. Thomas. The Deprotonation of Trialkylamine Cation Radicals by Amines. *J. Am. Chem. Soc.* **1986**, *108* (16), 4879–4881.
- (48) Lau, Y. K.; Ikuta, S.; Kebarle, P. Thermodynamics and Kinetics of the Gas-Phase Reactions $\text{H}_3\text{O}^+(\text{H}_2\text{O})_{n-1} + \text{Water} = \text{H}_3\text{O}^+(\text{H}_2\text{O})_n$. *J. Am. Chem. Soc.* **1982**, *104* (6), 1462–1469.
- (49) Owen, B. C.; Gao, J.; Borton, D. J.; Amundson, L. M.; Archibold, E. F.; Tan, X.; Azyat, K.; Tykwinski, R.; Gray, M.; Kenttämä, H. I. Carbon Disulfide Reagent Allows the Characterization of Nonpolar Analytes by Atmospheric Pressure Chemical Ionization Mass Spectrometry. *Rapid Commun. Mass Spectrom.* **2011**, *25* (14), 1924–1928.
- (50) Carroll, D. I.; Dzidic, I.; Stillwell, R. N.; Haegele, K. D.; Horning, E. C. Atmospheric Pressure Ionization Mass Spectrometry. Corona Discharge Ion Source for Use in a Liquid Chromatograph-Mass Spectrometer-Computer Analytical System. *Anal. Chem.* **1975**, *47* (14), 2369–2373.
- (51) Munson, M. S. B.; Field, F. H. Chemical Ionization Mass Spectrometry. I. General Introduction. *J. Am. Chem. Soc.* **1966**, *88* (12), 2621–2630.
- (52) Hunt, D. F.; Harvey, T. Michael. Nitric Oxide Chemical Ionization Mass Spectra of Alkanes. *Anal. Chem.* **1975**, *47* (12), 1965–1969.
- (53) March, R. E.; Todd, J. F. *Quadrupole Ion Trap Mass Spectrometry*; John Wiley & Sons, Hoboken, NJ, 2005.
- (54) Schwartz, J. C.; Senko, M. W.; Syka, J. E. P. A Two-Dimensional Quadrupole Ion Trap Mass Spectrometer. *J. Am. Soc. Mass Spectrom.* **2002**, *13* (6), 659–669.
- (55) O’Hair, R. A. J. The 3D Quadrupole Ion Trap Mass Spectrometer as a Complete Chemical Laboratory for Fundamental Gas-Phase Studies of Metal Mediated Chemistry. *Chem. Commun.* **2006**, 1469–1481.
- (56) March, R. E. An Introduction to Quadrupole Ion Trap Mass Spectrometry. *J. Mass Spectrom.* **1997**, *32* (4), 351–369.
- (57) Stafford, G. Ion Trap Mass Spectrometry: A Personal Perspective. *J. Am. Soc. Mass Spectrom.* **2002**, *13* (6), 589–596.
- (58) Huber, C.; Hölzl, G. Hyphenation of Capillary Electrochromatography and Mass Spectrometry: Instrumental Aspects, Separation Systems, and Applications. *J. Chromatogr. A* **2001**, *62*.
- (59) Snyder, D. T.; Peng, W. P.; Cooks, R. G. Resonance Methods in Quadrupole Ion Traps. *Chem. Phys. Lett.* **2017**, *668*, 69–89.

- (60) Guo, D.; Wang, Y.; Xiong, X.; Zhang, H.; Zhang, X.; Yuan, T.; Fang, X.; Xu, W. Space Charge Induced Nonlinear Effects in Quadrupole Ion Traps. *J. Am. Soc. Mass Spectrom.* **2014**, *25* (3), 498–508.
- (61) Hoffmann, E. de. Tandem Mass Spectrometry: A Primer. *J. Mass Spectrom.* **1996**, *31* (2), 129–137.
- (62) McLuckey, S. A. Principles of Collisional Activation in Analytical Mass Spectrometry. *J. Am. Soc. Mass Spectrom.* **1992**, *3* (6), 599–614.
- (63) Ichou, F.; Schwarzenberg, A.; Lesage, D.; Alves, S.; Junot, C.; Machuron-Mandard, X.; Tabet, J.-C. Comparison of the Activation Time Effects and the Internal Energy Distributions for the CID, PQD and HCD Excitation Modes. *J. of Mass Spectrom.* **2014**, *49* (6), 498–508.
- (64) Hua, L.; Hou, K.; Chen, P.; Xie, Y.; Jiang, J.; Wang, Y.; Wang, W.; Li, H. Realization of In-Source Collision-Induced Dissociation in Single-Photon Ionization Time-of-Flight Mass Spectrometry and Its Application for Differentiation of Isobaric Compounds. *Anal. Chem.* **2015**, *87* (4), 2427–2433.
- (65) Forbes, T. P.; Sisco, E. In-Source Collision Induced Dissociation of Inorganic Explosives for Mass Spectrometric Signature Detection and Chemical Imaging. *Anal. Chim. Acta* **2015**, *892*, 1–9.
- (66) Fan, X.; Zhang, X.-Y.; Dong, X.; Liao, J.-J.; Zhao, Y.-P.; Wei, X.-Y.; Ma, F.-Y.; Nulahong, A. Structural Insights of Four Thermal Dissolution Products of Dongming Lignite by Using In-Source Collision-Activated Dissociation Mass Spectrometry. *Fuel* **2018**, *230*, 78–82.
- (67) Sheng, H.; Tang, W.; Yerabolu, R.; Max, J.; Kotha, R. R.; Riedeman, J. S.; Nash, J. J.; Zhang, M.; Kenttämä, Hilka. I. Identification of N-Oxide and Sulfoxide Functionalities in Protonated Drug Metabolites by Using Ion–Molecule Reactions Followed by Collisionally Activated Dissociation in a Linear Quadrupole Ion Trap Mass Spectrometer. *J. Org. Chem.* **2016**, *81* (2), 575–586.
- (68) Gronert, S. Mass Spectrometric Studies of Organic Ion/Molecule Reactions. *Chem. Rev.* **2001**, *101* (2), 329–360.
- (69) Brodbelt, J. S. Analytical Applications of Ion-Molecule Reactions. *Mass Spectrom. Rev.* **1997**, *16* (2), 91–110.
- (70) Gronert, S. Estimation of Effective Ion Temperatures in a Quadrupole Ion Trap. *J. Am. Soc. Mass Spectrom.* **1998**, *9* (8), 845–848.
- (71) Pellerite, M. J.; Brauman, J. I. Intrinsic Barriers in Nucleophilic Displacements. *J. Am. Chem. Soc.* **1980**, *102* (19), 5993–5999.
- (72) Yerabolu, R.; Kotha, R. R.; Niyonsaba, E.; Dong, X.; Manheim, J. M.; Kong, J.; Riedeman, J. S.; Romanczyk, M.; Johnston, C. T.; Kilaz, G.; et al. Molecular Profiling of

- Crude Oil by Using Distillation Precipitation Fractionation Mass Spectrometry (DPF-MS). *Fuel* **2018**, *234*, 492–501.
- (73) Kingdon, K. H. A Method for the Neutralization of Electron Space Charge by Positive Ionization at Very Low Gas Pressures. *Phys. Rev.* **1923**, *21* (4), 408–418.
- (74) Hu, Q.; Noll, R. J.; Li, H.; Makarov, A.; Hardman, M.; Graham Cooks, R. The Orbitrap: A New Mass Spectrometer. *J. Mass Spectrom.* **2005**, *40* (4), 430–443.
- (75) Makarov, A.; Denisov, E.; Kholomeev, A.; Balschun, W.; Lange, O.; Strupat, K.; Horning, S. Performance Evaluation of a Hybrid Linear Ion Trap/Orbitrap Mass Spectrometer. *Anal. Chem.* **2006**, *78* (7), 2113–2120.
- (76) Ventura, G. T.; Kenig, F.; Reddy, C. M.; Frysinger, G. S.; Nelson, R. K.; Mooy, B. V.; Gaines, R. B. Analysis of Unresolved Complex Mixtures of Hydrocarbons Extracted from Late Archean Sediments by Comprehensive Two-Dimensional Gas Chromatography (GC×GC). *Org. Geochem.* **2008**, *39* (7), 846–867.
- (77) Fredericks, E. M.; Brooks, F. R. Gas Chromatography Analysis of Gaseous Hydrocarbons by Gas-Liquid Partition Chromatography. *Anal. Chem.* **1956**, *28* (3), 297–303.
- (78) Ray, N. H. Gas Chromatography I. The Separation and Estimation of Volatile Organic Compounds by Gas-Liquid Partition Chromatography. *J. Chem. Technol. Biotechnol.* **1954**, *4* (1), 21–25.
- (79) Sťávoová, J.; Stahl, D. C.; Seames, W. S.; Kubátová, A. Method Development for the Characterization of Biofuel Intermediate Products Using Gas Chromatography with Simultaneous Mass Spectrometric and Flame Ionization Detections. *J. Chromatogr. A* **2012**, *1224*, 79–88.
- (80) Ventura, G. T.; Raghuraman, B.; Nelson, R. K.; Mullins, O. C.; Reddy, C. M. Compound Class Oil Fingerprinting Techniques Using Comprehensive Two-Dimensional Gas Chromatography (GC×GC). *Org. Geochem.* **2010**, *41* (9), 1026–1035.
- (81) Liu, Z.; Phillips, J. B. Comprehensive Two-Dimensional Gas Chromatography Using an On-Column Thermal Modulator Interface. *J. Chromatogr. Sci.* **1991**, *29* (6), 227–231.
- (82) Wang, F. C.-Y.; Zhang, L. Chemical Composition of Group II Lubricant Oil Studied by High-Resolution Gas Chromatography and Comprehensive Two-Dimensional Gas Chromatography. *Energy Fuels* **2007**, *21* (6), 3477–3483.
- (83) van Mispelaar, V. G.; Smilde, A. K.; de Noord, O. E.; Blomberg, J.; Schoenmakers, P. J. Classification of Highly Similar Crude Oils Using Data Sets from Comprehensive Two-Dimensional Gas Chromatography and Multivariate Techniques. *J. Chromatogr. A* **2005**, *1096* (1), 156–164.

- (84) Mao, D.; Lookman, R.; Weghe, H. V. D.; Weltens, R.; Vanermen, G.; Brucker, N. D.; Diels, L. Estimation of Ecotoxicity of Petroleum Hydrocarbon Mixtures in Soil Based on HPLC–GC×GC Analysis. *Chemosphere* **2009**, *77* (11), 1508–1513.
- (85) Gómez, M. J.; Herrera, S.; Solé, D.; García-Calvo, E.; Fernández-Alba, A. R. Automatic Searching and Evaluation of Priority and Emerging Contaminants in Wastewater and River Water by Stir Bar Sorptive Extraction Followed by Comprehensive Two-Dimensional Gas Chromatography-Time-of-Flight Mass Spectrometry. *Anal. Chem.* **2011**, *83* (7), 2638–2647.
- (86) Manheim, J.; Wehde, K.; Zhang, W. T. J.; Vozka, P.; Romanczyk, M.; Kilaz, G.; Kenttämää, H. I. Identification and Quantitation of Linear Alkanes in Lubricant Base Oils by Using GC×GC/EI TOF Mass Spectrometry. *J. Am. Soc. Mass Spectrom.* **2019**, *30*, 2670–2677.
- (87) Prak, D. J. L.; Romanczyk, M.; Wehde, K. E.; Ye, S.; McLaughlin, M.; Prak, P. J. L.; Foley, M. P.; Kenttämää, H. I.; Trulove, P. C.; Kilaz, G.; et al. Analysis of Catalytic Hydrothermal Conversion Jet Fuel and Surrogate Mixture Formulation: Components, Properties, and Combustion. *Energy Fuels* **2017**, *31* (12), 13802–13814.
- (88) Jennerwein, M. K.; Eschner, M.; Gröger, T.; Wilharm, T.; Zimmermann, R. Complete Group-Type Quantification of Petroleum Middle Distillates Based on Comprehensive Two-Dimensional Gas Chromatography Time-of-Flight Mass Spectrometry (GC×GC-TOFMS) and Visual Basic Scripting. *Energy Fuels* **2014**, *28* (9), 5670–5681.
- (89) Edwards, M.; Mostafa, A.; Górecki, T. Modulation in Comprehensive Two-Dimensional Gas Chromatography: 20 Years of Innovation. *Anal. Bioanal. Chem.* **2011**, *401* (8), 2335–2349.

CHAPTER 3. AN AUTOMATED METHOD FOR CHEMICAL COMPOSITION ANALYSIS OF LUBRICANT BASE OILS BY USING ATMOSPHERIC PRESSURE CHEMICAL IONIZATION MASS SPECTROMETRY

Adapted with permission from Manheim, J.; Zhang, Y.; Viidanoja, J.; Kenttämää, H. I. *J. Am. Soc. Mass Spectrom.* 2019, 30, 2014-2021. Copyright 2019 American Chemical Society.

3.1 Introduction

Base oils are petroleum products manufactured from crude oil after it has been distilled, hydrogenated, and hydrocracked.¹ Base oils comprise 90% of lubricants that are used in motor vehicles and industrial machinery.² The key performance qualities of a lubricant base oil, such as viscosity, thermal stability, and volatility, are dictated by the chemical composition of the base oil.³ Base oils are primarily comprised of large (more than 15 carbon atoms) branched, cyclic and linear saturated hydrocarbons. Petroleum companies have the potential to improve the physical attributes of base oils by modifying their refinery methods to change the base oil's chemical composition.⁴ However, determining the accurate average molecular weight, range of the number of carbons, and relative amounts of each saturated hydrocarbon class in base oils is extremely difficult. This makes improving the quality of base oils challenging.

A plethora of analytical techniques are currently used by the petroleum industry to characterize the chemical composition of base oils. ¹³C NMR spectroscopy and infrared spectroscopy are utilized to provide bulk information, such as the presence of impurities.^{5,6} However, these techniques are limited as neither one can probe the identities of the individual saturated hydrocarbons in base oils. On the other hand, electron ionization mass spectrometry coupled to gas chromatography (GC/EI MS) can be used to determine the molecular weights and some structural information for individual saturated hydrocarbons in low viscosity base oils.⁷ As

discussed in Chapter 5, two-dimensional gas chromatography coupled with a mass spectrometer (GC×GC/MS) can also be used to identify many of the compounds in base oils.⁸ The major downside to these techniques is that it takes several hours to optimally separate the hundreds of saturated hydrocarbons in base oils. Even still, many of the compounds cannot be identified after optimal separation because EI often completely fragments saturated hydrocarbons upon ionization, thus eliminating molecular weight information. Furthermore, middle and high viscosity base oils cannot be analyzed with most GC columns because the columns degrade at temperatures required to evaporate the saturated hydrocarbons in these base oils.⁷ For these reasons, field ionization (FI) MS is commonly used in the petroleum industry to characterize samples containing large saturated hydrocarbons. FI can be used to analyze saturated hydrocarbons with a wide mass range with minimal fragmentation.⁹ Another benefit of FI is that it generates only one type of ions, the molecular ions ($M^{+\bullet}$), for each different analyte.^{10,11} However, FI MS suffers from sample carryover, poor reproducibility, variable levels of fragmentation for large saturated hydrocarbons, and tedious maintenance.^{10,11} Therefore, this technique cannot be used to provide quick and reliable data on the chemical composition of base oils.

Recent research performed to improve the analysis of base oils or large saturated hydrocarbons by mass spectrometry has focused on ionization methods. In general, saturated hydrocarbons are difficult to ionize without breaking their structure because they lack ionizable functional groups.¹² Derivatization of saturated hydrocarbons with heteroatom containing groups has been attempted to facilitate their ionization. These studies include oxidation upon desorption electrospray ionization¹³ and nitrogen atom insertion during paper spray ionization.¹⁴ Although insignificant levels of fragmentation were reported, all of these methods produce multiple ion types for each different analyte, complicating the interpretation of the mass spectra.

Currently, the most promising ionization technique is atmospheric pressure chemical ionization (APCI). Several studies have utilized APCI to analyze mixtures of large saturated hydrocarbons.¹⁵⁻¹⁹ For instance, a method was presented that generates only one type of ions per analyte, $[M-H]^+$ ions (carbenium ions), from saturated hydrocarbons in base oils upon direct injection (+)APCI with O₂ gas as the sheath/auxilliary gas and hexane as the solvent/reagent.¹¹ Although fragment ions were generated, similar semi-quantitative chemical information as FI MS for the same base oils was obtained with this method. Most importantly, the APCI/O₂/hexane method was demonstrated to have many advantages over FI MS including more stable ion signals, longer lifetime of the ionization source, and easier maintenance. However, like FI MS, this method causes some fragmentation and sample carryover from experiment to experiment.

The goal of the work discussed in this chapter was to automate the (+)APCI/O₂/saturated hydrocarbon solvent mass spectrometry method to improve its speed and accuracy when it is implemented in base oil analysis. Before automating the method, a model compound study was conducted to determine the solvent/APCI reagent that generated the lowest amount of fragmentation and the least amount of ionization bias for the different classes of saturated hydrocarbons. This was proceeded by sample carryover tests to minimize the time required to collect the base oil mass spectrum and to clean the instrument. Finally, the precision of the automated method was evaluated for different classes of saturated hydrocarbons in three base oils with varying viscosities.

3.2 Experimental Section

Chemicals. The solvents/APCI reagents *n*-pentane, *n*-hexane, *n*-heptane, *n*-decane, *n*-dodecane, 2,3-dimethylbutane, 2-methylpentane, isooctane, methylcyclopentane, and methylcyclohexane (all with purity $\geq 99\%$) were purchased from Sigma Aldrich (St. Louis, MO). Model compounds

tetracosane (99%), hexacosane (99%), octacosane (99%), dotriacontane (97%), 5- α -cholestane ($\geq 97\%$) and squalane (98.5%) were also purchased from Sigma Aldrich (St. Louis, MO). Pristane (95% purity), a branched saturated hydrocarbon, was purchased from TCI America. All compounds were used without further purification. Three base oil samples, each with a different viscosity, were provided by Neste, Finland. Ultrapure oxygen gas (99.993%) was used for the nebulizing gas and was purchased from Praxair, Inc. Helium (99.999% purity) was purchased from Indiana Oxygen and was used as the buffer gas in the ion trap.

Sample Preparation. The solvent used to dissolve all three base oils was isooctane (see section 3.3 for explanation). Sample concentration for the low and middle viscosity base oils was 10 mg/mL in isooctane. Sample concentration for the heavy viscosity base oil was 20 mg/mL in isooctane. The higher concentration for the heavier base oil was necessary to achieve the best total ion signal. Spiked base oil samples were prepared by first dissolving 1 mL of an 8 mg/mL solution of pristane in isooctane in 1 mL of a 20 mg/mL solution of the middle viscosity base oil in isooctane. The final concentration of pristane and the middle viscosity base oil was 4 mg/mL and 10 mg/mL, respectively, in isooctane; this solution served as the stock solution. The 2 mg/mL spiked pristane solution was prepared by taking 1 mL of the 4 mg/mL spiked solution and dissolving it in a 10 mg/mL solution of the middle viscosity base oil in isooctane. Four more spiked pristane solutions were prepared by dissolving half the volume of the previously made solution in a 10 mg/mL solution of the middle viscosity base oil in isooctane. In total, six spiked base oil samples were prepared with the following concentrations of pristane: 4.0 mg/mL, 2.0 mg/mL, 1.0 mg/mL, 0.5 mg/mL, 0.3 mg/mL, and 0.1 mg/mL.

Instrumentation. Direct infusion and automated positive-ion mode APCI experiments were conducted on a Thermo Fisher Scientific LTQ XL linear quadrupole ion trap (LQIT) mass spectrometer. Model compound mixtures (sample preparation is discussed in section 3.3) were directly injected using a 500 μL Hamilton syringe at a flow rate of 10 $\mu\text{L}/\text{min}$ through polyetheretherketone (PEEK) tubing into the APCI source. For automated experiments, spiked and nonspiked base oil samples were injected into the APCI source by using a Thermo Scientific isocratic pump and an autosampler (Dionex UltiMate 3000 series). 10 μL of each sample were introduced into the ion source through stainless steel tubing and mixed with neat isooctane that flowed at a rate of 20 $\mu\text{L}/\text{min}$. After each sample was injected, the syringe was automatically rinsed with five 25 μL portions of isooctane to remove any residual sample. For all samples, the APCI conditions were: sheath and auxiliary gas (O_2) flow rates, 60 and 30 arbitrary units, respectively; corona needle, ion transfer capillary tube, and tube lens voltages, 3.5 kV, 10 V, and 30 V, respectively; vaporizer temperature, 150 $^\circ\text{C}$; and ion transfer capillary tube temperature, 50 $^\circ\text{C}$. The operating conditions for cleaning the APCI source were similar except that the vaporizer temperature was set at 250 $^\circ\text{C}$, and the sheath and auxiliary gas flow rates were set at 10 and 5 arbitrary units, respectively. Lower temperatures were used for cleaning because of the safety concerns regarding the use of oxygen gas; lower flow rates were used to save the amount of expensive ultrapure oxygen used (~\$200 for a 100 L cylinder).

The Dionex UltiMate 3000 series isocratic pump and autosampler were synchronized to the LQIT via a peripheral control connection. Xcalibur 4.0 and Chromeleon Chromatography Data System (CDS) were used to setup the experimental sequence for automated experiments. Each nonspiked base oil sample was injected for two minutes (see section 3.3). All mass spectra were acquired and processed using Xcalibur 4.0 software. Ion abundances were monitored over the

whole experiment and the averaged mass spectra measured for the nonspiked base oil samples were used for chemical analysis.

Precision Measurements. The precision of all measurements was expressed as the relative standard deviation (RSD). Within day, between day, and total precision were determined for each saturated hydrocarbon class in each base oil by using the relative ion abundances observed in individual mass spectra. Three mass spectra were collected each day for six days for each nonspiked base oil for a total of 18 mass spectra per sample. Equation 3.1 was used to calculate the within day precision:

$$\text{Within Day Precision (RSD}_{\text{WD}}) = \sqrt{\frac{\sum_{k=1}^N (\text{RSD}_k)^2}{N}} \quad (\text{Equation 3.1})$$

where N is the number of days during which individual mass spectra were collected (6) and k is the RSD for the kth day. Equation 3.2 was used to calculate the between day precision:

$$\text{Between Day Precision (RSD}_{\text{BD}}) = \sqrt{\left(\text{RSD}_{\text{DM}}^2 - \frac{\text{RSD}_{\text{WD}}^2}{N}\right)} \quad (\text{Equation 3.2})$$

where RSD_{DM} is the RSD of the six-day averages measured.²⁰ Finally, the total precision was calculated using equation 3, which takes into account the within day and between day precision values.

$$\text{Total Precision} = \sqrt{\text{RSD}_{\text{WD}}^2 + \text{RSD}_{\text{BD}}^2} \quad (\text{Equation 3.3})$$

3.3 Results and Discussion

The main objective of this study was to improve the direct infusion (+)APCI/O₂/hexane method for the analysis of base oils. By implementing an isocratic pump and autosampler for

sample and wash solvent injections, sample carryover, a major drawback of the method, can be eliminated. Additionally, with 96 slots for 2 mL vials, the automated method has the ability to collect mass spectra for 95 different base oils (one vial must contain the wash solvent). Furthermore, the possibility of minimizing fragmentation and ionization biases of APCI was explored by testing ten different saturated hydrocarbon solvents/APCI reagents. After determining the best solvent/APCI reagent, the precision of the automated method to provide semi-quantitative information for the different saturated hydrocarbon classes in each base oil was evaluated.

3.3.1 Selection of the Solvent/APCI Reagent for Automated Experiments

As previously mentioned in Chapter 2, section 2.2, fragmentation of saturated hydrocarbons upon APCI complicates the interpretation of these mass spectra. According to the APCI mechanism proposed in literature for saturated hydrocarbons dissolved in saturated hydrocarbon solvents (see Chapter 2, section 2.2), carbenium ions generated from the APCI solvent/reagent abstract a hydride from neutral saturated analyte hydrocarbons (M) to generate $[M-H]^+$ carbenium ions and fragment ions. Therefore, carbenium ions generated from the APCI solvent/reagent were proposed to be responsible for ionization of saturated hydrocarbon analytes (this will be discussed in more detail in Chapter 4). Therefore, the choice of the solvent should influence the extent of fragmentation of saturated hydrocarbons. In order to test this hypothesis, ten different saturated hydrocarbon solvents/APCI reagents, including linear, branched, and cyclic saturated hydrocarbons, were studied to identify the optimal reagent for ionization of base oils. However, of the ten compounds studied, only three, namely *n*-hexane, isooctane, and methylcyclohexane, resulted in high quality APCI mass spectra (as defined by the observation of a near Gaussian ion distribution) for the middle viscosity base oil tested (data not shown). These three solvents/APCI reagents were selected for further model compound studies.

The reagent ions that caused the ionization of analyte saturated hydrocarbons were assumed to be the most abundant ions generated from neat *n*-hexane, isooctane, and methylcyclohexane upon APCI. For example, the most abundant ions formed upon (+)APCI/O₂ of neat isooctane were the fragment ions of *m/z* 57 ([M-C₄H₉]⁺; *tert*-butyl cation), while the most abundant ions for neat *n*-hexane and methylcyclohexane were [M-H]⁺ pseudo-molecular ions of *m/z* 85 and *m/z* 97, respectively (data not shown).

Three 2 mM equimolar mixtures consisting of tetracosane, hexacosane, octacosane, dotriacontane, 5- α -cholestane, and squalane dissolved in each of the three selected solvents were prepared to assess the performance of each reagent ion. APCI of these solutions generated [M-H]⁺ ions for each of the six model compounds in each sample, albeit with different relative abundances (Figure 3.1). In all three mass spectra, the branched and cyclic saturated hydrocarbons had significantly higher relative abundances than the linear saturated hydrocarbons. This was most likely due to the presence of tertiary carbon atoms in the branched/cyclic structures of squalane and 5- α -cholestane; more stable (tertiary) carbenium ions can be generated from these compounds without rearrangement than from the four linear saturated hydrocarbons studied. This result agreed with previous literature findings on hydride transfer between carbenium ions and saturated analyte hydrocarbons in a pulsed ion cyclotron resonance mass spectrometer.²¹ Furthermore, hydride abstraction from tertiary carbons in alkanes by carbenium ions has been reported to be more exothermic, and therefore, more favorable than hydride abstraction from primary and secondary carbon atoms. Curiously, the relative abundances of the [M-H]⁺ ions of squalane were lower than those of the [M-H]⁺ ions of cholestane when dissolved in isooctane but greater when dissolved in *n*-hexane and methylcyclohexane. At this time, this finding is not well understood. Due to the

ionization biases present in all three mass spectra, regardless of the solvent, the APCI method can only be semi-quantitative.

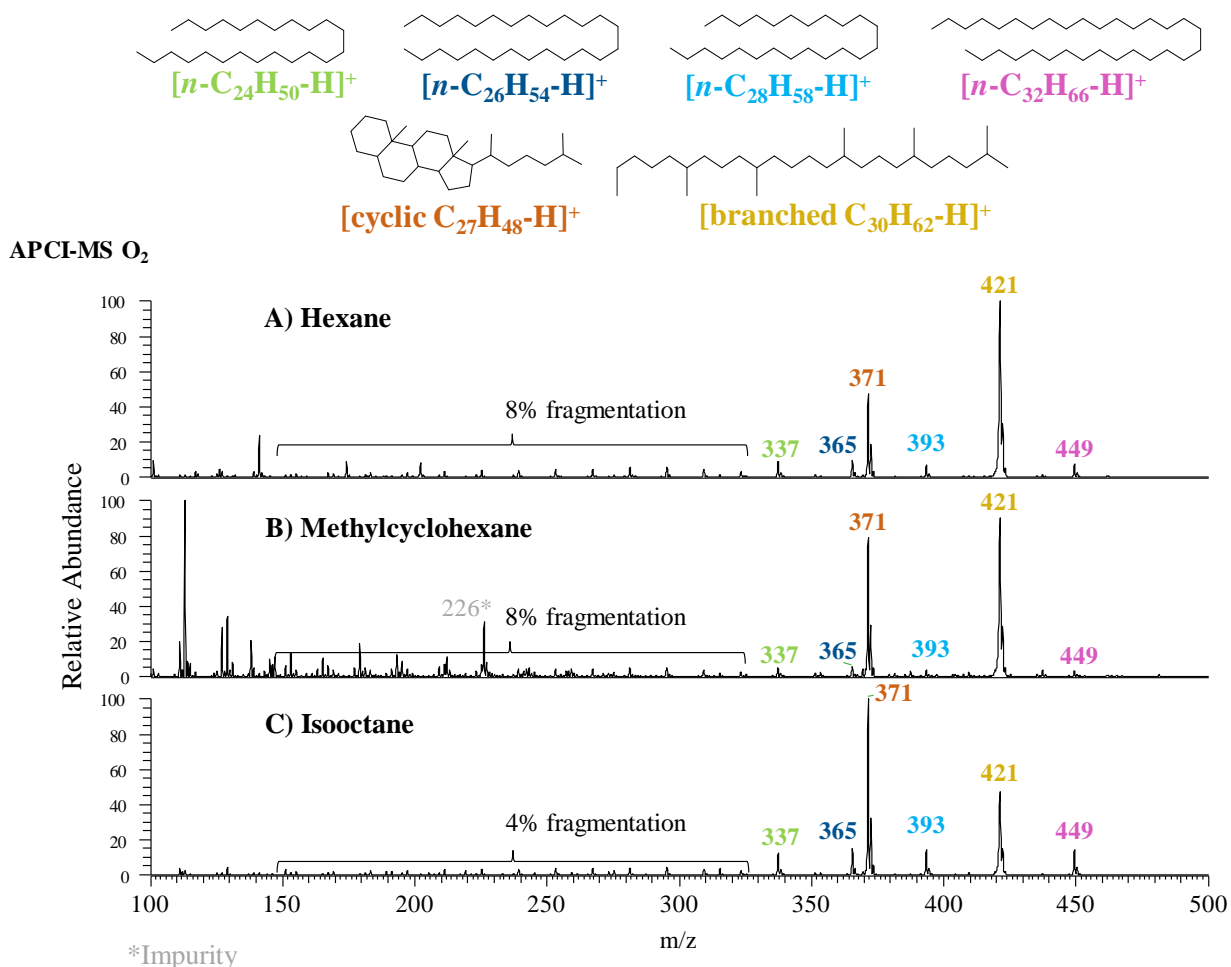


Figure 3.1 Direct-infusion positive-ion mode APCI/O₂ mass spectra of a 2 mM equimolar saturated hydrocarbon mixture dissolved in hexane (A), methylcyclohexane (B), and isooctane (C).

The level of fragmentation in all three mass spectra is low. As expected, the lowest level of fragmentation was observed for the model compound mixture dissolved in isooctane as the reagent ion m/z 57 is the least reactive reagent ion (Figure 3.1).²² The relative abundance of the most abundant fragment ions in the isooctane solution was 4%, while they were 8% for the *n*-hexane and methylcyclohexane solutions. To determine which saturated hydrocarbon model

Based on previous studies, four different ion-molecule reactions have the potential to give rise to fragment ions upon APCI of saturated hydrocarbons (M): $M + O_2^+$, $M + NO^+$, $M + H_3O^+$, and $M + R^+$ where R is a reagent carbenium ion.²³ Ion-molecule reaction experiments for all four reactions have shown that they are all exothermic and can lead to the formation of saturated hydrocarbon fragment ions.²⁴⁻²⁸ However, ion-molecule reaction experiments between different reagent carbenium ions (R^+) and neutral saturated hydrocarbon analytes were demonstrated to not generate fragment ions.¹¹ Therefore, it is unlikely that hydride abstraction by the reagent ions was the cause of fragmentation observed for the compounds in the equimolar mixture; this finding is elaborated on in Chapter 4. Nevertheless, isooctane was selected as the APCI reagent for the automated method.

3.3.2 Sample Carryover and Linear Dynamic Range Tests

Sample carryover and linear dynamic range experiments were conducted to evaluate the performance of the automated APCI/ O_2 /isooctane method. Table 3.1 shows the sequence used to assess carryover for each base oil dissolved in isooctane. After mass spectra had been collected for each base oil for two minutes, neat isooctane was injected into the APCI source using cleaning conditions. The extent of carryover was determined based on mass spectra measured between base oil samples for the neat isooctane under the same conditions as used for the samples. The first experiment began with a 12 minute cleaning time because, in combination with the two minute sample measurement time, the total analysis time (14 minutes) was similar to that of FI MS experiments. After the 12 minute cleaning, the neat isooctane mass spectrum showed no ions derived from saturated hydrocarbons in the base oils. However, after a two minute cleaning time, ions due to saturated hydrocarbons in the base oils were observed in the neat isooctane mass spectrum (data not shown). Therefore, since no ions of saturated hydrocarbons were detected after

a three minute cleaning after analysis of all base oils, this time was determined to be the ideal cleaning time. The total analysis time for each sample, regardless of the base oil's viscosity, was determined to be five minutes.

Table 3.1 Experimental sequence for evaluating base oil carryover and determining the shortest cleaning time required between sample measurements.

Sample name	Method	Time (minutes)	Injection Volume (μL)
Blank	Sample	2	10
Base Oil	Sample	2	10
Wash	Wash	12	10
Blank	Sample	2	10
Base Oil	Sample	2	10
Wash	Wash	11	10
...
Blank	Sample	2	10
Base Oil	Sample	2	10
Wash	Wash	3	10

Next, the linear dynamic range of the automated APCI/O₂/isooctane method was assessed. Pristane was selected as the model compound for these experiments for two reasons: 1) it is a branched saturated hydrocarbon, like many compounds found in base oils¹ and 2) its molecular weight is 268 Da, which falls outside the mass range of the saturated hydrocarbons in the middle viscosity base oil.¹¹ Although the [M-H]⁺ ion (m/z 267) of pristane did not overlap with any [M-H]⁺ ions of saturated hydrocarbons in the mass spectrum measured for the middle viscosity base oil, it did overlap with a fragment ion (data not shown). Therefore, fragment ions of saturated hydrocarbons in the middle viscosity base oil and ions of pristane contributed to the intensity of the ions of m/z 267.

APCI/O₂/isooctane mass spectra were measured for the six spiked base oil samples (see preparation of spiked samples in section 3.2). Figure 3.3 shows a linear relationship between the total ion abundance of the [M-H]⁺ ions (*m/z* 267) of pristane (and a fragment ion) and the concentration of pristane when the concentration was between ~0.25 mg/mL and ~3.0 mg/mL.

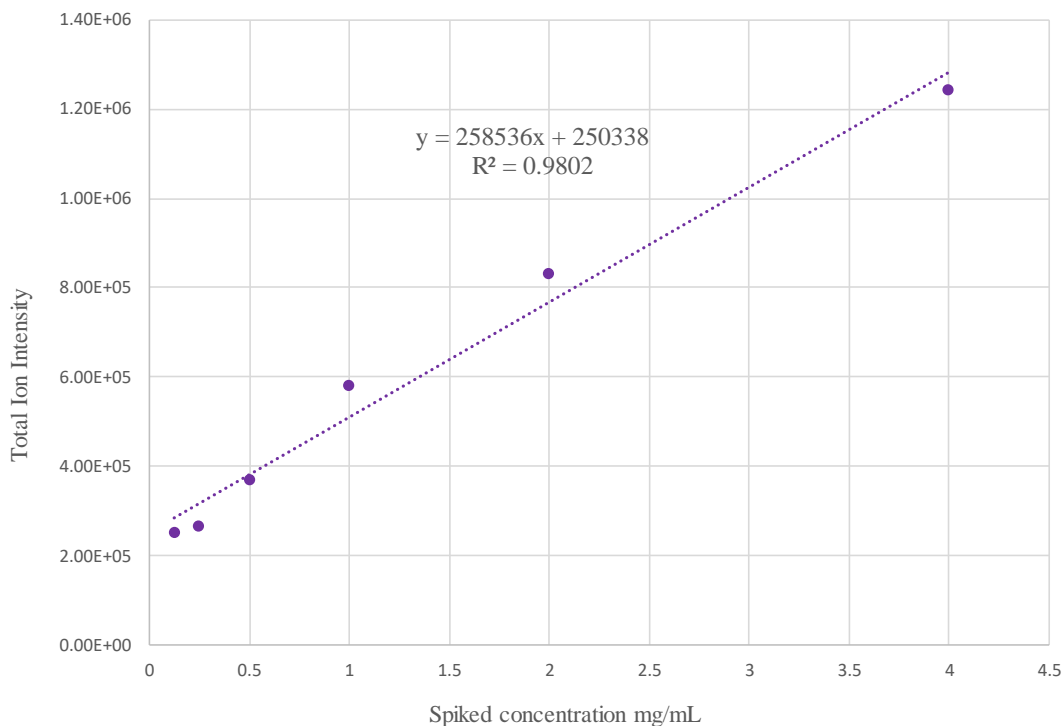


Figure 3.3 Total ion intensity of the [M-H]⁺ ions of pristane and fragment ions of saturated hydrocarbons in base oils (ions of *m/z* 267) dissolved in isooctane after spiking the middle viscosity base oil with six different amounts of pristane.

Based on this finding, six new middle viscosity base oil solutions with pristane concentrations ranging from 0.3 mg/mL to 3.0 mg/mL (in isooctane) were prepared and measured on three separate days to evaluate the reproducibility of the linear relationship. Figure 3.4 shows an overlay of the three plots of the relative abundances of ions of *m/z* 267 versus pristane concentration. Excellent linearity was observed as all R² values were greater than 0.996.

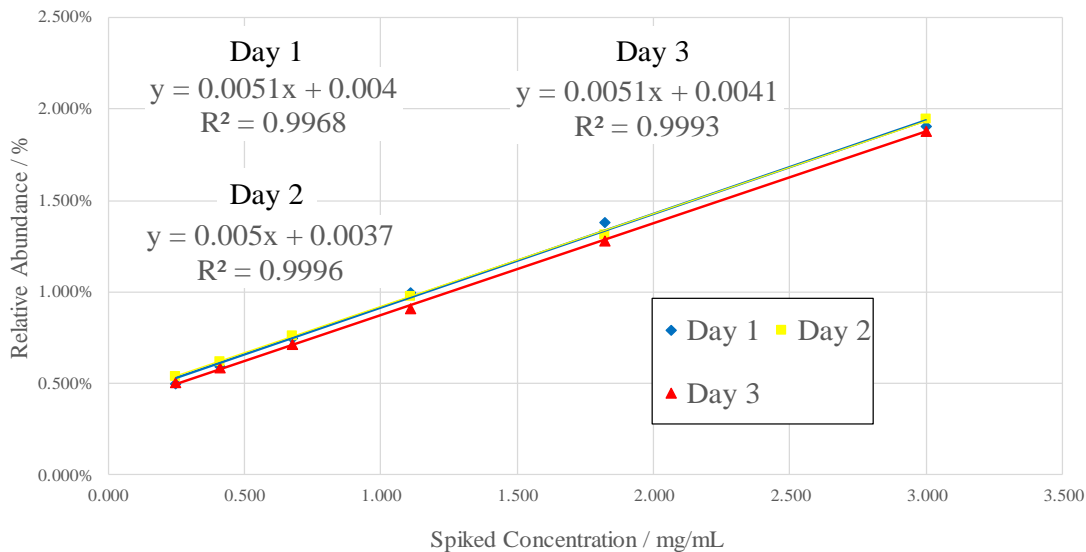


Figure 3.4 Triplicate measurements of the relative abundances of the $[M-H]^+$ ions (m/z 267) of pristane and fragment ions of saturated hydrocarbons in base oils (ions of m/z 267) dissolved in isooctane as a function of the concentration of pristane in the middle viscosity base oil. A linear relationship was observed between 0.3 mg/mL and 3.0 mg/mL.

3.3.3 Analysis of Base Oil Mass Spectra Measured by Using the Automated (+)APCI/O₂/Isooctane Method

Mass spectra of each nonspiked base oil (low, middle, and heavy viscosity) in isooctane were collected three times a day for six days. Figure 3.5 shows an individual (not average) (+)APCI/O₂/isooctane mass spectrum measured for each base oil. Based on previous analysis of these base oils,¹¹ the first distribution of ions represented the fragment ions (denoted in Figure 5), while the second distribution represented the $[M-H]^+$ ions of the saturated hydrocarbons. The greatest relative abundance of fragment ions was observed in the mass spectrum of the low viscosity base oil; the lowest relative abundance of fragment ions was observed in the mass spectrum of the heavy viscosity base oil. This finding suggests that a greater amount of branched and cyclic saturated hydrocarbons may be present in the low viscosity base oil since these classes of compounds generate the most abundant fragment ions.

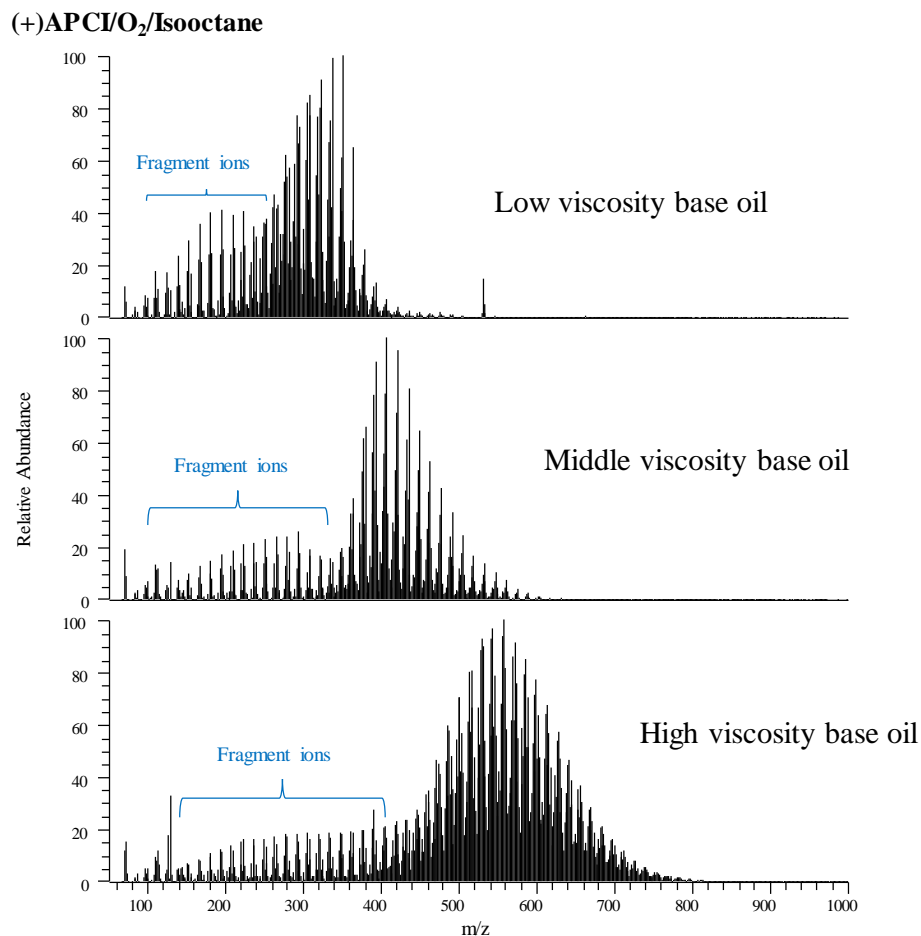


Figure 3.5 Individual (not averaged) positive ion mode APCI/O₂/isooctane mass spectra of the low, middle, and heavy viscosity base oils after injection using the automated method.

Determination of the range of the number of carbon atoms in the saturated hydrocarbons in the base oils can only be approximated due to the presence of fragment ions. Based on the bimodal distributions of the $[M-H]^+$ ions and fragment ions in the mass spectra measured for each base oil, the approximate ranges for the number of carbons were: 16-29 for saturated hydrocarbons in the low viscosity base oil, 26-43 for saturated hydrocarbons in the middle viscosity base oil, and 29-53 for saturated hydrocarbons in the heavy viscosity base oil. Furthermore, fragmentation presents some complications for semi-quantitative measurements: 1) small ions generated from saturated hydrocarbons in the base oils may be excluded because they overlap with the fragment

ion region, and 2) the relative abundances of the $[M-H]^+$ ions of saturated hydrocarbons may appear to be too low because some of them have fragmented. Table 3.2 displays the average distribution of the different classes of saturated hydrocarbons determined for the three base oils and their respective standard deviations; these values were determined based on 18 mass spectral measurements for each base oil. The six classes of saturated hydrocarbons in each base oil were identified in a previous study by using a LQIT equipped with a high-resolution orbitrap detector.¹¹ The low and middle viscosity base oils had similar saturated hydrocarbon class distributions: acyclic saturated hydrocarbons were the most abundant class followed by mono-, bi-, tri-, tetra-, and pentacyclic saturated hydrocarbons in that order. On the other hand, the saturated hydrocarbon distribution measured for the heavy viscosity base oil was different as the mono-, bi-, and tricyclic saturated hydrocarbons were the most abundant, followed by the tetracyclic, acyclic and pentacyclic saturated hydrocarbons.

Table 3.2 Saturated hydrocarbon class distribution percentages for each base oil determined based on the average of 18 positive-ion mode APCI/O₂/isooctane mass spectra.

Hydrocarbon class	Low viscosity	Middle viscosity	High viscosity
Pentacyclic saturated hydrocarbons	5.1% ± 0.3%	2.8% ± 0.1%	8.5% ± 0.4%
Tetracyclic saturated hydrocarbons	8.6% ± 0.3%	5.8% ± 0.1%	14.5% ± 0.4%
Tricyclic saturated hydrocarbons	14.7% ± 0.4%	11.4% ± 0.2%	20.1% ± 0.3%
Dicyclic saturated hydrocarbons	20.2% ± 0.2%	19.5% ± 0.2%	22.1% ± 0.3%
Monocyclic saturated hydrocarbons	21.5% ± 0.4%	27.2% ± 0.1%	20.0% ± 0.5%
Acyclic saturated hydrocarbons	25.1% ± 1.3%	33.3% ± 0.6%	14.9% ± 0.6%

Table 3.3 shows the within day, between day, and total precision results for the saturated hydrocarbon class distributions in each of the three base oils. Less than 5% within day and between

day precision values were achieved for all saturated hydrocarbon classes in each base oil. For all base oil samples, the pentacyclic saturated hydrocarbon class had the highest (the worst) total precision; 6.2% for the low viscosity, 4.9% for the middle viscosity, and 5.2% for the heavy viscosity base oil. Since ions generated from the pentacyclic saturated hydrocarbons have the smallest abundances of all six saturated hydrocarbon classes, minor changes in the ion abundances for this class will have a greater influence on the total precision than a similar abundance change for ions with greater abundances. On the contrary, the best total precision (most precise) measurement was made for the bicyclic saturated hydrocarbons in the low and heavy viscosity base oils (0.8% and 1.4%, respectively), while the best total precision measurement was made for the monocyclic saturated hydrocarbons in the middle viscosity base oil (0.5%). Overall, the total precision values were extremely low, suggesting that the automated (+)APCI/O₂/isooctane method was reproducible.

Table 3.3 Within day, between day, and total precision for the automated (+)APCI/O₂/isooctane method to determine the saturated hydrocarbon class distribution percentages in each base oil.

Hydrocarbon class	Low viscosity			Middle viscosity			High viscosity		
	RSD _{FWD}	RSD _{BD}	Total precision	RSD _{FWD}	RSD _{BD}	Total precision	RSD _{FWD}	RSD _{BD}	Total precision
Pentacyclic saturated hydrocarbons	4.2%	4.6%	6.2%	3.9 %	3.0 %	4.9 %	3.5 %	3.8 %	5.2 %
Tetracyclic saturated hydrocarbons	3.0%	2.6%	4.0%	1.9 %	1.3 %	2.3 %	2.1 %	2.1 %	3.0 %
Tricyclic saturated hydrocarbons	2.2%	1.8%	2.8%	1.5 %	1.1 %	1.9 %	1.1 %	1.4 %	1.7 %
Dicyclic saturated hydrocarbons	0.7%	0.4%	0.8%	0.7 %	0.6 %	0.9 %	1.2 %	0.6 %	1.4 %
Monocyclic saturated hydrocarbons	1.4%	1.1%	1.8%	0.4 %	0.2 %	0.5 %	1.8 %	2.0 %	2.7 %
Acyclic saturated hydrocarbons	3.9%	3.4%	5.2%	1.5 %	1.2 %	1.9 %	1.6 %	3.5 %	3.9 %

Nevertheless, the stability of the ion signals in the mass spectra of the base oils collected on the same day and between days were evaluated. Figure 3.6 demonstrates that consistent and

stable total ion signals were measured, regardless of the day and time, for the middle viscosity base oil by using the automated APCI/O₂/isooctane method. This was a major advantage over FI MS as the ion signals measured by FI MS were unstable and fluctuated between sample measurements.⁹ Furthermore, FI MS mass spectra measured for the same middle viscosity base oil showed variations in total ion signal, leading to inconsistent distributions of the different classes of saturated hydrocarbons.¹¹

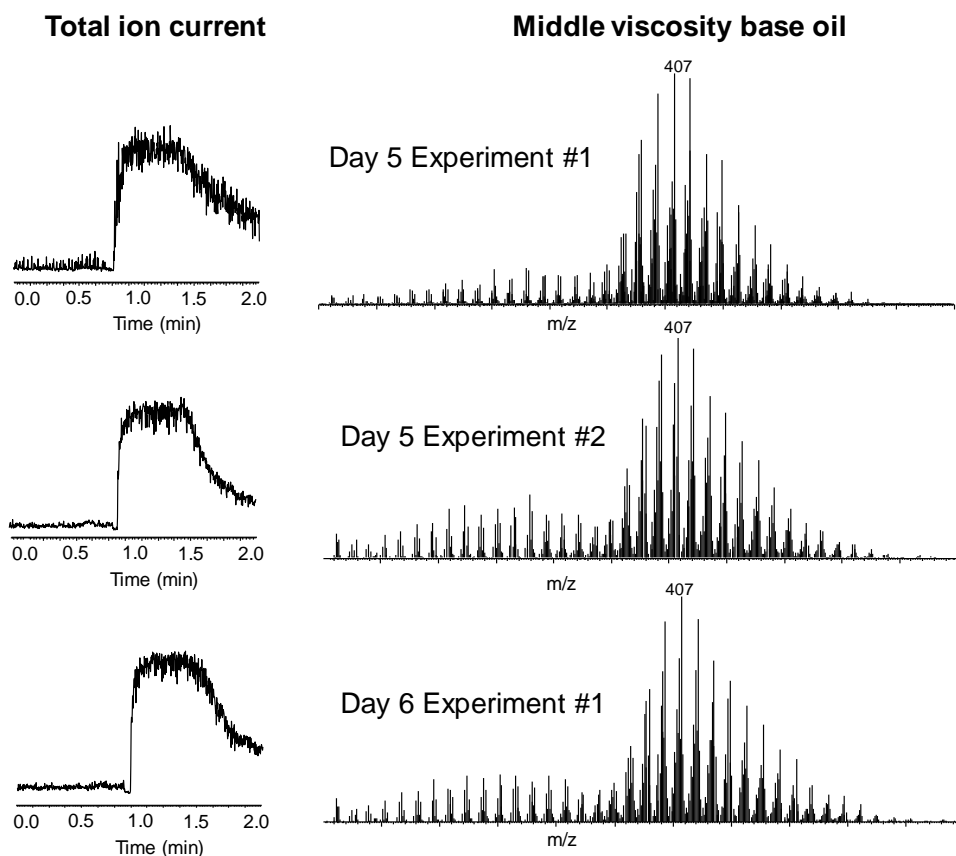


Figure 3.6 Three positive ion mode APCI/O₂/isooctane mass spectra measured on the same day (right; top and middle mass spectra) and on different days (right; top and middle mass spectra vs. bottom mass spectrum) for the middle viscosity base oil by using the automated method. Total ion chromatograms (left of the mass spectra) end at two minutes due to the two minute sample analysis time.

The individual ion abundances in replicate mass spectra were carefully examined to assess the consistency of ionization, *i.e.*, how similar the relative ion abundances for the same ionized saturated hydrocarbon were between replicate mass spectra, for the different saturated hydrocarbons in the three base oils. The ranges of ion abundances observed for ions generated from different types of saturated hydrocarbons in the low, middle and heavy viscosity base oil samples are displayed in Figure 3.7 - Figure 3.9. Figure 3.8 shows that none of the error bars (standard deviations) determined for the average ion abundances for the saturated hydrocarbons in the middle viscosity base oil overlap, suggesting consistent ionization of each saturated hydrocarbon. However, for the low viscosity base oil, in Figure 3.7, the error bars for some of the saturated hydrocarbons in the monocyclic and acyclic class overlap suggesting that ionization of monocyclic and acyclic saturated hydrocarbons may not be consistent between measurements. Furthermore, Figure 3.9 shows many overlapping error bars for the ion abundances for the mono-, bi-, tri-, tetracyclic, and acyclic saturated hydrocarbons in the heavy viscosity base oil suggesting that the ionization may not be consistent. However, in Figure 3.10, the ion abundance distributions as a function of the number of carbons from 36 up to 46 for the mono-, bi-, tri- and tetracyclic and acyclic saturated hydrocarbon classes in the heavy viscosity base oil are similar for all 18 mass spectra. The consistent distributions of the ion abundances for these five classes that shows overlapping error bars in Figure 3.9 suggests that consistent mass spectra were measured in different days.

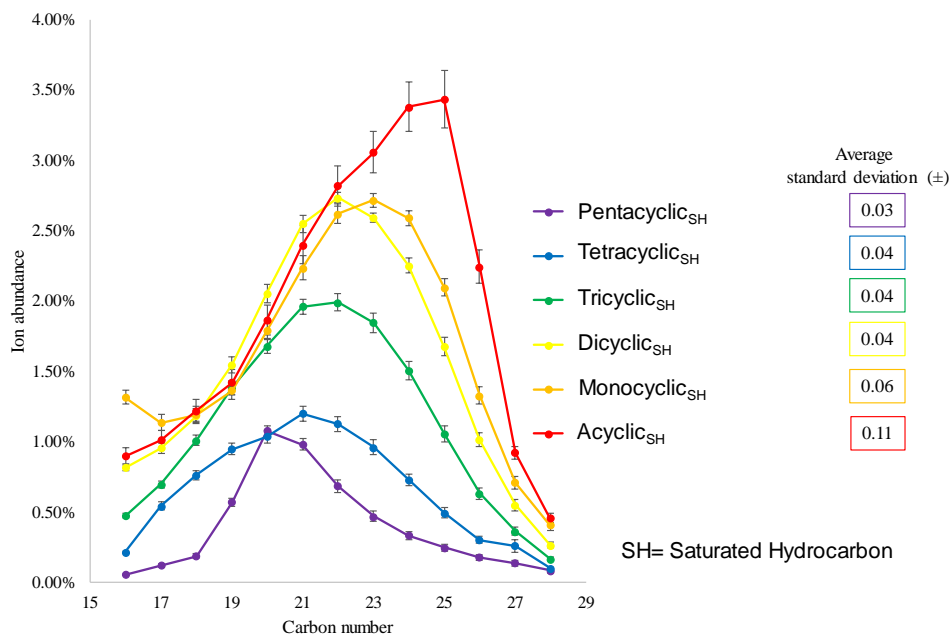


Figure 3.7 Ion abundance plotted as a function of the number of carbons for the six saturated hydrocarbon classes in the low viscosity base oil in isoctane. Ion abundances are an average of those measured in 18 mass spectra. Error bars represent the range of ion abundances for each carbon number.

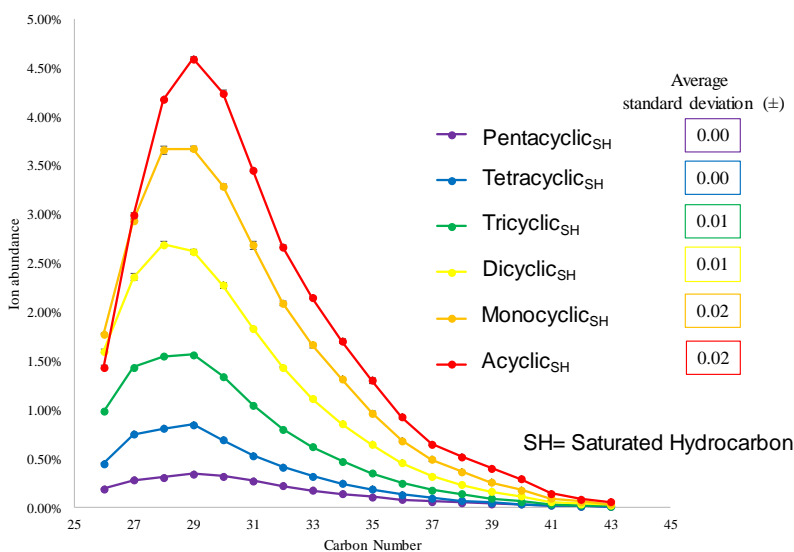


Figure 3.8 Ion abundance plotted as a function of the number of carbons for the six saturated hydrocarbon classes in the middle viscosity base oil in isoctane. Ion abundances are an average of those measured in 18 mass spectra. Error bars represent the range of ion abundances for each carbon number.

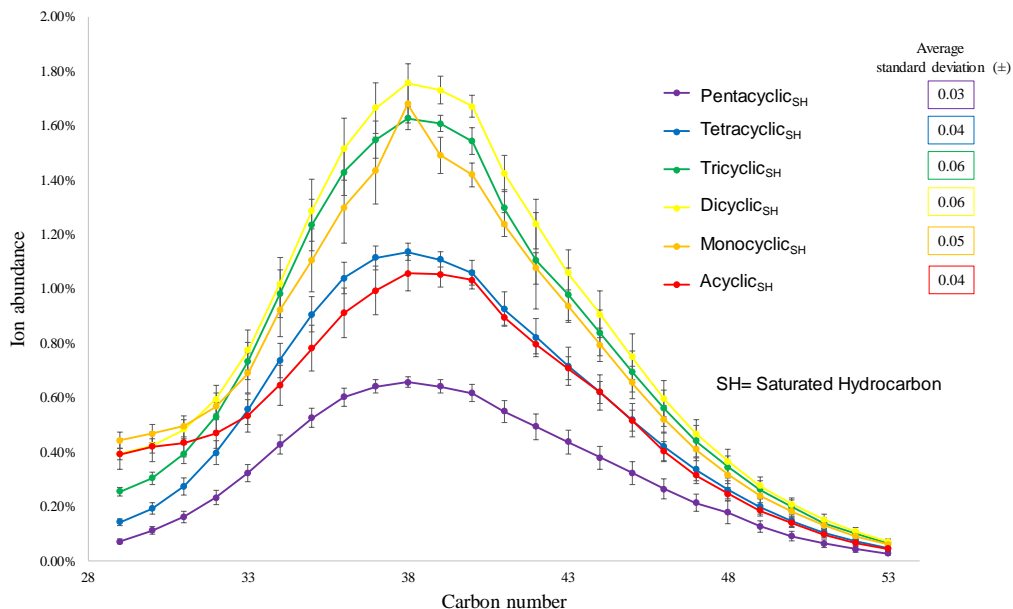


Figure 3.9 Ion abundance plotted as a function of the number of carbons for the six saturated hydrocarbon classes in the heavy viscosity base oil in isoctane. Ion abundances are an average of those measured in 18 mass spectra. Error bars represent the range of ion abundances for each carbon number.

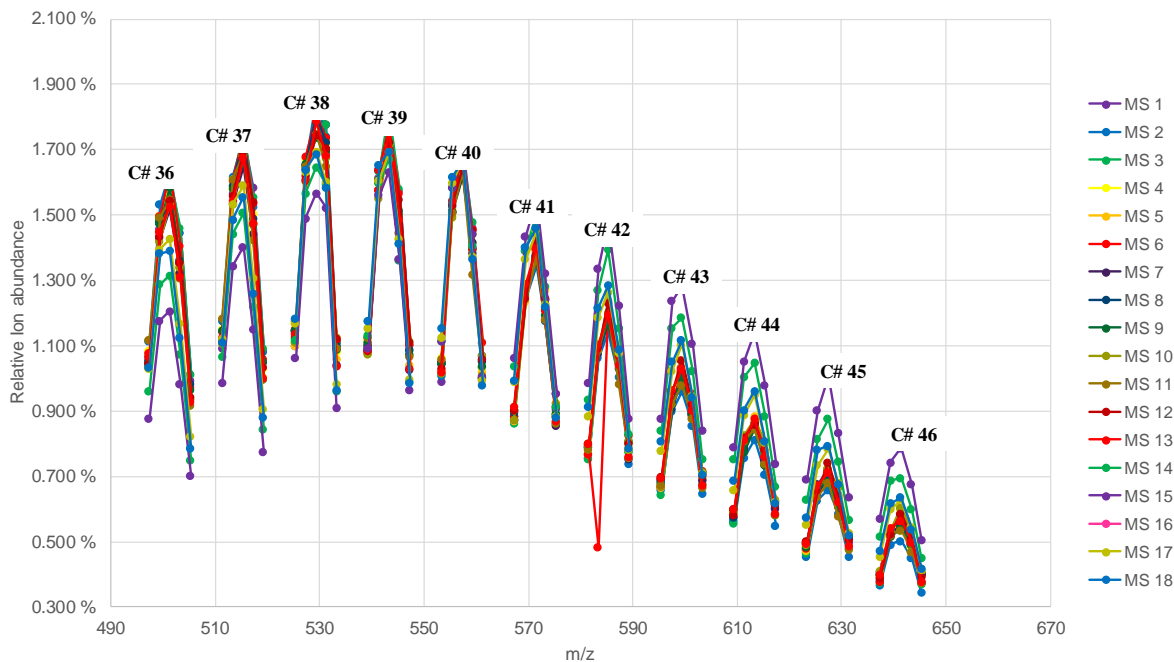


Figure 3.10 Ion abundances plotted as a function of m/z values ions generated from the mono-, di-, tri- and tetracyclic and acyclic saturated hydrocarbons with 36-46 carbon atoms in the heavy viscosity base oil in isoctane.

3.4 Conclusions

Automation of the APCI/O₂/isooctane MS method for the analysis of base oils was demonstrated to yield a highly reproducible method that requires minimal instrument cleaning time. Additional benefits of the method are that it only generates one type of ions, [M-H]⁺ ions, for each different type of saturated hydrocarbon studied, fragmentation was minimal, and base oils of different viscosities could be analyzed very fast. Additionally, the insignificant variability in the saturated hydrocarbon class distribution percentages measured for each base oil suggested that the method is capable of generating reproducible semi-quantitative data. Compared to FI MS, the automated APCI/O₂/isooctane method is superior and should help oil refineries to better evaluate their methods for converting crude oil into desired products.

Further improvements in determining the range of the number of carbons in the saturated hydrocarbons and the relative amounts of each saturated hydrocarbon class could be achieved by reducing, or eliminating, fragmentation caused by the APCI technique. Chapter 4 details experiments conducted to better understand the mechanism(s) of APCI of saturated hydrocarbons in order to advance the analysis of samples, such as base oils, that contain these compounds.

3.5 References

- (1) Prince, R. J. Base Oils from Petroleum. In *Chemistry and Technology of Lubricants*; Mortier, R. M., Orszulik, S. T., Eds.; Springer US: Boston, MA, 1994; pp 1–31.
- (2) Mistry, R.; Maynus, R. Crucial for Rotating Machines: Types and Properties of Lubricants and Proper Lubrication Methods. *IEEE Ind. Appl. Mag.* **2016**, 22 (6), 10–18.
- (3) Kramer, D. C.; Ziemer, J. N.; Cheng, M. T.; Fry, C. E.; Reynolds, R. N.; Lok, B. K.; Sztenderowicz, M. L.; Krug, R. R. Influence of Group II & III Base Oil Composition on VI AND Oxidation Stability. *NLGI spokesman*, **1999**, 1-36.

- (4) Duan, P.; Qian, K.; Habicht, S. C.; Pinkston, D. S.; Fu, M.; Kenttämäa, H. I. Analysis of Base Oil Fractions by $\text{ClMn}(\text{H}_2\text{O})^+$ Chemical Ionization Combined with Laser-Induced Acoustic Desorption/Fourier Transform Ion Cyclotron Resonance Mass Spectrometry. *Anal. Chem.* **2008**, *80* (6), 1847–1853.
- (5) Sarpal, A. S.; Kapur, G. S.; Mukherjee, S.; Jain, S. K. Characterization by ^{13}C NMR Spectroscopy of Base Oils Produced by Different Processes. *Fuel* **1997**, *76* (10), 931–937.
- (6) Sastry, M. I. S.; Chopra, A.; Sarpal, A. S.; Jain, S. K.; Srivastava, S. P.; Bhatnagar, A. K. Determination of Physicochemical Properties and Carbon-Type Analysis of Base Oils Using Mid-IR Spectroscopy and Partial Least-Squares Regression Analysis. *Energy Fuels* **1998**, *12* (2), 304–311.
- (7) Wang, F. C.-Y.; Zhang, L. Chemical Composition of Group II Lubricant Oil Studied by High-Resolution Gas Chromatography and Comprehensive Two-Dimensional Gas Chromatography. *Energy Fuels* **2007**, *21* (6), 3477–3483.
- (8) Manheim, J.; Wehde, K.; Zhang, W. T. J.; Vozka, P.; Romanczyk, M.; Kilaz, G.; Kenttämäa, H. I. Identification and Quantitation of Linear Alkanes in Lubricant Base Oils by Using GC×GC/EI TOF Mass Spectrometry. *J. Am. Soc. Mass Spectrom.* **2019**, *30*, 2670–2677.
- (9) Lattimer, R. P.; Schulten, H. R. Field Ionization and Field Desorption Mass Spectrometry: Past, Present, and Future. *Anal. Chem.* **1998**, *61* (21), 1201A–1215A
- (10) Klesper, G.; Röllgen, F. W. Field-Induced Ion Chemistry Leading to the Formation of $(\text{M}-2\text{nH})^+$ and $(2\text{M}-2\text{mH})^+$ Ions in Field Desorption Mass Spectrometry of Saturated Hydrocarbons. *J. Mass Spectrom.* **1996**, *31* (4), 383–388.
- (11) Jin, C.; Viidanoja, J.; Li, M.; Zhang, Y.; Ikonen, E.; Root, A.; Romanczyk, M.; Manheim, J.; Dziekonski, E.; Kenttämäa, H. I. Comparison of Atmospheric Pressure Chemical Ionization and Field Ionization Mass Spectrometry for the Analysis of Large Saturated Hydrocarbons. *Anal. Chem.* **2016**, *88* (21), 10592–10598.
- (12) Li, X.; Yan, X.; Cooks, R. G. Functionalization of Saturated Hydrocarbons Using Nitrogen Ion Insertion Reactions in Mass Spectrometry. *Int. J. Mass Spectrom.* **2017**, *418*, 79–85.
- (13) Wu, C.; Qian, K.; Nefliu, M.; Cooks, R. G. Ambient Analysis of Saturated Hydrocarbons Using Discharge-Induced Oxidation in Desorption Electrospray Ionization. *J. Amer. Soc. Mass Spectrom.* **2010**, *21* (2), 261–267.
- (14) Li, G.; Li, X.; Ouyang, Z.; Cooks, R. G. Carbon–Carbon Bond Activation in Saturated Hydrocarbons by Field-Assisted Nitrogen Fixation. *Angew. Chem. Int. Ed.* **2013**, *52* (3), 1040–1043.

- (15) Bell, S. E.; Ewing, R. G.; Eiceman, G. A.; Karpas, Z. Atmospheric Pressure Chemical Ionization of Alkanes, Alkenes, and Cycloalkanes. *J. Amer. Soc. Mass Spectrom.* **1994**, *5* (3), 177–185.
- (16) Hourani, N.; Kuhnert, N. Development of a Novel Direct-Infusion Atmospheric Pressure Chemical Ionization Mass Spectrometry Method for the Analysis of Heavy Hydrocarbons in Light Shredder Waste. *Anal. Methods* **2012**, *4* (3), 730–735.
- (17) Hourani, N.; Kuhnert, N. High Molecular Weight Non-Polar Hydrocarbons as Pure Model Substances and in Motor Oil Samples Can Be Ionized without Fragmentation by Atmospheric Pressure Chemical Ionization Mass Spectrometry. *Rapid Commun. Mass Spectrom.* **2012**, *26* (19), 2365–2371.
- (18) Hourani, N.; Muller, H.; Adam, F. M.; Panda, S. K.; Witt, M.; Al-Hajji, A. A.; Sarathy, S. M. Structural Level Characterization of Base Oils Using Advanced Analytical Techniques. *Energy Fuels* **2015**, *29* (5), 2962–2970.
- (19) Owen, B. C.; Gao, J.; Borton, D. J.; Amundson, L. M.; Archibold, E. F.; Tan, X.; Azyat, K.; Tykwinski, R.; Gray, M.; Kenttämaa, H. I. Carbon Disulfide Reagent Allows the Characterization of Nonpolar Analytes by Atmospheric Pressure Chemical Ionization Mass Spectrometry. *Rapid Commun. Mass Spectrom.* **2011**, *25* (14), 1924–1928.
- (20) Krouwer, J. S.; Rabinowitz, R. How to Improve Estimates of Imprecision. *Clin. Chem.* **1984**, *30* (2), 290–292.
- (21) Frash, M. V.; Solkan, V. N.; Kazansky, V. B. A Quantum-Chemical Study of Hydride Transfer from Alkanes to Carbenium Cations in the Gas Phase: A Comparison with Liquid- and Solid-Acid Catalytic Systems. *J. Chem. Soc., Faraday Trans.* **1997**, *93* (4), 515–520.
- (22) Douberly, G. E.; Ricks, A. M.; Ticknor, B. W.; Schleyer, P. v. R.; Duncan, M. A. Infrared Spectroscopy of the Tert-Butyl Cation in the Gas Phase. *J. Am. Chem. Soc.* **2007**, *129* (45), 13782–13783.
- (23) Marotta, E.; Paradisi, C. A Mass Spectrometry Study of Alkanes in Air Plasma at Atmospheric Pressure. *J. Amer. Soc. Mass Spectrom.* **2009**, *20* (4), 697–707.
- (24) Lias, S. G.; Eyler, J. R.; Ausloos, P. Hydride Transfer Reactions Involving Saturated Hydrocarbons and CCl_3^+ , CCl_2H^+ , CCl_2F^+ , CF_2Cl^+ , CF_2H^+ , CF_3^+ , NO^+ , C_2H_5^+ , $\text{Sec-C}_3\text{H}_7^+$ and $\text{t-C}_4\text{H}_9^+$. *Int. J. Mass Spectrom. Ion Phys.* **1976**, *19* (2), 219–239.
- (25) Arnold, S. T.; Viggiano, A. A.; Morris, R. A. Rate Constants and Branching Ratios for the Reactions of Selected Atmospheric Primary Cations with *n*-Octane and Isooctane (2,2,4-Trimethylpentane). *J. Phys. Chem. A* **1997**, *101* (49), 9351–9358.
- (26) Arnold, S. T.; Viggiano, A. A.; Morris, R. A. Rate Constants and Product Branching Fractions for the Reactions of H_3O^+ and NO^+ with C_2 – C_{12} Alkanes. *J. Phys. Chem. A* **1998**, *102* (45), 8881–8887.

- (27) Matsuoka, S.; Ikezoe, Y. Ion-Molecule Reactions and Thermal Decomposition of Ions in N₂-O₂-Alkane (C₂-C₈) Mixtures Studied by Time-Resolved Atmospheric Pressure Ionization Mass Spectrometry. *J. Phys. Chem.* **1988**, *92*, 1126–1133.
- (28) Španěl, P.; Smith, D. Selected Ion Flow Tube Studies of the Reactions of H₃O⁺, NO⁺, and O₂⁺ with Several Aromatic and Aliphatic Hydrocarbons. *Int. J. Mass Spectrom.* **1998**, *181* (1–3), 1–10.

CHAPTER 4. PROTON TRANSFER REACTIONS CAUSE FRAGMENTATION OF SATURATED HYDROCARBONS UPON ATMOSPHERIC PRESSURE CHEMICAL IONIZATION

4.1 Introduction

Accurate characterization of the saturated hydrocarbons in complex mixtures would help facilitate breakthroughs in many fields of science including petroleum research,¹ forensic science,² evolutionary biology,³ and food science.⁴ For instance, a better understanding of the chemical composition of mixtures of saturated hydrocarbons would enable faster and more environmentally beneficial processes to achieve desired end-products in crude oil refining.⁵ Unfortunately, modern analytical techniques have limited success in characterizing this class of compounds; section 3.1 of Chapter 3 highlights the drawbacks of current instrumentation. Of the numerous techniques discussed, atmospheric pressure chemical ionization (APCI) mass spectrometry has the greatest potential to accomplish these analyses.^{6,7}

Discussed in Chapter 3, APCI with O₂ as the sheath and auxiliary gas primarily generates [M-H]⁺ ions from saturated hydrocarbons with various saturated hydrocarbon solvents.⁷ The advantages of the APCI/O₂/isooctane method are that it's reproducible, quick, easy to conduct, and provides semi-quantitative information on the saturated hydrocarbon class distributions.⁷ Although this method was only applied to the analysis of base oils, the APCI/O₂/isooctane method can be used to characterize other complex mixtures of saturated hydrocarbons. The major drawback of this method is the undesirable production of fragment ions from saturated hydrocarbons, which complicate the mass spectrum. For example, fragmentation makes it difficult to determine the *exact* range of the number of carbon atoms in the compounds in the mixture. Additionally, fragmentation can exacerbate semi-quantitative measurements.

To reduce, or eliminate, the fragmentation of large saturated hydrocarbons in complex mixtures caused by APCI, it is imperative to understand the mechanism(s) involved in their ionization. Previously discussed in Chapters 2 section 2.2 and Chapter 3 section 3.3, APCI of saturated hydrocarbons involves multiple ionization steps. In the final step of the proposed APCI mechanism of saturated hydrocarbons, carbenium reagent ions generated from saturated hydrocarbon solvents abstract a hydride from analyte molecules to form analyte-derived $[M-H]^+$ ions.⁸⁻¹⁰ Therefore, the extent of saturated hydrocarbon fragmentation upon APCI is expected to be due to the exothermicity of the hydride abstraction reaction. However, such proposals have not been considered in previous studies. On the other hand, several groups have proposed that the fragmentation of saturated hydrocarbons upon APCI was caused by highly exothermic electron abstraction reactions by N_2^+ , N_4^+ and/or O_2^+ ions (generated upon corona discharge of N_2 or O_2 gas in the atmosphere).^{9,11} However, fragmentation of saturated hydrocarbons via electron abstraction reactions have never been experimentally investigated.

The goal of this study was to determine the reasons for the fragmentation of saturated hydrocarbons upon APCI. APCI of saturated hydrocarbons was modelled by studying ion-molecule reactions between neutral saturated hydrocarbons and reagent ions in a linear quadrupole ion trap mass spectrometer (LQIT MS). Additionally, a modified APCI source was built to test whether analyte interactions with the corona discharge in APCI caused fragmentation.

4.2 Experimental Section

Chemicals. *n*-Butylcyclohexane (99% purity), isooctane ($\geq 99\%$ purity), *n*-hexane ($\geq 99\%$ purity), formaldehyde (38% w/w in water), cyclohexane (99.5% purity), and cyclohexane- d_{12} (99.6% purity) were purchased from Sigma Aldrich (St. Louis, MO) and used as received. The lubricant base oil sample was provided by Neste, Finland; this base oil is the same as the middle viscosity

base oil studied in Chapter 3. Nitrogen gas was obtained from the boil-off of liquid nitrogen and ultrapure oxygen (99.995% purity) was purchased from Praxair, Inc.

Atmospheric Pressure Chemical Ionization (APCI) Mass Spectrometry. Positive-ion mode direct infusion APCI experiments were conducted on a Thermo Fisher Scientific LTQ XL linear quadrupole ion trap (LQIT) mass spectrometer. A Hamilton 500 μL syringe was used to inject liquid samples at a flow rate of 10 - 20 $\mu\text{L}/\text{min}$ through PEEK tubing with an inner diameter of 0.005 inches into the APCI source. Faster flow rates prevented complete evaporation of the sample and led to the formation of unwanted adducts, while slower flow rates resulted in low, irreproducible total ion signals. APCI source conditions were optimized for ionization of saturated hydrocarbons as reported in Chapter 3.⁷ The APCI conditions were: sheath and auxiliary gas (either nitrogen or oxygen); 60 and 30 arbitrary units, respectively; vaporizer temperature, 150 $^{\circ}\text{C}$; capillary tube temperature, 50 $^{\circ}\text{C}$; capillary voltage, 10 V; and tube lens voltage, 30 V. These optimized parameters provide the greatest total ion signal and the lowest amount of fragmentation.

Ion-Molecule Reactions in the Ion Trap. Ions produced via APCI were transferred into the ion trap. Reagent ions were isolated by ejecting all unwanted ions from the ion trap (see Chapter 2, section 2.3.3.3.2). The isolation window for each reagent ion varied and was selected based on the largest total ion signal that could be achieved without isolating nearby ions. Therefore, only reactions between the isolated reagent ions and neutral saturated hydrocarbons were studied. Neutral saturated hydrocarbons were introduced into the ion trap via a home-built manifold that was discussed in Chapter 2 section 2.5.¹² Neat, liquid saturated hydrocarbons were introduced into the manifold via a syringe drive at a flow rate of 5 $\mu\text{L}/\text{hr}$. The neutral saturated hydrocarbons were

diluted with helium and leaked into the ion trap at a flow rate of 2 mL/min. Evaporation of the saturated hydrocarbons into the helium flow was accomplished by heating the manifold to 70 °C by using heating tape. Isolated reagent ions and neutral saturated hydrocarbons were allowed to react in the ion trap for a variable time from 0.03 to 500 ms. Product ions, if any, generated from these reactions were scanned out of the ion trap and detected by the electron multipliers.

Ion Trap Collision-Activated Dissociation. Several product ions formed via ion-molecule reactions were isolated and subjected to collision-activated dissociation (CAD) to determine their structures. Discussed in chapter 2 section 2.3.3.3, these ions were accelerated via RF voltages and allowed to collide with the helium buffer gas. Precursor and fragment ions were scanned out of the ion trap to the electron multipliers for detection.

Stainless Steel Tube (SS) Ion Source Designs. The Jonathan Amy facility in the Chemistry Department at Purdue University modeled and built a new APCI source to help test whether saturated hydrocarbon interactions with a corona discharge caused fragmentation. The entire SS ion source had an inner diameter of approximately ~10 mm. A corona needle was situated inside the SS ion source that pointed 16 mm from the exit of the stainless steel tube (Figure 4.1A). Between the stainless steel tube and metal insert was a piece of peek that provided insulation. A voltage source supplied the corona needle, stainless steel tube, and metal insert with their own voltages that can be controlled independently from one another. The optimized voltages were corona needle, +6 kV; stainless steel tube, +3 kV; and metal insert, +1.5 kV. The SS tube was housed in a brass tube that was attached to a steel plate the size of the front window of the Thermo Scientific API house box (Figure 4.1B). When positioned inside the API house box, the SS tube

ion source was 12 mm from the entrance of the ion transfer capillary tube and positioned directly underneath the ceramic heater of the APCI source (Figure 4.1C). As shown in Figure 4.1C, the metal nozzle of the APCI source was removed for these experiments to prevent contact between the SS tube and APCI ion sources. The SS tube ion source could not be moved closer because otherwise it would block the opening of the APCI source and put a strain on the ceramic heater.

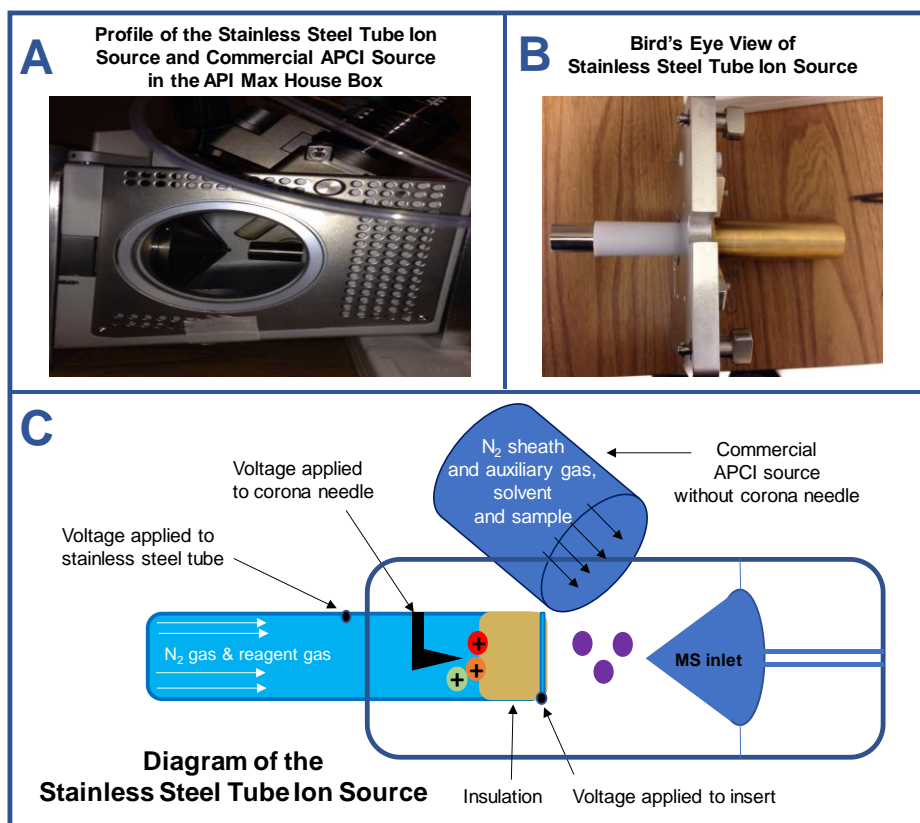


Figure 4.1 (A) Picture of the positioning of the stainless steel (SS) tube ion source in the API max house box. (B) Picture of the SS tube ion source. (C) Sketch of the SS tube ion source and commercial APCI source in the API house box. Voltages applied to the SS tube ion source and direction of sheath/auxiliary gas (N₂), reagent gas and sample flow are indicated on the diagram. Red, orange, and green dots represent reagent ions generated in the SS tube ion source. Purple dots represent neutral analyte compounds that come from the APCI source without a corona discharge needle.

Several gas lines and solvent pumps were externally connected to the SS tube ion source (Figure 4.2). The nebulizing gas first entered a drying tube to remove atmospheric moisture. The

gas then flowed into three locations: the APCI source and the two gas flow regulators. Isooctane (solvent) was injected using an injection pump at a flow rate of 1.2 mL/hr. Nebulizing gas mixed with the isooctane in a region that was heated to $\sim 100^\circ\text{C}$ by using heating tape. A second solvent injection pump was set up to test a combination of solvents for ionization, however, it was seldom used and did not improve, or change, the experimental outcomes. Lastly, solvent and nebulizing gas were mobilized through the SS tube ion source at a flow rate of 10 L/min.

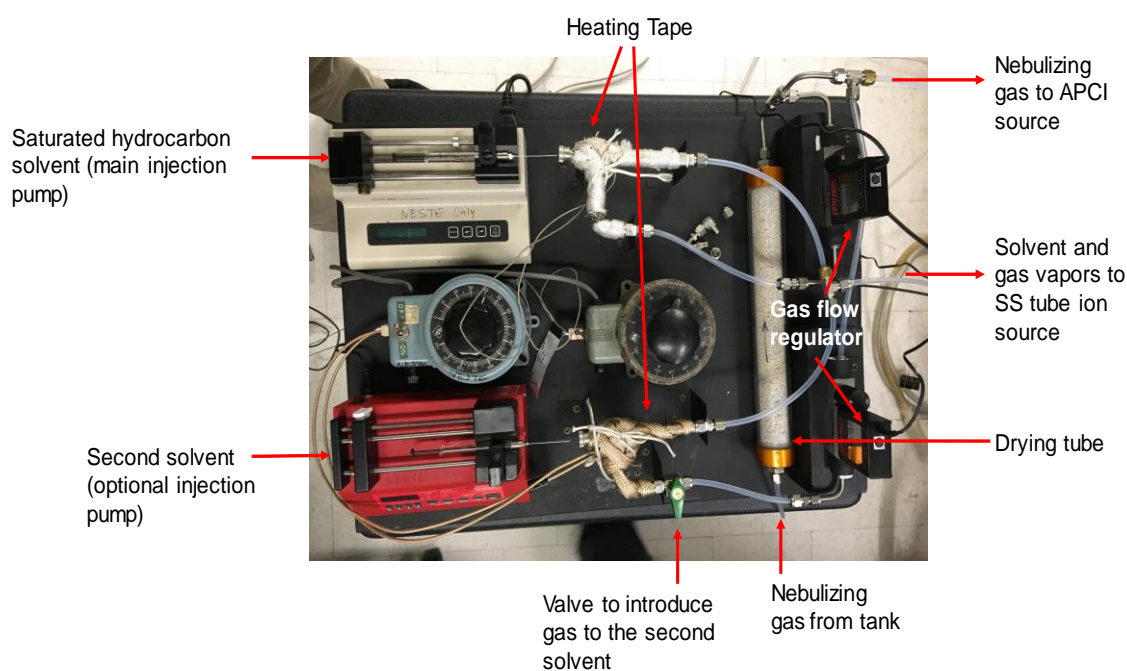


Figure 4.2 Photograph of the arrangement and connections of the equipment used to introduce gaseous solvent through the SS tube ion source.

Atmospheric ions were generated via corona discharge of the nebulizing gas and reagent gas at the tip of the corona needle inside the SS tube ion source. Positive ions formed inside the SS tube ion source were repelled by the positive-charged walls of the tube and metal insert and carried into the API house box by the nitrogen nebulizing gas. These ions underwent reactions with saturated hydrocarbon analytes that were introduced through the commercial APCI source

(Figure 4.1A). In this manner, saturated hydrocarbon analytes were solely ionized by the ions generated inside the SS tube ion source.

4.3 Results and Discussion

The goal of this work was to identify reagent ions that upon reactions with saturated hydrocarbons in the ion trap reproduced the fragmentation pattern observed for saturated hydrocarbons upon APCI. A necessary first step was to investigate the extent of fragmentation for an individual saturated hydrocarbon upon APCI. If the level of fragmentation in the APCI mass spectrum of an individual saturated hydrocarbon could be reproduced in the ion-molecule reaction mass spectrum between the neutral saturated hydrocarbon and the isolated reagent ion, then this reaction was a potential cause of fragmentation upon APCI. *n*-Butylcyclohexane was chosen as the model saturated hydrocarbon for several reasons: 1) it is a cyclic saturated hydrocarbon, which are abundant in complex mixtures of saturated hydrocarbons, 2) APCI of *n*-butylcyclohexane generated abundant fragment ions, and 3) its boiling point is below the 200 °C threshold of the manifold. Furthermore, nitrogen gas was selected as the nebulizing gas as this was the most commonly used nebulizing gas in APCI and it was less expensive than ultrapure oxygen gas (used in Chapter 3).^{9,13-16}

4.3.1 Fragmentation of *n*-Butylcyclohexane Dissolved in Isooctane upon APCI

To examine the fragmentation pattern of *n*-butylcyclohexane upon APCI, the positive-ion mode direct infusion APCI mass spectrum was measured for *n*-butylcyclohexane dissolved in isooctane at a concentration of 10 mg/mL (Figure 4.3, top). In this mass spectrum, [M-H]⁺ ions of isooctane, *m/z* 113, and of *n*-butylcyclohexane, *m/z* 139, were observed in addition to many fragment ions. To determine which fragment ions came from which saturated hydrocarbon, APCI

mass spectra of neat *n*-butylcyclohexane (Figure 4.3, middle) and isooctane (Figure 4.3, bottom) were measured. Fragment ions of m/z 97 and 83 were most abundant in the APCI mass spectrum of neat *n*-butylcyclohexane (Figure 4.3, middle) and were also observed in the APCI mass spectrum of *n*-butylcyclohexane dissolved in isooctane (Figure 4.3, top). However, these two ions were not observed in the APCI mass spectrum of neat isooctane (Figure 4.3, bottom) demonstrating that these fragment ions form exclusively from *n*-butylcyclohexane. Similarly, fragment ions of m/z 111, 99, and 71 form exclusively from isooctane as these ions were not present in the APCI mass spectrum of neat *n*-butylcyclohexane. Interestingly, the relative abundance of the most abundant fragment ion of *n*-butylcyclohexane, m/z 83, was similar in both the APCI mass spectra of neat *n*-butylcyclohexane and *n*-butylcyclohexane dissolved in isooctane (Figure 4.3, top, zoomed-in mass spectrum). With the APCI fragmentation pattern of *n*-butylcyclohexane identified, the causes for its fragmentation could then be investigated by using ion-molecule reactions.

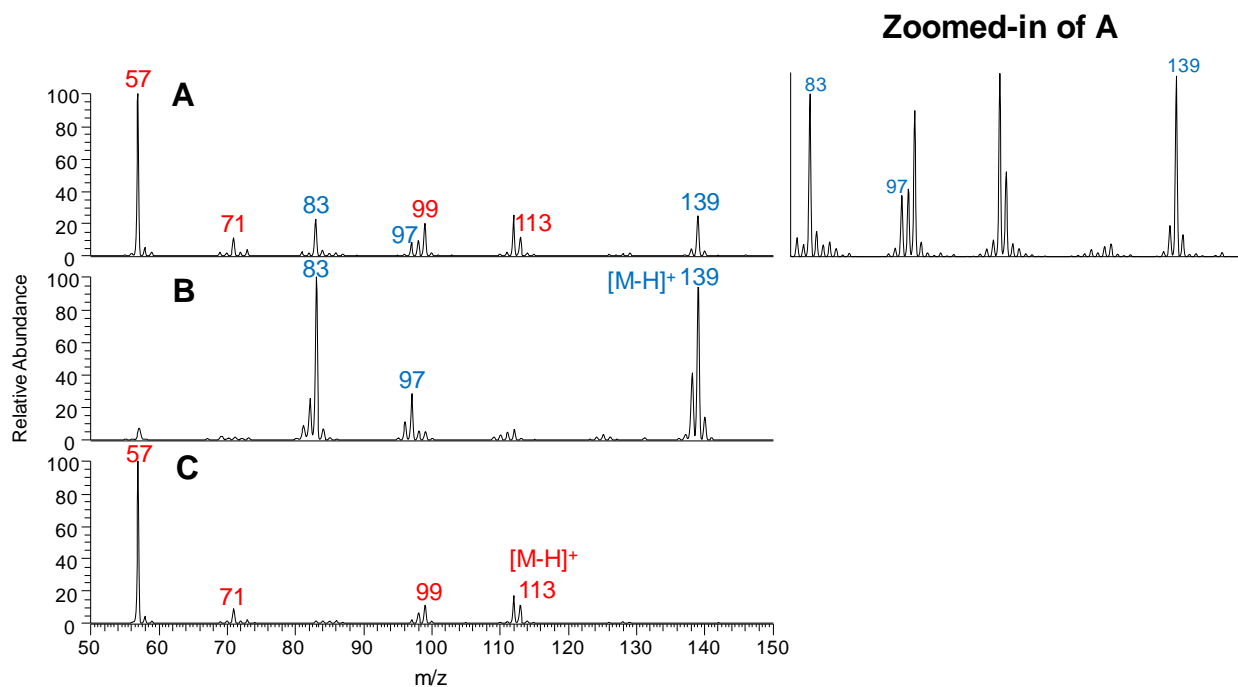


Figure 4.3 (A) Full and zoomed-in direct-infusion (+)APCI mass spectra of *n*-butylcyclohexane (MW 140 Da) dissolved in isooctane. The [M-H]⁺ and fragment ions of *n*-butylcyclohexane and isooctane are blue and red, respectively. (B) (+)APCI mass spectrum of neat *n*-butylcyclohexane. (C) (+)APCI mass spectrum of neat isooctane.

4.3.2 Ion-Molecule Reaction Experiments Between Neutral Saturated Hydrocarbons and Ions Proposed to Cause Their Fragmentation

As previously discussed, reactions between radical cations, $N_2^{+\bullet}$, $N_4^{+\bullet}$, and/or $O_2^{+\bullet}$, and saturated hydrocarbons were proposed to be the cause of saturated hydrocarbon fragmentation upon APCI.^{9,11} Unfortunately, nitrogen molecular ions ($N_2^{+\bullet}$) and nitrogen-solvated nitrogen molecular ions ($N_4^{+\bullet}$) could not be observed in APCI experiments (explained in Chapter 2 section 2.2), and therefore, these reagent ions could not be studied in these experiments. On the other hand, $O_2^{+\bullet}$ ions were observed in the APCI mass spectrum when only oxygen nebulizing gas was introduced through the ion source (data not shown). The bottom of Figure 4.4 displays the ion-molecule reaction mass spectrum measured for reactions of ions of m/z 32 ($O_2^{+\bullet}$) with *n*-butylcyclohexane after 0.03 ms reaction time. The [M-H]⁺ ions of *n*-butylcyclohexane were not

observed in the mass spectrum, but rather the molecular ions (m/z 140), $M^{+\bullet}$, of *n*-butylcyclohexane. Furthermore, the most abundant fragment ion in this mass spectrum was a fragment ion of m/z 82. A comparison between the ion-molecule reaction mass spectrum (Figure 4.4, bottom) to the direct-infusion APCI mass spectrum of neat *n*-butylcyclohexane (Figure 4.4, top) revealed that the relative abundances of the fragment ions of m/z 82 were much lower in the direct-infusion mass spectrum. This result suggests that electron abstraction of *n*-butylcyclohexane by $O_2^{+\bullet}$ radical cations were not the major cause of saturated hydrocarbon fragmentation upon APCI.

Since the ionization energies of O_2 (12.1 eV) and N_2 (15.6 eV) are both very large, the extent of saturated hydrocarbon fragmentation upon reactions with molecular ions derived from these gases is expected to be similar. Furthermore, since $N_2^{+\bullet}$, $N_4^{+\bullet}$, and $O_2^{+\bullet}$ ions are all even-mass radical cations, reactions between these ions and saturated hydrocarbons most likely produce similar types of fragment ions. Therefore, we hypothesized that the even-mass ions observed in the APCI mass spectra of saturated hydrocarbons (see Figure 4.3) were produced from the reactions between even-mass ions and neutral saturated hydrocarbons. Of all the ion-molecule reactions measured, the reactions between $O_2^{+\bullet}$ ions and neutral *n*-butylcyclohexane was the only one to produce even-mass fragment ions; all other reactions (discussed in the following sections) generated odd-mass fragment ions. However, the low relative abundances of the even-mass fragment ions compared to the odd-mass fragment ions implied that even-mass, radical cations were not the main species responsible for saturated hydrocarbon fragmentation.

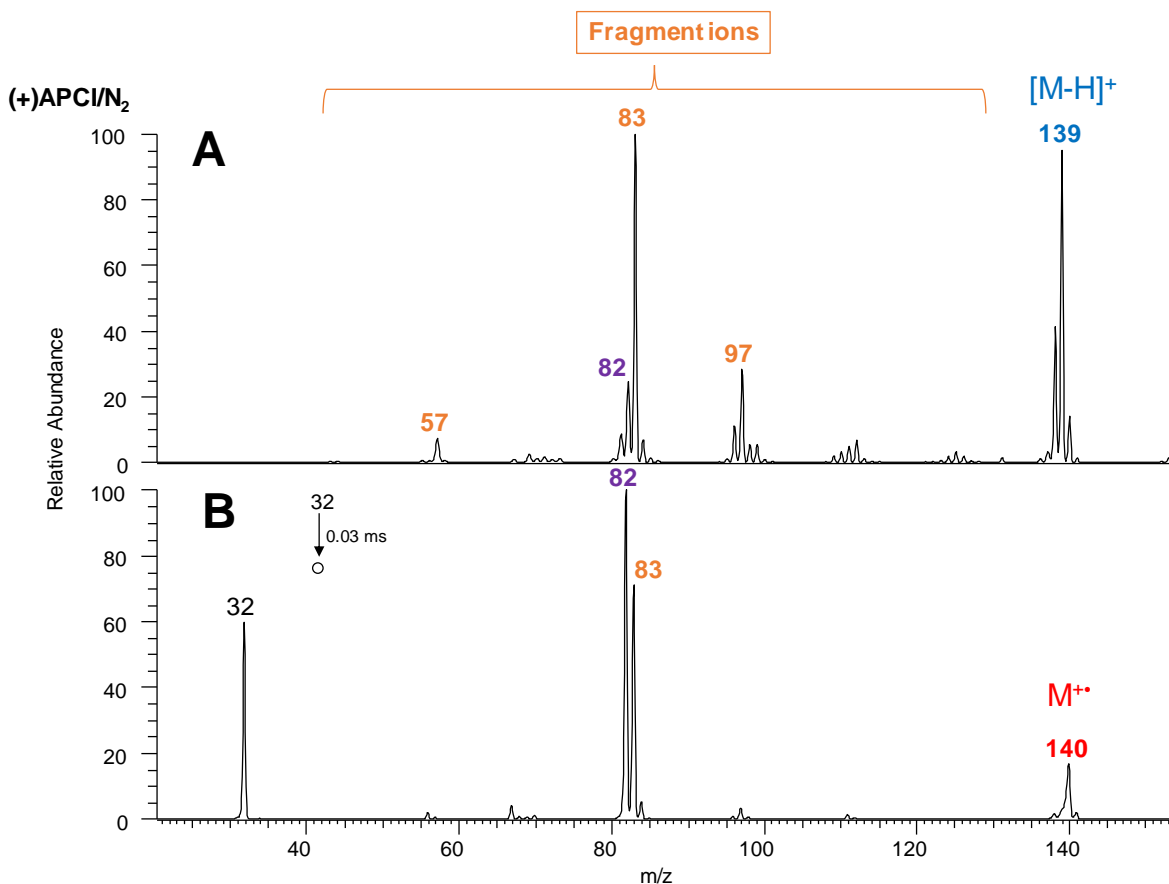


Figure 4.4 (A) Direct-infusion (+)APCI mass spectrum of neat *n*-butylcyclohexane. (B) Ion-molecule mass spectrum measured after 0.03 ms reaction between molecular ions of *m/z* 32 with neutral *n*-butylcyclohexane in the ion trap. The [M-H]⁺ ions of *n*-butylcyclohexane are colored blue, the M^{+•} ions of *n*-butylcyclohexane are colored red, odd-mass fragment ions of *n*-butylcyclohexane are colored orange, and even-mass fragment ions are colored purple.

Ion-molecule reactions with carbenium reagent ions, the species proposed to abstract a hydride from neutral saturated hydrocarbons in the APCI mechanism, were studied next. Ion-molecule reactions between ions of *m/z* 57 (the carbenium reagent ion generated from corona discharge of isooctane) and neutral *n*-butylcyclohexane (Figure 4.5) were conducted first. In Figure 4.5B, only [M-H]⁺ ions of *n*-butylcyclohexane, *m/z* 139, were observed, no fragment ions. It was considered, however, that the ions of *m/z* 57 gained excess energy during the APCI process (Scheme 2.3) and this excess energy lead to fragmentation upon their reactions with *n*-butylcyclohexane. This prospect was tested by supplying kinetic energy to the ions of *m/z* 57 in

the ion trap by applying a small “tickle” RF voltage; this voltage was the same voltage used to induce CAD (section 2.3.3.3.3). The RF voltage excited the isolated ions, without fragmenting them, and they collided with *n*-butylcyclohexane in the ion trap. Despite the increased energy of the ions of m/z 57, the level of fragmentation of *n*-butylcyclohexane was significantly lower than what was observed in the APCI mass spectrum of neat *n*-butylcyclohexane (Figure 4.5C and Figure 4.5D). The less abundant carbenium ions generated upon corona discharge of isooctane, including ions of m/z 71 and 99, were also tested; these reactions did not produce $[M-H]^+$ ions or fragment ions (Figure 4.6). Together, these results suggest that hydride abstraction reactions between carbenium ions and saturated hydrocarbons cannot account for the fragmentation of saturated hydrocarbons upon APCI.

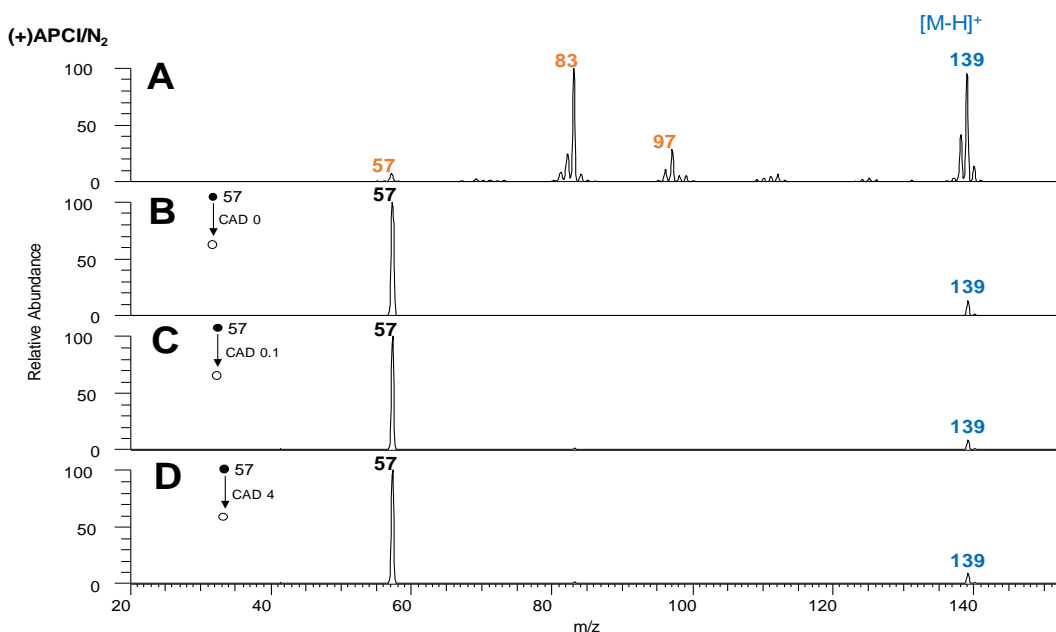


Figure 4.5 Direct-infusion (+)APCI mass spectrum of neat *n*-butylcyclohexane (A). Ion-molecule mass spectra measured after 500 ms reaction between the most abundant fragment ion of isooctane of m/z 57 and *n*-butylcyclohexane at normalized CAD energies of (B) 0, (C) 0.1, and (D) 4.0 (arbitrary units). CAD greater than 4 resulted in a poor signal. The $[M-H]^+$ ion of *n*-butylcyclohexane is colored blue and the fragment ions of *n*-butylcyclohexane are colored orange. Overlap between the isolated ion of m/z 57 and product fragment ions of m/z 57 from *n*-butylcyclohexane is unlikely because the more abundant fragment ions of m/z 83 and 97 are not observed.

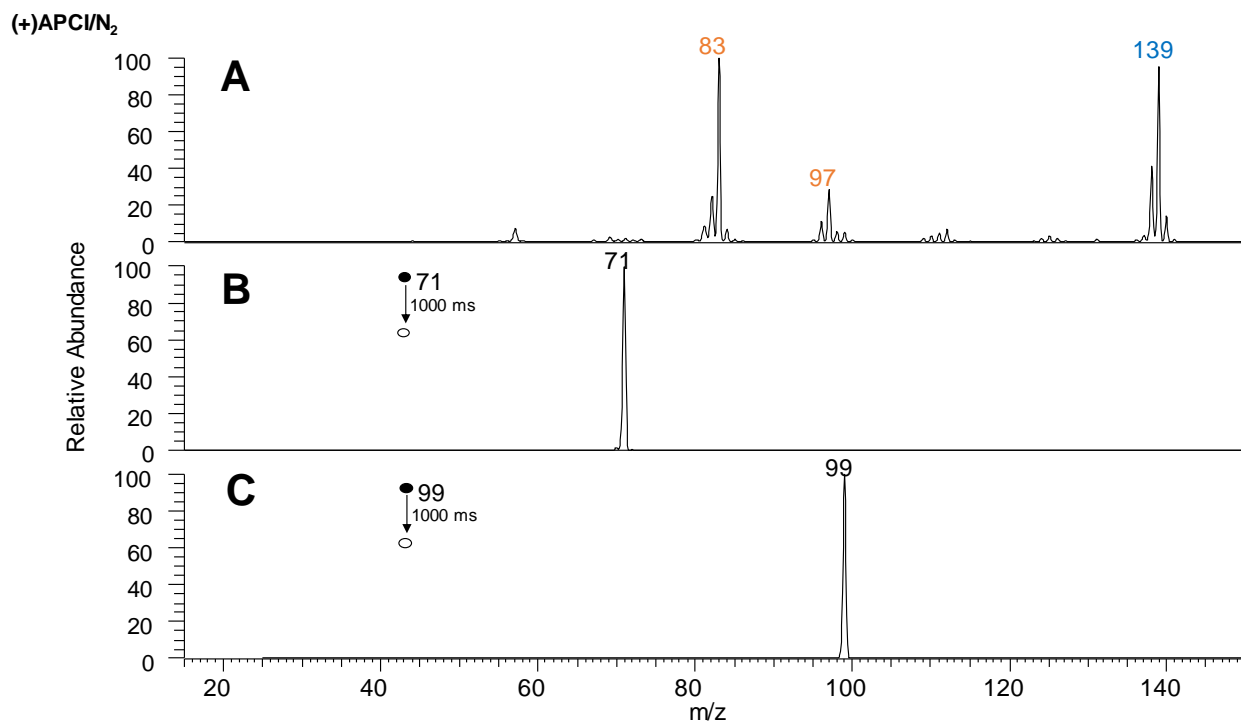


Figure 4.6 Direct-infusion (+)APCI mass spectrum of neat *n*-butylcyclohexane (A). The $[M-H]^+$ ion of *n*-butylcyclohexane is colored blue and the fragment ions of *n*-butylcyclohexane are colored orange. Ion-molecule mass spectra measured after 1000 ms reaction between the minor fragment ions of isooctane of *m/z* 71 (B) and *m/z* 99 (C) and *n*-butylcyclohexane.

4.3.3 New Ion Source Experiments

The high-energy plasma formed at the corona discharge needle initiates ion-molecule reactions in the APCI technique.¹⁷ As reactions proposed in the literature to cause fragmentation of saturated hydrocarbons were experimentally proven incorrect, analyte interactions with the corona discharge may be the problem. The stainless steel (SS) tube ion source was built to test this possibility. In this design, vaporized analytes introduced through a commercial APCI source were ionized by reagent ions generated inside the SS tube; analytes never came into contact with the corona discharge needle. The middle viscosity base oil (see Chapter 3) was ionized with both the SS tube ion source as well as the commercial APCI ion source, and the extent of fragmentation

observed in their respective mass spectra were compared. The total ion intensity measured for the SS tube ion source mass spectrum for the middle viscosity base oil (Figure 4.7, bottom) was an order of magnitude lower than that of the commercial APCI source mass spectrum (Figure 4.7, top). This was most likely due to the distance of the corona needle from the ion source - 2 mm in the commercial APCI source vs 28 mm in the SS tube ion source. Most importantly, the level of fragmentation in both mass spectra was the same, implying that saturated hydrocarbon contact with the corona discharge in APCI was not the cause of fragmentation.

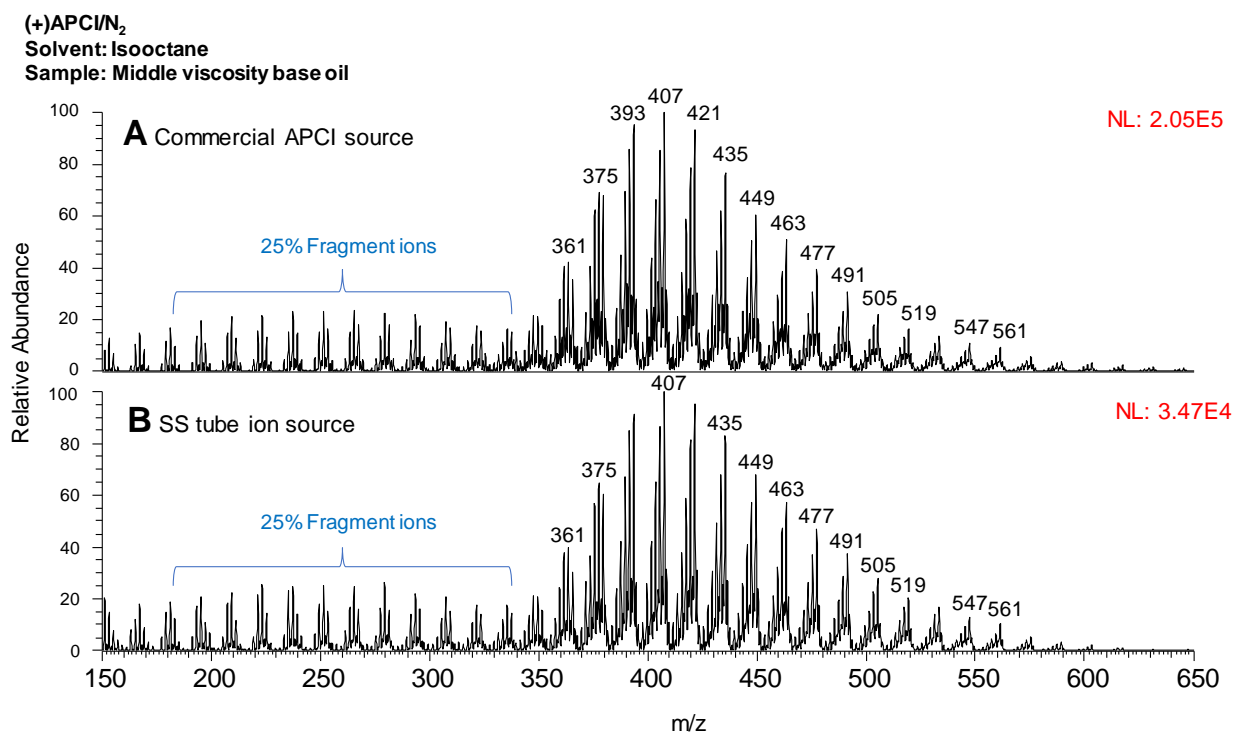


Figure 4.7 (A) Direct-infusion (+)APCI mass spectrum of the middle viscosity base oil dissolved in isooctane. (B) Direct-infusion (+)SS tube ion source mass spectrum of the middle viscosity base oil dissolved in isooctane.

4.3.4 Ion-Molecule Reaction Experiments Between Neutral Saturated Hydrocarbons and Ions Generated from Air

As all above experiments failed to account for the fragmentation of *n*-butylcyclohexane upon (+)APCI, reactions between ions formed from air upon APCI and saturated hydrocarbons were next considered. Previously described in Chapter 2, the most abundant species measured from a corona discharge in air were water ion clusters (i.e. $\text{H}_3\text{O}^+\cdot\text{H}_2\text{O}_n$).¹⁸ In agreement with past observations, the (+)APCI mass spectrum of only N_2 nebulizing gas primarily displayed protonated dimers (m/z 37) and trimers (m/z 55) of water (Figure 4.8, top). Ion-molecule reactions between these ions and *n*-butylcyclohexane at the maximum reaction time of 10 s did not reveal any $[\text{M}-\text{H}]^+$ or fragment ions (data not shown).

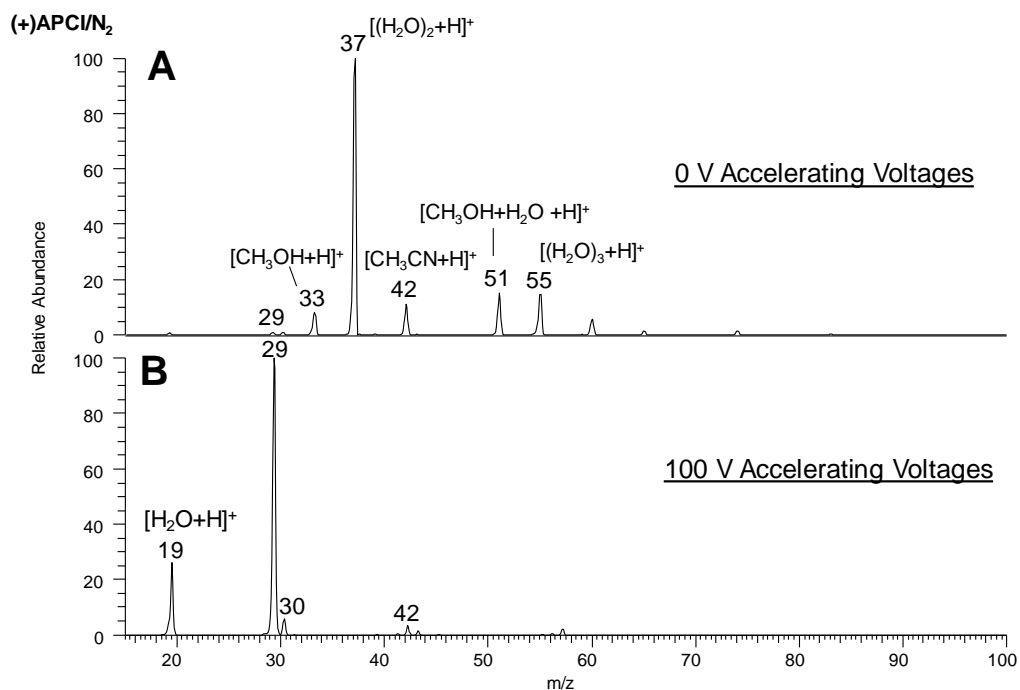


Figure 4.8 (A) Direct-infusion (+)APCI mass spectrum measured for N_2 gas without accelerating voltages. (B) Direct-infusion (+)APCI mass spectrum measured for N_2 gas with 100 V accelerating voltages.

Discussed in Chapter 2 section 2.2, water cluster ions were not the first species generated upon a corona discharge. Ions formed in the corona discharge have been previously measured by increasing the DC voltages on the multipoles and lenses of the ion optics; the most abundant ions observed were ions of protonated water (m/z 19) and m/z 29 - this ion was hypothesized to be protonated nitrogen.¹¹ Similarly, when the DC voltages of the ion optics of the LQIT MS were increased, abundant ions of m/z 19 and 29 were observed (Figure 4.8, bottom). Traditionally, increasing these voltages was done to perform in-source CAD (Chapter 2 section 2.3.3.3.4), which fragments ions. However, its application here was not to fragment, but rather to prevent reactions between the ions produced by the corona discharge and atmospheric water; therefore, the increase in these voltages was referred to as “acceleration voltages.” The success of acceleration voltages to reveal ions formed at the corona discharge region was hypothesized to be due to the increased kinetic energies of the ions travelling from the corona discharge to the ion trap. Ions with sufficiently high kinetic energies cannot form reaction complexes with neutral molecules long-lived enough to proceed towards products.¹⁹ Therefore, it was proposed that ions of m/z 19 and 29 were generated before the ion optics region of the LQIT MS and reactions between these ions and saturated hydrocarbons may result in fragmentation.

Ion-molecule reactions between *n*-butylcyclohexane and ions of m/z 19, H_3O^+ , could not be conducted, as protonated water could not be isolated regardless of the isolation window, most likely due to its proximity to the low mass cutoff of the LQIT (m/z 15). On the other hand, the ion-molecule reaction mass spectrum could be measured for the reactions between ions of m/z 29 and *n*-butylcyclohexane (Figure 4.9, bottom). Surprisingly, the direct-infusion APCI mass spectrum of *n*-butylcyclohexane (Figure 4.9, top) was similar to the ion-molecule reaction mass spectrum (Figure 4.9, bottom). In both mass spectra, the most abundant ions are the fragment ions of m/z 83

followed by the $[M-H]^+$ ions of m/z 139. Additionally, smaller fragment ions including ions of m/z 97, 81, 69, and 57 were present in both mass spectra. There are two differences between these mass spectra: 1) some of the fragment ions in the ion-molecule reaction mass spectrum (Figure 4.9, bottom) have higher relative abundances and 2) even-mass fragment ions are only observed in the APCI mass spectrum (Figure 4.9, top).

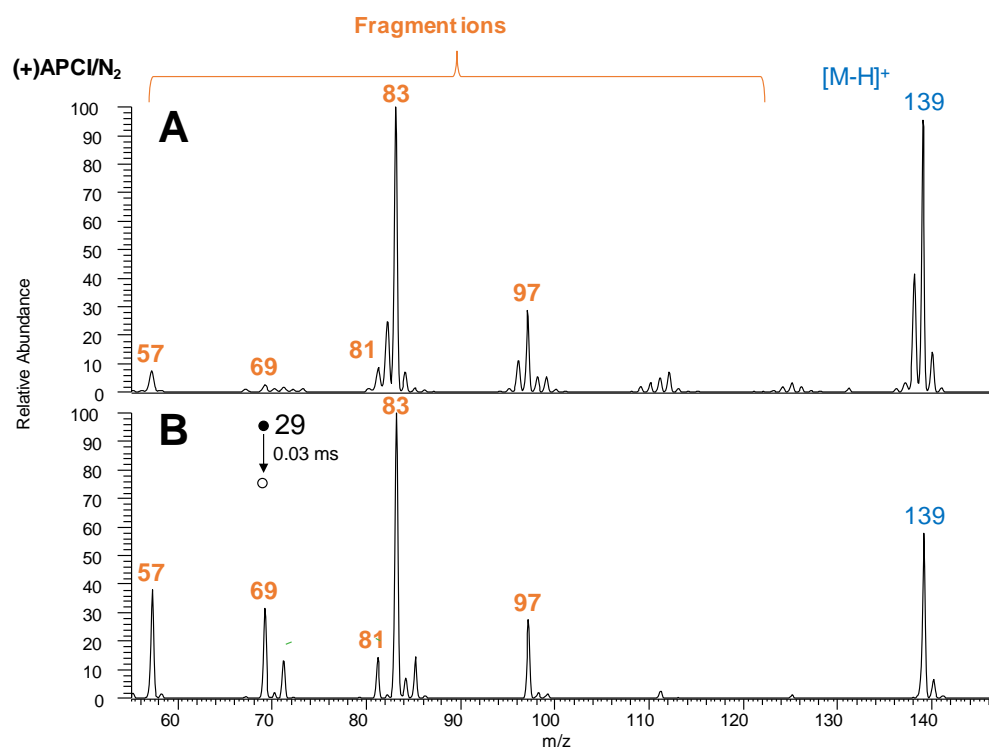


Figure 4.9 (A) Direct-infusion (+)APCI mass spectrum of neat *n*-butylcyclohexane. (B) Ion-molecule mass spectrum measured after 0.03 ms reaction between ions of m/z 29 and neutral *n*-butylcyclohexane. The $[M-H]^+$ ion of *n*-butylcyclohexane is colored blue and fragment ions of *n*-butylcyclohexane are colored orange. Both mass spectra are zoomed-in on the m/z range 55–150.

Despite these two differences, this reaction warranted further investigation as this was the only ion-molecule reaction thus far that produced products similar to those in the direct-infusion APCI mass spectrum of neat *n*-butylcyclohexane. Although ions of m/z 29 have been proposed to be N_2H^+ ions, this prediction was never experimentally confirmed.¹¹ Based on the elemental

composition of the atmosphere, 78% nitrogen, 21% oxygen, and trace amounts of carbon dioxide, nitrous oxide, and water,²⁰ and with the assistance of the NIST database,²¹ ions of m/z 29 could be one of four cations: CH_2NH^+ , C_2H_5^+ , COH^+ , and N_2H^+ . To determine the identity of the ions of m/z 29, a *bracketing experiment*, which takes advantage of the different proton affinities of the conjugate bases of these four cations, was conducted by using ion-molecule reactions. For these experiments, the observation of a proton transfer reaction between ions of m/z 29 and a neutral base indicates that the proton affinity of the neutral base is greater than that of the conjugate base of the ions of m/z 29. Table 4.1 lists the proton affinities (PA) of the four conjugate bases of the ions of m/z 29 and the neutral bases. For example, if a proton transfer reaction was observed between ions of m/z 29 and hexafluorobenzene (PA= 155 kcal/mol), then ions of m/z 29 were either COH^+ or N_2H^+ because the PAs' of the conjugate bases of these ions were lower (139.6 kcal/mol and 118.3 kcal/mol, respectively) than that of hexafluorobenzene. Figure 4.10 displays a diagram of the potential outcomes for the proton transfer reactions and the identities of the ions of m/z 29 based on these results.

Table 4.1 Proton affinities for the potential conjugate bases of the ions of m/z 29 and the neutral molecules selected for bracketing experiments.

Molecule	Proton Affinity (kcal/mol)	Reference/Level of Theory
CH ₂ N [•]	172	B3LYP/6-311++G(d,p)
C ₂ N ₄	163	NIST
CO	140	NIST
N ₂	118	NIST
Benzene, C ₆ H ₆	179	NIST
2,2,2-Trifluoroethanol, C ₂ H ₃ F ₃ O	167	NIST
Hexafluorobenzene, C ₆ F ₆	155	NIST
CO ₂	131	NIST

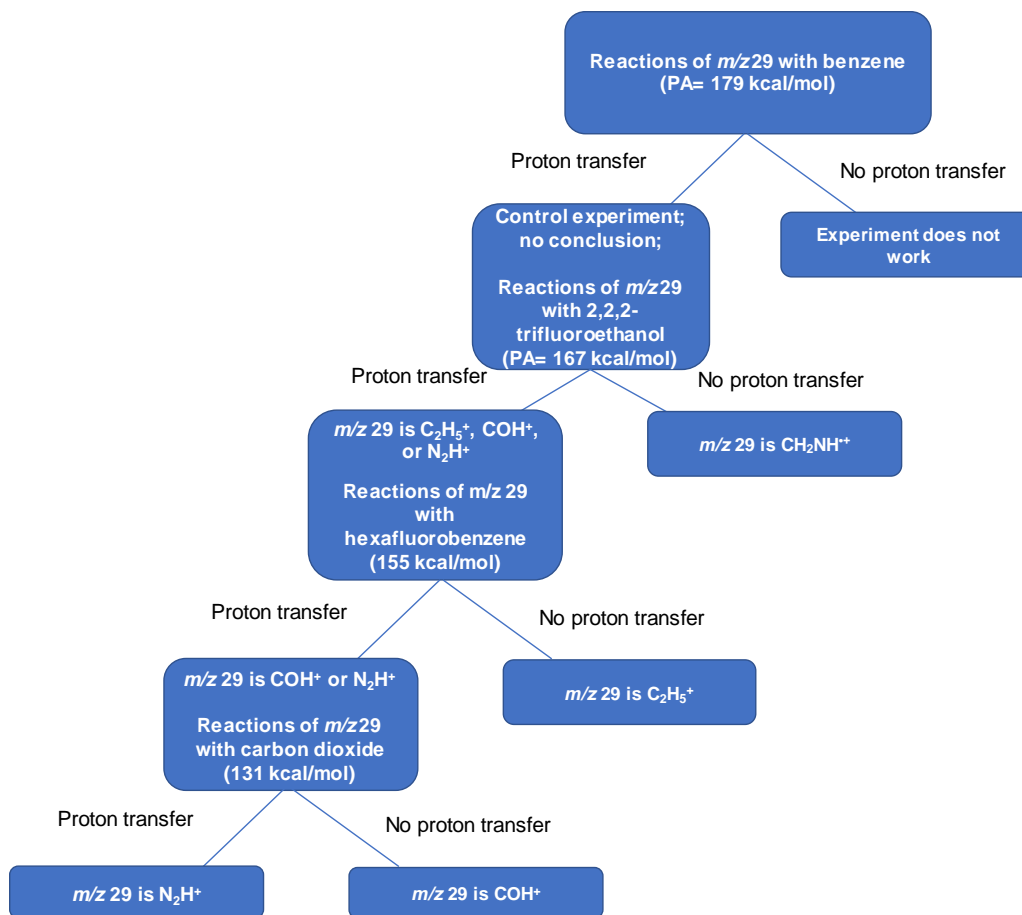


Figure 4.10 Flow chart demonstrating the possible identities of ions of m/z 29 from proton transfer reactions.

Figure 4.11 shows the mass spectra measured for three of the four ion-molecule reaction experiments conducted with ions of m/z 29. First, a peak of m/z 19, H_3O^+ , was observed in all three mass spectra most likely due to protonation of water (PA= 167 kcal/mol) that was present in the ion trap by ions of m/z 29. This observation eliminates CH_2NH^+ as the identity of ions of m/z 29 as its proton affinity is greater than waters. Interestingly, protonated benzene (Figure 4.11; top, m/z 79), protonated hexafluorobenzene (Figure 4.11; middle, m/z 187), and protonated carbon dioxide (Figure 4.11; bottom, m/z 45) were all observed in their respective ion-molecule reaction mass spectra. These results imply that the PA of the conjugate base of ions of m/z 29 was lower than that of all three neutral bases. The only cationic species acidic enough to protonate these three

species was protonated nitrogen, N_2H^+ . Although ions of m/z 29 were confirmed to be protonated nitrogen, the mechanism by which N_2H^+ reacts with *n*-butylcyclohexane to generate $[M-H]^+$ and fragment ions required stringent examination.

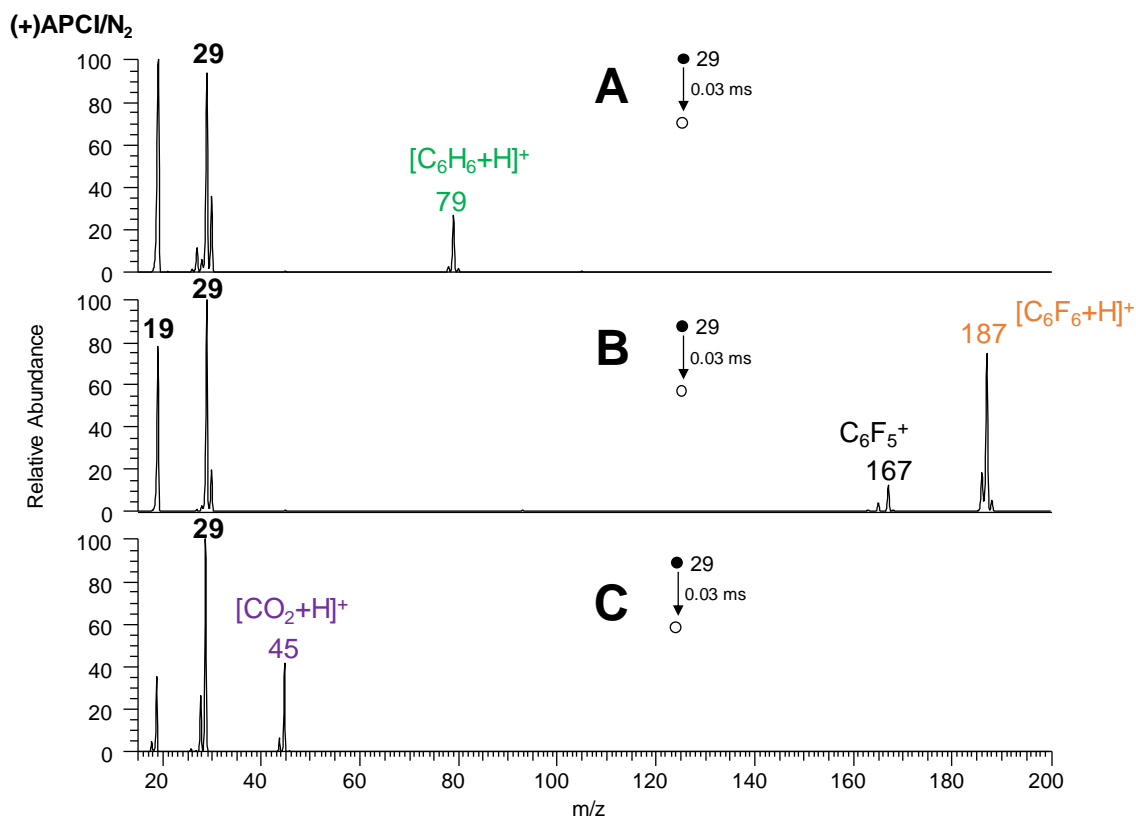


Figure 4.11 Ion-molecule mass spectra measured after 0.03 ms reaction between ions of m/z 29 with (A) benzene, (B) hexafluorobenzene, (C) carbon dioxide. Protonated product ions were observed in all three mass spectra.

4.3.5 Determination of the Ion-Molecule Reaction Mechanism Between Protonated Molecules and Saturated Hydrocarbons

The preceding results demonstrate that N_2H^+ ions protonate a variety of neutral molecules, however, upon reacting with *n*-butylcyclohexane, ions of m/z 141 (protonated *n*-butylcyclohexane) were not observed, but rather $[M-H]^+$ ions and fragment ions. Although hydride abstraction reactions by ions of N_2H^+ were considered, protonation of saturated hydrocarbons by strong acids

have been observed. For example, reactions between super acids and saturated hydrocarbons were observed to form $[M-H]^+$ ions after the loss of gaseous H_2 .²² Also, CI of saturated hydrocarbons by protonated methane produce $[M-H]^+$ ions and fragment ions.²³ Furthermore, the mechanism of acid-catalyzed hydrocracking of saturated hydrocarbons proposes the formation of intermediate carbonium ions (CR_5^+) followed by fragmentation to give neutral saturated hydrocarbons and fragment ions.²⁴ Additionally, protonation reactions in the gas phase are barrierless, and therefore, were expected to occur extremely fast compared to hydride abstraction reactions.²⁵ The extremely fast reaction between N_2H^+ ions and *n*-butylcyclohexane (Figure 4.9, bottom; 0.03 ms) versus the slow reaction between ions of m/z 57 and *n*-butylcyclohexane (Figure 4.5, B-D; 500 ms) suggests that the former reaction is most likely a protonation reaction. Therefore, it was hypothesized that protonation reactions are the cause of saturated hydrocarbon fragmentation upon APCI.

Hydronium ions of m/z 19 (H_3O^+ ; generated by APCI as described above) were also expected to transfer a proton to saturated hydrocarbons, however, these ions could not be isolated. Therefore, reactions that take place between protonated formaldehyde and *n*-butylcyclohexane were studied instead as formaldehyde has a proton affinity of 170.4 kcal/mol, which is slightly greater than but similar to that of water (165.1 kcal/mol). Figure 4.12 compares the direct-infusion APCI mass spectrum of neat *n*-butylcyclohexane (top) to the ion-molecule reaction mass spectrum measured between ions of m/z 31 and neutral *n*-butylcyclohexane (bottom). Similar to the reactions with N_2H^+ ions, ion-molecule reactions between protonated formaldehyde and *n*-butylcyclohexane produced $[M-H]^+$ ions and fragment ions. However, the fragment ions in both mass spectra of Figure 4.12 have similar relative abundance ratios. The lower relative abundance of the fragment ions in this ion-molecule mass spectrum compared to the one between protonated nitrogen and *n*-butylcyclohexane (Figure 4.9, bottom) may be due to the lower exothermicity of the reaction (see

section 4.3.6). Additionally, since the PA of formaldehyde is larger than that of waters, these results imply that protonated water can also react with *n*-butylcyclohexane to generate $[M-H]^+$ ions and fragment ions.

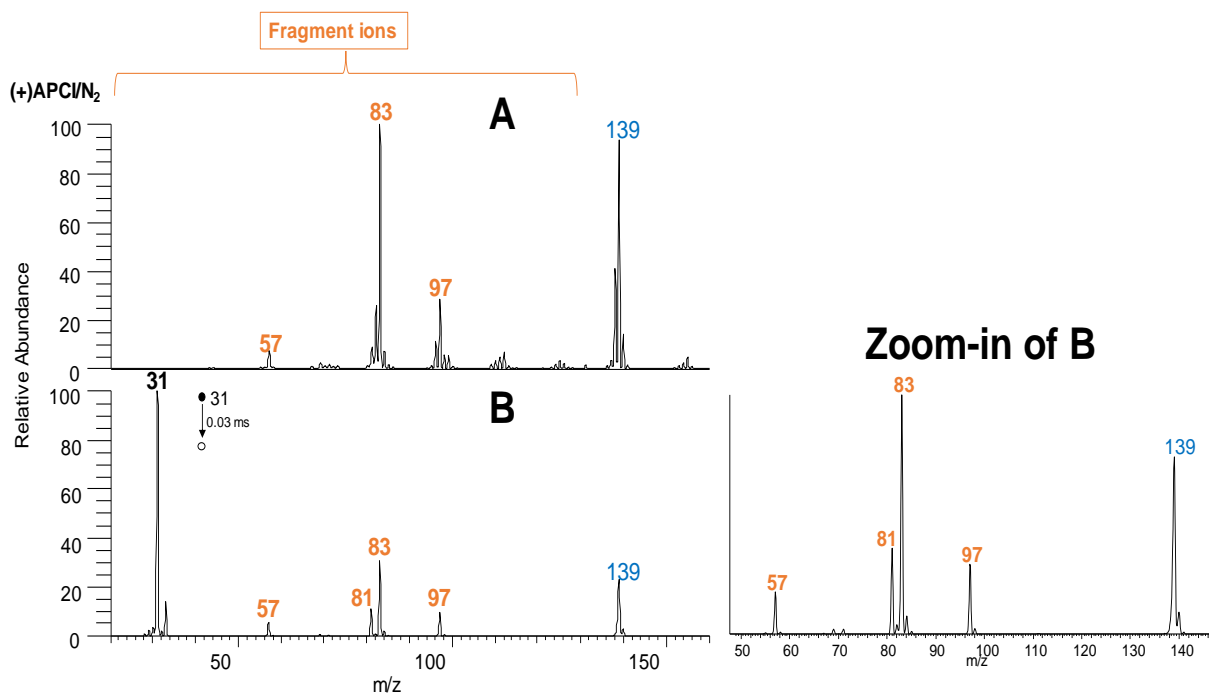


Figure 4.12 (A) Direct infusion (+)APCI mass spectrum of neat *n*-butylcyclohexane. (B) Full and zoomed-in ion-molecule mass spectra measured after 0.03 ms reaction between protonated formaldehyde (m/z 31) and neutral *n*-butylcyclohexane. The $[M-H]^+$ ion of *n*-butylcyclohexane is colored blue and fragment ions of *n*-butylcyclohexane are colored orange.

Protonated formaldehyde could react with saturated hydrocarbons via protonation or hydride abstraction. From George Olah's research on reactions between super acids and methane- d_4 , some unreacted methane- d_4 had undergone hydrogen-deuterium (H-D) exchange, thus proving that super acids protonated saturated hydrocarbons. Therefore, mass spectra were measured following reactions of cyclohexane (MW 84 Da) and completely deuterated cyclohexane (cyclohexane- d_{12} ; MW 96 Da) with protonated formaldehyde (Figure 4.13) as only the proton transfer reaction should result in H-D exchange. While the mass spectrum measured for cyclohexane showed only one product ion ($[M-H]^+$ ion of m/z 83; Figure 4.13A), the mass

spectrum measured between protonated formaldehyde and neutral cyclohexane-d₁₂ (Figure 4.13B) resulted in two pseudo-molecular product ions: ions of m/z 94 and m/z 93. Ions of m/z 94, [M-D]⁺, were the only product ions predicted to form if protonated formaldehyde underwent deuteride abstraction reactions. The formation of ions of m/z 93, [M-D₂+H]⁺, suggests H-D exchange occurred, and thus protonated formaldehyde transferred a proton to cyclohexane-d₁₂; deuteride abstraction cannot account for the ions of m/z 93. CAD experiments were performed to confirm the identities of the two product ions derived from cyclohexane-d₁₂.

Figure 4.14 shows the CAD mass spectra of ions of m/z 94 (top) and m/z 93 (bottom). Fragment ions of m/z 62, (C₄D₇⁺) were observed in the CAD mass spectrum of ions of m/z 94, while fragment ions of m/z 62 (C₄D₇⁺) and m/z 61 (C₄D₆H⁺) were observed in the CAD mass spectrum of ions of m/z 93. The presence of fragment ions of m/z 61, which are 1 Da greater than the fragment ions of m/z 62, confirms that the ions of m/z 93 have a hydrogen atom in its structure. Therefore, the identity of the ions of m/z 93 are [M-D₂+H]⁺. This ion must have formed through hydrogen-deuterium (H-D) exchange with protonated formaldehyde followed by a net loss of D₂. *This result unquestionably proves that protonated molecules can protonate saturated hydrocarbons to produce [M-H]⁺ pseudo-molecular ions and fragment ions.*

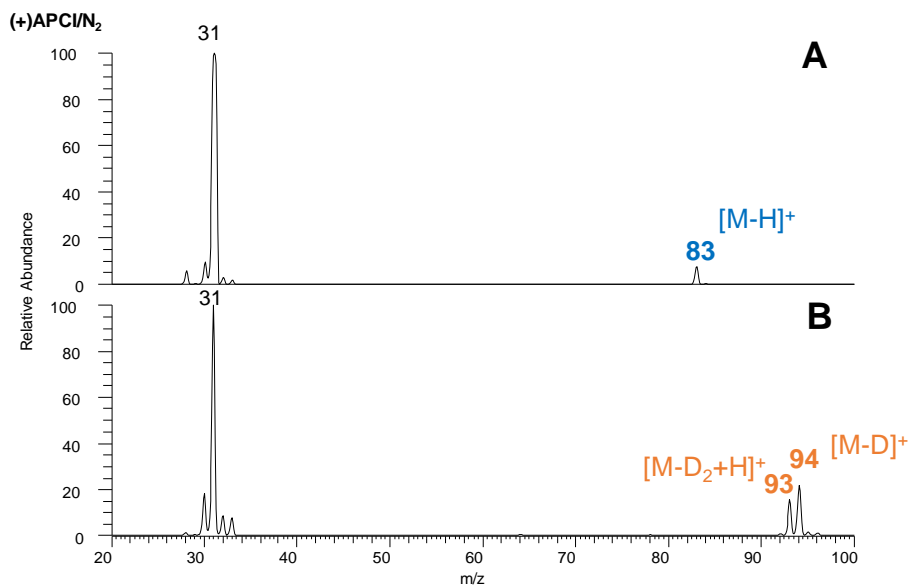


Figure 4.13 Ion-molecule mass spectra measured after 0.03 ms reaction between protonated formaldehyde (m/z 31) and cyclohexane (A) and cyclohexane- d_{12} (B). The $[M-H]^+$ ion of cyclohexane is colored **blue**, and the $[M-D]^+$ and $[M-D_2+H]^+$ ions of cyclohexane- d_{12} are colored **orange**.

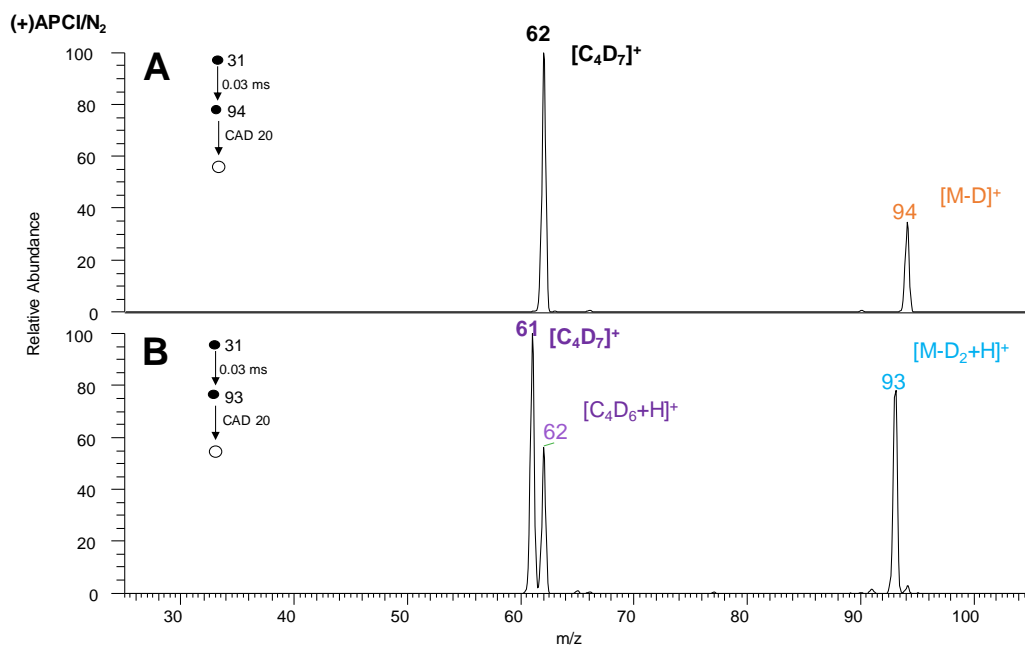


Figure 4.14 MS/MS/MS CAD mass spectra of the ion of m/z 94 (top) and the ion of m/z 93 (bottom). Mass spectra were measured at normalized collision energy of 20. The $[M-D]^+$ ion of cyclohexane- d_{12} is colored **orange**, the fragment ion of m/z 94 is colored **black**, the $[M-D_2+H]^+$ ion of cyclohexane- d_{12} is colored **blue**, and the fragment ions of m/z 93 are colored **purple**.

4.3.6 Proposal for the Reduction of Saturated Hydrocarbon Fragmentation Upon APCI

For the first time, saturated hydrocarbon fragmentation upon APCI has been experimentally tested, and the results suggest that protonated species formed in the corona discharge are responsible. However, thus far, only reactions with cyclic saturated hydrocarbons have been studied. Therefore, similar ion-molecule reactions were conducted with isooctane (MW 114 Da), a branched saturated hydrocarbon, and *n*-hexane (MW 86 Da), a linear saturated hydrocarbon. Figure 4.15A compares the direct infusion APCI mass spectrum of isooctane with the mass spectra measured following reactions between ions of m/z 29 and m/z 31 with neutral isooctane (Figure 4.15B and C, respectively). As expected, fragment ions of isooctane were more abundant in Figure 4.15B than in Figure 4.15C. Furthermore, fragment ions of m/z 99 were present when isooctane reacted with protonated nitrogen (Figure 4.15B) but not when it reacted with protonated formaldehyde (Figure 4.15C). This result is most likely due to differences in the exothermicities of both reactions – the proton affinity of nitrogen (118.3 kcal/mol) is much lower than that of formaldehyde's (171.8 kcal/mol). Therefore, this result suggests that the difference in proton affinity between the conjugate base of the protonated molecule and the neutral saturated hydrocarbon influences the extent of fragmentation. The mass spectra measured following reactions between ions of m/z 29 and m/z 31 with neutral *n*-hexane support this conclusion. The fragment ion relative abundances observed in Figure 4.16C are significantly lower than that observed in Figure 4.16B. These results demonstrate that the relative abundance of fragment ions of saturated hydrocarbons generated upon APCI depend on the proton affinity difference between the conjugate base of the protonated species and the saturated hydrocarbon.

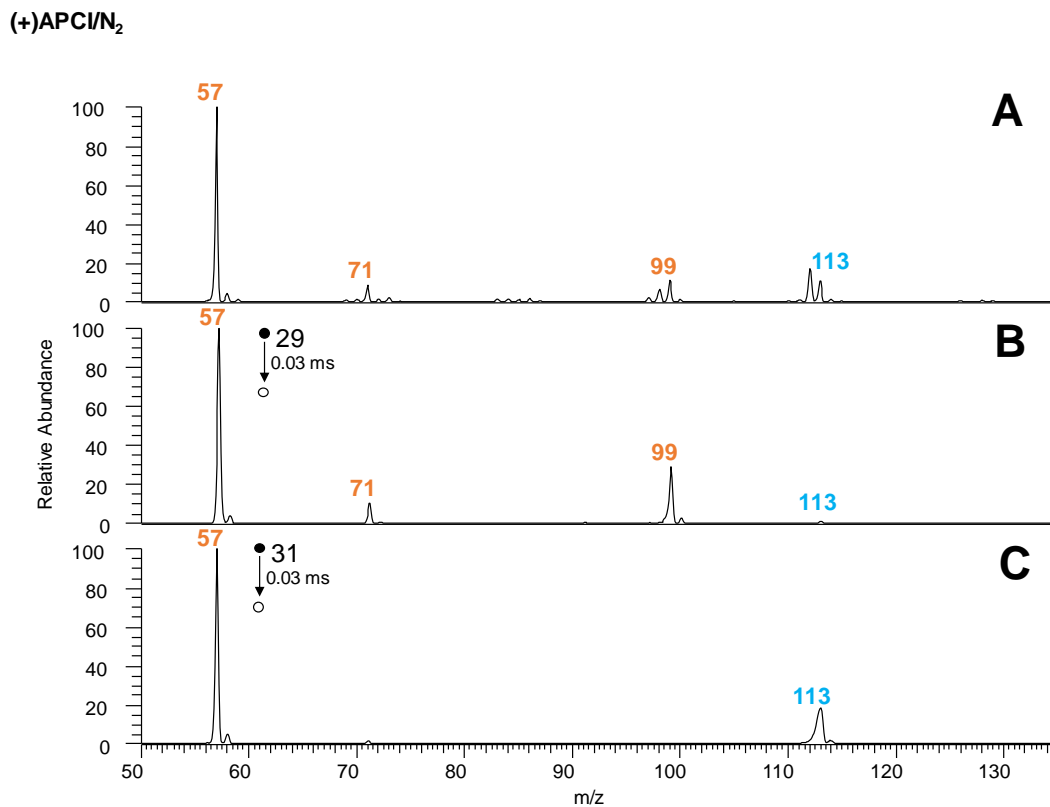


Figure 4.15 Direct infusion (+)APCI mass spectrum of neat isooctane (A). Ion-molecule mass spectra measured after 0.03 ms reaction between the protonated molecule of nitrogen (m/z 29) with neutral isooctane (B). Ion-molecule mass spectra measured after 0.03 ms reaction between the protonated molecule of formaldehyde (m/z 31) with neutral isooctane (C). The $[M-H]^+$ ion of isooctane is colored blue and fragment ions are colored orange. All mass spectra are zoomed-in on the m/z range 50-140.

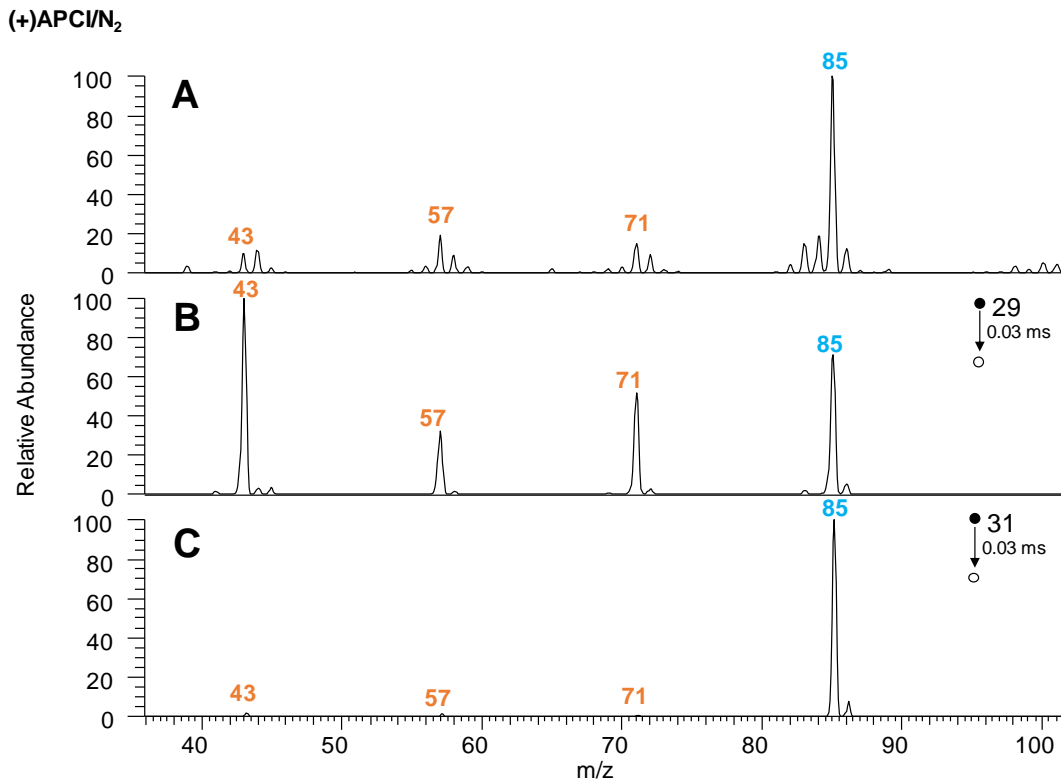
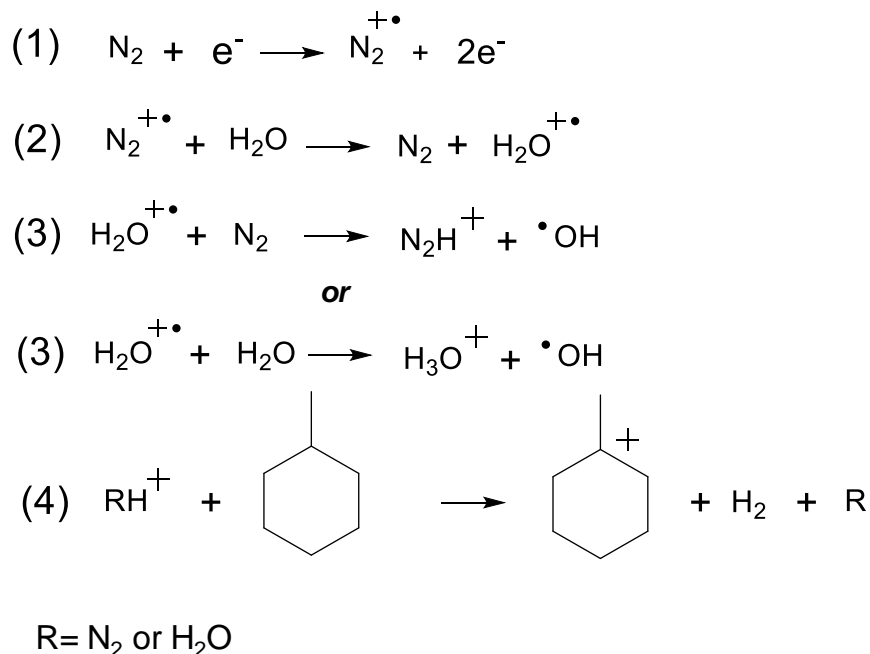


Figure 4.16 Direct infusion (+)APCI mass spectrum of neat hexane (A). Ion-molecule mass spectra measured after 0.03 ms reaction between the protonated molecule of nitrogen (m/z 29) with neutral hexane (B). Ion-molecule mass spectra measured after 0.03 ms reaction between the protonated molecule of formaldehyde (m/z 31) with neutral isooctane (C). The $[M-H]^+$ ion of hexane is colored blue and fragment ions are colored orange. All mass spectra are zoomed-in on the m/z range 50-140.

Scheme 4.1 shows the newly proposed mechanism for saturated hydrocarbon ionization upon APCI. Step 4 is the ion-molecule reaction predicted to control the extent of saturated hydrocarbon fragmentation. Although R is suggested to be N₂ or H₂O, it is unclear at this time which species, if either of them, are the main species protonating saturated hydrocarbons in APCI. Although the direct-infusion APCI mass spectrum measured for nitrogen gas with increased accelerating voltages showed only N₂H⁺ and H₃O⁺ species, this does not exclude the possibility that other protonated species may be responsible. For instance, it is possible that protonated nitrogen or protonated water protonate the saturated hydrocarbon solvent that the analyte is

dissolved in. The protonated solvent, before it releases H₂ and forms [M-H]⁺ ions, could then protonate the analyte. Unfortunately, this experiment could not be tested as protonated saturated hydrocarbon solvents are not stable enough for detection in the ion trap.



Scheme 4.1 The newly proposed APCI mechanism of saturated hydrocarbons. Methylcyclohexane is used as the example saturated hydrocarbon analyte. Step 4 shows the formation of [M-H]⁺ product ions; this step also leads to the formation of fragment ions.

It is hypothesized that by controlling the extent of the exothermicity of the proton transfer reaction between protonated molecules formed in the corona discharge and saturated hydrocarbons would likely reduce, or eliminate, their fragmentation upon APCI. A logical approach to solving this problem requires knowledge of the proton affinities of saturated hydrocarbons. Currently, the proton affinities of methane, ethane, and propane have been experimentally determined as these protonated species have been observed.²⁶ For larger saturated hydrocarbons like those in complex mixtures including base oils⁷ and crude oil,²⁷ determining these PAs are essential for rationally

reducing their fragmentation upon APCI with the appropriate reagent. One potential method for determining these PAs is to use bracketing experiments with ion-molecule reactions, similar to those conducted for determining the identity of the ions of m/z 29. Based on the extent of fragmentation and the relative abundance of the $[M-H]^+$ ions measured in the ion-molecule mass spectrum following reactions between various protonated species (with known PAs) and saturated hydrocarbons, an estimate for the proton affinity of the saturated hydrocarbon can be determined.

4.4 Conclusions

Mass spectra measured for the reactions between even-mass, radical cations of the nebulizing gas and carbenium reagent ions with saturated hydrocarbons did not show similar fragmentation patterns as the (+)APCI mass spectra of saturated hydrocarbons. Therefore, these reagent ions were concluded to not cause saturated hydrocarbon fragmentation upon (+)APCI. Additionally, saturated hydrocarbon interactions with the high-energy plasma of the corona discharge were also tested and concluded to not induce saturated hydrocarbon fragmentation. Ion-molecule reactions between saturated hydrocarbons and protonated molecules generated both the $[M-H]^+$ ions and fragment ions at similar relative abundances as are observed in the (+)APCI mass spectrum of saturated hydrocarbons. The mechanism by which $[M-H]^+$ ions and fragment ions were generated was determined to be through proton transfer reactions between the protonated molecule and the saturated hydrocarbon followed by the loss of H_2 molecules and neutral saturated hydrocarbons, respectively.

This hypothesis was further supported by the lower levels of fragmentation observed in the mass spectra measured following reactions between neutral saturated hydrocarbons and protonated formaldehyde compared to those measured with protonated nitrogen. Therefore, these results demonstrate that the extent of saturated hydrocarbon fragmentation is controlled by the

exothermicity of the proton transfer reaction. If, upon APCI, the difference in proton affinity between a given saturated hydrocarbon and the conjugate base of the species that protonates it can be minimized, then fragmentation should be reduced. The first step to achieving this goal would be to conduct fundamental ion-molecule reactions to determine the proton affinities of saturated hydrocarbons. In this manner, saturated hydrocarbon fragmentation upon APCI can be rationally eliminated, thus better enabling the accurate analysis of complex mixtures of saturated hydrocarbons.

4.5 References

- (1) Rodgers, R. P.; McKenna, A. M. Petroleum Analysis. *Anal. Chem.* **2011**, *83* (12), 4665–4687.
- (2) Moore, H. E.; Butcher, J. B.; Day, C. R.; Drijfhout, F. P. Adult Fly Age Estimations Using Cuticular Hydrocarbons and Artificial Neural Networks in Forensically Important Calliphoridae Species. *Forensic Sci. Int.* **2017**, *280*, 233–244.
- (3) Rajpurohit, S.; Hanus, R.; Vrkoslav, V.; Behrman, E. L.; Bergland, A. O.; Petrov, D.; Cvačka, J.; Schmidt, P. S. Adaptive Dynamics of Cuticular Hydrocarbons in *Drosophila*. *J. Evolution. Biol.* **2017**, *30* (1), 66–80.
- (4) Pineda, M.; Rojas, M.; Gálvez-Valdivieso, G.; Aguilar, M. The Origin of Aliphatic Hydrocarbons in Olive Oil. *J. Sci. Food Agric.* **2017**, *97* (14), 4827–4834.
- (5) Wang, J.; Bi, P.; Zhang, Y.; Xue, H.; Jiang, P.; Wu, X.; Liu, J.; Wang, T.; Li, Q. Preparation of Jet Fuel Range Hydrocarbons by Catalytic Transformation of Bio-Oil Derived from Fast Pyrolysis of Straw Stalk. *Energy* **2015**, *86*, 488–499.
- (6) Jin, C.; Viidanoja, J.; Li, M.; Zhang, Y.; Ikonen, E.; Root, A.; Romanczyk, M.; Manheim, J.; Dziekonski, E.; Kenttämä, H. I. Comparison of Atmospheric Pressure Chemical Ionization and Field Ionization Mass Spectrometry for the Analysis of Large Saturated Hydrocarbons. *Anal. Chem.* **2016**, *88* (21), 10592–10598.
- (7) Manheim, J.; Zhang, Y.; Viidanoja, J.; Kenttämä, H. I. An Automated Method for Chemical Composition Analysis of Lubricant Base Oils by Using Atmospheric Pressure Chemical Ionization Mass Spectrometry. *J. Am. Soc. Mass Spectrom.* **2019**, *30*, 2014–2021.

- (8) Tose, L. V.; Cardoso, F. M. R.; Fleming, F. P.; Vicente, M. A.; Silva, S. R. C.; Aquije, G. M. F. V.; Vaz, B. G.; Romão, W. Analyzes of Hydrocarbons by Atmosphere Pressure Chemical Ionization FT-ICR Mass Spectrometry Using Isooctane as Ionizing Reagent. *Fuel* **2015**, *153*, 346–354.
- (9) Carroll, D. I.; Dzidic, I.; Stillwell, R. N.; Haegele, K. D.; Horning, E. C. Atmospheric Pressure Ionization Mass Spectrometry. Corona Discharge Ion Source for Use in a Liquid Chromatograph-Mass Spectrometer-Computer Analytical System. *Anal. Chem.* **1975**, *47* (14), 2369–2373.
- (10) Gao, J.; Owen, B. C.; Borton, D. J.; Jin, Z.; Kenttämä, H. I. HPLC/APCI Mass Spectrometry of Saturated and Unsaturated Hydrocarbons by Using Hydrocarbon Solvents as the APCI Reagent and HPLC Mobile Phase. *J. Am. Soc. Mass Spectrom.* **2012**, *23* (5), 816–822.
- (11) Marotta, E.; Paradisi, C. A Mass Spectrometry Study of Alkanes in Air Plasma at Atmospheric Pressure. *J. Amer. Soc. Mass Spectrom.* **2009**, *20* (4), 697–707.
- (12) Gronert, S. Estimation of Effective Ion Temperatures in a Quadrupole Ion Trap. *J. Amer. Soc. Mass Spectrom.* **1998**, *9* (8), 845–848.
- (13) Bogusz, M. J.; Maier, R. D.; Krüger, K. D.; Kohls, U. Determination of Common Drugs of Abuse in Body Fluids Using One Isolation Procedure and Liquid Chromatography--Atmospheric-Pressure Chemical-Ionization Mass Spectrometry. *J. Anal. Toxicol.* **1998**, *22* (7), 549–558.
- (14) Hourani, N.; Kuhnert, N. Development of a Novel Direct-Infusion Atmospheric Pressure Chemical Ionization Mass Spectrometry Method for the Analysis of Heavy Hydrocarbons in Light Shredder Waste. *Anal. Methods* **2012**, *4* (3), 730–735.
- (15) Hourani, N.; Kuhnert, N. High Molecular Weight Non-Polar Hydrocarbons as Pure Model Substances and in Motor Oil Samples Can Be Ionized without Fragmentation by Atmospheric Pressure Chemical Ionization Mass Spectrometry. *Rapid Commun. Mass Spectrom.* **2012**, *26* (19), 2365–2371.
- (16) McEwen, C. N.; McKay, R. G.; Larsen, B. S. Analysis of Solids, Liquids, and Biological Tissues Using Solids Probe Introduction at Atmospheric Pressure on Commercial LC/MS Instruments. *Anal. Chem.* **2005**, *77* (23), 7826–7831.
- (17) *The Encyclopedia of Mass Spectrometry*, 1st ed.; Gross, M. L., Caprioli, R. M., Eds.; Elsevier: Amsterdam ; Boston, 2003.
- (18) Kolakowski, B. M.; Grossert, J. S.; Ramaley, L. Studies on the Positive-Ion Mass Spectra from Atmospheric Pressure Chemical Ionization of Gases and Solvents Used in Liquid Chromatography and Direct Liquid Injection. *J. Amer. Soc. Mass Spectrom.* **2004**, *15* (3), 311–324.

- (19) Wu, H.-F.; Brodbelt, J. S. Effects of Reactant Ion Kinetic Energy on Both Endothermic and Exothermic Ion/Molecule Reactions in a Quadrupole Ion Trap Mass Spectrometer. *Int. J. Mass Spectrom. Ion Process.* **1993**, *124* (3), 175–184
- (20) Allen, C. W.; Cox, A. N. *Allen's Astrophysical Quantities*, 4th ed.; AIP Press : Springer: New York, 2000.
- (21) P.J. Linstrom and W.G. Mallard, Eds., "Proton Affinity Evaluation" by Edward P. Hunter and Sharon G. Lias in NIST Chemistry WebBook, NIST Standard Reference Database Number 69, National Institute of Standards and Technology, Gaithersburg (retrieved January 23, 2020).
- (22) Olah, G. A.; Schlosberg, R. H. Chemistry in Super Acids. I. Hydrogen Exchange and Polycondensation of Methane and Alkanes in FSO₃H-SbF₅ ("magic Acid") Solution. Protonation of Alkanes and the Intermediacy of CH₅⁺ and Related Hydrocarbon Ions. The High Chemical Reactivity of "Paraffins" in Ionic Solution Reactions. *J. Am. Chem. Soc.* **1968**, *90* (10), 2726–2727.
- (23) Houriet, R.; Parisod, G.; Gaumann, T. The Mechanism of Chemical Ionization of N-Paraffins. *J. Am. Chem. Soc.* **1977**, *99* (11), 3599–3602.
- (24) Hansford, R. C. Mechanism of Catalytic Cracking. *Ind. Eng. Chem.* **1947**, *39* (7), 849–852.
- (25) Uggerud, E. Properties and Reactions of Protonated Molecules in the Gas Phase. Experiment and Theory. *Mass Spectrom. Rev.* **1992**, *11* (5), 389–430.
- (26) Hunter, E. P. L.; Lias, S. G. Evaluated Gas Phase Basicities and Proton Affinities of Molecules: An Update. *J. Phys. Chem. Ref. Data* **1998**, *27* (3), 413–656.
- (27) Yerabolu, R.; Kotha, R. R.; Niyonsaba, E.; Dong, X.; Manheim, J. M.; Kong, J.; Riedeman, J. S.; Romanczyk, M.; Johnston, C. T.; Kilaz, G.; et al. Molecular Profiling of Crude Oil by Using Distillation Precipitation Fractionation Mass Spectrometry (DPF-MS). *Fuel* **2018**, *234*, 492–501.

CHAPTER 5. IDENTIFICATION AND QUANTITATION OF LINEAR SATURATED HYDROCARBONS IN LUBRICANT BASE OILS BY USING GC×GC/EI TOF MASS SPECTROMETRY

Adapted with permission from Manheim, J.; Wehde, K.; Zhang, W. T. J.; Vozka, P.; Romanczyk, M.; Kilaz, G.; Kenttämä, H. I. *J. Am. Soc. Mass Spectrom.* 2019, 30(10), 2670-2677. Copyright 2019 American Chemical Society.

5.1 Introduction

As mentioned in Chapter 3, the ability to characterize the different classes of saturated hydrocarbons in base oils is paramount for improving oil refinery methods to produce the desired end products.¹ Specifically, the structures and abundances of linear saturated hydrocarbons in base oils is of special interest because this class of compounds is known to be detrimental to the flow properties of lubricants due to their high pour points.² Furthermore, a large abundance of linear saturated hydrocarbons can lead to wax precipitation.² Therefore, refinery processes aim to convert linear saturated hydrocarbons in crude oil to branched and cyclic saturated hydrocarbons; these two classes of saturated hydrocarbons have superior fluidity, even at low temperatures. An analytical technique that can be used to identify and quantify linear saturated hydrocarbons in base oils is necessary to evaluate the success of refining processes to manufacture the optimal base oil product.

Unfortunately, differentiating linear and branched saturated hydrocarbon isomers that are present in complex mixtures is not possible by using the (+)APCI/O₂/isooctane method discussed in Chapters 3 and 4. Furthermore, CAD cannot be used to distinguish linear and branched saturated hydrocarbon isomers because their fragmentation patterns are similar (data not shown). To overcome this obstacle, gas chromatography coupled with mass spectrometry can be used to separate linear and branched saturated hydrocarbon isomers in volatile mixtures prior to ionization

and detection.³⁻⁹ However, the greater the number of compounds in the mixture, the more difficult it is to separate and identify the different saturated hydrocarbons.¹⁰ For example, it was reported that many of the peaks in the GC chromatogram measured for a base oil were unresolved due to the presence of multiple isomers of linear, branched and cyclic saturated hydrocarbons.¹¹ On the other hand, the use of two consecutive GC columns (GC×GC) instead of just one has been demonstrated to be significantly more effective for base oil analysis, leading to an increase in the number of compounds detected, and improved sensitivity and separation.¹¹ Detailed in Chapter 2, section 2.5, the superior capabilities of GC×GC compared to GC arise from the use of two columns of different polarities (*i.e.*, nonpolar and polar), and a modulator that cryo-focuses eluate eluting off the first column. Several recent studies have demonstrated the superior separation of saturated hydrocarbons in crude oil samples by using GC×GC.^{10,12-16} However, few studies have used GC×GC for the identification and quantitation of the saturated hydrocarbons in base oils.^{11,17,18}

Flame ionization detectors (FID) are commonly coupled with GC×GC to quantify the individual compounds in complex mixtures as this technique provides chromatographic peak areas for organic compounds that are proportional to their concentrations; this is not always true when a mass spectrometer is used as the detector.¹⁹ However, the main disadvantage of GC×GC/FID is that it cannot be used to identify the eluting compounds without model compounds.¹⁹ GC×GC coupled to an EI source and a time-of-flight mass spectrometer (TOF MS), however, often enables compound identification even if two peaks coelute.¹² Furthermore, the NIST library (as described in Chapter 2, section 2.5.3) often enables identification of unknown compounds by matching an unknown mass spectrum to a known mass spectrum in the database, assuming that the correct compound is in the database. Most importantly, the EI mass spectra of individual linear saturated hydrocarbons can be distinguished from the EI mass spectra of individual branched and cyclic

saturated hydrocarbons due to their unique fragmentation patterns. However, since EI (generally used at 70 eV electron kinetic energy) of linear saturated hydrocarbons with more than ten carbon atoms does not generate the molecular ions, identification of these compounds in complex mixtures requires the measurement of both the EI mass spectra and the retention times in both GC×GC columns as well as the use of model linear saturated hydrocarbons.

Additionally, several studies have demonstrated that GC×GC/EI TOF MS can be used to provide semi-quantitative data for different classes of compounds by measuring a set of appropriate model compounds to obtain class-specific response factors.^{12,20,21} Linear saturated hydrocarbon model compounds, in particular, have been used to determine response factors for semi-quantitation of all saturated hydrocarbon classes in base oils by using GC×GC/EI TOF MS.¹⁷ However, this approach has never been used to accurately and precisely quantify the linear saturated hydrocarbons class, nor has it been validated.²²

In this study, a GC×GC/EI TOF MS method was developed and validated for the identification and quantitation of linear alkanes in base oils. Two base oils were analyzed to determine the percentage of linear saturated hydrocarbons present in each sample. The percentage of linear saturated hydrocarbons measured by the GC×GC/EI TOF MS method was then compared to the percentages measured by a GC×GC/FID with the same column configuration.

5.2 Experimental Section

Chemicals. *n*-Butylbenzene ($\geq 99\%$ purity), *n*-hexane ($\geq 97\%$), isooctane ($\geq 99.8\%$ purity), and linear saturated hydrocarbons containing 14 - 27 carbon atoms ($\geq 99\%$) were purchased from Sigma Aldrich and used as received. Helium (99.999% purity) was purchased from Indiana Oxygen and used as the buffer gas in the ion trap of the LQIT MS. Ultrapure oxygen gas (99.993%)

purchased from Praxair, Inc was used as the nebulizing gas. The two base oils studied will be referred to as Base Oil A and Base Oil B.

(+)APCI/O₂/Isooctane LQIT MS. A Thermo Fisher Scientific LQIT MS (San Jose, CA), similar to the one used in research described in Chapters 3 and 4, was used to determine the approximate range of the number of carbon atoms in the linear saturated hydrocarbons in the two base oils. 10 mg of each base oil were dissolved in 1 mL of isooctane. The sample was injected through PEEK tubing into the APCI source with a 500 μ L Hamilton syringe at a flow rate of 10 mL/min. The APCI source conditions were: vaporizer temperature, 150 °C; ion transfer capillary temperature, 50 °C, sheath and auxiliary gas flow rate, 60 and 30 arbitrary units, respectively; corona discharge voltage, 6 kV; ion transfer capillary tube voltage, 10 V; and tube lens voltage, 30 V. Xcalibur 2.2 software was used to acquire and analyze the mass spectra.

GC \times GC/EI TOF Mass Spectrometry. An Agilent 7890A GC \times GC coupled to a Pegasus HRT 4D (EI) TOF mass spectrometer (Leco Co., St. Joseph, MI, USA) was used for all GC \times GC/MS measurements. 0.5 μ L of each sample was injected into the GC \times GC by using an Agilent 7693 autosampler. Ultrapure helium (99.9999%) was used as the mobile phase at a constant flow rate of 1.25 mL/min. The reversed-phase column configuration that comprised of a 60 m polar primary capillary column and a 2 m nonpolar secondary capillary column was used in all GC \times GC experiments. Each column was located in its separate oven. Located in the first GC oven is a quad-jet dual stage thermal modulator; part of the 2 m secondary nonpolar column was positioned in the modulator. The modulator time was 5 s with a hot jet pulse time of 0.75 s and a cold jet pulse time of 1.75 s. The primary GC oven was programmed to start at 65 °C and was held at this temperature

for one minute. The temperature was then increased at a rate of 1 °C/min until reaching a final temperature of 270 °C that was held for six minutes. The secondary GC oven temperature was offset by + 10 °C from the primary GC oven temperature, while the modulator temperature was offset by + 50 °C from the secondary GC oven temperature. Table 5.1 shows a detailed overview of both GC columns and the separation method.

Table 5.1 Overview of the GC×GC MS method used in the following experiments.

Columns	Rxi-17Sil MS (60 m × 0.25 mm × 0.25 μm) Rxi-1ms (1.1 m × 0.25 mm × 0.25 μm)
Injection	0.5 μL split 20:1, inlet temperature 280 °C
Oven program	40-250 °C, rate 1 °C/min
Mobile gas	UHP helium, 1.25 mL/min
Offsets	secondary oven 35 °C, modulator 15 °C
Modulation	8.0 s, hot pulse 1.3 s
Detector	FID, 300 °C, 200 Hz
Acquisition delay	165 s

Saturated hydrocarbons eluting from the secondary column entered the EI source from a transfer line that was held at 300 °C. The compounds were ionized by EI at 70 eV electron energy in a 10⁻⁴ torr pressure region. Molecular ions and fragment ions were accelerated and focused into the TOF MS (20 m flight path) for medium resolution measurements (25,000 at ions of *m/z* 219). Before all TOF MS measurements, the EI TOF MS system was calibrated and tuned using perfluorotributylamine (PFTBA). Additionally, the grid to guide the electrons into the ion source was turned on after a 350 ms delay to extend the life of the filament and prevent ionization of the

solvent, *n*-hexane. The mass spectral acquisition rate was set to 200 mass spectra/second over a *m/z* range of 15-500. LECO Visual Basic Scripting (VBS) software, ChromaTOF Version 1.90.60.0.43266, was used for acquisition and analysis of the mass spectra.

GC×GC Flame Ionization Detection. The GC×GC system utilized for these experiments was composed of an Agilent 7890B dual gas chromatograph, a flame ionization detector (FID), a liquid nitrogen thermal modulator (LECO Corporation, Saint Joseph, MI), an Agilent 7683B series injector, and an HP 7683 series auto sampler. The experimental parameters for this method are listed in Table 5.2. Classification of saturated hydrocarbons was performed using ChromaTOF software (version 4.71.0.0 optimized for GC×GC FID); a detailed description has been published previously.²³ The weight percentage (wt. %) of the linear saturated hydrocarbons was determined by dividing the relevant GC×GC peak areas measured for both columns by the sum of all peak areas in the GC×GC chromatogram.

Table 5.2 Experimental conditions of GC×GC FID analysis.

Columns	Rxi-17Sil MS (60 m × 0.25 mm × 0.25 μm) Rxi-1ms (2 m × 0.25 mm × 0.25 μm)
Injection	0.5 μL split 20:1, inlet temperature 280 °C
Oven program	40-250 °C, rate 1 °C/min
Mobile gas	UHP helium, 1.25 mL/min
Offsets	secondary oven 35 °C, modulator 15 °C
Modulation	8.0 s, hot pulse 1.3 s
Detector	FID, 300 °C, 200 Hz
Acquisition delay	165 s

Sample Preparation for GC×GC/MS Experiments. Mixtures of model linear saturated hydrocarbons were prepared by executing serial dilutions of a stock solution. The stock solution was prepared by dissolving 3.0 mg of each linear saturated hydrocarbon in a total of 10.0 mL of *n*-hexane. Considering the density of *n*-hexane (0.659 g/mL), the final stock solution contained 4550 ppm (by weight) of each saturated hydrocarbon. For calibration measurements, six diluted solutions with mass fractions of 4.6, 15.2, 25.8, 36.4, 47.0 and 57.7 ppm (by weight) were prepared from the stock solution. The total volume of each diluted solution studied was 1.0 mL. Each diluted solution was doped with 20.0 μL of a 3030 ppm (by weight) stock solution of *n*-butylbenzene in *n*-hexane; this served as the internal standard.

Furthermore, the two base oil solutions dissolved in *n*-hexane were doped by 20.0 μL of the above 3030 ppm (by weight) stock solution of *n*-butylbenzene. The optimal mass fraction for identifying and quantifying the linear saturated hydrocarbons in each base oil was experimentally determined by analyzing GC×GC total ion current chromatograms of the base oil solutions dissolved in *n*-hexane that were prepared at different mass fractions. Determination of the ideal base oil concentration is discussed in more detail in section 5.3.

Validation Tests. Based on the work by Shah *et al.*, a new validated method must have acceptable accuracy percentages greater than 85% and precision percentages less than 15% except at the lower limit of quantitation (LLOQ), where the accuracy must be greater than 80% and the precision less than 20%.²⁴ To validate the GC×GC/MS method for quantitation of linear saturated hydrocarbons, four mass fractions of each linear saturated hydrocarbon that were not used to generate the calibration plots were examined. The *y*-axis on the calibration plots was the chromatographic peak area of the linear saturated hydrocarbon divided by the chromatographic peak area of the internal

standard, *n*-butylbenzene, and the *x*-axis was the mass fraction of each linear saturated hydrocarbon in ppm (by weight). Chromatographic peak areas measured for each of the linear saturated hydrocarbons in the four mass fractions divided by the chromatographic peak area measured for *n*-butylbenzene were referred to as the theoretical peak areas (TP). The experimental peak areas (EP) for the linear saturated hydrocarbons in the four mass fractions samples were calculated from the equations of the calibration plots. Based on the TP and EP values, accuracy was calculated using the formula $100 - \left(\frac{|EP-TP|}{TP} \right) * 100$.²⁵ Within day, between day, and total precision values were determined from nine total measurements of each of the four mass fractions - three measurements a day for three days. Within day and between day precision values were obtained using equations (5.1) and (5.2), respectively (same equations as in Chapter 3):

$$\text{Within Day Precision (WD)} = \sqrt{\frac{\sum_{k=1}^N (RSD_k)^2}{N}} \quad (\text{Equation 5.1})$$

$$\text{Between Day Precision (BD)} = \sqrt{\left(RSD_{DM}^2 - \frac{WD^2}{N} \right)} \quad (\text{Equation 5.2})$$

where RSD is the relative standard deviation of the TP, N is the number of days individual GC×GC total ion current chromatograms were collected (N=3), k is the RSD for the kth day, and RSD_{DM} (equation 2) is the RSD of the three-day averages.²⁶ The total precision was calculated by using equation 3 (same equation as in Chapter 3).

$$\text{Total Precision} = \sqrt{WD^2 + BD^2} \quad (\text{Equation 5.3})$$

Total Linear Saturated Hydrocarbon Content Determinations. After determining the optimal base oil concentrations (see section 5.3), Base Oil A and Base Oil B were analyzed once a day using the GC×GC/EI TOF MS for two days. The mass fractions of the linear saturated hydrocarbons present in each base oil were determined by using the calibration plots of each linear saturated hydrocarbon. The mass fractions were then summed for the total linear saturated hydrocarbon content in each base oil. Lastly, the sum was divided by the concentration of the base oil that was injected into the GC×GC/EI TOF MS to obtain the percentage of linear saturated hydrocarbons present in the entire base oil.

5.3 Results and Discussion

The purpose of this study was to develop and validate a mass spectrometry method for quantifying the linear saturated hydrocarbons in base oils. Due to ionization biases for different types of compounds, mass spectrometry is rarely utilized for quantitative applications and is primarily used to identify unknown compounds. Therefore, successful application of a mass spectrometry-based method to quantify a specific class of compounds would make the technique significantly more useful in the analysis of unknown compounds in various samples.

5.3.1 Identification of the Linear Saturated Hydrocarbons in Base Oils

Identification of the linear saturated hydrocarbons in each base oil was performed by comparing the EI mass spectra and both retention times of each unknown compound with those measured for model linear saturated hydrocarbons. Selection of the model linear saturated hydrocarbons was based on (+)APCI/O₂/isooctane mass spectra measured for each base oil. The use of the (+)APCI/O₂/isooctane MS method is not necessary for pre-selection of the model compounds, however, without it, a mixture of standards with 10-40 carbon atoms (typical for base

oils) would have to be examined using the GC×GC/EI TOF MS. Therefore, for consideration of time and cost, the approximate range of the number of carbon atoms in the base oils was first investigated using (+)APCI/O₂/isooctane MS.

Figure 5.1 displays the APCI mass spectra measured for Base Oil A and Base Oil B. A bimodal distribution of ions was observed for both base oils. As previously mentioned in Chapter 3, the first distribution of ions represented the fragment ions (and is denoted as such in Figure 5.1), and the second distribution of ions represented the [M-H]⁺ ions. The approximate range of the number of carbon atoms in saturated hydrocarbons in Base Oil A and Base Oil B are 14 - 21 and 15 - 27, respectively.

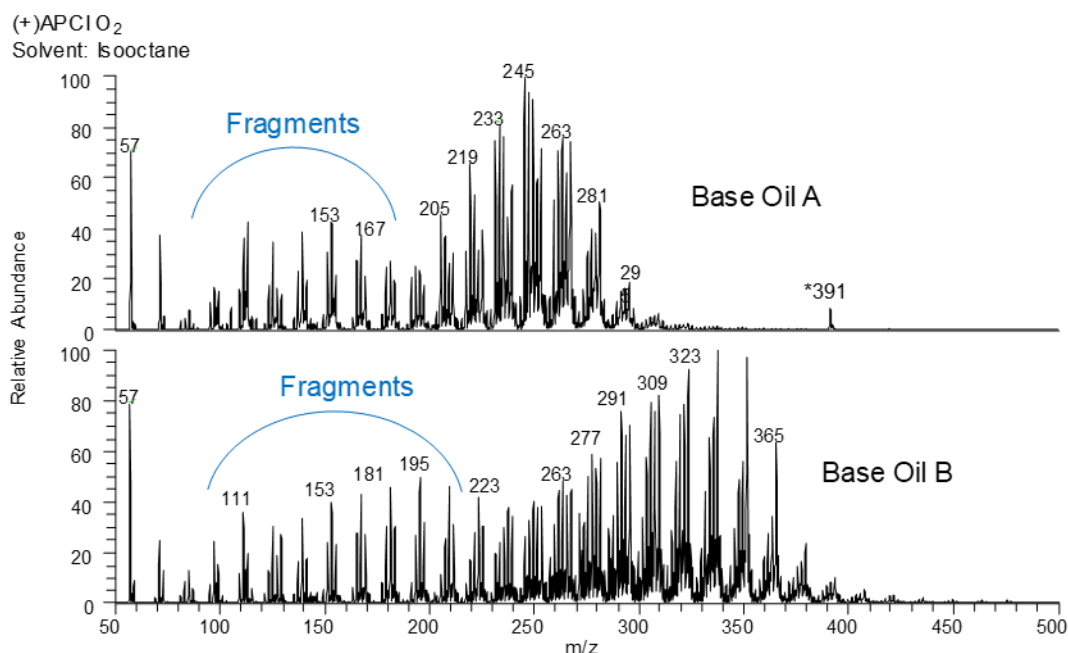


Figure 5.1 Direct-infusion (+)APCI/O₂/isooctane LQIT mass spectra measured for Base Oil A (top) and Base Oil B (bottom). The ions of *m/z* 391 originated from the PEEK tubing.

Based on the approximate range of the number of carbon atoms identified in the APCI mass spectra of each base oil, a mixture of model linear saturated hydrocarbons

with 14 - 27 carbon atoms was prepared at a mass fraction of 37.9 ppm in hexane (total volume 1 mL) and measured using the GC×GC/EI TOF MS. As expected, the molecular ions of the linear saturated hydrocarbons were not observed in any of the EI mass spectra due to extensive fragmentation caused by EI at 70 eV electron energy. Therefore, the algorithm that matches the measured EI mass spectrum to the NIST library mass spectrum made many incorrect assignments. For example, Figure 5.2 and Figure 5.3 show the EI mass spectra measured for tetradecane and pentadecane, respectively, and the software matched NIST library EI mass spectra. In both figures, the NIST library prediction was incorrect - tetradecane was predicted to be pentadecane and pentadecane was predicted to be heptadecane. Therefore, the retention times measured for each compound in both columns were used to aid in the identification of the linear saturated hydrocarbons in the base oils.

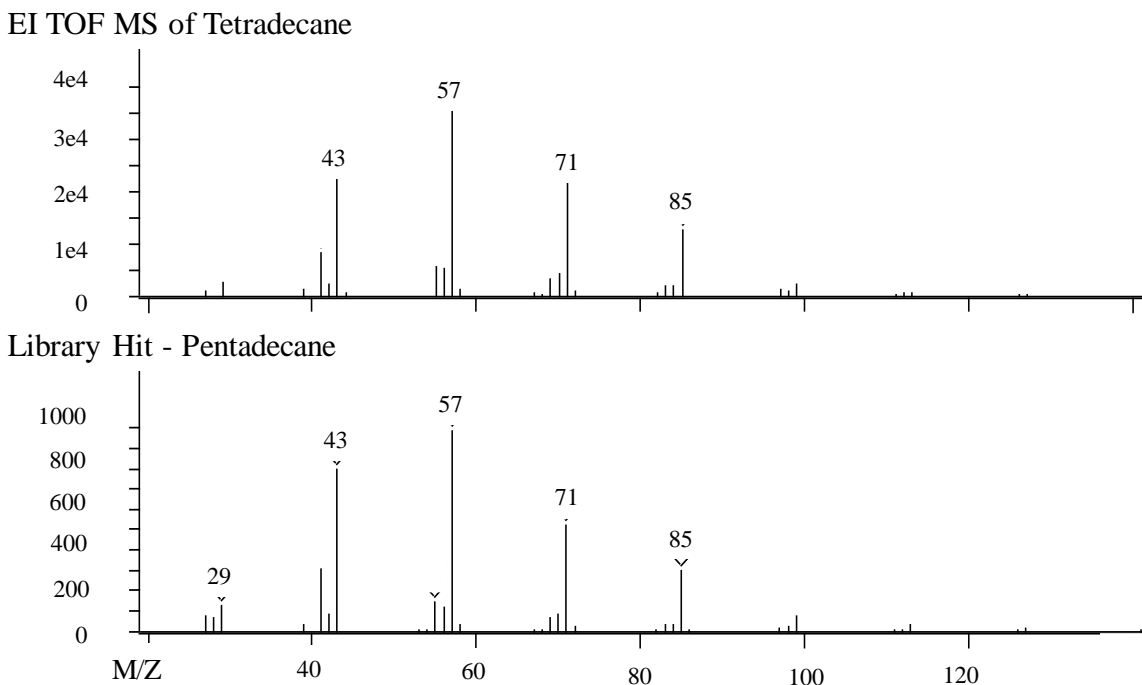


Figure 5.2 EI (70 eV) TOF mass spectrum measured for tetradecane by GC×GC/EI TOF MS (top) and the best matched EI mass spectrum from the NIST library- pentadecane.

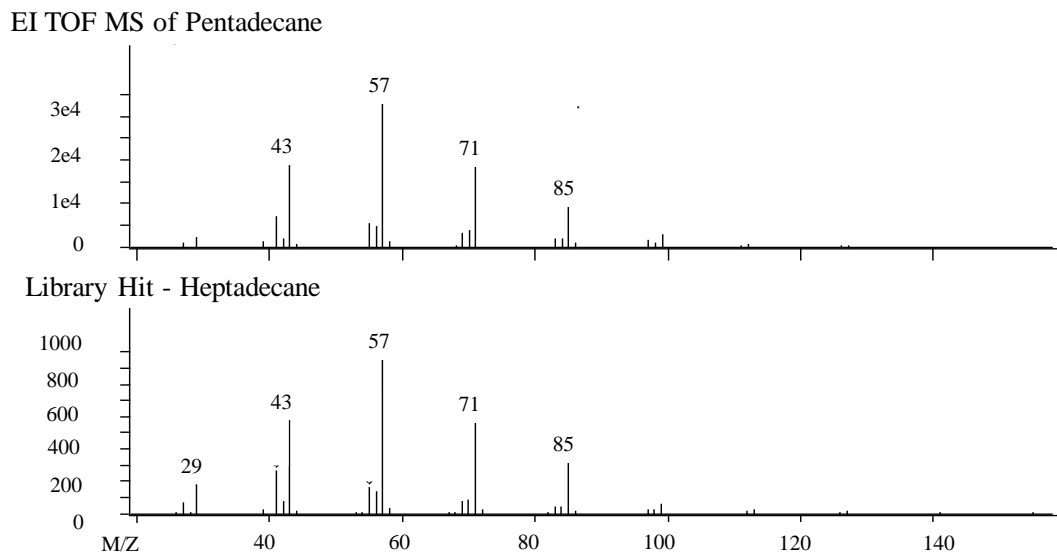


Figure 5.3 EI (70 eV) TOF mass spectrum measured for pentadecane by GC×GC/EI TOF MS (top) and the best matched EI mass spectrum from the NIST library- heptadecane.

Each base oil, prepared at a mass fraction of 1538.5 ppm in hexane (1 mg of base oil in 1 mL of *n*-hexane) and doped with 30.3 ppm *n*-butylbenzene (for following quantitative measurements), was then measured by using the GC×GC/EI TOF MS. GC×GC total ion current chromatograms measured for Base Oil A and Base Oil B (Figure 5.4) revealed hundreds of compounds in the two base oils. The purple circle indicates the chromatographic peak for *n*-butylbenzene. All other peaks are derived from saturated hydrocarbons as previously determined by using model compounds.¹⁷ Here, green dots correspond to branched saturated hydrocarbons, red dots correspond to mono-, di-, and tricyclic saturated hydrocarbons, and blue dots correspond to tetra- and pentacyclic saturated hydrocarbons. The black squares indicate the linear saturated hydrocarbons identified in each base oil; this was determined by comparing their retention times and EI mass spectra to those of the model compounds. Table 5.3 shows the retention times for the linear saturated hydrocarbon model compounds and the compounds in the base oils with similar retention times. Not surprisingly, unknown compounds and model compounds with similar

retention times produced identical EI mass spectra. Interestingly, linear saturated hydrocarbons with 19 - 27 carbon atoms were not detected in either sample. Based on the retention times and EI mass spectra, linear saturated hydrocarbons with 14 – 18 carbon atoms were identified in Base Oil A and with 15 – 18 carbon atoms in Base Oil B.

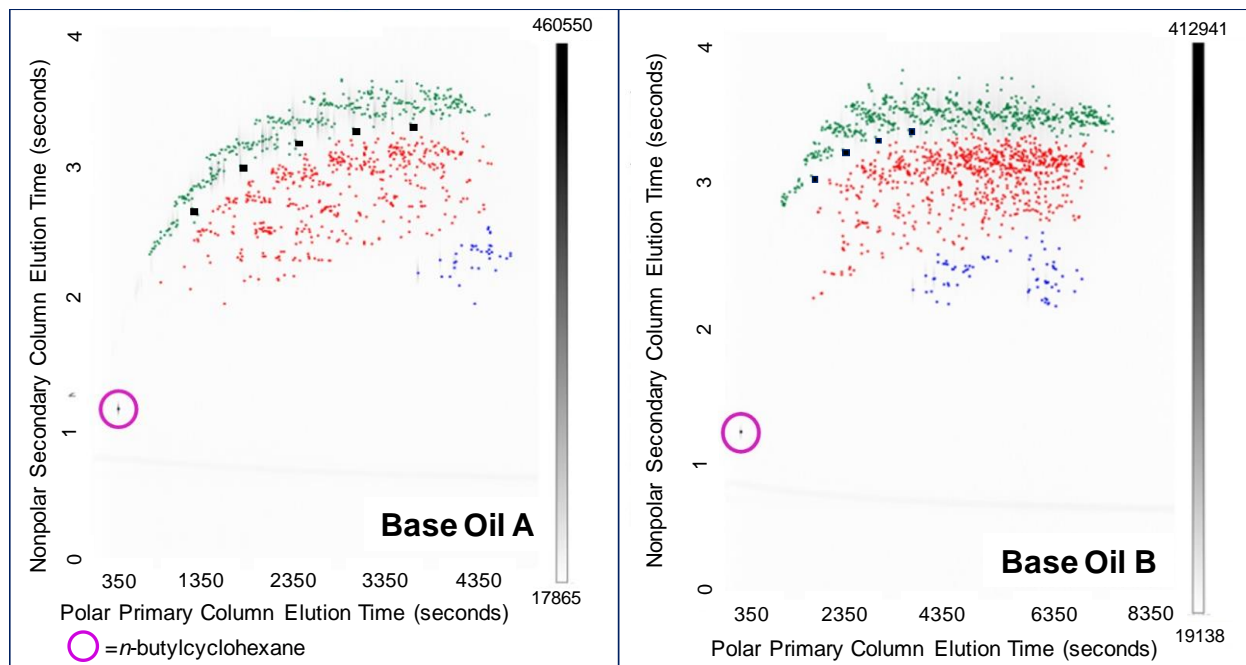


Figure 5.4 GC×GC total ion current chromatograms measured for Base Oil A (left) and Base Oil B (right), respectively, by using GC×GC/EI TOF MS. Black squares represent the linear saturated hydrocarbons, green dots represent the branched saturated hydrocarbons, red dots represent the mono-, di-, and tricyclic saturated hydrocarbons, and blue dots represent the tetra- and pentacyclic saturated hydrocarbons. The greyscale legend at the right of each total ion current chromatogram is indicative of the chromatographic peak areas.

Table 5.3 Retention times in the polar and nonpolar columns for standard linear saturated hydrocarbons that have similar retention times as compounds in Base Oil A and Base Oil B. N/A denotes “not applicable” as a compound with this retention time was not found in the base oils.

Linear Alkane	Polar Column Retention Time (s)			Nonpolar Column Retention Time (s)		
	Standard	Base Oil A	Base Oil B	Standard	Base Oil A	Base Oil B
C14	1384.76	1384.76	N/A	2.664	2.664	N/A
C15	1894.65	1894.65	1894.65	2.988	2.978	2.993
C16	2464.52	2464.52	2469.52	3.168	3.168	3.178
C17	3064.38	3064.38	3064.38	3.261	3.258	3.266
C18	3664.25	3664.25	3669.25	3.286	3.291	3.317
C19	4249.11	N/A	N/A	3.343	N/A	N/A
C20	4823.98	N/A	N/A	3.338	N/A	N/A
C21	5373.86	N/A	N/A	3.312	N/A	N/A
C22	5903.74	N/A	N/A	3.297	N/A	N/A
C23	6413.62	N/A	N/A	3.286	N/A	N/A

5.3.2 Determination of the Accuracy and Precision of the GC×GC/EI TOF MS Method to Quantitate Linear Saturated Hydrocarbons

Mixtures of model linear saturated hydrocarbons with 14 - 18 carbon atoms were prepared at different mass fractions to create calibration plots. 57.7 ppm was selected as the highest mass fraction for the calibration plot as this was the highest mass fraction for all linear saturated hydrocarbons that was below the saturation limit of the detector (1×10^7 arbitrary units). 4.55 ppm was selected as the lowest mass fraction as this was the lowest mass fraction for all linear saturated hydrocarbons that demonstrated a total ion current signal-to-noise ratio greater than 3:1. Calibration plots for all five linear saturated hydrocarbons in the model compound mixtures were constructed from an average of three measurements for each mass fraction (Figure 5.5). All five

plots demonstrate excellent linearity as all R^2 values are greater than 0.996. However, the linear dynamic range is only about one order of magnitude, which limits the ppm range for accurate quantitation of linear saturated hydrocarbons in complex samples. On the other hand, this dynamic range is comparable to similar methods that have been reported in literature.²⁷

Linear Saturated Hydrocarbon Calibration Plots

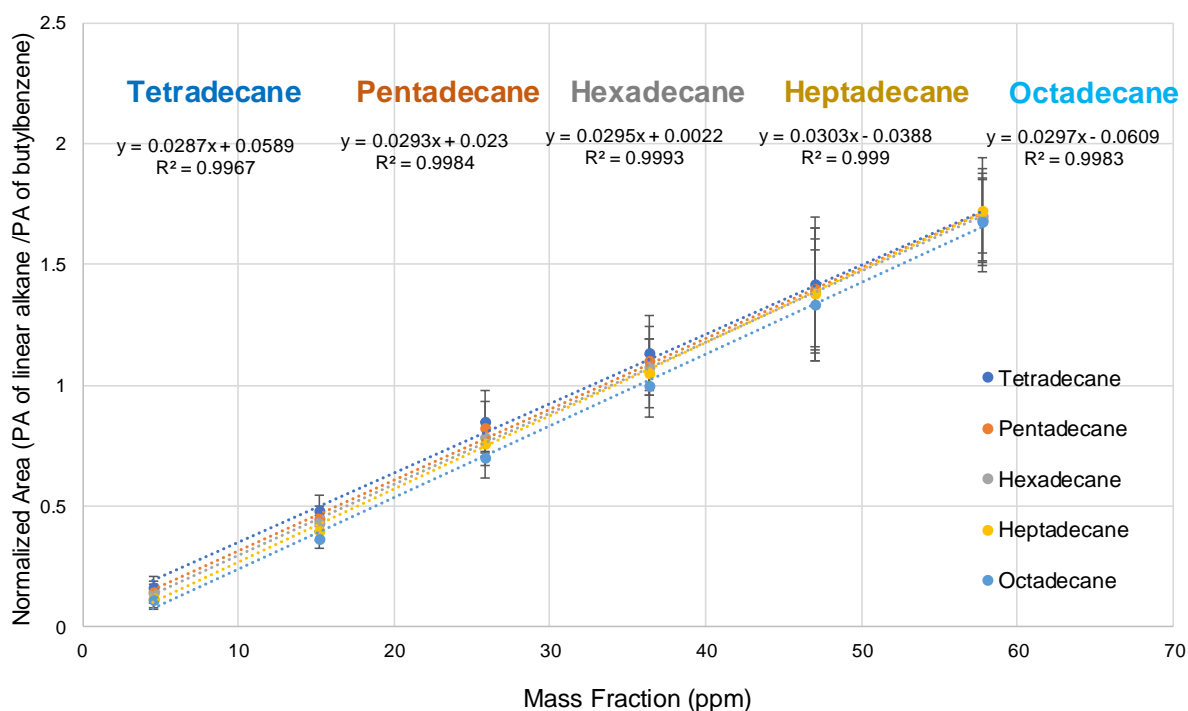


Figure 5.5 Calibration plots for mixtures of standard linear saturated hydrocarbons C₁₄-C₁₈. Each point is the average of three measurements and the error bars represent the standard deviation.

Four mass fractions of the model linear saturated hydrocarbon mixture that were not used to prepare the calibration plots were chosen to test the accuracy and precision of the GC×GC/EI TOF MS method in quantitation of linear saturated hydrocarbons: 12.1, 30.3, 42.5 and 53.1 ppm. Table 5.4 shows the average accuracy, within day precision, between day precision, and total precision based on the three days of measurements. The accuracy and precision values for all mass

fractions of each linear saturated hydrocarbon were better than the acceptable limits of a new validated method of 85% and 15%, respectively, except for the 14-carbon linear saturated hydrocarbon at a mass fraction of 12.1 ppm.²⁴ This mass fraction yielded an average accuracy of 83.8% and a total precision of 17.2%. However, 12.1 ppm is close to the LLOQ for tetradecane (10 ppm); this was determined based on the IUPAC definition of the LLOQ.²⁴ Therefore, the method was successfully validated for it achieved better than the acceptable minimum accuracy of 80% and maximum total precision of 20%.²⁴

Table 5.4 Average accuracy, average within day precision, average between day precision, and total precision for GC×GC/EI TOF MS quantitation of mixtures of model linear saturated hydrocarbons C₁₄-C₁₈ at four different mass fractions.

Number of Carbon Atoms	Average Accuracy				Averaged Within Day Precision				Between Day Precision				Total Precision			
	12.1 ppm	30.3 ppm	42.5 ppm	53.1 ppm	12.1 ppm	30.3 ppm	42.5 ppm	53.1 ppm	12.1 ppm	30.3 ppm	42.5 ppm	53.1 ppm	12.1 ppm	30.3 ppm	42.5 ppm	53.1 ppm
14	83.83%	92.15%	99.00%	94.46%	6.0%	2.5%	2.1%	1.6%	16.1%	11.2%	10.0%	4.4%	17.2%	11.5%	10.2%	4.6%
15	89.60%	93.33%	99.88%	95.35%	4.9%	1.1%	1.6%	1.0%	10.0%	13.0%	12.6%	6.9%	11.1%	13.1%	12.8%	7.0%
16	91.58%	93.85%	99.21%	97.22%	5.1%	1.2%	2.1%	1.6%	8.1%	13.1%	13.3%	9.3%	9.6%	13.1%	13.5%	9.4%
17	92.86%	93.32%	99.97%	96.19%	4.6%	0.9%	1.8%	0.9%	7.0%	9.4%	9.3%	5.3%	8.4%	9.5%	9.4%	5.4%
18	97.76%	96.32%	96.98%	99.89%	3.7%	1.7%	1.1%	1.7%	0.8%	9.1%	13.1%	8.8%	3.8%	9.2%	13.1%	9.0%

5.3.3 Determination of the Percentage of Total Linear Saturated Hydrocarbon Content in Base Oils

Base oil concentrations were selected so that all, or most, linear saturated hydrocarbons in the samples had mass fractions that fell between the lowest and highest mass fractions of the calibration plots. Therefore, the mass fraction of Base Oil A was chosen to be 4550 ppm in 1 mL of *n*-hexane and the mass fraction of Base Oil B was 11400 ppm in 1 mL of *n*-hexane. All the mass fractions measured for the linear saturated hydrocarbons present in the base oils were within the

range of the calibration plots except for the linear saturated hydrocarbon with 15 carbon atoms in Base Oil B (Table 5.5). The average total linear saturated hydrocarbon contents measured for Base Oil A and Base Oil B (two measurements each) were 146 ± 8 ppm and 49.2 ± 21 ppm, respectively. Based on the original total concentration of each base oil, the average total linear saturated hydrocarbon percentage present in Base Oil A was $3.7\% \pm 0.5\%$ (by weight percent) and in Base Oil B was $0.8\% \pm 0.2\%$ (Table 5.6).

Table 5.5 Example set of concentrations (ppm) of the linear saturated hydrocarbons identified in each base oil as determined by GC×GC/EI TOF MS. Peak areas in both columns were used. The concentration of pentadecane (C₁₅) in Base Oil B falls outside of the linear dynamic range of the calibration curve.

Base oil A 4552 ppm mass fraction							Total PPM	TOF MS value	
	butylbenzene	C14	C15	C16	C17	C18			
Peak Area (PA)	1890144	843427	1402805	1380947	836416	628018		151	% linear
Normalized PA	/	0.44622	1.66322	0.98442	0.60568	0.75084			
PPM	/	13.5	56.0	33.4	21.2	27.3	3.3%		
Base oil B 11380 ppm mass fraction							Total PPM	TOF MS value	
	butylbenzene	C14	C15	C16	C17	C18			
Peak Area (PA)	2212919	N/A	178508	605139	557536	532558		31.0	% linear
Normalized PA	/	N/A	0.08067	0.27346	0.25195	0.24066			
PPM	/	N/A	2.00	9.20	9.60	9.30	0.7%		

To further validate the quantitation of linear saturated hydrocarbons by using GC×GC/EI TOF MS, a GC×GC/FID with the same column configuration as the GC×GC/EI TOF MS was used to determine the linear saturated hydrocarbon mass fractions in both base oil samples. Each base oil sample was analyzed twice on the GC×GC/FID. The average linear saturated hydrocarbon mass fraction in Base Oil A was determined to be $4.3\% \pm 0.8\%$ and in Base Oil B, $0.7\% \pm 0.1\%$ (Table 5.6). These values are in close agreement with the results obtained using the GC×GC/EI TOF MS (Table 5.6), substantiating that the GC×GC/EI TOF MS method can be successfully used to quantitate linear saturated hydrocarbons in base oils. Although the GC×GC/FID is a cheaper

instrument than the GC×GC/EI TOF MS, the latter instrument can be used to not only quantitate but also identify compounds in base oils.

Table 5.6 Total linear saturated hydrocarbon (by weight percent) content identified in each base oil as determined by GC×GC/EI TOF MS and GC×GC/FID.

Base Oil A 4550 ppm mass fraction		
Total PPM	TOF MS value	FID value
	% linear	% linear
146 ± 7.9	3.7% ± 0.5%	4.3% ± 0.8%
Base Oil B 11400 ppm mass fraction		
Total PPM	TOF MS value	FID value
	% linear	% linear
49.2 ± 20.8	0.8% ± 0.2%	0.7% ± 0.1%

5.4 Conclusions

A GC×GC/EI TOF MS method was successfully validated for the identification and quantitation of linear saturated hydrocarbons in base oils. Mixtures of model linear saturated hydrocarbons enable the identification of linear saturated hydrocarbons in base oils by comparing model compound retention times in both columns and EI mass spectra to those of the unknown compounds in two base oils. The accuracy and precision of the GC×GC/EI TOF MS method in quantitation of linear saturated hydrocarbons were assessed by comparing the measured and calculated peak areas of four mass fractions of each linear saturated hydrocarbon present in the base oils. All accuracy and precision measurements surpassed the minimum requirements for validation of a new method for quantitative purposes. Furthermore, the linear saturated hydrocarbon mass fraction in Base oil A and Base oil B determined by the GC×GC/EI TOF MS method was similar to that determined by GC×GC/FID. Therefore, this work expands the benefits

of the GC×GC/EI TOF MS method to not only provide structural information of compounds in complex mixtures, but to also quantitate linear saturated hydrocarbons in complex mixtures.

5.5 References

- (1) Kramer, D. C.; Ziemer, J. N.; Cheng, M. T.; Fry, C. E.; Reynolds, R. N.; Lok, B. K.; Sztenderowicz, M. L.; Krug, R. R. Influence of Group II & III Base Oil Composition on VI AND Oxidation Stability. *NLGI spokesman*, **1999**, 1-36.
- (2) Weijun, W.; Jun, L.; Yifeng, H.; Hongwei, S.; Songbai, T.; Hui, Z. Influence of Different Hydrocarbon Molecules on Physical Properties of Mineral Base Oils. *China Pet. Proc. PE*. **2017**, *19* (1), 33–45.
- (3) Rhodes, Gerald.; Opsal, R. B.; Meek, J. T.; Reilly, J. P. Analysis of Polyaromatic Hydrocarbon Mixtures with Laser Ionization Gas Chromatography/Mass Spectrometry. *Anal. Chem.* **1983**, *55* (2), 280–286.
- (4) Ventura, G. T.; Kenig, F.; Reddy, C. M.; Frysinger, G. S.; Nelson, R. K.; Mooy, B. V.; Gaines, R. B. Analysis of Unresolved Complex Mixtures of Hydrocarbons Extracted from Late Archean Sediments by Comprehensive Two-Dimensional Gas Chromatography (GC×GC). *Org Geochem.* **2008**, *39* (7), 846–867.
- (5) Fredericks, E. M.; Brooks, F. R. Gas Chromatography Analysis of Gaseous Hydrocarbons by Gas-Liquid Partition Chromatography. *Anal. Chem.* **1956**, *28* (3), 297–303.
- (6) Ray, N. H. Gas Chromatography I. The Separation and Estimation of Volatile Organic Compounds by Gas-Liquid Partition Chromatography. *J. Chem. Technol. Biotechnol.* **1954**, *4* (1), 21–25.
- (7) Isaacman, G.; Wilson, K. R.; Chan, A. W. H.; Worton, D. R.; Kimmel, J. R.; Nah, T.; Hohaus, T.; Gonin, M.; Kroll, J. H.; Worsnop, D. R., Goldstein, A.H. Improved Resolution of Hydrocarbon Structures and Constitutional Isomers in Complex Mixtures Using Gas Chromatography-Vacuum Ultraviolet-Mass Spectrometry. *Anal. Chem.* **2012**, *84* (5), 2335–2342.
- (8) Sřávořová, J.; Stahl, D. C.; Seames, W. S.; Kubátová, A. Method Development for the Characterization of Biofuel Intermediate Products Using Gas Chromatography with Simultaneous Mass Spectrometric and Flame Ionization Detections. *J. Chromatogr. A*. **2012**, *1224*, 79–88.
- (9) Downing, D. T.; Kranz, Z. H.; Murray, K. E. Studies in Waxes. XIV. An Investigation of the Aliphatic Constituents of Hydrolysed Wool Wax by Gas Chromatography. *Aust. J. Chem.* **1960**, *13* (1), 80–94.

- (10) Ventura, G. T.; Raghuraman, B.; Nelson, R. K.; Mullins, O. C.; Reddy, C. M. Compound Class Oil Fingerprinting Techniques Using Comprehensive Two-Dimensional Gas Chromatography (GC×GC). *Org. Geochem.* **2010**, *41* (9), 1026–1035.
- (11) Wang, F. C.-Y.; Zhang, L. Chemical Composition of Group II Lubricant Oil Studied by High-Resolution Gas Chromatography and Comprehensive Two-Dimensional Gas Chromatography. *Energy Fuels* **2007**, *21* (6), 3477–3483.
- (12) Jennerwein, M. K.; Eschner, M.; Gröger, T.; Wilharm, T.; Zimmermann, R. Complete Group-Type Quantification of Petroleum Middle Distillates Based on Comprehensive Two-Dimensional Gas Chromatography Time-of-Flight Mass Spectrometry (GC×GC-TOFMS) and Visual Basic Scripting. *Energy Fuels* **2014**, *28* (9), 5670–5681.
- (13) Mao, D.; Weghe, H. V. D.; Lookman, R.; Vanermen, G.; Brucker, N. D.; Diels, L. Resolving the Unresolved Complex Mixture in Motor Oils Using High-Performance Liquid Chromatography Followed by Comprehensive Two-Dimensional Gas Chromatography. *Fuel* **2009**, *88* (2), 312–318.
- (14) Genuit, W.; Chaabani, H. Comprehensive Two-Dimensional Gas Chromatography-Field Ionization Time-of-Flight Mass Spectrometry (GC×GC-FI-TOFMS) for Detailed Hydrocarbon Middle Distillate Analysis. *Int. J. Mass Spectrom.* **2017**, *413*, 27–32.
- (15) Li, S.; Cao, J.; Hu, S. Analyzing Hydrocarbon Fractions in Crude Oils by Two-Dimensional Gas Chromatography/Time-of-Flight Mass Spectrometry under Reversed-Phase Column System. *Fuel* **2015**, *158*, 191–199.
- (16) Zhang, W.; Zhu, S.; He, S.; Wang, Y. Screening of Oil Sources by Using Comprehensive Two-Dimensional Gas Chromatography/Time-of-Flight Mass Spectrometry and Multivariate Statistical Analysis. *J. Chromatogr. A* **2015**, *1380*, 162–170.
- (17) Liang, Z.; Chen, L.; Alam, M. S.; Zeraati Rezaei, S.; Stark, C.; Xu, H.; Harrison, R. M. Comprehensive Chemical Characterization of Lubricating Oils Used in Modern Vehicular Engines Utilizing GC × GC-TOFMS. *Fuel* **2018**, *220*, 792–799.
- (18) Hourani, N.; Muller, H.; Adam, F. M.; Panda, S. K.; Witt, M.; Al-Hajji, A. A.; Sarathy, S. M. Structural Level Characterization of Base Oils Using Advanced Analytical Techniques. *Energy Fuels* **2015**, *29* (5), 2962–2970.
- (19) Mao, D.; Lookman, R.; Weghe, H. V. D.; Weltens, R.; Vanermen, G.; Brucker, N. D.; Diels, L. Combining HPLC-GCXGC, GCXGC/ToF-MS, and Selected Ecotoxicity Assays for Detailed Monitoring of Petroleum Hydrocarbon Degradation in Soil and Leaching Water. *Environ. Sci. Technol.* **2009**, *43* (20), 7651–7657.
- (20) Coutinho, D. M.; França, D.; Vanini, G.; Mendes, L. A. N.; Gomes, A. O.; Pereira, V. B.; Ávila, B. M. F.; Azevedo, D. A. Rapid Hydrocarbon Group-Type Semi-Quantification in Crude Oils by Comprehensive Two-Dimensional Gas Chromatography. *Fuel* **2018**, *220*, 379–388.

- (21) Prak, D. J. L.; Romanczyk, M.; Wehde, K. E.; Ye, S.; McLaughlin, M.; Prak, P. J. L.; Foley, M. P.; Kenttämää, H. I.; Trulove, P. C.; Kilaz, G.; et al. Analysis of Catalytic Hydrothermal Conversion Jet Fuel and Surrogate Mixture Formulation: Components, Properties, and Combustion. *Energy Fuels* **2017**, *31*, 13802-13814.
- (22) Rambla-Alegre, M.; Esteve-Romero, J.; Carda-Broch, S. Is It Really Necessary to Validate an Analytical Method or Not? That Is the Question. *J. Chromatogr. A* **2012**, *1232*, 101–109.
- (23) Vozka, P.; Kilaz, G. How to Obtain a Detailed Chemical Composition for Middle Distillates via GC × GC-FID without the Need of GC × GC-TOF/MS. *Fuel* **2019**, *247*, 368–377.
- (24) Shah, V. P.; Midha, K. K.; Findlay, J. W. A.; Hill, H. M.; Hulse, J. D.; McGilveray, I. J.; McKay, G.; Miller, K. J.; Patnaik, R. N.; Powell, M. L.; et al. Bioanalytical Method Validation—A Revisit with a Decade of Progress. *Pharm. Res.* **2000**, *17* (12), 1551–1557.
- (25) Dietzel, K. D.; Campbell, J. L.; Bartlett, M. G.; Witten, M. L.; Fisher, J. W. Validation of a Gas Chromatography/Mass Spectrometry Method for the Quantification of Aerosolized Jet Propellant 8. *J. Chromatogr. A* **2005**, *1093* (1–2), 11–20.
- (26) Krouwer, J. S.; Rabinowitz, R. How to Improve Estimates of Imprecision. *Clin. Chem.* **1984**, *30* (2), 290–292.
- (27) Smith, L. L.; Strickland, J. R. Improved GC/MS Method for Quantitation of *n*-Alkanes in Plant and Fecal Material. *J. Agric. Food Chem.* **2007**, *55* (18), 7301–7307.

CHAPTER 6. ANALYSIS OF CRUDE OIL COMPONENTS THAT STRONGLY BIND TO KAOLINITE

6.1 Introduction

Due to the ever increasing energy demand, the world's light crude oil reserves are diminishing.¹ In order to be able to recover the ~66% of crude oil that still remains in underground reservoirs after primary and secondary oil recovery processes, novel extraction methods must be developed. One of the most intriguing tertiary recovery methods is chemically enhanced oil recovery (cEOR).² The goal of this process is to mobilize bound oil in the reservoir by introducing a combination of salts, surfactants, and polymers into the water flooding solution.³ The salts and surfactants decrease the interfacial tension of the oil bound to the reservoir surface, while the polymers increase the viscosity of the injected water and thereby facilitate motion of the displaced oil.³ However, petroleum companies rarely invest in cEOR efforts due to the insufficient levels of oil recovered compared to the amount of money spent on developing cEOR approaches.² An improved understanding of the types of compounds in oil that tightly bind to the reservoir surface would facilitate the development of successful cEOR formulations, i.e., optimal salt/surfactant/polymer mixtures, for more efficient extraction of the oil from the ground.

While oil reservoirs can have numerous geological features, the clays present in the rock are believed to adsorb most of the oil as they cover most of the rock surface area.⁴ One of the most prevalent clay minerals in oil reservoirs is kaolinite. It has been extensively studied due to its high affinity for crude oil.⁵ Kaolinite is an aluminosilicate with the chemical composition $\text{Al}_2\text{Si}_2\text{O}_5(\text{OH})_4$. It is a layered mineral with one sheet of silica (SiO_4) connected via oxygen atoms to a sheet of alumina (AlO_6). Exposed OH groups on the sheet of alumina of kaolinite create favorable interactions between the clay and the most polar molecules present in crude oil,

especially the polar compounds in asphaltenes.⁶⁻⁸ On the other hand, the siloxane surface of kaolinite has been reported to have favorable interactions with the most nonpolar compounds in crude oil.⁹ The affinity kaolinite can have for both polar and nonpolar compounds makes it challenging to develop a successful combination of chemicals to release the bound oil. Therefore, a better understanding on which particular chemical compounds in crude oil bind strongly to kaolinite could accelerate the development of better cEOR formulations.

While many efforts have been made to computationally model the adsorption of compounds present in crude oil to kaolinite,¹⁰⁻¹⁵ only few experimental studies have been conducted. Two independent studies determined positive correlations between the nitrogen content in asphaltene samples and the amount of asphaltenes adsorbed to kaolinite.^{7,16} On the contrary, based on X-ray photoelectron spectroscopy profile measurements of asphaltenes adsorbed to kaolinite surfaces, nitrogen- and sulfur-rich polar compounds were demonstrated not to be strongly adsorbed to kaolinite.⁸ Surprisingly, an experimental study determining the types of compounds in whole crude oil, and not just in asphaltenes, that strongly bind to kaolinite has not been performed. Furthermore, the analytical techniques utilized in the above studies provide only bulk chemical information for the compounds strongly bound to kaolinites. Therefore, no molecular level information has been obtained thus far.

High-resolution mass spectrometry measurements of crude oil as well as asphaltenes have been critical in obtaining molecular level information for these mixtures, including the average molecular weight and the elemental compositions and the number of aromatic rings in individual compounds.¹⁷⁻²⁰ Due to the great molecular complexity of crude oil, it is typically separated into several fractions containing compounds with different polarities prior to accurate mass spectrometry analysis. These fractions of crude oil may include those containing saturated

hydrocarbons, aromatic compounds, heteroaromatic compounds, polar compounds, and asphaltenes.²¹ Recently, our research group developed an improved method for fractionating and analyzing crude oil.²⁰ In the same study, an optimized mass spectrometric ionization technique was developed for each fraction to minimize ionization biases.²⁰ This method, referred to as distillation, precipitation, and fractionation mass spectrometry (DPF MS), can be applied to study the individual compounds in crude oil that bind strongly to kaolinite.

In this research, a kaolinite sample containing tightly bound crude oil components was deposited on a silica cartridge. Different solvents were then used to simultaneously remove the crude oil components from the kaolinite and fractionate them as performed²⁰ in the DPF MS method. Thermogravimetric analysis (TGA) and Fourier transform infrared spectroscopy (FTIR) analysis were conducted on the oil-treated kaolinite, before and after removal of the bound oil, to determine whether all of the bound oil had been removed. The fractionation step of the DPF MS method was also used to fractionate the components of the crude oil that were not strongly bound to kaolinite. All fractions collected in these experiments were analyzed by using the optimal ionization and mass spectrometry methods developed for DPF MS.

6.2 Experimental Section

Chemicals. . A medium API gravity crude oil sample was provided by Neste, Finland. Kaolinite KGa-1b was obtained from Washington, GA. Nitrogen gas was obtained from the boil-off of liquid nitrogen. Fluorene (98%), dibenzothiophene (98%), dibenzofuran (96%), carbazole (>99%), 1-heptadecylbenzene (>97%), and sodium chloride (>99.5%) were purchased from Sigma Aldrich (St. Louis, MO) and used as received. CS₂ (99.9 % purity) was purchased from Alfa Aesar (Haverhill, MA). Methanol (Optima LC/MS Grade) was purchased from Fisher Scientific

(Hampton, NH). HPLC grade *n*-hexane, dichloromethane, and isopropanol were purchased from Fisher Chemical (West Lafayette, IN) and used as received.

Exposure of Crude Oil to Kaolinite. Crude oil was exposed to kaolinite by combining ~9 g of crude oil with ~6 g of dried, powdered kaolinite clay in a cortex centrifuge tube. The tube contents were thoroughly mixed via a centrifuge tube rotator at 50 RPM for seven days. The centrifuge tube was then shaken by hand followed by centrifugation for 30 minutes at 3000 RPM. This process separated the nonbound oil components (NBO; as a liquid) from the crude oil components that were strongly bound to kaolinite (KBO). NBO was poured into a pre-weighed vial. Three 10 mL portions of brine solution made with 9400 ppm (by moles) of sodium chloride were then added into the tube to remove those oil components that can be recovered via water flooding - this oil was not analyzed. Lastly, both NBO and the kaolinite sample with KBO were vacuum dried at 60 °C to boil off the light saturated hydrocarbons from each sample.

Removal of Crude Oil Bound to Kaolinite (KBO) and Fractionation of KBO and NBO . KBO was simultaneously removed from kaolinite and fractionated into three fractions containing compounds with different polarities by using the fractionation step of the DPF method²¹ (Figure 6.1). The same fractionation method of the DPF method was also used to separate the NBO sample into the same three fractions. This was performed using a CombiFlash RF+ Lumen auto-column with UV, UV-Vis, and evaporative light scattering (ELS) detectors.

Approximately 0.5 g of NBO, or 2.7 g of kaolinite containing KBO, were weighed and loaded onto a frit that was inside a 25 g RediSep RF cartridge that was tightly packed with silica gel (Sorbitech). Beneath the RediSep RF cartridge was a 40 g silica flash column that was utilized

to enhance separation of the compounds in both samples. HPLC grade *n*-hexane, dichloromethane, and isopropanol were used as the eluting solvents. 100% *n*-hexane was first introduced through the cartridge at a flow rate of 40 mL/min for ten minutes. The *n*-hexane removed the heavy saturated and alkyl aromatic hydrocarbons from the oil-treated kaolinite and NBO. Then, 100% dichloromethane was introduced at the same flow rate for ten minutes, which removed the heteroaromatic compounds from both samples. Lastly, 100% isopropanol was injected for ten minutes to remove the most polar components. In this manner, the three solvents simultaneously removed and fractionated KBO from the kaolinite sample and fractionated NBO.

The solvent was removed from the three fractions obtained from NBO and KBO by using a rotary evaporator. Each fraction was stored in a pre-weighed vial for later analysis by mass spectrometry. Additionally, each fraction was weighed gravimetrically to determine their weight percentage in NBO and KBO. Successful removal of all crude oil that was bound to kaolinite was assessed by using TGA and FTIR spectroscopy (see section 6.3.1).

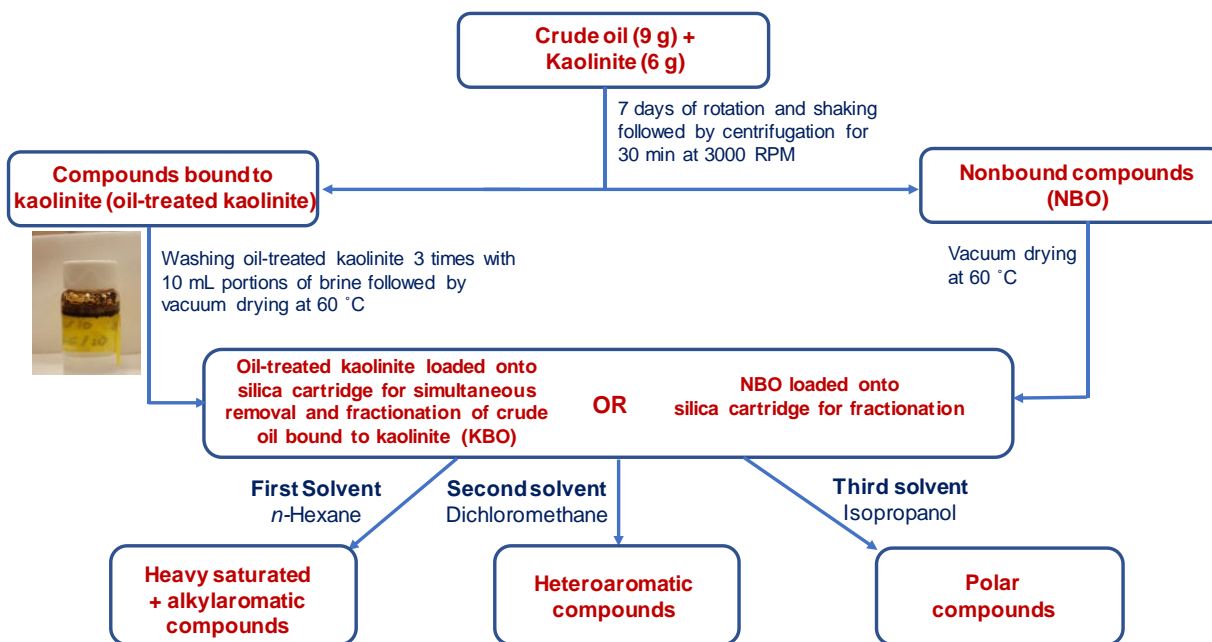


Figure 6.1 Flow chart demonstrating how the KBO and NBO samples were prepared and separated into three fractions containing compounds of different polarities.

Thermogravimetric Analysis (TGA). 0.04-0.06 grams of kaolinite samples, *i.e.*, kaolinite exposed to crude oil, kaolinite exposed to crude oil after *n*-hexane extraction, kaolinite exposed to crude oil after *n*-hexane and dichloromethane extractions, and kaolinite exposed to crude oil after *n*-hexane, dichloromethane, and isopropanol extractions, were loaded onto the tray of a Mettler Toledo Tga Sdta851 thermogravimetric analyzer. The initial temperature was set to 25 °C and it was increased at a rate of 20 °C/min until it reached a final temperature of 1,000 °C.

Fourier Transform Infrared Spectroscopy (FTIR). All FTIR spectra were collected using a Thermo Nicolet 380 FTIR spectrometer. 0.01 g of kaolinite samples, *i.e.*, kaolinite exposed to crude oil, kaolinite exposed to crude oil after *n*-hexane extraction, kaolinite exposed to crude oil after *n*-hexane and dichloromethane extraction, and kaolinite exposed to crude oil after *n*-hexane, dichloromethane, and isopropanol extraction, were combined with 0.19 g of KBr in a ball and mill followed by vigorous mixing by using a mechanical vibrator. FTIR spectra were measured between 4,000 – 500 cm⁻¹. Before acquiring FTIR spectra of the samples, a background FTIR spectrum was collected for 0.2 g of KBr. Each KBr sample was prepared fresh before measurements.

Gas Chromatography / Electron Ionization Mass Spectrometry (GC/EI MS). 1 mg of the artificial model compound mixture bound to kaolinite and 1 mg of the nonbound artificial model compound mixture (see section 6.3.3 for more details on the artificial model compound mixtures) were each dissolved in 1 mL of dichloromethane prior to GC/EI MS analysis using Shimadzu GC-2010/MS-QP2010 GC/MS instrument. The instrument consisted of a non-functionalized column, an EI source, and a quadrupole mass analyzer. The GC oven temperature program was 40 °C –

200 °C at a temperature ramp rate of 10 °C/min. 70 eV EI mass spectra were collected using a m/z range of 50 – 500.

Atmospheric Pressure Chemical Ionization (APCI) Linear Quadrupole Ion Trap (LQIT) Orbitrap Mass Spectrometry. Direct infusion positive-ion mode APCI experiments were conducted on a LQIT coupled with a high-resolution orbitrap XL mass spectrometer (Orbitrap XL MS; Thermo Fischer Scientific, San Jose, CA). All high-resolution measurements were performed at a resolution of 100,000 at m/z 400. The lock mass feature was utilized for internal calibration during mass spectral data collection (see next section for more details).

Details of these experiments are provided below. Based on literature, 40 mg of the *n*-hexane-soluble and dichloromethane-soluble fractions were dissolved in 1 mL carbon disulfide, while 40 mg of the isopropanol-soluble fraction were dissolved in 1 mL of 50:50 hexane:methanol.²¹ Each fraction was doped with an internal standard to conduct lock mass measurements for high-resolution mass spectrometry. The internal standard, 1-heptadecylbenzene (MW = 316 Da), was selected for “locking” because its molecular weight was within the molecular weight range of the compounds in the fractions obtained from NBO and KBO. The internal standard was prepared in a separate vial by dissolving 10 mg of 1-heptadecylbenzene in 2 mL of solvent – CS₂ for the *n*-hexane and dichloromethane fractions and 50:50 *n*-hexane:methanol for the isopropanol fraction. For direct infusion experiments, 450 μL of each sample solution and 50 μL of the corresponding internal standard solution were drawn into the same 500 μL Hamilton syringe and injected into the APCI source. The APCI source conditions for all analyses were as follows: vaporizer temperature 300 °C, capillary temperature 280 °C, nitrogen sheath gas flow rate

30 (arbitrary units), nitrogen auxiliary gas flow rate 10 (arbitrary units), ion transfer capillary voltage 10 V, tube lens voltage 40 V, and Hamilton syringe flow rate 10-30 $\mu\text{L}/\text{min}$.

All mass spectra were acquired and analyzed using Xcalibur software version 2.2 (Thermo Fisher Scientific, Inc., San Jose, CA). Average molecular weight (AvgMW) (Equation 6.1) of compounds in each fraction was determined by using the mass spectra collected at unit resolution on the LQIT. All ions observed in the unit resolution mass spectra were singly charged ions, and therefore, the mass (m) of each ion was used to calculate the AvgMW. Their abundances were determined based on their MS peak areas. All unit resolution mass spectra had a minimum normalized peak height threshold set at 1% of the most abundant ion.

$$\text{AvgMW} = \frac{\sum(m) * \text{abundances}}{\sum \text{abundances}} \quad (\text{Equation 6.1})$$

All high-resolution orbitrap mass spectra had a minimum normalized peak height threshold set at 5% of the most abundant ion (note: in several high-resolution mass spectra, the most abundant ions were ions derived from impurities; instead of these, the abundances of ions derived from the compounds in each sample were normalized to the most abundant ions derived from the compounds in each sample). Elemental composition assignments were limited to a maximum mass accuracy error of 5 ppm. The elements selected for elemental composition determination were carbon (C), hydrogen (H), nitrogen (N), oxygen (O) and sulfur (S). The maximum number of N, O, and S atoms was set to 3, while no limits were placed to the number of C and H atoms. Relative ring and double bond equivalence (*RDBE*) values were set to range from -0.5 to 40. *RDBE* indicates the number of double bonds and the number of rings present in compounds with each

predicted molecular formula. The Xcalibur software calculates the RDBE by using Equation 6.2 for molecular formula of $C_cH_hN_nO_oS_s$.

$$\text{RDBE} = c - (h/2) + (n/2) + 1 \quad (\text{Equation 6.2})$$

Microsoft Excel 2019 was used to sort heteroatom-containing ions as well as to organize the data for generating bar graphs. Originpro 2018 was used to create the RDBE versus number of carbon atoms plots for each oil fraction. The size of the sphere in each plot is indicative of the relative abundance for that ion in the mass spectrum.

6.3 Results and Discussion

The goal of this work was to identify the types of compounds in crude oil that strongly bind to kaolinite (KBO). Kaolinite was exposed to crude oil (as described above) and centrifuged to produce two samples, kaolinite containing KBO and compounds not strongly bound to kaolinite (NBO). The oil-treated kaolinite was loaded onto a silica cartridge and placed in an auto-column to simultaneously remove KBO from the kaolinite and fractionate it by eluting the kaolinite sample with *n*-hexane, dichloromethane, and isopropanol. TGA and FTIR spectroscopy measurements of several kaolinite samples (see discussion on TGA and FTIR in section 6.2 for details) were conducted to determine whether KBO was successfully removed from kaolinite. The elemental compositions and relative abundances of ions detected in the high-resolution mass spectra measured for the KBO and NBO samples were determined. Finally, to better understand the results of this comparison, a 0.02 mM equimolar model compound mixture containing fluorene, dibenzothiophene, dibenzofuran, and carbazole was exposed to kaolinite by using the same method as for the crude oil (see “Exposure of Crude Oil to Kaolinite” in the Experimental Section for

details). The model compounds that were strongly bound and not bound to kaolinite were identified and quantified by using GC/EI MS. The results are discussed below in this order.

6.3.1 Removal of KBO from Kaolinite and Fractionation of KBO and NBO

After exposure of kaolinite to crude oil, 2.7 g of oil-treated kaolinite was placed in between two frits on a solid-phase silica cartridge. The heavy saturated and alkyl aromatic compounds in KBO were removed from the oil-treated kaolinite by eluting *n*-hexane through the silica cartridge, while the heteroaromatic compounds in KBO were removed by using dichloromethane, and the polar compounds by using isopropanol. Similarly, 0.5 g of NBO was loaded onto a frit in a silica cartridge and the NBO was separated into the same three fractions with different polarities as KBO by using *n*-hexane, dichloromethane, and isopropanol.

Before analyzing the three fractions obtained from both KBO and NBO, it was necessary to ensure that none of the KBO remained on the oil-treated kaolinite. TGA and FTIR spectroscopy were utilized to accomplish this task. Figure 6.2 shows the TGA plot of kaolinite before it was exposed to crude oil. The 13.3% mass loss from kaolinite observed in the TGA plot between 450 – 650 °C is due to the loss of water from kaolinite. Figure 6.3 shows an overlay of four TGA plots and their first derivative plots for four differently treated kaolinite samples: kaolinite containing KBO (sample #1; red), kaolinite with KBO after elution by *n*-hexane (sample #2; green), kaolinite with KBO after elution with *n*-hexane and dichloromethane (sample #3; pink), and kaolinite with KBO after elution with *n*-hexane, dichloromethane, and isopropanol (sample #4; black). Interestingly, about 13% of the KBO was removed from the kaolinite by just *n*-hexane elution. Furthermore, the TGA plot for kaolinite with KBO after elution by *n*-hexane, dichloromethane, and isopropanol (sample #4, black) in Figure 6.3 looks identical to the TGA plot of pure kaolinite in Figure 6.2, suggesting that the three solvents successfully removed all of the KBO from kaolinite.

Pure kaolinite

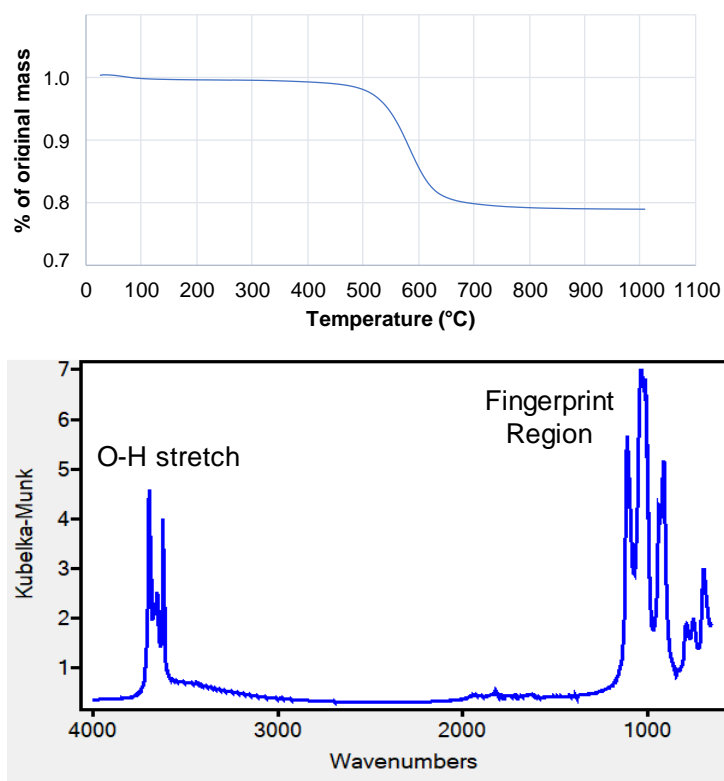


Figure 6.2 TGA plot (top) and FTIR spectrum (bottom) measured for pure kaolinite. A 13.3% mass loss was observed between 450 – 650 °C in the TGA plot.

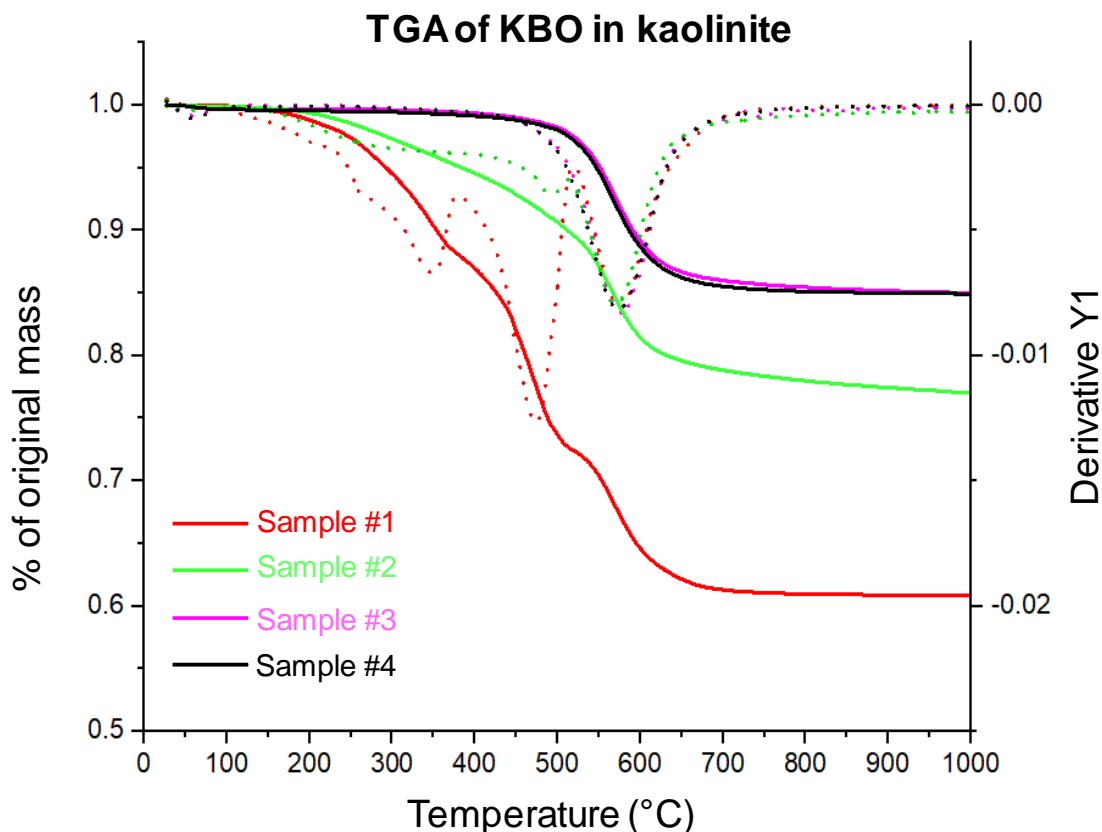


Figure 6.3 TGA plot of kaolinite with KBO (**sample #1; red**), kaolinite with KBO after elution by *n*-hexane (**sample #2, green**), kaolinite with KBO after elution by *n*-hexane and dichloromethane (**sample #3, pink**), and kaolinite with KBO after elution by *n*-hexane, dichloromethane, and isopropanol (**sample #4, black**). Dashed traces are the first derivatives of the solid traces. For instance, the red dash is the first derivative of the solid red dash.

Figure 6.2 (bottom) shows the FTIR spectrum measured for the kaolinite before exposure to crude oil. The peaks corresponding to an O-H stretch are indicated. Figure 6.4 shows an overlay of four FTIR spectra measured for kaolinite containing KBO (sample #1; light blue), kaolinite with KBO after elution by *n*-hexane (sample #2; light green), kaolinite with KBO after elution with *n*-hexane and dichloromethane (sample #3; dark green), and kaolinite with KBO after elution with *n*-hexane, dichloromethane, and isopropanol (sample #4; pink). Peaks that were observed in the FTIR spectrum for the kaolinite containing KBO (Figure 6.4; sample #1; light blue) that were not observed in the FTIR spectrum for kaolinite before exposure to crude oil (Figure 6.2; bottom) were

assigned to KBO. The peaks corresponding to KBO were C-H stretch ($\sim 2950\text{ cm}^{-1}$), CH_2 scissoring ($\sim 1470\text{ cm}^{-1}$), and CH_2 wagging ($\sim 1400\text{ cm}^{-1}$). These peaks were significantly smaller after *n*-hexane elution compared to when no extraction had been performed (light blue trace compared to light green trace). Also, the pink trace (kaolinite with KBO after elution with *n*-hexane, dichloromethane, and isopropanol; sample #4) appears identical to the FTIR spectrum of kaolinite before it was exposed to crude oil (Figure 2; bottom), thus substantiating the conclusion that *n*-hexane, dichloromethane, and isopropanol removed all of the KBO from kaolinite.

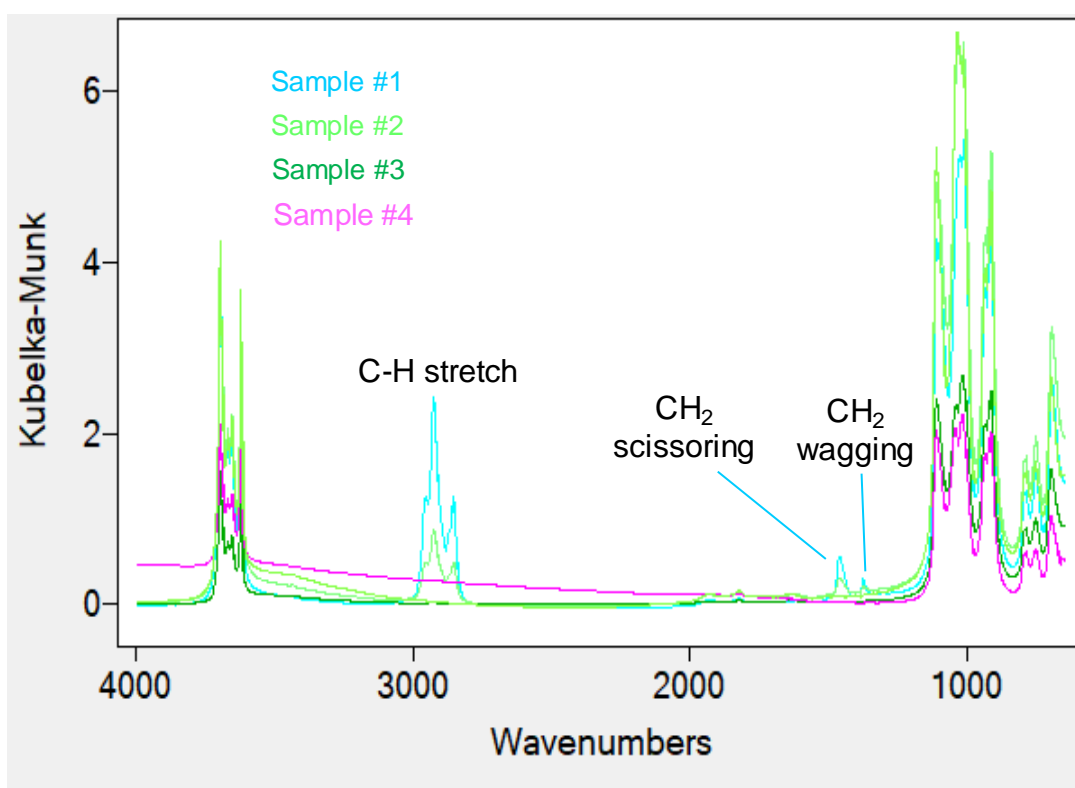


Figure 6.4 FTIR spectra of kaolinite with KBO (sample #1; light blue), kaolinite with KBO after elution with *n*-hexane (sample #2; light green), kaolinite with KBO after elution with *n*-hexane and dichloromethane (sample #3; dark green), and kaolinite with KBO after elution with *n*-hexane, dichloromethane, and isopropanol (sample #4; pink).

6.3.2 Comparison of the Chemical Compositions of KBO and NBO

Low-resolution mass spectra measured using the LQIT for each fraction obtained from the NBO and KBO samples were used to determine the average molecular weight of the compounds in each fraction. The average molecular weights of the corresponding fractions obtained from each sample were similar (Table 6.1). Interestingly, the isopropanol fraction obtained from each sample had a larger average molecular weight (~530 Da) than the other two fractions (~440 Da). Analysis of the high-resolution orbitrap mass spectra (Figures 6.5 and 6.6) revealed that the average RDBE and average number of carbons in compounds in each fraction obtained from both samples were similar, with the exception of the average RDBE for the isopropanol fraction (Table 6.2). It is unclear at this time as to why the average RDBE of the isopropanol fraction of KBO (7) is greater than that measured for NBO (3).

Table 6.1 Average molecular weight of compounds in individual fractions of nonbound oil components (NBO) and kaolinite bound oil components (KBO) determined from low-resolution mass spectra.

Oil Fraction	NBO	KBO
Hexane	435 Da	436 Da
Dichloromethane	449 Da	443 Da
Isopropanol	528 Da	535 Da

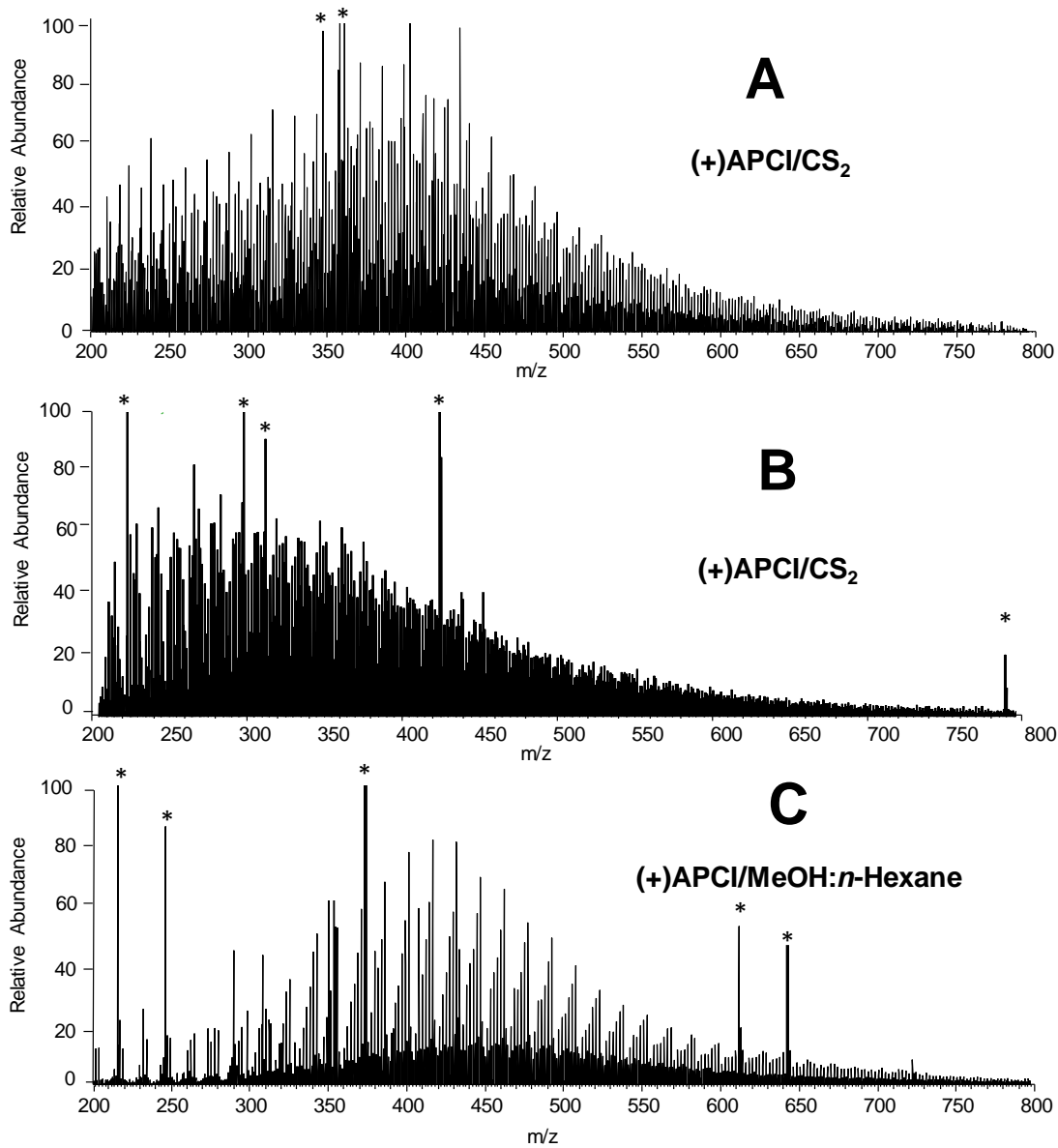


Figure 6.5 (+)APCI mass spectra of the *n*-hexane (A), dichloromethane (B), and isopropanol (C) fractions of the KBO sample. Ions marked with * are due to impurities.

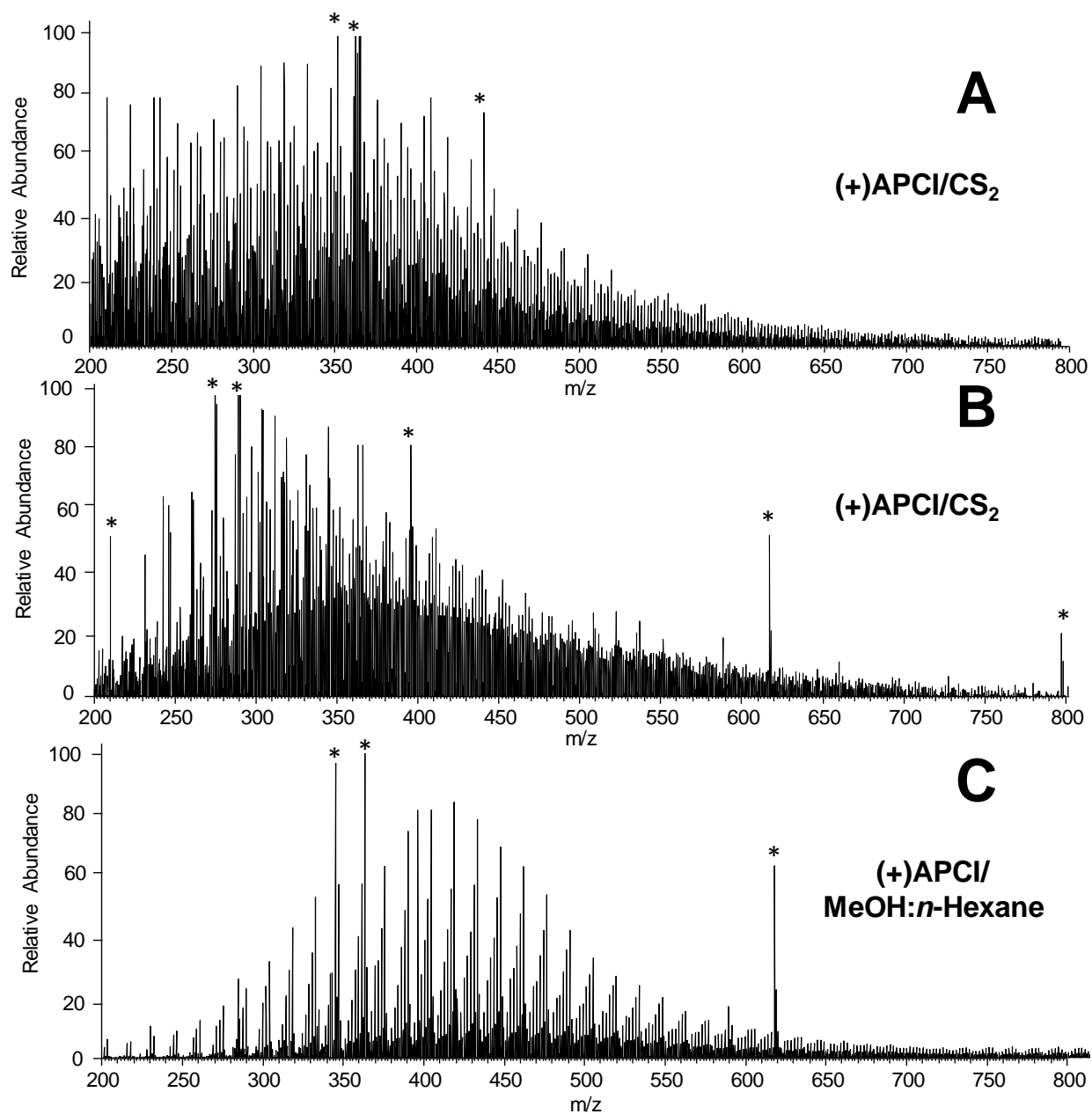


Figure 6.6 (+)APCI mass spectra of the *n*-hexane (A), dichloromethane (B), and isopropanol (C) fractions of the NBO sample. Ions marked with * are impurities.

Table 6.2 Average RDBE and the average number of carbons for compounds in the individual fractions collected from the NBO and KBO samples, as determined from high-resolution mass spectra.

Fraction of Oil	Kaolinite Bound Oil Components		Nonbound Oil Components	
	Avg. RDBE	Avg. C#	Avg. RDBE	Avg. C#
Alkyl Aromatics	7	29	7	28
Heteroaromatics	12	24	12	26
Polar Compounds	7	30	3	29

However, plotting the RDBE values as a function of the number of carbon atoms for compounds in each fraction (Figure 6.7) revealed more ions that only contain carbon and hydrogen atoms (black dots) for KBO than for NBO. Based on this result, the entire KBO sample contains more nonpolar compounds than the entire NBO sample. To determine the relative amounts of the different chemical compound classes in KBO and in NBO, the approximate weight percentage of compounds with eight different chemical compositions including only carbon and hydrogen atoms (C_xH_y) and carbon and hydrogen atoms as nitrogen atoms (N_x), oxygen atoms (O_x), sulfur atoms (S_x), nitrogen and oxygen atoms (N_xO_y), nitrogen and sulfur atoms (N_xS_y), oxygen and sulfur atoms (O_xS_y), and nitrogen, oxygen and sulfur atoms ($N_xO_yS_z$) were determined by using equation 6.3, where i is elemental composition, wt% is the gravimetric weight percent of each crude oil fraction (Table 6.3), and x is the number of each crude oil fraction (1-3).

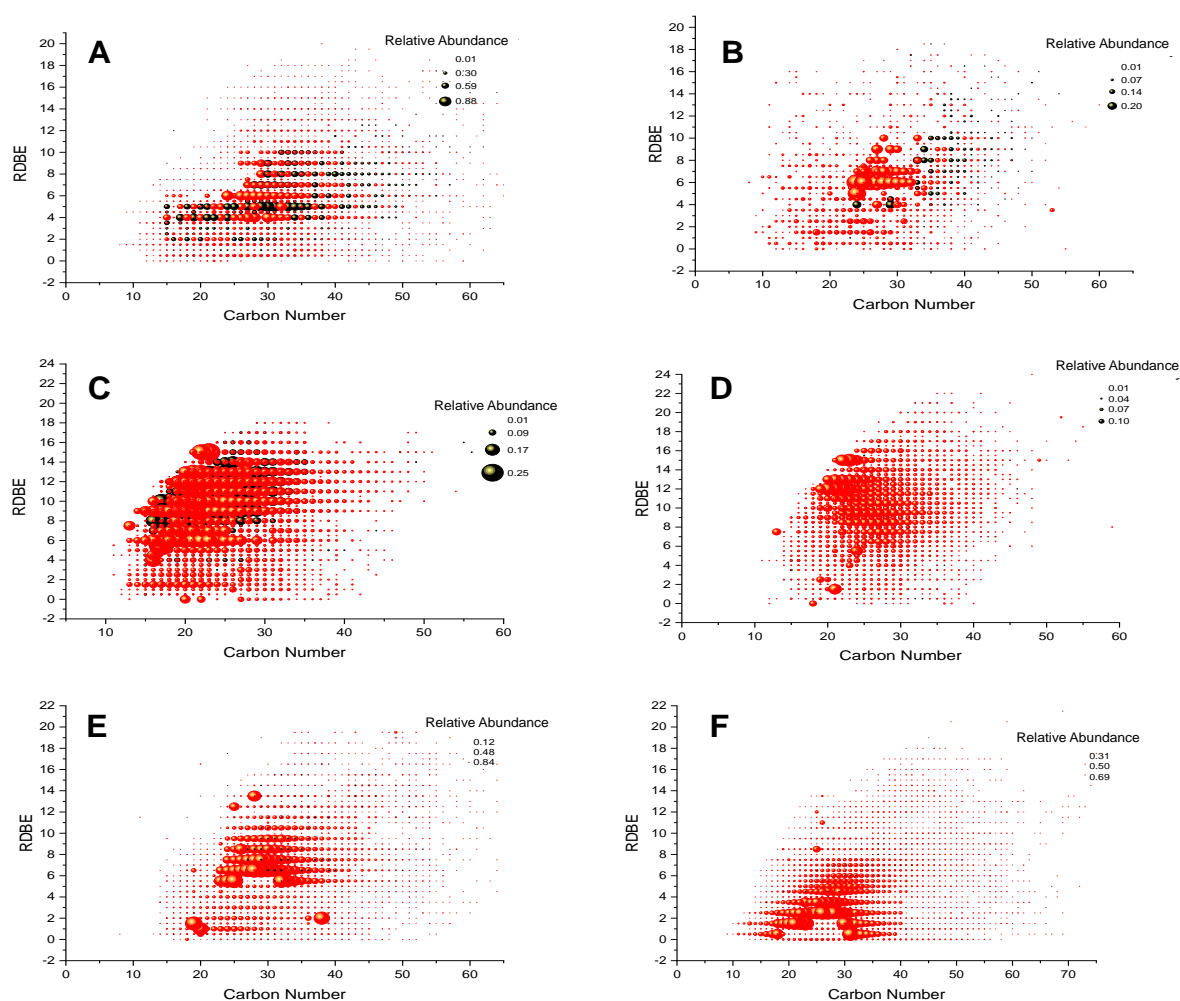


Figure 6.7 RDBE presented as a function of the number of carbon atoms for compounds in the *n*-hexane, dichloromethane, and isopropanol fractions of KBO (A, C, and E, respectively) and NBO (B, D, and F, respectively). Black dots represent compounds that contain only carbon and hydrogen atoms. Red dots represent compounds that contain carbon and hydrogen atoms as well as heteroatoms, including oxygen, nitrogen, and/or sulfur.

Table 6.3 Gravimetric weight percentage of the fractions of nonbound oil components (NBO) and kaolinite bound oil components (KBO).

Oil Fraction	Gravimetric weight % NBO	Gravimetric weight % KBO
Hexane	86%	94%
Dichloromethane	5%	4%
Isopropanol	9%	2%

Approximate weight percentage of each consolidated elemental composition

$$\sum_{x=1}^3 \left(\frac{\sum i_x \text{ abundance}}{\sum x \text{ abundance}} * wt\%(x) \right) \quad (\text{Equation 6.3})$$

The data shown in Figure 6.8 support the observation made for the plots of RDBE as a function of the number of carbon atoms (Figure 6.7) that the “C_xH_y” class of compounds is 2.5 times more abundant in KBO than in NBO. All other heteroatom containing compound classes, except O_x, have greater abundances in the NBO sample than in the KBO sample. These results suggest that compounds containing only carbon and hydrogen atoms bind more strongly to kaolinite than heteroatom containing compounds. Furthermore, these results imply that the hydrophobic surface of kaolinite plays a greater role in adsorption of oil components than the hydrophilic surface. Further studies on the effects of pH and salinity on the adsorption of compounds in crude oil to kaolinite need to be conducted.

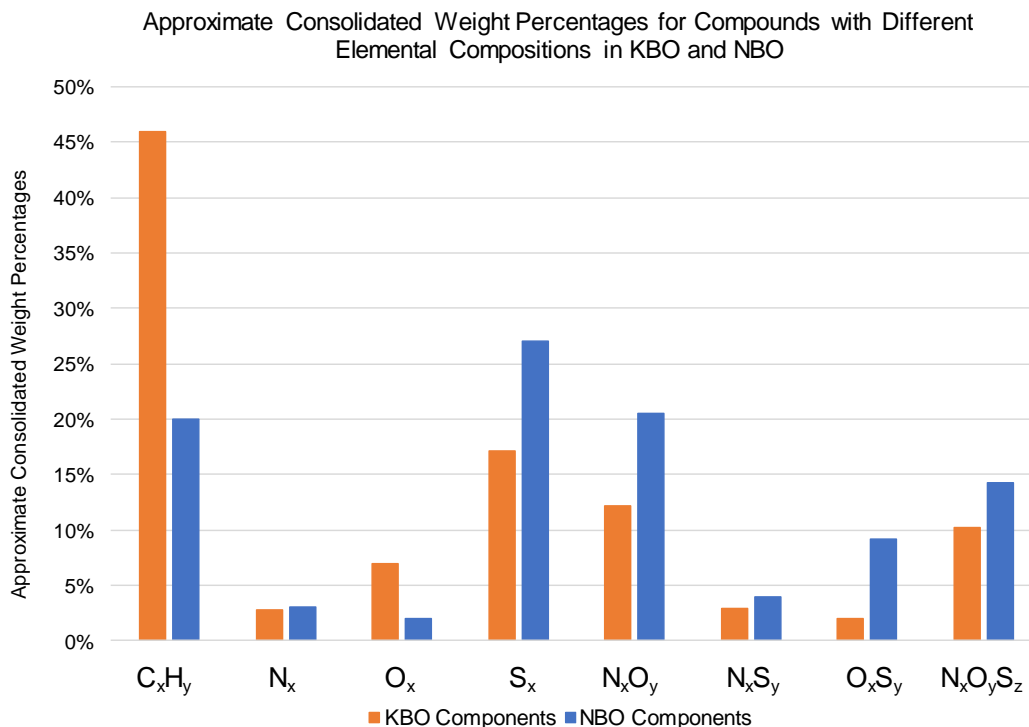


Figure 6.8 Approximate consolidated weight percentages for compounds with different elemental compositions derived from equation 6.3 for compounds in KBO and NBO. The subscripts x, y, and z are any positive integer numbers (not zero).

6.3.3 Model Compound Study

Additional kaolinite adsorption tests were conducted with model compounds to corroborate the above finding that nonpolar hydrocarbons bind to kaolinite more strongly than heteroatom-containing compounds. A 0.02 M equimolar solution of fluorene ($C_{13}H_{10}$), dibenzothiophene ($C_{12}H_8S$), dibenzofuran ($C_{12}H_8O$), and carbazole ($C_{12}H_9N$) was prepared in 6 mL of toluene (see Figure 6.9 for the structures of the chemicals). Toluene was selected as the solvent because it dissolved all compounds. 4 g of dried, powdered, kaolinite clay was added into the solution. The model compound solution was exposed to kaolinite by using the same method that was used to expose the crude oil to kaolinite (see “Preparation of Crude Oil Bound to Kaolinite” in the methods section for details). Also, the method for separating the nonbound model compounds from the

bound model compounds was the same as for separating NBO from KBO. The model compounds that were bound to kaolinite stronger were removed from kaolinite by using the same fractionation step of the DPF MS method as discussed above (see “Fractionation of NBO and Components in Crude Oil Bound to Kaolinite” in the methods section for details). After separation, 1 mg of the strongly bound model compound mixture and 1 mg of the nonbound model compound mixture were each dissolved in 1 mL of dichloromethane. These two solutions were analyzed by using a Shimadzu GC-2010/MS-QP2010 (GC/EI MS). The relative abundances of each of the model compounds in each sample were determined by dividing the chromatogram peak area for each compound by the sum of the chromatogram peak areas of all the compounds.

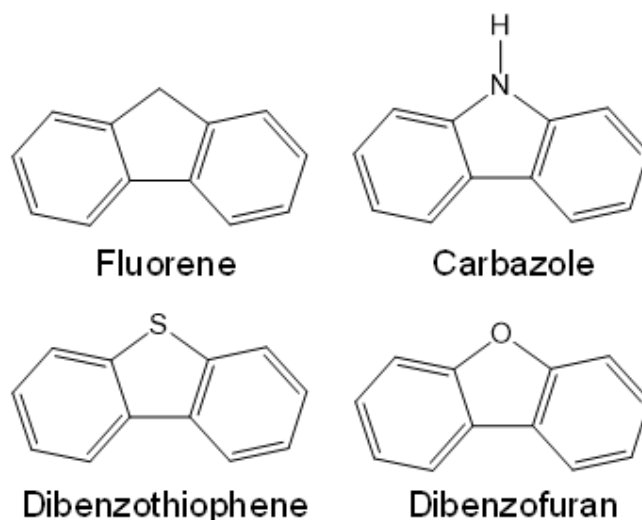


Figure 6.9 Structures of the four model compounds that were used to make the artificial mixture.

Figure 6.10 shows a bar graph of the relative GC peak areas for each of the four compounds in each sample - nonbound model compounds (blue) and kaolinite bound model compounds (orange). Error bars represent the standard deviations calculated from three replicate measurements collected on three different days. In agreement with the previous results, the most nonpolar compound (fluorene) was found to have a slightly greater relative abundance in the

kaolinite bound sample (~30%) than in the nonbound sample (~25%), while the nitrogen- and oxygen-containing compounds had substantially greater relative abundances in the nonbound sample (~21% and ~24%, respectively) than in the kaolinite bound sample (~13% and ~18% respectively). This finding supports the conclusion made in the crude oil study that compounds containing only carbon and hydrogen atoms are more strongly bound to kaolinite than nitrogen- and oxygen-containing compounds. Furthermore, greater amounts of the sulfur-containing compound (dibenzothiophene) were found to be present in the kaolinite bound sample than in the nonbound sample. Based on this result, nonpolar hydrocarbons have a higher affinity for kaolinite (before exposure to crude oil) than polar compounds. Although sulfur-containing compounds derived from the crude oil had greater abundances in the NBO sample than the KBO sample, one possible explanation for this discrepancy is that the crude oil contains many sulfur-compounds with different structures and not just dibenzothiophene. Therefore, different sulfur-containing model compounds need to be studied.

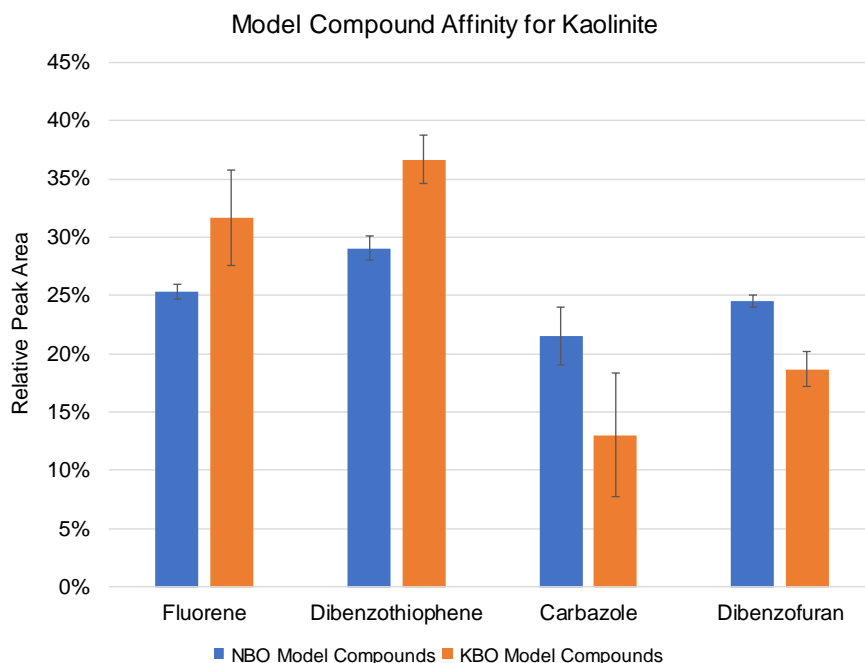


Figure 6.10 Relative GC peak area for each model compound in the nonbound and kaolinite bound samples measured by using GC/EI MS.

6.4 Conclusions

The compounds in crude oil that were bound to kaolinite were compared to the nonbound compounds in crude oil. The average MWs of the compounds in corresponding heavy saturate and alkyl aromatic compounds fractions, heteroaromatic compounds fractions, and polar compounds fractions were similar for both samples; the average RDBE values were also similar between corresponding fractions with the exception of the polar compounds fraction. Compounds in crude oil containing only carbon and hydrogen atoms were found to more strongly bind to kaolinite than polar compounds containing heteroatoms. The results from a model compound study with aromatic and heteroaromatic compounds corroborated this finding as well as demonstrated that nonpolar hydrocarbons including dibenzothiophene, a sulfur-containing compound, prefer to bind to kaolinite. Therefore, an increase in crude oil recovered from the ground may be possible if surfactants and polymers are designed to target the nonpolar hydrocarbons. Furthermore, the

results from this study suggest that the more useful and valuable oil components (compounds containing only carbon and hydrogen atoms) still remains in the ground after water flooding, and therefore, cEOR efforts with the appropriate formulation could be economically favorable.

The method developed here for exposing crude oil to kaolinite as well as the method developed for recovering the bound oil components can be applied to other powdered clays. Furthermore, in combination with high-resolution mass spectrometry for chemical analysis, the chemical composition of oil components that strongly bind to different types of powdered clays can be studied. The effects of pH and salinity will be explored in the future to determine whether these variables change the types of compounds in crude oil that bind to kaolinite.

6.5 References

- (1) Hasan, S. W.; Ghannam, M. T.; Esmail, N. Heavy Crude Oil Viscosity Reduction and Rheology for Pipeline Transportation. *Fuel* 2010, 89 (5), 1095–1100.
- (2) Kokal, S.; Al-Kaabi, A. Enhanced Oil Recovery: Challenges & Opportunities. World Petroleum Council: Official Publication 2010, 64.
- (3) Olajire, A. A. Review of ASP EOR (Alkaline Surfactant Polymer Enhanced Oil Recovery) Technology in the Petroleum Industry: Prospects and Challenges. *Energy* 2014, 77, 963–982.
- (4) Iglauer, S.; Wu, Y.; Shuler, P.; Tang, Y.; Goddard, W. A. New Surfactant Classes for Enhanced Oil Recovery and Their Tertiary Oil Recovery Potential. *J. Petrol. Sci. Eng.* 2010, 71 (1), 23–29.
- (5) Saada, A.; Siffert, B.; Papirer, E. Comparison of the Hydrophilicity/Hydrophobicity of Illites and Kaolinites. *J. Colloid Interf. Sci.* 1995, 174 (1), 185–190.
- (6) Chen, Q.; Gray, M. R.; Liu, Q. Irreversible Adsorption of Asphaltenes on Kaolinite: Influence of Dehydroxylation. *Energy Fuels* 2017, 31 (9), 9328–9336.
- (7) Pernyeszi, T.; Patzkó, Á.; Berkesi, O.; Dékány, I. Asphaltene Adsorption on Clays and Crude Oil Reservoir Rocks. *Colloid Surface A* 1998, 137 (1), 373–384.
- (8) Wang, S.; Liu, Q.; Tan, X.; Xu, C.; Gray, M. R. Study of Asphaltene Adsorption on Kaolinite by X-Ray Photoelectron Spectroscopy and Time-of-Flight Secondary Ion Mass Spectroscopy. *Energy Fuels* 2013, 27 (5), 2465–2473.

- (9) Tian, S.; Erastova, V.; Lu, S.; Greenwell, H. C.; Underwood, T. R.; Xue, H.; Zeng, F.; Chen, G.; Wu, C.; Zhao, R. Understanding Model Crude Oil Component Interactions on Kaolinite Silicate and Aluminol Surfaces: Toward Improved Understanding of Shale Oil Recovery. *Energy Fuels* 2018, 32 (2), 1155–1165.
- (10) Greathouse, J. A.; Cygan, R. T.; Fredrich, J. T.; Jerauld, G. R. Adsorption of Aqueous Crude Oil Components on the Basal Surfaces of Clay Minerals: Molecular Simulations Including Salinity and Temperature Effects. *J. Phys. Chem. C* 2017, 121 (41), 22773–22786.
- (11) Hlushak, S.; Kovalenko, A. Effective Interactions and Adsorption of Heterocyclic Aromatic Hydrocarbons in Kaolinite Organic Solutions Studied by 3D-RISM-KH Molecular Theory of Solvation. *J. Phys. Chem. C* 2017, 121 (40), 22092–22104.
- (12) Zhang, L.; Lu, X.; Liu, X.; Yang, K.; Zhou, H. Surface Wettability of Basal Surfaces of Clay Minerals: Insights from Molecular Dynamics Simulation. *Energy Fuels* 2016, 30 (1), 149–160.
- (13) Johnson, E. R.; Otero-de-la-Roza, A. Adsorption of Organic Molecules on Kaolinite from the Exchange-Hole Dipole Moment Dispersion Model. *J. Chem. Theory Comput.* 2012, 8 (12), 5124–5131.
- (14) Bai, Y.; Sui, H.; Liu, X.; He, L.; Li, X.; Thormann, E. Effects of the N, O, and S Heteroatoms on the Adsorption and Desorption of Asphaltenes on Silica Surface: A Molecular Dynamics Simulation. *Fuel* 2019, 240, 252–261.
- (15) Huang, W.; Dedzo, G. K.; Stoyanov, S. R.; Lyubimova, O.; Gusarov, S.; Singh, S.; Lao, H.; Kovalenko, A.; Detellier, C. Molecule–Surface Recognition between Heterocyclic Aromatic Compounds and Kaolinite in Toluene Investigated by Molecular Theory of Solvation and Thermodynamic and Kinetic Experiments. *J. Phys. Chem. C* 2014, 118 (41), 23821–23834.
- (16) Dudášová, D.; Simon, S.; Hemmingsen, P. V.; Sjöblom, J. Study of Asphaltenes Adsorption onto Different Minerals and Clays: Part 1. Experimental Adsorption with UV Depletion Detection. *Colloid Surface A* 2008, 317 (1), 1–9.
- (17) Pinkston, D. S.; Duan, P.; Gallardo, V. A.; Habicht, S. C.; Tan, X.; Qian, K.; Gray, M.; Müllen, K.; Kenttämaa, H. I. Analysis of Asphaltenes and Asphaltene Model Compounds by Laser-Induced Acoustic Desorption/Fourier Transform Ion Cyclotron Resonance Mass Spectrometry. *Energy Fuels* 2009, 23 (11), 5564–5570.
- (18) Pomerantz, A. E.; Hammond, M. R.; Morrow, A. L.; Mullins, O. C.; Zare, R. N. Two-Step Laser Mass Spectrometry of Asphaltenes. *J. Am. Chem. Soc.* 2008, 130 (23), 7216–7217.
- (19) Fan, X.; Zhang, X.-Y.; Dong, X.; Liao, J.-J.; Zhao, Y.-P.; Wei, X.-Y.; Ma, F.-Y.; Nulahong, A. Structural Insights of Four Thermal Dissolution Products of Dongming Lignite by Using In-Source Collision-Activated Dissociation Mass Spectrometry. *Fuel* 2018, 230, 78–82.

- (20) Niyonsaba, E.; Manheim, J. M.; Yerabolu, R.; Kenttämä, H. I. Recent Advances in Petroleum Analysis by Mass Spectrometry. *Anal. Chem.* 2019, 91 (1), 156–177.
- (21) Yerabolu, R.; Kotha, R. R.; Niyonsaba, E.; Dong, X.; Manheim, J. M.; Kong, J.; Riedeman, J. S.; Romanczyk, M.; Johnston, C. T.; Kilaz, G.; et al. Molecular Profiling of Crude Oil by Using Distillation Precipitation Fractionation Mass Spectrometry (DPF-MS). *Fuel* 2018, 234, 492–501.

VITA

Jeremy Marc Manheim was born in Queens, New York. He attended Townsend Harris High School and the University at Albany, SUNY where he majored in Chemistry with an emphasis in forensic science. He conducted two-and-a-half years of undergraduate research under the tutelage of Professor Igor Lednev. After receiving his BS in Chemistry in 2015, he enrolled at Purdue University to obtain a PhD in Chemistry.

PUBLICATIONS

Manheim, J.; Milton, J.; Zhang, Y.; Kenttämäa, H. I. Proton Transfer Reactions Cause Fragmentation of Saturated Hydrocarbons upon Atmospheric Pressure Chemical Ionization *Anal. Chem.* **2020**, *Submitted*.

Manheim, J.; Wehde, K.; Zhang, W. T. J.; Vozka, P.; Romanczyk, M.; Kilaz, G.; Kenttämäa, H. I. Identification and Quantitation of Linear Alkanes in Lubricant Base Oils by Using GC×GC/EI TOF Mass Spectrometry. *J. Am. Soc. Mass Spectrom.* **2019**, *30*(10), 2670-2677.

Manheim, J.; Zhang, Y.; Viidanoja, J.; Kenttämäa, H. I. An Automated Method for Chemical Composition Analysis of Lubricant Base Oils by Using Atmospheric Pressure Chemical Ionization Mass Spectrometry. *J. Am. Soc. Mass Spectrom.* **2019**, *30*, 2014-2021.

Niyonsaba, E.; **Manheim, J. M.;** Yerabolu, R.; Kenttämäa, H. I. Recent Advances in Petroleum Analysis by Mass Spectrometry. *Anal. Chem.* **2019**, *91* (1), 156–177.

Yerabolu, R.; Kotha, R. R.; Niyonsaba, E.; Dong, X.; **Manheim, J. M.;** Kong, J.; Riedeman, J. S.; Romanczyk, M.; Johnston, C. T.; Kilaz, G.; et al. Molecular Profiling of Crude Oil by Using Distillation Precipitation Fractionation Mass Spectrometry (DPF-MS). *Fuel* **2018**, *234*, 492–501.

Jin, C.; Viidanoja, J.; Li, M.; Zhang, Y.; Ikonen, E.; Root, A.; Romanczyk, M.; **Manheim, J.;** Dziekonski, E.; Kenttämäa, H. I. Comparison of Atmospheric Pressure Chemical Ionization and Field Ionization Mass Spectrometry for the Analysis of Large Saturated Hydrocarbons. *Anal. Chem.* **2016**, *88* (21), 10592–10598.